

INFORMATION TO USERS

This manuscript has been reproduced from the microfilm master. UMI films the text directly from the original or copy submitted. Thus, some thesis and dissertation copies are in typewriter face, while others may be from any type of computer printer.

The quality of this reproduction is dependent upon the quality of the copy submitted. Broken or indistinct print, colored or poor quality illustrations and photographs, print bleedthrough, substandard margins, and improper alignment can adversely affect reproduction.

In the unlikely event that the author did not send UMI a complete manuscript and there are missing pages, these will be noted. Also, if unauthorized copyright material had to be removed, a note will indicate the deletion.

Oversize materials (e.g., maps, drawings, charts) are reproduced by sectioning the original, beginning at the upper left-hand corner and continuing from left to right in equal sections with small overlaps. Each original is also photographed in one exposure and is included in reduced form at the back of the book.

Photographs included in the original manuscript have been reproduced xerographically in this copy. Higher quality 6" x 9" black and white photographic prints are available for any photographs or illustrations appearing in this copy for an additional charge. Contact UMI directly to order.

U·M·I

University Microfilms International
A Bell & Howell Information Company
300 North Zeeb Road, Ann Arbor, MI 48106-1346 USA
313/761-4700 800/521-0600

Order Number 9315052

Wave interaction with a pair of flexible cylinders

Duggal, Arun Sanjay, Ph.D.

Texas A&M University, 1992

U·M·I
300 N. Zeeb Rd.
Ann Arbor, MI 48106

**WAVE INTERACTION WITH A PAIR
OF FLEXIBLE CYLINDERS**

A Dissertation

by

ARUN SANJAY DUGGAL

Submitted to the Office of Graduate Studies of
Texas A&M University
in partial fulfillment of the requirements for the degree of
DOCTOR OF PHILOSOPHY

December 1992

Major Subject: Ocean Engineering

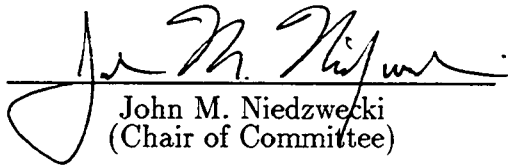
**WAVE INTERACTION WITH A PAIR
OF FLEXIBLE CYLINDERS**


A Dissertation

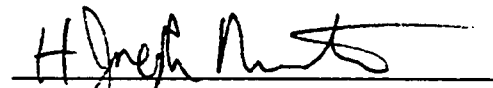
by

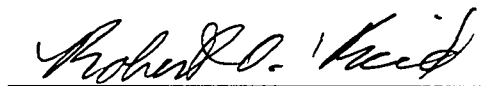
ARUN SANJAY DUGGAL


Approved as to style and content by:


John M. Niedzwecki
(Chair of Committee)


Loren D. Lutes
(Member)


H. Joseph Newton
(Member)


Robert O. Reid
(Member)


James T. P. Yao
(Head of Department)

December 1992

ABSTRACT

Wave Interaction with a Pair of Flexible Cylinders. (December 1992)

Arun Sanjay Duggal, B. Tech., Indian Institute of Technology, Madras, India;

M. S., University of Miami, Florida, U. S. A.

Chair of Advisory Committee: Dr. John M. Niedzwecki

This research study focused on regular and random wave interaction with a pair of long, flexible cylinders in close proximity, representative of Tension Leg Platform tendons or risers in 1006 m (3300 ft) of water. The objective was to study the mean square and extreme response of the cylinders with an emphasis on modeling the collision behavior of the cylinders. Also of interest was the modification of the wave-induced response as a function of spacing and orientation of the cylinders with respect to the incident waves. Due to the complexity of the phenomenon and the inherent uncertainty associated with the wave kinematics, the study comprised of an extensive large scale experimental investigation of the phenomenon and analysis of the extreme response and collision behavior in a probabilistic framework.

The experiments were conducted in the deepwater wave basin at the Offshore Technology Research Center (OTRC) at Texas A&M University. A consistent methodology for the distorted scaling of flexible deepwater structures was developed and applied to the design of the models. Unique instrumentation and techniques were also developed to estimate the inline and transverse displacement fields of the cylinders. Other measurements included the cylinder tension and reactions at the supports.

The single cylinder data were analyzed with an emphasis on understanding the wave-structure interaction. Comparisons between the inline response predicted using a standard finite element model, and that measured experimentally indicated the deficiency of the finite element model to predict the response accurately. Interference ratios, comparing the paired cylinder root mean square response to that of a single cylinder, were determined as a function of orientation and spacing.

The relative motion process between a pair of cylinders in tandem was studied for long duration random wave simulations. The hydrodynamic coupling between the cylinders was identified as an important collision mechanism in addition to the cylin-

der pretension difference and spacing. The collision process was modeled by adapting first-passage time and barrier crossing formulations from probabilistic mechanics. Non-Gaussian extreme response estimates were formulated using the Hermite transformation technique. Comparisons between the models and the experimental data showed the Hermite models to predict the extreme response fairly accurately while the Gaussian estimates were unconservative.

DEDICATION

This dissertation is dedicated to:

My mother and father, Lalita and Manohar Lal Duggal,
and my wife Anne

for all their love, patience and support;

and

my teachers and professors at:

St. Joseph's Boys' High School, Bangalore, India;

Indian Institute of Technology, Madras, India;

University of Miami, Florida, U.S.A.; and

Texas A&M University, Texas, U.S.A.

all of whom have contributed to this study.

ACKNOWLEDGEMENTS

I would like to express my sincere gratitude to my advisor and committee chairman, Professor John M. Niedzwecki, for his advice, encouragement, patience and guidance throughout the course of my study at Texas A&M University. His friendship will always be appreciated. I would also like to thank the rest of my committee, Professor Loren D. Lutes, Professor H. Joseph Newton, and Professor Robert O. Reid for their review and valuable comments on this research study. I would also like to thank Dr. Robert Runnels for serving as the Graduate Council Representative on my committee. I am grateful to Dr. Steve Winterstein, Stanford University, for an enlightening discussion on non-Gaussian extreme response estimation and for the use of some of his computer programs.

An experimental investigation of this magnitude could not have been accomplished without the help of many people. I would like to thank Mr. Peter Johnson, Facility Manager, OTRC, for his numerous suggestions during the course of the experimental program and the long nights spent in acquiring the data. I would also like to thank the rest of the OTRC technical staff: Mr. Darrell Ambler, Mr. Mike Linger, Mr. Fred Sims and Mr. John McIntyre for their help in the design and construction of the models and instrumentation, and in conducting the experiments, and Professor Finn Michelson for his help in designing some of the model components. I am grateful to Mr. Carl Fredrickson of the Structural Engineering Laboratory for his help in the design and construction of the curvature transducers. I am also grateful to Dr. Don Allen of Shell Development Company for his advice on materials and instrumentation for fluid-structure interaction experiments, and Dr. Richard Mercier, also of Shell Development Company, for his help in obtaining prototype structural properties of deepwater tendons and risers.

I would also like to thank all my friends and colleagues at Texas A&M University who have made my stay at the University so challenging and enjoyable. Finally, I would like to express my gratitude to my wife Anne for her constant love, encouragement and support throughout the course of my stay at Texas A&M University.

This study was supported in part by the Offshore Technology Research Center, National Science Foundation Engineering Research Centers Program Grant Number CDR—8721512. This support is gratefully acknowledged.

TABLE OF CONTENTS

	Page
1 INTRODUCTION	1
1.1 Overview of the Research Study	3
1.2 Objectives of the Research Study	6
2 DISTORTED MODELING OF FLEXIBLE DEEPWATER STRUCTURES	10
2.1 Inspectional Analysis	12
2.1.1 Uniform Beam with Constant Axial Tension and Distributed Lateral Load	12
2.1.2 Modeling TLP Tendons or Risers	14
2.2 Distorted Scale Modeling Applied to TLPs	17
2.2.1 Example: Design of a Distorted Scale Model for a TLP in 2,000 m of Water	18
2.3 Summary	20
3 EXPERIMENTAL INVESTIGATION: DESIGN AND PROCEDURES . .	22
3.1 Objectives of the Experimental Investigation	22
3.2 Prototype Wave and Structural Parameters	23
3.2.1 Wave Parameters	23
3.2.2 Structural Parameters	25
3.3 Description of the Experimental Facility	26
3.3.1 The OTRC Deep Water Wave Basin	26
3.3.2 Data Acquisition System	27
3.3.3 The GEDAP Data Acquisition and Analysis Software	28
3.4 Design of the Flexible Cylinder Models	28
3.4.1 Scaling the TLP Tendon and Riser	28
3.5 Estimating Cylinder Displacement	30
3.5.1 Estimating Displacement from Curvature	32
3.6 Flexible Cylinder Instrumentation	34
3.6.1 Curvature Transducers	34
3.6.2 Force Transducers	39

	Page
3.6.3 Tension Cells	40
3.6.4 Wave Gages	40
3.7 Model Construction and Installation	40
3.8 Experimental Program Summary	43
3.8.1 Wave Conditions	46
3.8.2 Single Cylinder and Paired Cylinder Tests	46
3.8.3 Testing Procedure	47
3.9 Comparison of Predicted and Measured Natural Frequencies	49
4 CHARACTERIZATION OF CYLINDER RESPONSE IN WAVE FLOWS	54
4.1 Background	54
4.2 General Description of Data	57
4.3 Analysis of the Single Cylinder Data	67
4.3.1 Regular Waves	67
4.3.2 Random Waves	80
4.4 Analysis of the Paired Cylinder Data	85
4.4.1 Characterization of Paired Cylinder Response	90
4.4.2 The Relative Motion/Collision Process	101
4.5 Summary of Data Analysis	105
5 PROBABILISTIC ANALYSIS OF THE PAIRED CYLINDER COLLISION BEHAVIOR	107
5.1 Collision Process Formulation	107
5.2 Probabilistic Formulation of the Collision Process	114
5.2.1 The First-Passage Time	115
5.2.2 Non-Gaussian Statistics by Hermitian Transformation of a Gaus- sian Process	119
5.3 Analysis of the Collision Behavior	122
5.4 Summary	134
6 SUMMARY AND CONCLUSIONS	136
6.1 Distorted Scale Modeling Methodology and Application	137
6.2 Fluid-Structure Interaction Phenomena	138
6.3 Probabilistic Modeling of the Collision Behavior	139

	Page
6.4 A Perspective on Future Research	141
REFERENCES	143
APPENDIX A: FINITE ELEMENT MODEL	147
A.1 Finite Element Formulation	147
A.1.1 Element Matrices	148
A.2 Finite Element Program	150
APPENDIX B: INSTRUMENT CALIBRATION AND DATA ACQUISITION	152
APPENDIX C: EXPERIMENTAL PROGRAM LOG	165
VITA	176

LIST OF FIGURES

Figure	Page
1.1 Tension leg platform (TLP).	2
1.2 Definition sketch of wave interaction with flexible cylinders.	4
1.3 Scope of research study.	7
2.1 Uniform beam with constant axial tension and lateral load.	12
2.2 Definition sketch of a TLP riser or tendon.	15
3.1 Layout of the OTRC wave basin.	27
3.2 Definition sketch of relationship between curvature and displacement.	32
3.3 Curvature, $\kappa(x)$, along the length of the cylinder.	35
3.4 Comparison between displacement computed from the finite element model and estimate from integration of curvature.	35
3.5 Comparison between computed and integrated displacement time series at -1.52 m for $T = 1.4$ seconds.	36
3.6 Comparison between computed and integrated displacement time series at -3.05 m for $T = 3.2$ seconds.	36
3.7 Comparison between computed and integrated displacement time series at -3.05 m for the random wave simulation.	37
3.8 Comparison between computed and integrated displacement spectra at -3.05 m for the random wave simulation.	37
3.9 Definition sketch of flexible cylinder model instrumentation.	38
3.10 Assembly of the flexible cylinder models.	42
3.11 Attachment of cylinder model to top support plate.	44
3.12 Attachment of cylinder model to bottom support plate.	44
3.13 Installation of the flexible cylinder models.	45
3.14 Measured free vibration spectrum for pretension T_1	51
3.15 Measured free vibration spectrum for pretension T_2	51
4.1 Sample data: random wave elevation.	59
4.2 Sample data: top tension.	60
4.3 Sample data: inline curvature (-7.47 m).	61

Figure	Page
4.4 Sample data: transverse curvature (-7.47 m).	62
4.5 Sample data: inline top reaction.	63
4.6 Sample data: transverse top reaction.	64
4.7 Time snapshots of inline curvature and the estimated displacement of the single cylinder.	65
4.8 Time snapshots of transverse curvature and the estimated displacement of the single cylinder.	66
4.9 Inline top reaction for a single wave cycle as a function of N_{KC}	70
4.10 Spectra of inline top reaction as a function of N_{KC}	71
4.11 Transverse top reaction for a single wave cycle as a function of N_{KC}	72
4.12 Spectra of transverse top reaction as a function of N_{KC}	73
4.13 Top reaction and curvature (-7.47 m) patterns for 5 wave cycles, $T =$ 1.4 seconds.	77
4.14 Inline and transverse displacement envelopes for a single cylinder with $T = 1.4$ seconds and pretension, T_1	78
4.15 Comparison between FE predictions and measured data for inline top reaction and curvature (-7.47 m) with $T = 1.4$ seconds.	79
4.16 Top reaction and curvature (-7.47 m) patterns for 5 wave cycles, $T =$ 2.6 seconds.	81
4.17 Comparison of filtered components of the inline curvature (-7.47 m) to (a) incident wave elevation and (b) transverse curvature.	82
4.18 Comparison between FE predictions and measured data for inline top reaction and curvature (-2.91 m), $T = 2.6$ seconds.	83
4.19 Comparison between low-pass filtered components of the inline curva- ture (-2.91 m) and FE predictions at (a) 0.4 Hz, and (b) 0.8 Hz.	84
4.20 Comparison between inline and transverse top reaction spectra for the two pretension conditions, random wave case.	86
4.21 Comparison between inline and transverse curvature (-7.47 m) spectra for the two pretension conditions, random wave case.	87
4.22 Comparison between spectra from FE model and the measured inline top reaction and inline curvature (-7.47 m).	88
4.23 Comparison between displacement spectra from FE model and esti- mated from the curvature data.	89

Figure	Page
4.24 Interference ratios for the inline and transverse top reactions for Cylinder 1, random wave case.	92
4.25 Interference ratios for the inline and transverse top reactions for Cylinder 2, random wave case.	93
4.26 Interference ratios for the inline and transverse curvature (-7.47 m) for Cylinder 1, random wave case.	94
4.27 Interference ratios for the inline and transverse curvature (-7.47 m) for Cylinder 2, random wave case.	95
4.28 Interference ratios for the inline and transverse top reactions for Cylinder 1, $T = 1.4$ seconds.	96
4.29 Interference ratios for the inline and transverse top reactions for Cylinder 2, $T = 1.4$ seconds.	97
4.30 Interference ratios for the inline and transverse top reactions for Cylinder 1, $T = 2.6$ seconds.	98
4.31 Interference ratios for the inline and transverse top reactions for Cylinder 2, $T = 2.6$ seconds.	99
4.32 Top reaction patterns for Cylinders 1 and 2 for $T = 1.4$ seconds. (a) tandem (0°), $2.5D$, (b) tandem (0°), $10D$, and (c) 22.5° , $2.5D$	100
4.33 Displacement time series for $T = 2.6$ seconds at location -9.06 m for Cylinders 1 and 2 (tandem, $2.5D$).	102
4.34 Displacement spectra for random wave excitation at location -9.06 m for Cylinders 1 and 2 (tandem, $2.5D$).	102
4.35 Relative motion as a function of tension difference between cylinders for random wave excitation (tandem, $2.5D$).	104
4.36 Relative motion as a function of cylinder spacing for random wave excitation with pretension $[T_1, T_1]$	104
5.1 Definition sketch: relative displacement/cylinder collision process.	108
5.2 Time snapshots for a pair of cylinders (tandem, $2.5D$) with pretension $[T_1, T_1]$ for random waves.	109
5.3 Time snapshots for a pair of cylinders (tandem, $2.5D$) with pretension $[T_1, T_1]$ for $T = 2.6$ seconds.	111
5.4 Time snapshots for a pair of cylinders (tandem, $2.5D$) with pretension $[T_1, T_2]$ for $T = 2.6$ seconds.	112

Figure	Page
5.5 R.m.s. relative displacement as a function of cylinder length for the pair of cylinders (tandem, $2.5D$) with pretension $[T_1, T_1]$ for random waves.	113
5.6 R.m.s. relative displacement as a function of cylinder length for the pair of cylinders (tandem, $2.5D$) with pretension $[T_1, T_2]$ for random waves.	113
5.7 Definition sketch: first-passage time.	116
5.8 Probability density function estimates for the incident random wave elevation (single cylinder, pretension T_1).	124
5.9 Probability density function estimates for the top tension (single cylinder, pretension T_1).	124
5.10 Probability density function estimates for the inline curvature at location -7.47 m (single cylinder, pretension T_1).	125
5.11 Probability density function estimates for the transverse curvature at location -7.47 m (single cylinder, pretension T_1).	125
5.12 Probability density function estimates for the inline top reaction (single cylinder, pretension T_1).	126
5.13 Probability density function estimates for the transverse top reaction (single cylinder, pretension T_1).	126
5.14 Probability density function estimates for the collision process at location -8.13 m (tandem, $2.5D$) with pretension $[T_1, T_1]$	128
5.15 Probability density function estimates for the collision process at location -8.13 m (tandem, $2.5D$) with pretension $[T_1, T_2]$	128
5.16 Upcrossing rate estimates for the collision process at location -8.13 m (tandem, $2.5D$) with pretension $[T_1, T_1]$	129
5.17 Upcrossing rate estimates for the collision process at location -8.13 m (tandem, $2.5D$) with pretension $[T_1, T_2]$	129
5.18 Reliability estimates for a barrier of $2.5D$ for the collision process at location -8.13 m (tandem, $2.5D$) with pretension $[T_1, T_1]$	130
5.19 Reliability estimates for a barrier of $2.5D$ for the collision process at location -8.13 m (tandem, $2.5D$) with pretension $[T_1, T_2]$	130
5.20 Reliability estimates for a duration $T = 100$ seconds for the collision process at location -8.13 m (tandem, $2.5D$) with pretension $[T_1, T_1]$	132

Figure	Page
5.21 Reliability estimates for a duration $T = 100$ seconds for the collision process at location -8.13 m (tandem, $2.5D$) with pretension $[T_1, T_2]$. .	132
5.22 Probability density function of the simulated (FEM) collision process at -9.06 m (tandem, $2.5D$) with pretension $[T_1, T_2]$	133
5.23 Upcrossing rates for the simulated (FEM) collision process at location -9.06 m (tandem, $2.5D$) with pretension $[T_1, T_2]$	133
5.24 Reliability estimates for the simulated (FEM) collision process at location -9.06 m (tandem, $2.5D$) with pretension $[T_1, T_2]$	134
A.1 Linear beam element used in finite element model of flexible cylinder.	148
B.1 Sample calibration curve: shear web force transducer.	155
B.2 Sample calibration curve: tension cell.	156
B.3 Sample calibration curve: curvature transducer (ABS).	157
B.4 Sample calibration curve: wave gage.	158

LIST OF TABLES

Table	Page
2.1 Distorted and undistorted scale relationships.	13
2.2 Distorted scale relationships for a TLP tendon or riser.	16
2.3 TLP hull properties.	18
2.4 TLP tendon properties.	19
3.1 Prototype regular wave conditions.	24
3.2 Prototype TLP tendon and riser properties.	25
3.3 Scaled model TLP tendon and riser properties.	29
3.4 Scaled regular wave conditions.	30
3.5 Summary of the single cylinder tests.	47
3.6 Summary of the paired cylinder tests.	48
3.7 Measured, predicted and desired natural frequencies [T_1].	52
3.8 Measured, predicted and desired natural frequencies [T_2].	53
4.1 Peak natural frequencies and corresponding reduced velocities for all single cylinder regular wave conditions.	74
4.2 Influence of pretension on r.m.s. cylinder response.	75
5.1 Computed moments of the incident waves and various response mea- surements.	114
5.2 Value of c_n for a softening system ($\alpha_4 > 3$).	121
B.1 Instrument calibration details.	152
B.2 Single cylinder tests: channel list 1.	159
B.3 Single cylinder tests: channel list 2.	160
B.4 Paired cylinder tests: channel list 1	161
B.5 Paired cylinder tests: channel list 2.	163
C.1 Single cylinder test log.	166
C.2 Paired cylinder test log.	168

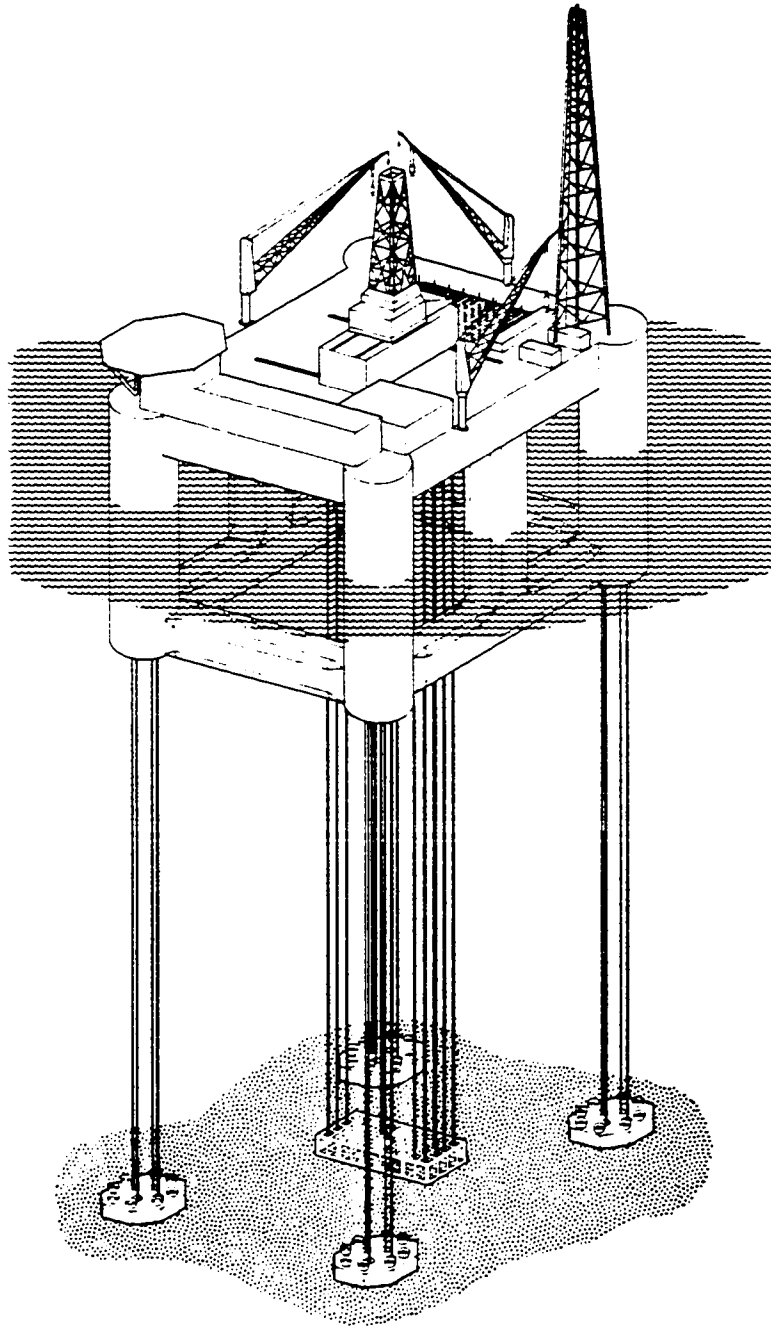
1. INTRODUCTION

With the reduction of oil reserves on land and on the continental shelf, the focus of the oil industry for domestic oil production has shifted to the large reserves of oil and gas located in water depths of 914 to 3048 m (3000 to 10,000 ft). At these water depths, conventional fixed platforms are no longer economically viable, and over the past two decades much research has been focused on alternative platforms and techniques to develop these fields. From the various structural concepts proposed, the Tension Leg Platform (TLP) is considered to be the choice for large field production. Two TLPs have already been deployed; the Hutton TLP in 150 m (492 ft) of water in the North Sea (1984) and Jolliet (1989) in 520 m (1706 ft) in the Gulf of Mexico (Hunter et al. 1990). A third, Auger, is under construction and is scheduled to be deployed in 1993 in 872 meters (2860 ft) of water in the Gulf of Mexico (Britton 1992). Additional projects are also under way in the North Sea where two TLPs, Snorre and Heidrun are under development for deployment in 310 and 350 m (1017 and 1150 ft) respectively (Lappegaard and Solheim 1991).

Figure 1.1 is an illustrative sketch of a Tension Leg Platform. The TLP consists of a large hull, anchored by vertical moorings kept under tension by the excess buoyancy of the hull provided by the large legs and pontoons. The deck is approximately 100 m (328 ft) square and the main legs have diameters of the order of 18.3 m (60 ft). The vertical mooring lines, called tethers or tendons, are constructed from steel tubulars and are approximately 0.6 to 1 m (2 to 3.3 ft) in diameter (Demirbilek 1989). Several production risers, which transport the oil and gas from the seafloor to the surface, run from the deck to the wellheads on the seafloor beneath the TLP.

The dynamic response of the risers and tendons due to the influence of loading due to waves, currents and hull motions, is a major area of concern in the design of Tension Leg Platforms. An accurate estimate of the dynamic response of these components is essential in determining their fatigue life and in assessing the reliability of the entire structure. The response estimates require an adequate understanding of the interaction of the flexible structural members with the environmental loading. Although the interaction phenomenon between waves and slender, flexible cylinders has been studied previously, there are many fundamental phenomena that are not

This dissertation follows the style of the ASCE *Journal of Engineering Mechanics*.



(Demirbilek 1989)

Figure 1.1: Tension leg platform (TLP).

well understood (Sarpkaya and Isaacson 1981). For marine risers or TLP tendons the fluid-structure interaction phenomenon is further complicated as they are usually deployed in groups in close proximity with one another. This group arrangement causes interference between the individual risers or tendons and can lead to a modification of the wave and current induced loads on them. Due to the flow separation around the cylinders and the partial shielding between the cylinders, the modifications in loading can be in both frequency and magnitude. Large or extreme displacements or response can lead to collisions between the individual tendons or risers and as a result can drastically reduce the reliability of the entire structure. An additional complication is that ocean waves are random in amplitude and frequency and can be multi-directional. This leads to complicated loading time histories and complicated system response behavior that is best described in a probabilistic manner.

1.1 Overview of the Research Study

This study focuses on the fundamental phenomenon resulting from the interaction of surface waves with long, flexible cylinders. Specifically the focus is on the dynamic response of, and interaction between a pair of flexible cylinders subjected to regular and random waves, as shown schematically in Figure 1.2. The flexible cylinders are representative of TLP risers and tendons in approximately 1006 m (3300 ft) of water. Of particular interest is the mean square and extreme structural response, and the collision behavior of the cylinders in close proximity with one another. Also of interest is the modification of the wave-induced loads and response of the cylinders due to the interference or shielding between them. Due to the complexity and uncertainty of the wave-flexible cylinder interaction, and the probabilistic nature of the wave kinematics, this phenomenon is studied by making an extensive experimental investigation of the interaction phenomenon and describing the extreme response and collision behavior of the cylinders in a probabilistic framework. The study integrates results from the experimental investigation and the response analyses to arrive at a consistent description of the extreme response and collision behavior of the cylinders.

In order to arrive at extreme response statistics, one requires an accurate description of the probability density function of the response process, and related phenomenon like the upcrossing rate and the probability density of the first-passage time. For nonlinear structures subjected to nonlinear wave forces, like the risers or tendons being considered, the response process is non-Gaussian even if the incident wave elevation process is assumed to be Gaussian. Therefore, the assumption that

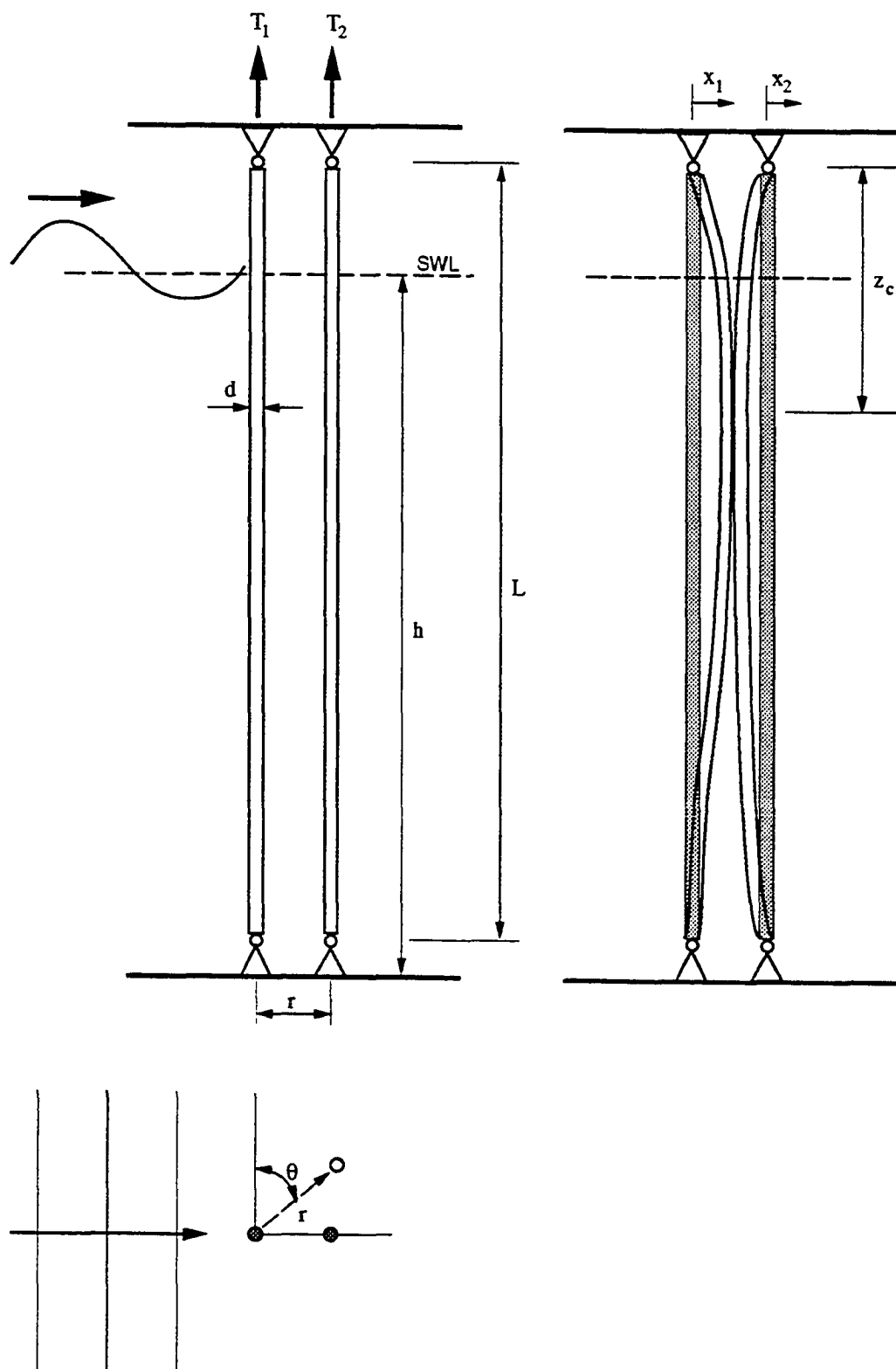


Figure 1.2: Definition sketch of wave interaction with flexible cylinders.

the response processes are Gaussian can lead to significant errors in the estimation of the extreme statistics. The probabilistic analysis addresses this point by comparing estimates from Gaussian and non-Gaussian formulations of the statistics and comparing them to non-parametric estimates obtained from the data. Approximations inherent in the estimation of the upcrossing rates and the first passage time probability density function are also discussed with respect to data from the experimental program.

The experimental response data are also compared to numerical simulations of the response obtained from a 2-D finite element model of the cylinders using the relative motion form of the Morison's equation (Morison et al. 1950) to model the inline wave forces. Due to the use of the Morison representation of wave loading, some physical phenomena that may influence the response are not accounted for in the simulations; e.g., vortex shedding and the hydrodynamic interference between the pair of cylinders. Comparisons between the response estimates from the numerical simulations and the experimental data help in assessing the influence of interference, vortex shedding, and other physical phenomena not accounted for in the equations of motion.

The experimental investigation is a systematic study of the interaction phenomenon as a function of wave and structural parameters as illustrated in Figure 1.2. The experiments were conducted in the three-dimensional wave basin at the Offshore Technology Research Center (OTRC). The wave basin has a length of 45.7 m (150 ft), width of 30.5 meters (100 feet) and a maximum depth of 16.76 m (55 ft), and is capable of generating waves with a maximum height of 0.84 m (2.75 ft). The tests are first conducted with a single cylinder to provide data for comparison with data from the paired cylinder tests. As there have been no systematic experimental studies at this scale in waves, the experimental investigation provides new data and insight into the problem and allows for characterizing the wave-induced forces and response as a function of cylinder spacing and orientation with respect to the incident waves. A unique aspect of the experimental study is the estimation of the complete inline and transverse displacement fields of the cylinders using instrumentation and techniques developed as part of this study. This information is necessary for studying the collision behavior of the cylinders as it provides estimates of the relative motion between the cylinders along the complete length of the cylinders.

Most previous experimental investigations on flow past flexible cylinders studying the interference phenomenon between cylinders in close proximity, have been con-

ducted with steady or oscillating flow (Sarpkaya and Isaacson 1981, Blevins 1990). These studies have shown the interaction between the cylinders to be influenced by both the fluid and structural parameters as well as by the interference due to flow separation and the proximity of the cylinders. In the design of the experimental investigation, care was taken to ensure that the wave and structural dynamic characteristics of the prototype were preserved in the models, to provide a realistic representation of the physical phenomena being studied.

The study also addresses the use of distorted scaling techniques to model flexible deepwater structures. Use of conventional Froude scaling in modeling flexible structures in very deep water, usually results in the model scale being determined by the ratio of tank to prototype water depths. This can result in undesirably small model scales. Due to the non-similitude of Reynold's number, tests conducted at small model scales are subject to errors caused by viscous scale effects. The use of small model scales also tends to require wave generation out of the best operating range of the wave basin, and also increases the difficulty in model construction and instrumentation. Distorted scale modeling as approached in this study allows one the ability to represent a flexible structure by a model with a horizontal length scale based on the optimum operating conditions of the wave basin and by a vertical scale "distorted" to the ratio of tank to prototype water depths. This helps reduce the errors due to scale effects due to the use of larger model scales, and ease the design and constructability issues associated with scale model tests.

1.2 Objectives of the Research Study

The scope of the research study is presented in Figure 1.3. Due to the uncertainty of the wave-structure interaction phenomenon, and the shortcomings of analytical and numerical models to adequately describe it, this study involves integrating a detailed experimental investigation of the phenomenon and the development of a probabilistic description of the cylinder response. The focus of the experimental investigation is to provide fundamental data relating to the response of the cylinders as a function of their orientation and spacing with respect to the incident waves. These data are also used in conjunction with the probabilistic models applied to describe the extreme response and collision behavior of the cylinders.

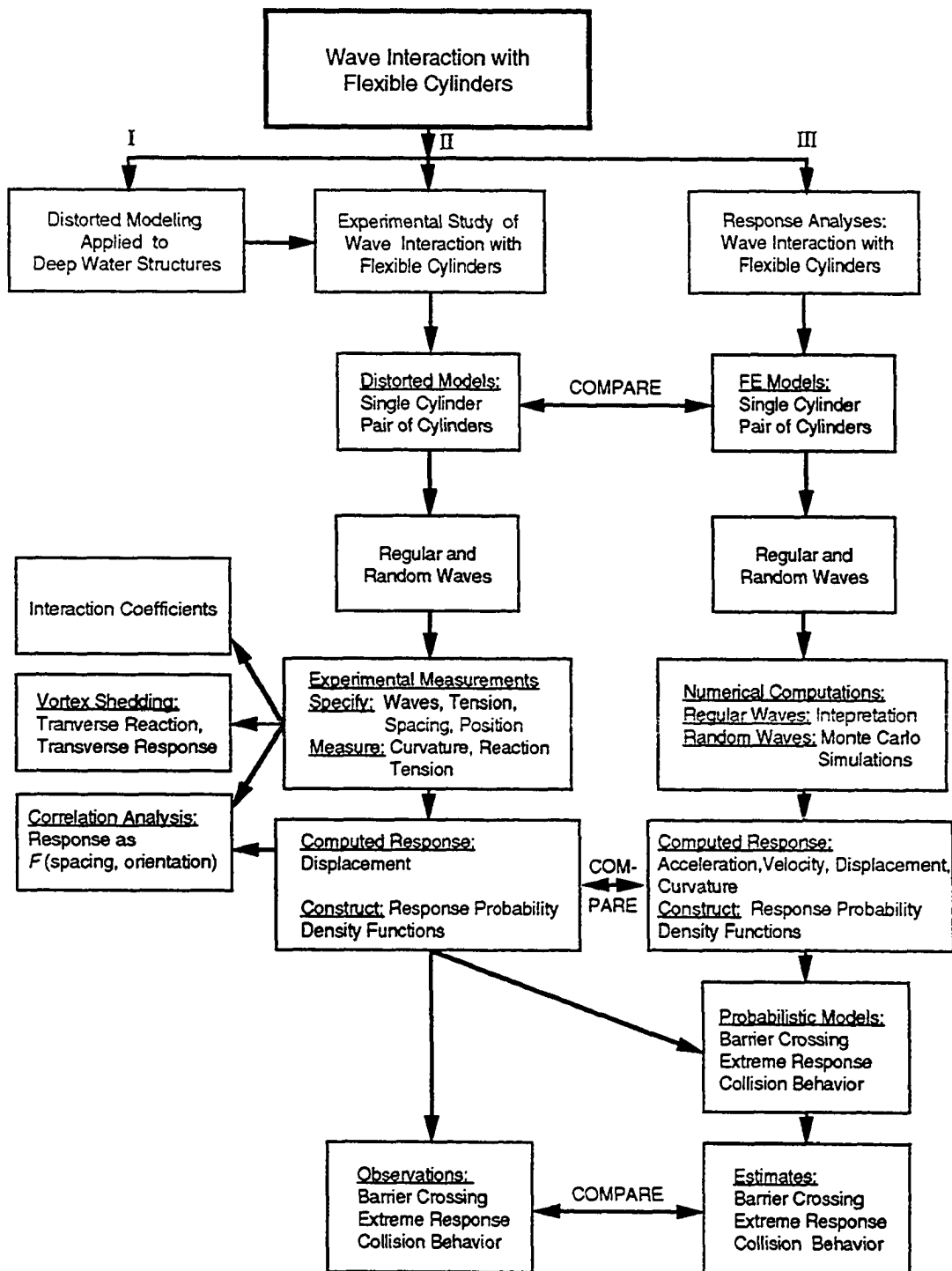


Figure 1.3: Scope of research study.

The objectives of the research study are to:

- study the extreme response and collision behavior of a pair of flexible cylinders in close proximity, in both regular and random seaways;
- characterize the wave-induced response and forces on the cylinders as a function of their orientation and spacing with respect to the incident waves;
- compare the measured wave-induced forces and response of the cylinders to those predicted by finite element models of the cylinders;
- address the use of distorted scale modeling techniques for the scale modeling and testing of flexible, deepwater structures.

Section 2 focuses on the application of distorted scale modeling techniques to flexible deep water structures. The “inspectional analysis” approach (Le Méhauté 1964) is used to determine distorted scaling relationships from the differential equation of motion. This approach is illustrated by using a simple example of a uniform beam subjected to lateral loading and axial tension. The case of a flexible cylinder with uniformly varying tension, representative of a riser or tendon, is then considered. For this case the use of distorted modeling leads to inconsistencies between the scaled mass and weight of the structure. These inconsistencies are discussed and guidelines are presented to allow the selection of parameters for the model. The final section focuses on the more general application of this methodology to the design of a distorted physical model of a TLP.

Section 3 describes in detail the experimental design, set-up and test matrix for the experimental investigation. The physical models are designed based on the distorted scale relationships and guidelines derived in the previous section, using typical prototype properties of TLP risers and tendons in 1006 m (3300 ft) of water. The technique and instrumentation used to estimate the displacement field of the cylinders from the curvature measurements is presented. Extensive numerical simulations of the models were conducted with a finite element model of the cylinder to verify the technique, determine the number and location of the curvature transducers, and in the selection of force and tension instrumentation. The cylinders were instrumented to obtain the inline and transverse curvature field, the top and bottom inline and transverse reactions, and the tension at the ends of the cylinders. The experimental test matrix and procedures used are summarized at the end of the section.

The data obtained from the experiments are analyzed in Section 4. The single cylinder data are studied as a function of non-dimensional parameters like the Keulegan–Carpenter number and the reduced velocity to allow comparison with results obtained from previous experimental investigations (Blevins 1990). Comparisons between the experimental data and the numerical simulations are made for the inline reaction and curvature. The paired cylinder data are presented as interference ratios, relative to the root mean square (r.m.s.) response of a single cylinder, as a function of cylinder orientation and spacing. Some examples were also chosen to further illustrate the complex behavior observed. The section ends with an introduction to the relative displacement process which is studied in more detail in Section 5.

Section 5 focuses on the probabilistic formulation of the collision process between the two cylinders arranged in tandem. The collision behavior of the cylinders is formulated as a random process with a collision being equivalent to crossing a barrier equal to the spacing between the cylinders. This allows the use of barrier crossing and first-passage time formulations from probabilistic mechanics to describe the extreme statistics of the collision process. Due to the non-Gaussian nature of the response, non-Gaussian extreme response formulations are obtained by applying the Hermite transformation technique using the first four moments of the response (Winterstein 1985). Comparisons are made between the Gaussian and non-Gaussian statistics, and non-parametric estimates from the experimental data. The comparisons show the appropriateness of the first-passage formulation to describe the collision behavior of the cylinders and the importance of accounting for the non-Gaussian nature of the response in determining the extreme statistics.

Section 6 summarizes the results obtained from the various aspects of this research study and concludes with a perspective on future research. Appendix A provides a brief description of the formulation of the finite element model used extensively in this study to design the experiments and for comparison with the data. Appendix B provides details about the instrumentation calibration and the data acquisition and Appendix C summarizes the test log of the experimental investigation and the archiving of the data.

2. DISTORTED MODELING OF FLEXIBLE DEEPWATER STRUCTURES

Conventional scale modeling of structures in waves uses Froude similitude with one geometric scale. Using this approach, the scale at which model tests of deepwater structures are conducted is usually determined by the ratio of tank depth to prototype water depth. For example, to test a flexible structure in 1006 m (3300 ft) of water in a deepwater wave basin 16.76 m (55 ft) deep (e.g., the OTRC wave basin) would restrict the model scale to 1:60. This ratio gets smaller as we consider structures in even deeper water depths, or are restricted to wave basins with smaller depths.

Conducting experiments at small model scales results in a number of problems. Due to the requirement for the similitude of Froude number for water wave modeling, and the use of water, the Reynold's number of the flow is not scaled properly. This problem increases by the power of $3/2$ with a linear decrease in length scale and leads to significant errors in representing the viscous flow regime around the structure especially for drag dominated structures (Carneiro 1981, Pranesh and Mani 1988, Munson et al. 1990). Another problem with small scale models is that the desired scaled wave conditions may not be at the best operating range of the wave tank. For example, in large wave basins like the OTRC wave basin capable of reproducing storm waves at a scale of 1:25, operating at scales smaller than 1:100 results in a less than desirable wave field with an increase in the tendency to produce crosstank waves and problems in reproducing the high frequency end of the wave spectrum. Modeling of flexible structures introduces the additional complication of requiring Cauchy similitude (elasticity). The difficulty in obtaining the desired stiffness of the structure increases as the model scale gets smaller due with a lack of materials with a low enough modulus of elasticity and good mechanical properties. In the case of slender flexible structures like tendons and risers, small model scales make it very difficult to build and instrument the structural members.

To test flexible deepwater structures like a TLP, one would like to conduct the experiments at the optimal scale for the given structure and wave basin, rather than be restricted by the ratio of tank to prototype water depths. In principle, distorted scale modeling provides one with the flexibility to do so. Distorted scale modeling, as considered for this study, allows one to choose the horizontal length scale based

on the optimum operating range of the wave basin and model size, while the vertical length scale is “distorted” to the ratio of the tank to prototype water depths. The waves are modeled using Froude similitude and the horizontal scale only.

To model the wave-structure interaction phenomenon correctly, the scale model of the flexible structure when subjected to the desired scaled wave conditions, should behave in a manner similar to that of the prototype. To apply the above idea of distorted scale modeling, one needs relationships which allow one to scale the pertinent wave and structural prototype properties to model properties in terms of the two length scales. These relationships are generally obtained by dimensional analysis, inspectional analysis, or by deriving the laws from the Navier-Stokes equation and the theory of elasticity (Le Méhauté 1962, 1965).

Dawson (1977), Carneiro (1981) and Pranesh and Mani (1988) illustrate the application of dimensional analysis in deriving laws of similitude for wave-flexible structure interaction. However, the physics of the wave-flexible structure interaction is significantly oversimplified in arriving at the similitude relationships. The inspectional analysis approach described by Le Méhauté (1962, 1965) requires the problem to be formulated mathematically as a differential equation from which the laws are derived by inspection. This approach also aids in determining the influence of scale effects and in the analysis of the results. The differential equation does not need to be integrated; as noted by Le Méhauté (1965) a well designed scale model can be considered as the best analog computer.

Le Méhauté (1965) illustrates the application of the inspectional analysis approach, and Dillingham (1984) the use of dimensional analysis, to the modeling of marine risers and TLP tendons using a single length scale. The relationships for the various wave and structural parameters obtained from the two approaches were the same. However, the inspectional analysis approach used by Le Méhauté is easily extensible to distorted modeling with two length scales.

In the sections to follow, the inspectional analysis approach is used to derive distorted scale relationships for flexible, deepwater structures. To illustrate the approach, the case of a uniform beam under constant axial tension, subjected to a distributed lateral load is first considered. This example is then extended to apply to a TLP riser or tendon subjected to wave loading. For the case of the riser or tendon, the inconsistencies between the scaled mass and weight of the structure due to distorted scaling, are discussed in detail and guidelines are presented to allow one to arrive at the optimal model. The final section considers the application of the

distorted scale modeling techniques to design a realistic physical model of a TLP in very deep water.

2.1 Inspectional Analysis

2.1.1 Uniform Beam with Constant Axial Tension and Distributed Lateral Load

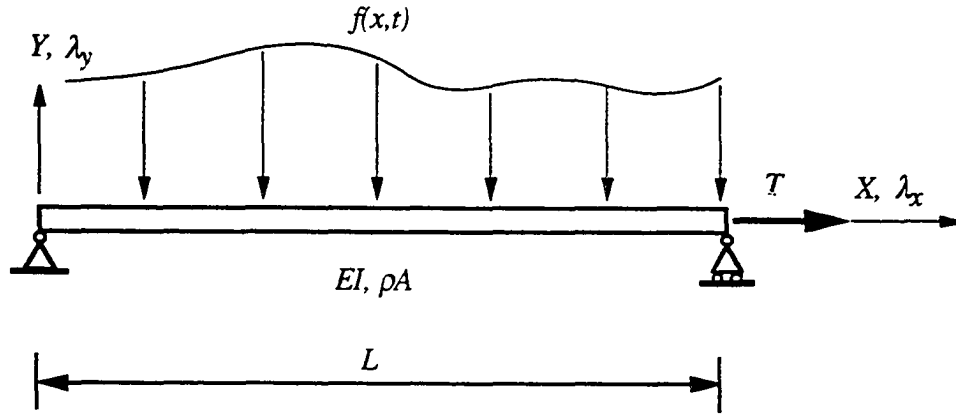


Figure 2.1: Uniform beam with constant axial tension and lateral load.

The equation of motion of the uniform beam with constant axial tension, T , subjected to a laterally distributed load, $f(x,t)$, as illustrated in Figure 2.1 is given by (Craig 1981)

$$-EI \frac{\partial^4 y}{\partial x^4} + T \frac{\partial^2 y}{\partial x^2} - \rho A \frac{\partial^2 y}{\partial t^2} = f(x,t) \quad (2.1)$$

where E is the modulus of elasticity, I is the moment of inertia, ρ is the density of the material, and A is the cross-sectional area of the beam.

The length scale along the X axis, λ_x , is defined as the ratio of the model to prototype lengths in the X direction. The corresponding length scale along the Y axis is λ_y . The total lateral force, $F(t)$, is scaled using Froude scaling with λ_y . Keeping in mind that ultimately the lateral loading of interest is due to water waves, using Froude similitude the lateral force scales as λ_y^3 . Therefore the lateral loading

intensity, $f(x, t)$, will scale as

$$\lambda_{f(x,t)} = \frac{\lambda_y^3}{\lambda_x} \quad (2.2)$$

To ensure dimensionality, the other terms in Equation 2.1 have to scale with the same relationship. Therefore,

$$\lambda \left[EI \frac{\partial^4 y}{\partial x^4} \right], \lambda \left[T \frac{\partial^2 y}{\partial x^2} \right], \lambda \left[\rho A \frac{\partial^2 y}{\partial t^2} \right] = \frac{\lambda_y^3}{\lambda_x} \quad (2.3)$$

Considering the lateral stiffness term, $EI \partial^4 y / \partial x^4$, from the definition of a derivative we see that:

$$\lambda \left[\frac{\partial^4 y}{\partial x^4} \right] = \frac{\lambda_y}{\lambda_x^4} \quad (2.4)$$

The lateral stiffness, EI , will scale as

$$\lambda_{EI} = \lambda_y^2 \lambda_x^3 \quad (2.5)$$

Similarly, scale relationships for ρA and T are derived and presented in Table 2.1. Also presented in the table are the scale relationships obtained by considering conventional undistorted scaling techniques (Le Méhauté 1965, Dillingham 1984). It can be seen that for λ_x equal to λ_y , the distorted scale relationships reduce to the undistorted relationships.

Table 2.1: Distorted and undistorted scale relationships.

Parameter	Undistorted Scales	Distorted Scales
Length, L_x	λ	λ_x
Length, L_y	λ	λ_y
Time, t	$\lambda^{0.5}$	$\lambda_y^{0.5}$
Force, F_y	λ^3	λ_y^3
Mass/unit length, ρA	λ^2	λ_y^3 / λ_x
Lateral Stiffness, EI	λ^5	$\lambda_y^2 \lambda_x^3$
Tension, T	λ^3	$\lambda_y^2 \lambda_x$

It is of interest to verify if the natural frequencies and lateral displacement of the beam scale consistently. The natural frequencies of the uniform beam defined by Figure 2.1 and Equation 2.1 are given by the closed form expression

$$\omega_i = \sqrt{\left(\frac{i\pi}{l}\right)^4 \left(\frac{EI}{\rho A}\right) + \left(\frac{i\pi}{l}\right)^2 \left(\frac{T}{\rho A}\right)} \quad (2.6)$$

where, ω_i corresponds to the natural frequency of i^{th} mode of vibration. Using the distorted scale relationships in Table 2.1 we can express the scale relationship between model and prototype natural frequencies (ω_m/ω_p) as

$$\lambda_\omega = \sqrt{\left(\frac{1}{\lambda_x^4}\right) (\lambda_y^2 \lambda_x^3) \left(\frac{\lambda_x}{\lambda_y^3}\right) + \left(\frac{1}{\lambda_x^2}\right) (\lambda_y^2 \lambda_x) \left(\frac{\lambda_x}{\lambda_y^3}\right)} = \lambda_y^{-0.5} \quad (2.7)$$

It is seen that this scales with the same relationship as the frequency of the incident waves (Froude scaling). This is important from a dynamic view point as it ensures that for the distorted scale model, the ratio of forcing frequency to natural frequency is maintained from the prototype.

The displacement of the beam due to a concentrated load at the center, P , is given by

$$\delta_{\frac{L}{2}} = \frac{PL^3}{4TL^2 + 48EI} \quad (2.8)$$

Using the distorted scale relationships the scale ratio between model and prototype lateral displacement (δ_m/δ_p) is given by

$$\lambda_\delta = \frac{\lambda_y^3 \lambda_x^3}{\lambda_y^2 \lambda_x \lambda_x^2 + \lambda_y^2 \lambda_x^3} = \lambda_y \quad (2.9)$$

Again, this is consistent with our definition of the scale relationships. The above examples show that for the distorted model of a uniform beam under constant axial tension, the ratio of forcing frequency to natural frequency is maintained from prototype to model, both being scaled by $\lambda_y^{-0.5}$. It is also seen that the lateral displacements scale by λ_y .

2.1.2 Modeling TLP Tendons or Risers

A TLP riser or tendon can be represented by a long beam under tension, T_o , applied at the top as illustrated by Figure 2.2. Due to the effective weight of the riser, the tension will vary as a function of water depth, with the minimum tension being at the bottom of the riser or tendon. For the case of a uniform riser or tendon whose effective weight is constant along its length, the tension can be assumed to vary linearly with

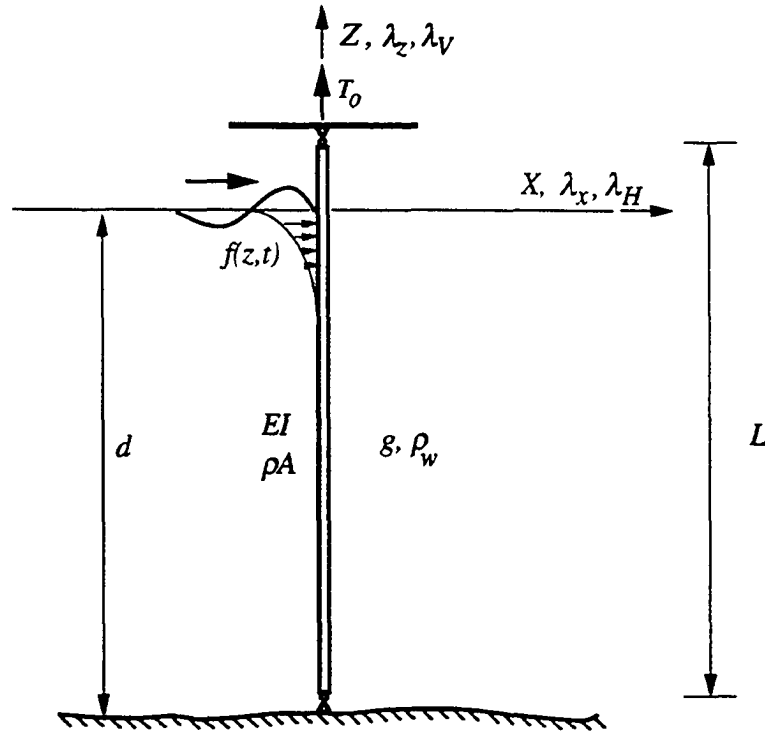


Figure 2.2: Definition sketch of a TLP riser or tendon.

water depth. From Figure 2.2 and Equation 2.1, the equation of motion for such a riser or tendon is given by

$$EI \frac{\partial^4 x}{\partial z^4} - [T_0 - T'z] \frac{\partial^2 x}{\partial z^2} + T' \frac{\partial x}{\partial z} + \rho A \frac{\partial^2 x}{\partial t^2} = f(z,t) \quad (2.10)$$

where, T' is the linear variation of tension along the length of the riser, equivalent to the effective weight per unit length, $g\rho_w$, where ρ_w is the density of the water and g is acceleration due to gravity.

Based on Figure 2.2, the horizontal length scale, λ_H , is equal to λ_x which is defined as the ratio of the model length to prototype length in the X direction. Likewise, λ_V is the vertical length scale equal to λ_z in the Z direction.

Assuming that the lateral loading is due to waves, and that the wave loading is modeled using Froude similitude and the horizontal scale, the lateral loading intensity scales as in Equation 2.2

$$\lambda_{f(z,t)} = \frac{\lambda_H^3}{\lambda_V} \quad (2.11)$$

Table 2.2: Distorted scale relationships for a TLP tendon or riser.

Cylinder Parameter	Distorted Scale
Outer Diameter, D	λ_H
Cylinder Length, L	λ_V
Time, t	$\lambda_H^{0.5}$
Total Wave Force, $F(t)$	λ_H^3
Mass/unit length, ρA	λ_H^3/λ_V
Lateral Stiffness, EI	$\lambda_H^2 \lambda_V^3$
Top Tension, T_o	$\lambda_H^2 \lambda_V$
Effective Weight, T'	λ_H^2

As in the previous section, scale factors for the parameters in Equation 2.10 can be derived and are presented in Table 2.2.

Comparing the equations of motion of the uniform beam under tension with that of the riser or tendon it is seen that the difference between the two equations is the parameter T' which accounts for the influence of the effective weight of the riser/tendon. As this parameter accounts for the weight of the structure its scale should be the same as the mass, ρA , as the scale of acceleration due to gravity, λ_g , equals 1. Comparing the two scale relationships in Table 2.2 it is seen that they are not the same. This inconsistency is brought about by the distortion of the model and is seen to increase linearly with an increase in the distortion of the model (λ_H/λ_V). Another inconsistency due to distorted modeling is the distribution of wave loading on the riser or tendon. Froude scaling ensures that the total wave force is scaled consistently; however, for a distorted scale model a larger percentage of the length of the riser or tendon will be subjected to wave loading than in the prototype. This has to be considered when analyzing results from such a model design.

The mass/weight inconsistency is important as, along with the tension, it has a direct influence on the dynamic behavior of the riser or tendon. Previous studies of flow interaction with flexible cylinders have determined that a non-dimensional ratio called the mass ratio is important in characterizing the fluid-induced dynamic behavior of the structure (Blevins 1990). To ensure dynamic similarity, the mass ratio in the model should be chosen to be the same as that in the prototype. The

mass ratio, M_r , is defined as the ratio of the structural mass to the mass of fluid it displaces

$$M_r = \frac{m}{\rho_w D^2} \quad (2.12)$$

where m represents the mass/unit length of the structure (usually includes the added mass) and $\rho_w D^2$ represents the mass of water displaced. As the ratio of fluid mass to structural mass increases, the structure is more susceptible to flow-induced vibration.

The mass ratio can be used as a guideline in determining the mass or weight/unit length of the model. The mass/unit length of the distorted model should be chosen so that the mass ratio is that of the prototype. Then the top tension applied to the riser or tendon should be used to “tune” the distorted model to provide the desired natural frequencies as scaled from the prototype. This can be done using a finite element model of the riser/tendon like the one described in Appendix A. This process is illustrated in Section 3 where the flexible cylinders used for the experiments are designed using distorted scaling.

2.2 Distorted Scale Modeling Applied to TLPs

As illustrated and discussed in Section 1, a TLP consists of a large, rigid, floating hull moored in place by flexible tendons. Due to the size of the hull and the exponential decay of the magnitude of wave kinematics with water depth, a majority of the wave induced forces are on the hull of the TLP. The tendons thus serve to provide the lateral and axial stiffness of the system. In many conventional model tests of TLPs, the focus has mainly been on the overall dynamics of the system and not on the specifics of the riser or tendon dynamics. In these cases, the groups of risers and tendons are replaced by a representative riser or tendon with equivalent dynamic properties. In cases where the behavior of the risers and tendons are also of interest, the risers and tendons have to be designed so that the fluid-structure interaction phenomenon is represented adequately and that they can be instrumented.

In a distorted scale model of a TLP, the hull and the waves are designed using Froude similitude and the horizontal scale (λ_H) only. This ensures that the wave-structure interaction phenomenon can be modeled at the largest scale possible in the wave basin used for the tests, reducing the viscous scale effects. The tendons and risers can be modeled using the distorted scale techniques outlined in the previous section with the vertical scale equal to the ratio of tank to prototype water depths and the same horizontal scale as that used in the design of the hull. As most of the

wave forces will be on the hull, the influence of wave force distribution distortion on the risers and tendons will not significantly alter the dynamics of the entire system. This approach to modeling a deep water TLP is illustrated in the following example where a hypothetical TLP in 2,000 meters of water is modeled in a tank of depth 16.76 m.

2.2.1 Example: Design of a Distorted Scale Model for a TLP in 2,000 m of Water

The hypothetical TLP is to be modeled in a wave basin 16.76 m deep. The basic prototype properties of the TLP hull and tendons are presented in Tables 2.3 and 2.4. For this example two wave conditions are chosen to represent the domain of interest; Wave 1 is representative of a design wave with a height of 22 m (72.18 ft) and a period of 15 seconds, and Wave 2 is a high frequency wave of height 2 m (6.56 ft) and period 7 seconds.

Table 2.3: TLP hull properties.

Parameter	Prototype	Undistorted	Distorted
Column Diameter (m)	25.0	0.208	0.833
Pontoon c.s. (m)	11.0 × 11.0	0.092 × 0.092	0.36 × 0.367
Draft (m)	37.5	0.313	1.25
C/C spacing	76.0	0.633	2.533
Platform Displacement (N)	1.045 × 10 ⁹	604.75	38703.7
N_R Wave 1	1.33 × 10 ⁸	101446	814464
N_R Wave 2	2.67 × 10 ⁷	19750	158262

If one were to use conventional Froude scaling to model the entire structure, the model scale would be 1:120 (tank depth/prototype depth). Using this model scale the prototype properties of the TLP are scaled and presented in the third column of Tables 2.3 and 2.4. The tables indicate the small size of the model and the tendons, where the TLP hull is reduced to a 0.83 by 0.83 meter structure with tendons 7 mm in diameter. The wave conditions are also at the high frequency end of most wave basin wave generating capabilities and would probably be undesirable. The

Table 2.4: TLP tendon properties.

Parameter	Prototype	Undistorted	Distorted
Depth, d (m)	2000	16.66	16.66
Outer Diameter, D (m)	0.8128	6.77×10^{-3}	2.71×10^{-2}
Lateral Stiffness, EI (N-m ²)	1.44×10^6	5.79×10^{-2}	9.27×10^{-1}
Mass/length, ρA (kg/m)	727.91	5.06×10^{-2}	0.8183*
Added Mass/length, $\rho_w V$ (kg/m)	518.87	3.60×10^{-2}	0.576*
Weight/length (air), w_a (N/m)	7141	4.13×10^{-3}	8.02*
Buoyancy/length (N/m)	5090	2.95×10^{-3}	5.65*
Effective Weight/length, (N/m)	2051	1.19×10^{-3}	2.377*
Top Tension, T (N)	2.0×10^7	11.57	46.55*
Mass Ratio, M_r	1.9	1.9	1.9
N_R Wave 1	4.33×10^6	3295	26483
N_R Wave 2	8.44×10^5	642	5146

*Inconsistent due to distorted scaling.

Reynold's numbers are also seen to be very low for the 1:120 model. In a large wave basin facility like the OTRC, the optimum wave generation envelope lies between 1 and 3 seconds, with a maximum attainable wave height of approximately 0.8 to 1.0 m between 2 and 3 seconds. If one were to scale the waves at a scale of 1:30, the wave conditions would be at the optimum operating conditions of the wave basin. Choosing the horizontal scale to be 1:30 and distorting the vertical scale to 1:120, the distorted model properties are presented in column four of Tables 2.3 and 2.4. The hull is modeled based on the 1:30 scale only while the tendons are modeled using the distorted scaling relationships presented in Table 2.2. It is observed that the distorted model has much larger dimensions ($\times 4$) and that the Reynold's number increased by almost an order of magnitude.

The scaling of the mass and weight of the tendons is incompatible as described earlier. In order to maintain dynamic similarity the adjustments have to be made to the mass, axial stiffness and weight of the hull and tendons. Assuming the added mass of the model tendons and maintaining the mass ratio of 1.9 of the tendons, the

required mass/unit length of the tendons is obtained. Based on this value of the mass and the requirement that the natural frequencies of the tendons should scale with the wave frequencies, the required pretension is calculated using Equation 2.6 as a first estimate. As the tension is less than that required by the scaling laws, the weight of the platform has to be adjusted to provide the desired tension. However by modifying the weight of the platform to provide the right tendon dynamics, the TLP natural frequencies will be affected. By adjusting stiffnesses in the tendons these frequencies can also be adjusted. For example, to scale the heave natural frequency of the structure with that of the waves, the axial stiffness of the tendons can be adjusted to account for the change in deck and tendon mass including the change in added mass (heave) caused by the change in diameter (from prototype to model).

The above example, though by no means a complete design of a distorted TLP model, serves to illustrate the distorted modeling technique. It is seen that there are several advantages to using a distorted scale model, especially for deepwater structures. Even though the distorted modeling technique gives rise to inconsistencies in weight and mass, dynamically similar models can be designed by appropriate modification of various tendon and hull parameters.

2.3 Summary

The section presents a consistent and practical approach to designing distorted scale models of flexible deepwater structures. This distorted modeling approach allows the ability to determine the model scale on the optimal operating conditions of the wave basin and does not force the model scale to be restricted by the available tank depth.

The inspectional analysis approach was used to obtain distorted scale relationships for flexible deepwater structures. Three examples, with increasing levels of difficulty, were used to illustrate the technique. The first considered a uniform beam subjected to uniform tension and lateral loading and was found to scale correctly. For the tendon/riser example, inconsistencies between the scaled mass and the weight of the structure, and in the wave force distribution were observed. However this was overcome by adjusting the pretension to provide the desired natural frequencies. The third example focused on modeling the entire TLP structure where the hull was modeled using the horizontal scale only, while the tendons were modeled using the distorted scale relationships. The advantages of distorting the models was shown by comparing a distorted model to an undistorted one (at a much smaller scale). It was also shown that by appropriate adjustment of hull and tendon parameters, a

dynamically similar model can be obtained whose dimensions are optimized to match the best operating conditions of the wave basin, while best representing the wave structure interaction phenomenon.

3. EXPERIMENTAL INVESTIGATION: DESIGN AND PROCEDURES

The experimental investigation focused on the interaction of regular and random waves with a pair of flexible cylinders in close proximity. One main objective was to obtain measurements of the displacement of the cylinder to study the extreme response and collision behavior of the cylinders. Another objective was to characterize the wave-induced response as a function of orientation and spacing with respect to the incident wave direction. Tests were also conducted with a single cylinder for all wave and pretension conditions to provide insight into the wave-structure interaction phenomenon and to serve as a comparison with the paired cylinder data.

The scale models were designed to have physical and dynamic properties representative of TLP tendons or risers in 1006 m (3300 ft) of water using the distorted scale relationships derived in the previous section. The experiments were conducted in the three-dimensional deepwater wave basin facility at the Offshore Technology Research Center (OTRC) at Texas A&M University, College Station, Texas. As the experiments were the first of their kind conducted at this scale and magnitude, they provided new data and physical insight into the complicated wave-structure interaction problem.

3.1 Objectives of the Experimental Investigation

The specific objectives of the experimental portion of this research study were to:

- design and implement realistic physical scale models representative of TLP risers and tendons in 1006 m (3300 ft) of water. The emphasis in the model design was to ensure that the dynamic behavior of the model cylinders was representative of the prototype and the testing was conducted at the largest model scale possible in the wave basin to minimize viscous scale effects;
- obtain accurate estimates of the displacement field along the length of the cylinders to study the collision behavior. This was accomplished by designing and implementing instrumentation to measure the cylinder curvature, and numerically integrating the measured data to obtain accurate displacement estimates.

The models were also instrumented to provide measurements of the inline and transverse reactions and the tension at both ends of the cylinders;

- study the wave-induced dynamic response of a single flexible cylinder under regular and random waves. These experiments provided data for comparison with that from the paired cylinder tests to study the effects of cylinder proximity (spacing and orientation) on the cylinder response;
- study and observe the extreme response and collision behavior of a pair of cylinders subjected to one hundred year storm waves (random). Experiments were conducted at various spacings and orientations, with an emphasis on the tandem arrangement, with similar and dissimilar tensions; and
- characterize the wave-induced response of the cylinders as a function of orientation and spacing with respect to the incident waves. This was accomplished with both regular and random waves.

3.2 Prototype Wave and Structural Parameters

This section gives an outline of the prototype wave and structural parameters which were used to design the scale models and to develop the experimental program. These prototype parameters are scaled to model parameters using the distorted scale relationships presented in Section 2.

3.2.1 Wave Parameters

The experimental program considers two type of wave conditions:

1. regular waves, and
2. unidirectional random waves.

The use of regular waves allows one to study the wave-structure interaction phenomena for a single wave frequency. This allows characterization of the wave-structure interaction by means of the Keulegan-Carpenter number, N_{KC} defined as

$$N_{KC} = \frac{UT}{D} \quad (3.1)$$

where U is the maximum horizontal particle velocity at the still water level, T is the wave period and D is the equivalent diameter of the structure. This parameter has been shown to be an important parameter in classifying the wave-structure interaction

phenomenon, and has been used extensively by previous investigators for harmonic flows and waves (Blevins 1990). The regular wave tests are also a means to study the complex wave-structure interaction phenomena without the additional complication of including the randomness of the wave kinematics. This allows the simplification of the problem and provides the insight to attempt to study the random wave interaction.

Another important parameter in wave-flexible structure interaction is the ratio of the forcing frequencies to the natural frequencies of the structure as this has an influence on the structure's response behavior (modes of vibration and amplitude). Therefore a major objective in the design of the experiments was to ensure that these ratios would be maintained at the model level. Also, the regular wave test matrix was determined by taking the natural frequencies of the cylinder into consideration so that different modes of vibration could be excited. Table 3.1 shows the prototype regular wave conditions considered for this study and the approximate range of the wave-structure interaction parameters (riser-tendon).

Table 3.1: Prototype regular wave conditions.

Period T (s)	Height H (m)	Steepness H/L	N_{KC} UT/D	N_R UD/ν
15.5	13.12	0.035	171.5–62.1	761450–2103507
13	9.23	0.035	119.2–43.1	630724–1742377
10	5.46	0.035	70.3–25.5	484016–1337096
7	2.68	0.035	34.5–12.5	339350–937454

The random waves tests were primarily conducted to study the response of the cylinders subjected to storm wave conditions. A JONSWAP spectrum, representative of a 100 year storm in the Gulf of Mexico, with a significant wave height, H_s , of 12.5 m (40.5 ft), peak period, T_p of 14.7 seconds and a peak parameter, γ of 2.0 was used.

There were two main objectives associated with the random wave tests. The first objective was to characterize the wave-structure interaction phenomena in a manner similar to that used for the regular waves. This was accomplished by using the root mean square (r.m.s.) estimates of wave force and cylinder response. The accurate r.m.s. estimates of force and response required wave time histories containing approximately 200 waves, corresponding to a duration of approximately 35 minutes at prototype scale.

The second and primary objective was to study the extreme response and collision behavior of the cylinders in close proximity. As the collisions are rare events, an accurate probabilistic analysis of the data required time series of longer duration than those required for the r.m.s. response estimates. Random wave time histories with at least 1000 waves were selected to be used for the extreme wave tests. This corresponded to approximately 3 hours of storm data at prototype scale.

3.2.2 Structural Parameters

Table 3.2 presents the structural characteristics for TLP risers and tendons in approximately 1006 m (3300 ft) of water (Mercier 1991). These properties are used in the design of the flexible cylinder models for the experiments.

Table 3.2: Prototype TLP tendon and riser properties.

Parameter	TLP Tendon	TLP Riser
Depth, d (m)	1006	1006
Outer Diameter, D (m)	0.671	0.244
Lateral Stiffness, EI (kN-m ²)	6.61×10^5	1.57×10^4
Mass/length, ρA (kg/m)	574.4	172.3
Added Mass/length $\rho_w V$ (kg/m)	354.2	47.9
Weight/length (air), W_a (kN/m)	5.546	1.897
Buoyancy/length, w_b (kN/m)	3.502	0.467
Effective Weight/length, T' (kN/m)	2.043	1.430
Top Tension, T_o (kN)	8896	1690
Mass Ratio, M_r	2.06	3.70

Due to the large length and small moment of inertia of the riser or tendon, the contribution of the lateral (bending) stiffness, EI , to the overall “stiffness” of the riser or tendon is very small. In fact for the lower modes of vibration, the equation of a string, where the only stiffness contribution is due to the tension, can be used to get accurate estimates of the natural frequencies. Therefore the pretension of the riser or tendon is a very important parameter in determining its dynamic characteristics. Another important structural parameter is the outer diameter, D , of the riser or

tendon as it determines the magnitude of the wave force on the riser or tendon as well as the flow conditions. Both the riser and the tendon have a diameter very much smaller than that of the wave length (order of 10^{-3} to 10^{-4}), therefore the loading is drag dominated. The spacing and orientation of the pair of cylinders with respect to the incident wave direction can also be considered as structural parameters.

The TLP riser or tendon can thus be simplified to be represented by a flexible cylinder with a pretension applied at the top, and pin-pin boundary conditions as shown in Figure 1.1. The tension is a very important structural parameter as a change in tension implies a change in system characteristics, both in amplitude and phase of response. By varying the applied pretension, the cylinder can be tuned to exhibit different dynamic properties. Therefore the wave-structure interaction problem can be studied by varying the orientation and spacing of the cylinders with respect to the incident waves and by changing the pretension of the cylinder.

3.3 Description of the Experimental Facility

3.3.1 The OTRC Deep Water Wave Basin

The OTRC wave basin is 45.7 m (150 ft) long, 30.5 m (100 ft) wide, and has a primary water depth of 5.8 m (19 ft). In the center of the basin is a well 9.1 m (30 ft) long, 4.6 m (15 ft) wide, with a vertically adjustable floor so that water depths from 5.8 m (19 ft) to 16.76 m (55 ft) are possible. The layout of the basin is illustrated in Figure 3.1.

The multi-directional wave maker, situated at the North end of the basin, consists of 48 single hinged boards, each 0.6 m (2 ft) wide and 3 m (9.84 ft) high. The wave boards are driven by servo-controlled, linear hydraulic actuators, each one being individually programmed. The wave maker can be programmed to make a variety of wave conditions ranging from uni-directional regular waves to multi-directional random seas. Drive signals for the wave are created using the GEDAP software on a VAX 3500 and then downloaded to three MCUs that control the wave boards. The wave maker is capable of generating waves with periods ranging from 0.5 to 4 seconds, with a maximum regular wave height of 0.84 m (2.75 ft) over the range of periods 2.3 to 3.0 seconds. Wave absorption is provided by a progressive wave absorber located at the South end of the basin. The absorber uses expanded metal screens, which progressively decrease in porosity and spacing along the depth of the absorber.

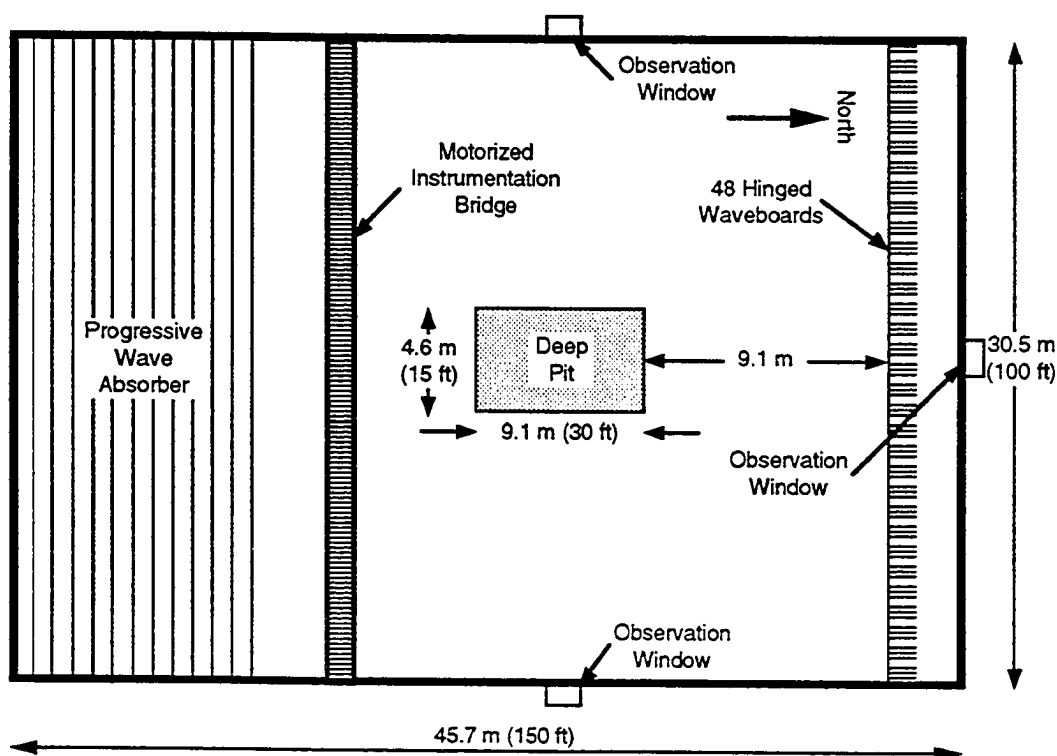


Figure 3.1: Layout of the OTRC wave basin.

3.3.2 Data Acquisition System

Data acquisition is provided by a NEFF System 620 which is controlled by a VAX 3500 computer. All programming of the data acquisition is accomplished using the GEDAP software package on the VAX with the NEFF acquiring the data and digitizing it for storage on the VAX. The NEFF System 620 is a modular data acquisition system allowing a maximum of 256 channels and having an overall sampling rate of 50 kHz at a 15 bit resolution.

The NEFF system allows individual channel signal conditioning, amplification and anti-alias filtering. For the present study, 4 high level channels (25 mV to 10 V input), and 56 low level channels (5 mV to 1 V input) for a total of 60 channels were used. 10 Hz anti-aliasing filters were used on each channel and data were acquired at 40 Hz. The instruments used in this experimental program are described in detail in a later section. Appendix B contains detailed information about the channel lists, excitation and gain settings.

3.3.3 The GEDAP Data Acquisition and Analysis Software

The GEDAP software package has been specifically developed for wave basin testing and analysis by the National Research Council of Canada. The software is installed on the VAX 3500 and is used to generate drive signals for the wave maker, control the NEFF for data acquisition and storage, and for the post processing and analysis of data. Data acquired by the software is stored in a single multiplexed data file called the *primary data file* (file extension .pdf) and is accompanied by a file called a *port file* (file extension .pf) which contains all the relevant information about the test, for example, the channel list with the calibration factors, offsets, channel description and units, time and date of test, etc. These two files contain all the test data and information and can be demultiplexed for data processing. As the GEDAP file format retains all information about the test and the data, data archiving is made very simple (see Appendix C). Post processing of the data is done using a series of modular analysis routines which can be combined to form a single procedure file to perform all the analysis and plotting unattended. Details about the GEDAP software and its capabilities are described in Miles (1990).

3.4 Design of the Flexible Cylinder Models

The flexible model cylinders are designed to exhibit the scaled dynamic properties of the TLP riser or tendon presented in Table 3.2. In this section the design of the physical scale models is outlined using the distorted scale relationships and methodology described in Section 2.

3.4.1 Scaling the TLP Tendon and Riser

Section 2 outlined the methodology of distorted scaling of flexible structures in deep water and was illustrated with an example of a TLP in 2000 m (6561 ft) of water. Here the same approach is applied to the TLP tendon and riser detailed in Table 3.2 to arrive at a design of a realistic scaled physical model representative of the TLP riser and tendon.

As the diameter of the prototype riser and tendon were small (ranging from 0.244 to 0.671 m (0.8 to 2.2 ft)), the horizontal scale had to be as large as possible to obtain reasonable model dimensions, especially as instrumentation had to be placed inside the model. This also reduced the viscous scale effects by maximizing the Reynolds number. Based on the capabilities of the OTRC wave basin and the target

Table 3.3: Scaled model TLP tendon and riser properties.

Parameter	Tendon	Riser	Model
Depth, d (m)	16.76	16.76	16.21
Outer Diameter, D (cm)	2.69	0.97	3.175
Lateral Stiffness, EI (N-m ²)	4.90	0.12	42.58
Mass/length, ρA (kg/m)	2.206*	0.184*	1.225
Added Mass/length, $\rho_w V$ (kg/m)	1.38*	0.18*	0.79
Weight/length (air), w_a (N/m)	21.63*	6.49*	12.02
Buoyancy/length (N/m)	1.24*	1.802*	7.75
Effective Weight/length, T' , (N/m)	3.27*	2.29*	4.27
Top Tension, T (N)	237.2	45.1	222.4/135.7

*Inconsistent due to distorted scaling.

wave conditions desired, a horizontal scale, λ_H , of 1:25 was chosen. At this scale an undistorted model would require a tank of depth approximately 40.2 m (132 ft). As the available depth in the OTRC wave basin was 16.76 m (55 ft), the vertical length scale, λ_V , was distorted to a scale of 1:60. Using these distorted scales the TLP riser and tendon properties presented Table 3.2, were scaled using the distorted scale relationships derived in Section 2 and the scaled properties are presented in Table 3.3. The wave conditions are scaled using the λ_H only. The random wave spectrum scales to a significant wave height, H_s , of 0.5 m (1.64 ft), peak period, T_p , of 2.94 s, with the peak enhancement factor, γ of 2.0. The regular wave conditions at model scale are presented in Table 3.4.

From Table 3.3 it is seen that for a horizontal scale of 1:25 the model diameter would range from 0.97 cm (0.39 inches) for the riser to 2.69 cm (1.06 inches) for the tendon. As it would be almost impossible to construct a model of diameter 0.98 cm (0.385 inches) if it also had to contain instrumentation and cables, the decision was made to use a model of diameter 2.5 to 3.175 cm (1 to 1.25 inches). Therefore the model would be physically more representative of a TLP tendon than a production riser. However, the top tension could be adjusted to provide natural frequencies representative of a tendon or a riser.

Table 3.4: Scaled regular wave conditions.

Period T (s)	Height H (m)	Steepness H/L	N_{KC} UT/D	N_R UD/ν
3.1	0.525	0.035	52.7	19852
2.6	0.369	0.035	36.6	16432
2.0	0.218	0.035	21.6	12610
1.4	0.107	0.035	10.6	8843

As the model was physically more representative of a tendon, a mass ratio of 2.0 was chosen to be maintained in the model. Based on this mass ratio, the mass/length of the model cylinder in air was determined to be 1.225 kg/m (0.0256 slugs/ft). Another consideration in the design was to obtain a material which would exhibit the desired mechanical properties with a linear stress-strain relationship and excellent creep resistance. The creep resistance was a very important characteristic since if the cylinder crept after being pretensioned, the tension would be relieved, thus modifying the dynamic characteristics of the cylinder and requiring constant readjustment of the tension. ABS plastic, which has a modulus of elasticity of 1.72×10^4 kN/m² (5.184×10^7 lb/ft²) with excellent mechanical properties and creep resistance was chosen to be the model material. The final design was obtained after using the design procedure outlined in the API RP 2A (American Petroleum Institute 1987) for a flexible conductor subjected to combined axial and bending stresses and hydrostatic pressure. Using a factor of safety of 2.0, ABS tubing with an outer diameter of 3.175 cm (1.25 inches) and wall thickness of 1.6 mm (0.0625 in) satisfied the requirements. The ABS tubing chosen had a lateral stiffness, EI , of 42.57 kN-m² which was an order of magnitude of that required. However, as the stiffness of the cylinder is tension dominated, this was shown to have no significant effect on the lower modes of vibration. Table 3.3 compares the actual model properties to those obtained by scaling the prototype conditions in Table 3.2. The detailed construction of the cylinder is discussed in a later section.

3.5 Estimating Cylinder Displacement

A unique aspect of the experimental study was the accurate estimation of the displacement field over the entire length of the cylinders. The displacement information

is important as it provides estimates of the relative displacement between the two cylinders, which leads directly to the analysis of the collision behavior of the cylinders.

Displacement measurements of submerged flexible structures have traditionally been very difficult to make. Contact type instruments like MLDTs and LVDTs cannot be used in this environment as besides being inconvenient and nearly impossible to install, they would interfere with (modify) the fluid-structure interaction process. Optical tracking systems are ideal in the sense that they are non-contact systems and do not require any instrumentation in or on the cylinders. However, most optical tracking systems track a limited number of points in the field of view of the cameras and in this specific application where estimates of the entire displacement field beneath the water surface is required, this would lead to a large number of such systems at an exorbitant cost.

Another solution was the use of accelerometers placed in the cylinder at predetermined intervals. The accelerometer data could then be integrated in the frequency domain to give estimates of the displacement at those locations. This approach has been used successfully in steady flow-flexible cylinder interaction (Vandiver and Chung 1988). However, this approach has severe limitations when applied to wave-structure interaction problems.

Steady flow induced vibrations of the type studied by Vandiver and Chung (1988) occur at relatively high frequencies (of the order of 20 Hz), leading to vibrations with large accelerations and correspondingly small displacements. Therefore the motion of the accelerometer in the tube is mainly translational with negligible rotation. However, waves are at lower frequencies (less than 1 Hz) and the resulting cylinder motions are relatively larger, with small accelerations. For example, finite element simulations of the wave-cylinder interaction being considered in this study showed that the maximum accelerations would range between $0.01g$ to $0.1g$. Due to the relatively large motions, the accelerometers would also undergo rotation of about 1 to 2 degrees. This would cause the translational acceleration signal from the accelerometer to be corrupted by the corresponding component of earth's acceleration due to rotation ($\simeq 0.01g$ to $0.02g$) which is also measured by the transducer. Comparing the maximum anticipated accelerations to the magnitude of the signal due to rotation, it is seen that using an accelerometer would lead to unacceptably large errors. This was confirmed both experimentally by placing the accelerometer at the end of a cantilever and measuring both acceleration and the displacement, and numerically by

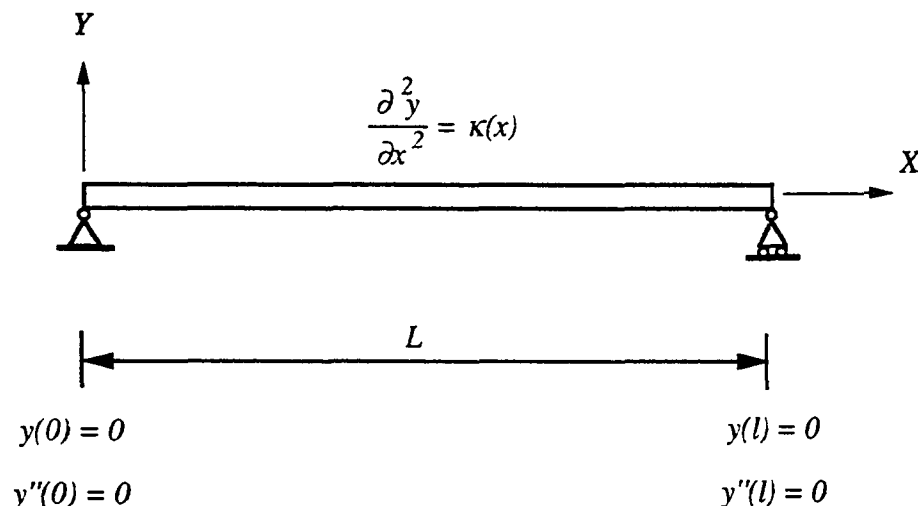


Figure 3.2: Definition sketch of relationship between curvature and displacement.

simulating the above conditions with the finite element model. This problem could be circumvented if the rotations at each accelerometer location could be measured to correct the accelerometer signal, but due to size and cost restrictions this was not possible.

3.5.1 Estimating Displacement from Curvature

The approach chosen to arrive at displacement estimates of the flexible cylinders was based on Bernoulli–Euler beam theory. From beam theory the relationship between the curvature, $\kappa(x)$, and the displacement, $y(x)$, of a beam is

$$\frac{\partial^2 y}{\partial x^2} = \kappa(x) \quad (3.2)$$

which is a second order differential equation. Therefore given the boundary conditions and the curvature, Equation (3.2) can be solved for $y(x)$.

Figure 3.2 illustrates the problem at hand. The cylinder has pin-pin boundary conditions which imply that the curvature and displacement at each end is zero. Therefore, given an estimate of the curvature along the beam the displacement can be obtained by solving the boundary value problem.

The problem is thus to estimate the curvature over the entire length of the beam, $\kappa(x)$. From beam theory curvature is directly related to the bending moment by the

relationship

$$\kappa(x) = -\frac{M}{EI} \quad (3.3)$$

The bending moment can be measured at specific locations using strain gages arranged in a full-bridge bending configuration. If a sufficient number of discrete bending moment measurements can be obtained over the length of the beam, the curvature, $\kappa(x)$, can be estimated by interpolation. Therefore, the number of discrete curvature measurements and their location need to be determined to obtain an accurate description of the curvature. Evidently the number of discrete measurements required and their location is a function of the response of the cylinders. Therefore a detailed knowledge of the cylinder response is required.

The finite element model of the flexible cylinder outlined in Appendix A was used extensively to optimize the number and locations of the curvature transducers. The initial simulations were conducted to determine the number of elements required to obtain accurate estimates of curvature (stress), as a finite element model which gave accurate estimates of displacement may be too coarse to provide accurate estimates of the curvature. Based on the convergence of the finite element solution for the curvature, a 104 node model was used. Simulations were then run with all anticipated wave and structural conditions to arrive at the final number of transducers and their locations. Simulations were also run at twice the desired wave frequencies in an attempt to simulate the vibrations due to vortex shedding for determining transverse displacement. Eight transducers were found to be the minimum number required to provide accurate results; eleven were finally decided upon to provide redundancy and provide accuracy for high frequency vibrations. Appendix B contains details about the locations of the transducers on each model cylinder.

Figures 3.3 through 3.8 illustrate final results from the simulation with the optimum number of transducers at the determined locations. They also serve to outline the approach used. The finite element program provides estimates of curvature (FEM) at all the 104 nodes as a function of time. Figure 3.3 shows the curvature, $\kappa(x)$, at an instant of time, t_0 , over the length of the flexible cylinder. The solid line represents the computed curvature at all 104 nodes. The dashed line is a cubic spline fit through discrete estimates of curvature represented by the solid circles. The discrete curvature estimates represent curvature measurements at the determined locations. It is seen that the spline fit compares very well with the 104 node solution. The interpolated curvature data is then integrated using a Runge-Kutta "shoot-to-fit" scheme (Press et al. 1988) to provide estimates of the displacement at all the interpolated locations.

Figure 3.4 compares the displacement obtained by integrating the spline fit curvature in Figure 3.3 with that obtained directly from the finite element model. It is seen that the agreement between the two is excellent.

Figures 3.5 and 3.6 compare time histories of displacement at specific locations obtained directly from the finite element model and those obtained by integration. Figure 3.5 is the displacement time history at location -1.52 m (-5 ft) for a regular wave of period, T , equal to 1.4 seconds, which was the smallest wave period considered. Figure 3.6 is at location -3.05 m (-10 ft) for a wave of period 3.2 seconds which was the largest period wave considered. For both cases the accuracy of the integrated displacement time history is excellent.

Figures 3.7 and 3.8 provide a final comparison between integrated and computed displacement. Figure 3.7 compares the displacement time histories for the random wave condition desired and once again excellent agreement is observed. Figure 3.8 compares the two displacement spectra, and it is observed that the agreement is excellent up to a frequency of 2.5 Hz. After 2.5 Hz, the two solutions deviate, but the influence on the overall displacement of the cylinder is negligible as relatively little energy is present at those frequencies.

3.6 Flexible Cylinder Instrumentation

This section describes the instrumentation used in these experiments in some detail. Figure 3.9 illustrates the instruments used and their location on each cylinder. Appendix B contains more detailed information about calibration, channel lists and other data acquisition details.

3.6.1 Curvature Transducers

The curvature transducers were designed to be an integral part of the flexible cylinder model. The transducer basically consisted of a 15 cm (6 inch) piece of the ABS tubing, in which strain gages were mounted in the middle to provide 2 full bridge bending moment transducers, one for each bending axis (inline, X , and transverse, Y).

The strain gages selected for this application had resistances of 1000Ω and large surface areas which allowed the use of relatively high excitation voltages, increasing the sensitivity and the signal to noise ratio of the transducer (Measurements Group Inc. 1988). This was very important as the anticipated strain was very small and use of a very poor heat conductor like ABS as the substrate would not allow dissipation of

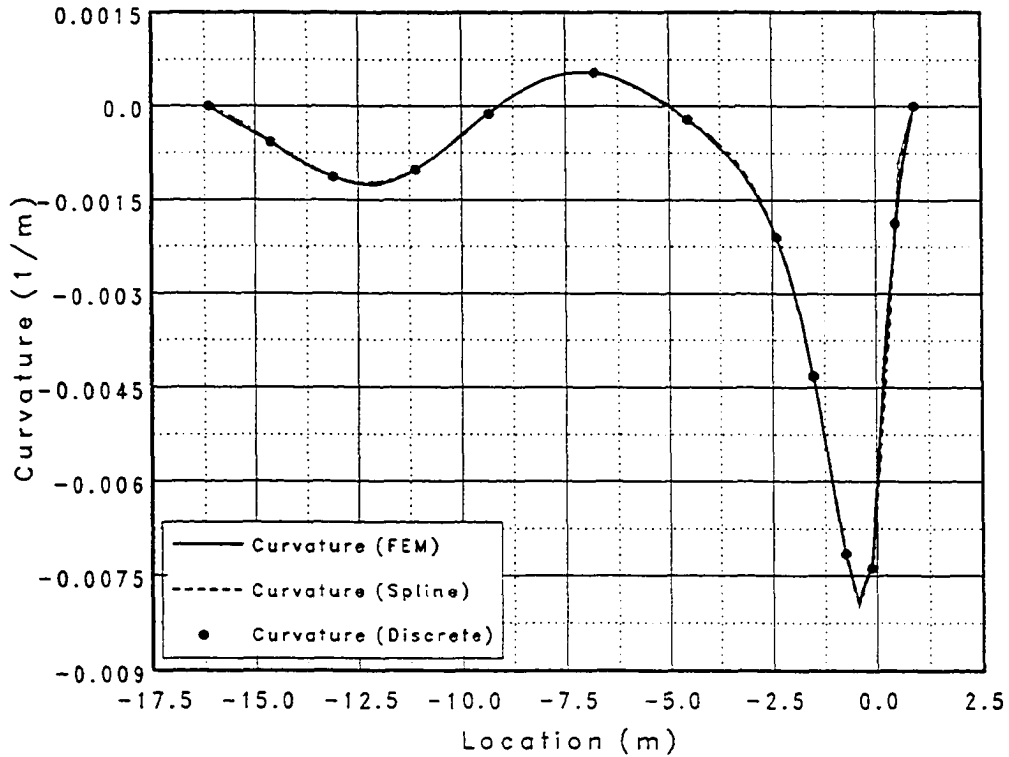


Figure 3.3: Curvature, $\kappa(x)$, along the length of the cylinder.

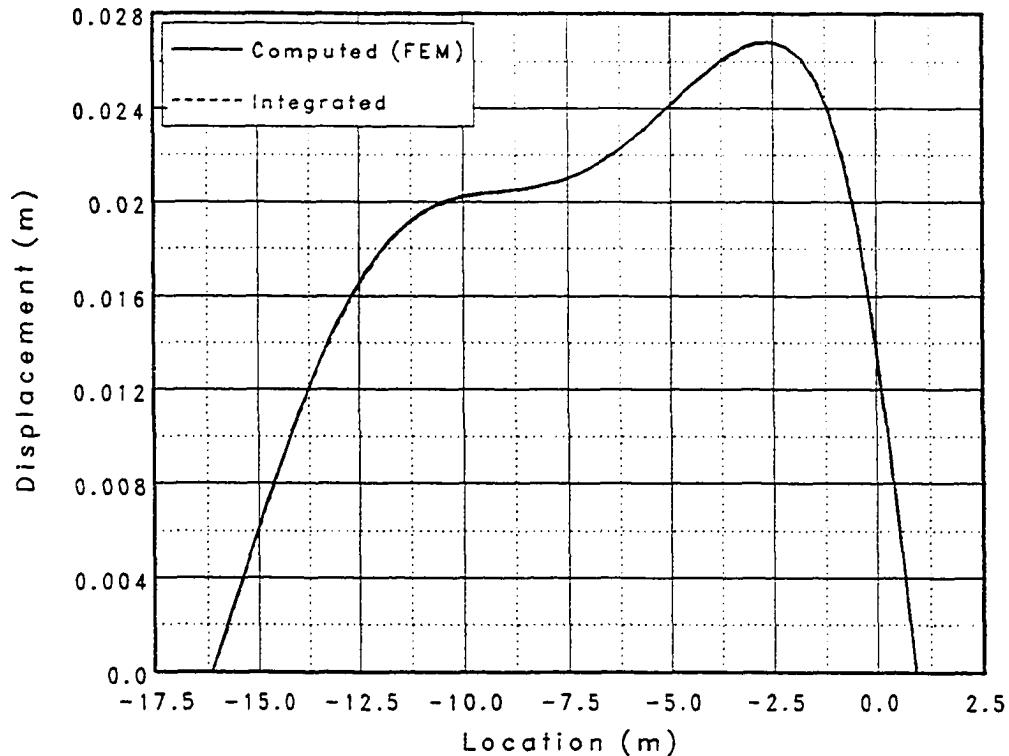


Figure 3.4: Comparison between displacement computed from the finite element model and estimate from integration of curvature.

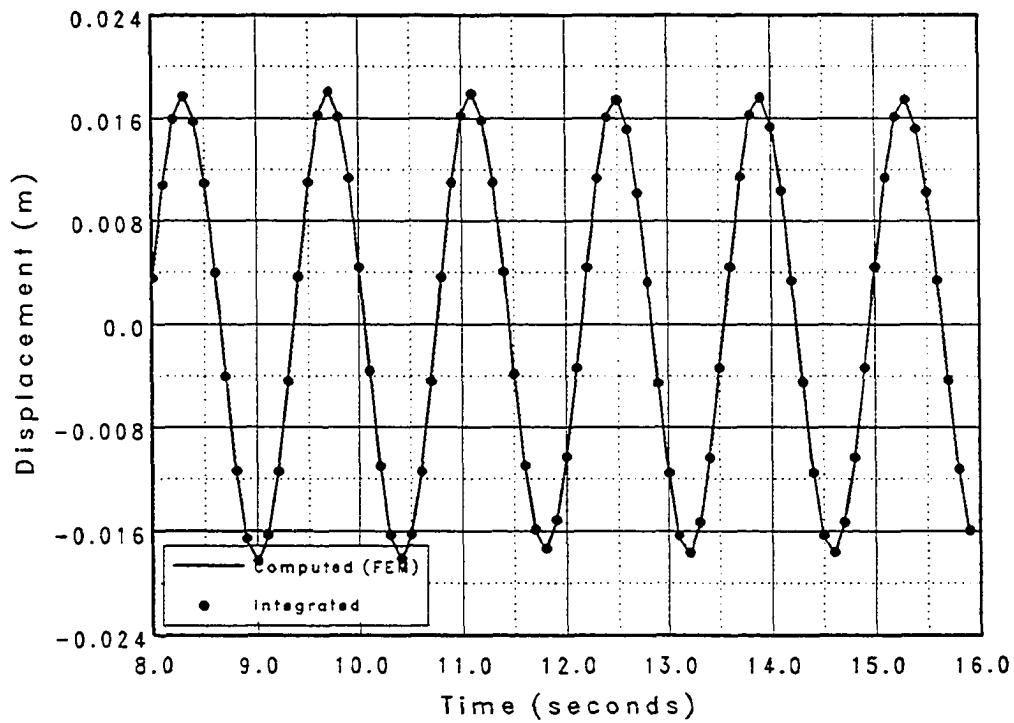


Figure 3.5: Comparison between computed and integrated displacement time series at -1.52 m for $T = 1.4$ seconds.

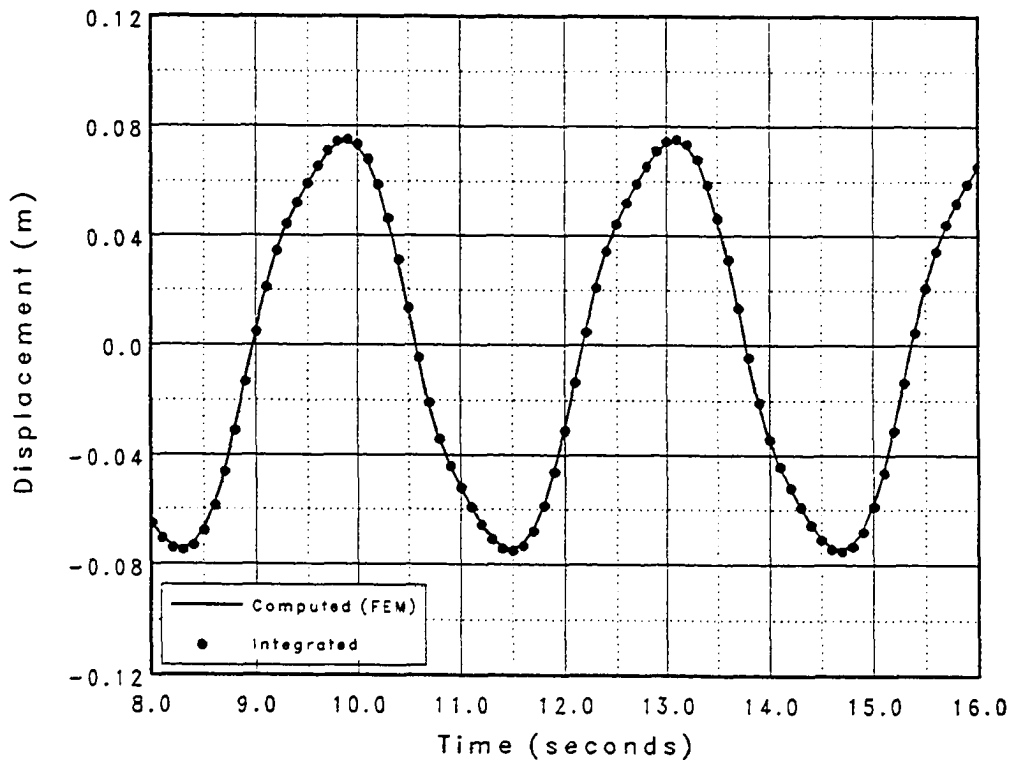


Figure 3.6: Comparison between computed and integrated displacement time series at -3.05 m for $T = 3.2$ seconds.

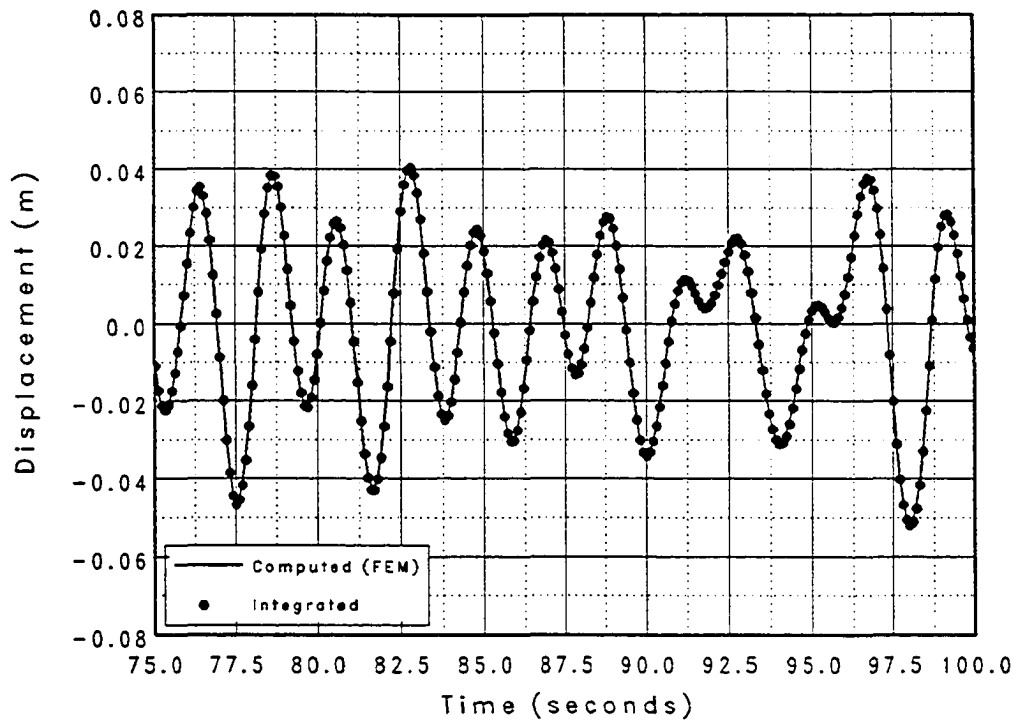


Figure 3.7: Comparison between computed and integrated displacement time series at -3.05 m for the random wave simulation.

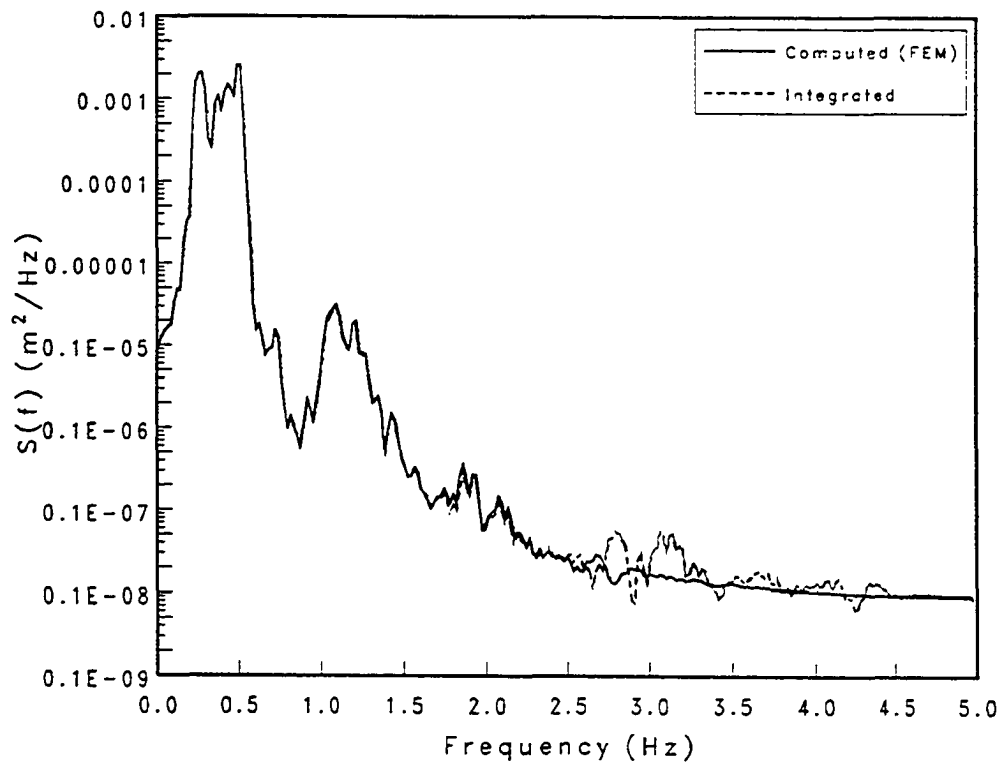


Figure 3.8: Comparison between computed and integrated displacement spectra at -3.05 m for the random wave simulation.

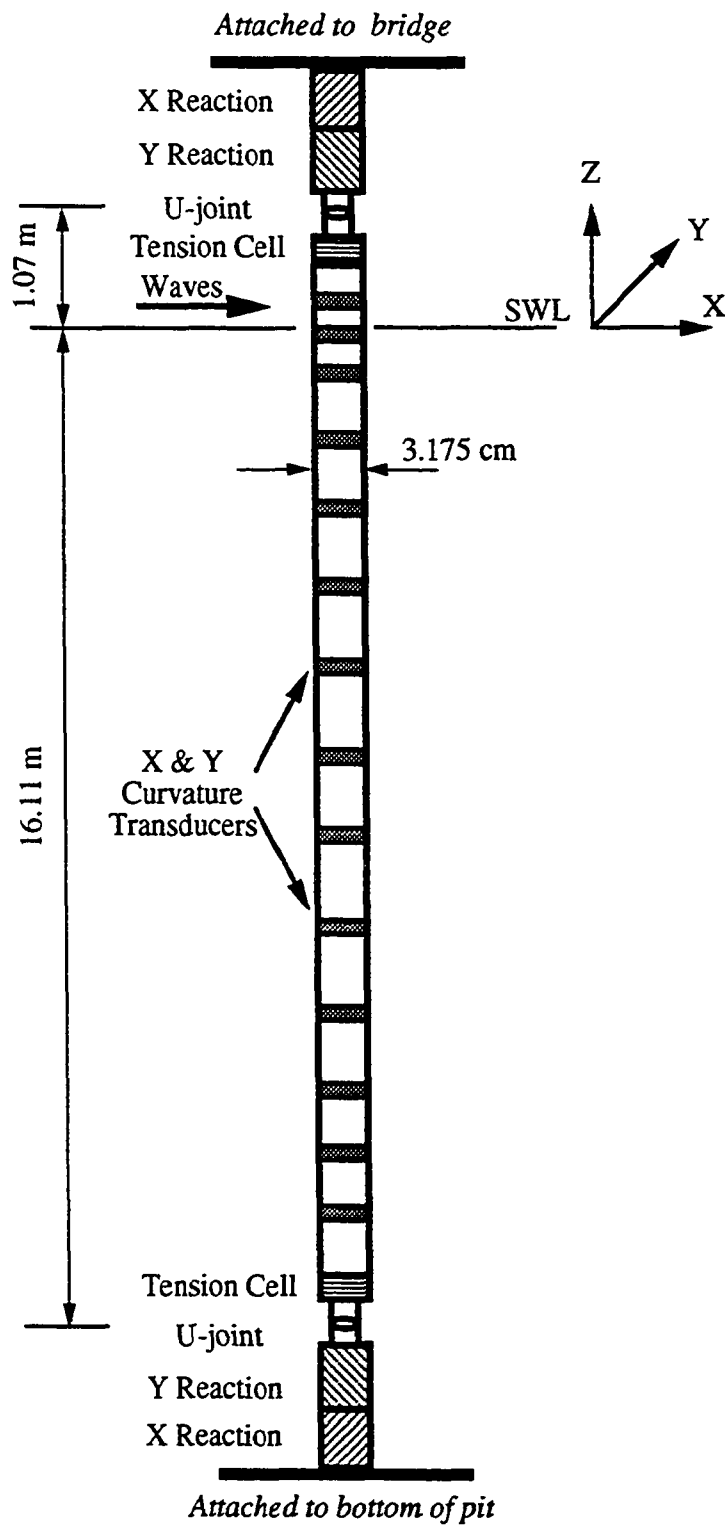


Figure 3.9: Definition sketch of flexible cylinder model instrumentation.

the heat generated in the gages, leading to possible instability and zero-drift problems.

Theoretically a properly designed and implemented full-bridge for bending moment is insensitive to axial tension, torsion and out of plane bending as the resulting strains are “cancelled” in the Wheatstone bridge circuit. Therefore the output of the transducer corresponds to the pure bending or curvature. This was verified by a series of tests with a prototype transducer which was subjected to combined axial and transverse loading with both X and Y transducers monitored. The crosstalk between the X and Y transducers, and the influence of the axial tension was below 0.5% of the applied load. The excitation voltage was optimized to be 2.5 V which did not provide any significant zero-drift or instabilities. Calibration of the prototype showed linearity within 0.5% of the loading range.

The transducers for the model were custom made and were provided with solder tabs to which a 6 conductor 28 gage shielded cable was attached (signal, excitation, and sense). The gaged areas inside the tubes were coated with a tough silicone adhesive to protect the gages and the delicate wiring from abrasion by the cables running by the transducer. The cables were also anchored to the ABS using this adhesive to prevent any strain on the solder tabs. The transducers were calibrated after the entire model was assembled by placing the cylinder over precision made curved surfaces. The process was very repeatable and the calibrations were generally linear within 1 to 2% of the range of calibration.

3.6.2 Force Transducers

The force transducers were used to measure the top and bottom reaction forces at each end of the cylinders. The reaction forces measured are from two sources: (1) the inline and transverse wave-induced forces on the cylinders, and (2) the inertia forces due to the motion of the cylinders.

Shear web force transducers with a rating of 44.5 N (10 lb) were used for this purpose. One important constraint was that they had to have an overall diameter less than that of the cylinder to enable the cylinders to be placed close to one another without the loadcells causing any interference. Each individual loadcell measured the shear force applied along the axis in the plane of the web. Two such loadcells, mounted one above the other with the web axes at 90°, would provide resolution of the shear force along the two axes.

The loadcells used at the bottom of the cylinder were provided with underwater cables and were waterproofed using silicone as seen in Figure 3.12. The loadcells were

calibrated by applying an axial tension (to simulate the actual installed condition) and using weights as listed in Appendix B. Crosstalk between the X and Y loadcells and the influence of applied tension and moment were found to be under 0.5% of the applied load. The calibrations of the loadcells were linear within 0.1% of the range of calibration.

3.6.3 Tension Cells

The tension cells were used to provide measurements of the tension fluctuations at the top and bottom of the cylinders as the waves interacted with the cylinders. They were also used to monitor the applied pretension to verify that the clamping mechanism used to maintain the tension had not slipped.

Sensotec (Model 31) tension cells with a rating of 1112 N (250 lb) were used. The tension cells at the bottom of the cylinder were submersible with underwater cables. The tension cells were calibrated as listed in Appendix B and the calibrations were found to be linear within 0.5% of the applied range.

3.6.4 Wave Gages

The wave gages were used to determine and monitor the wave elevations, and to provide phase information between the incident waves and the cylinder response. The capacitance-type wave gages used consisted of a rigid support frame with a Teflon coated wire as the probe. During the wave condition set-up phase of the experimental program, the probes were placed at the location of the model. During the actual cylinder tests, probes were placed 1.52 m (5 ft) to the east and west of the lead cylinder to provide phase information. The wave gages were calibrated daily at the start of the tests and were found to be linear within 1% of the calibration range.

3.7 Model Construction and Installation

The cylinder was constructed using ABS tubing with a weight/length in air of 1.48 N/m. To achieve the required 12.02 N/m, egg-shaped lead weights were used to make up the deficit after accounting for the weight of the transducer cables and the packing material.

From the finite element model simulations it was seen that 11 transducers were required at specific locations to provide accurate estimates of the displacement under all anticipated loading conditions. To provide some additional redundancy and

backup, two additional locations were chosen in case a transducer failed after the cylinder was assembled. Therefore each cylinder consisted of 13 instrumented sections and 14 sections of the required lengths as tabulated in Appendix B for a total of 27 segments.

The construction of the model cylinder started from the bottom. The lead weight required for each section was threaded on a line, evenly distributed and then clamped in place. The line with the lead weights and the cables from the preceding transducers were bundled inside a rubber foam hose. When the number of cables became large the bundle was formed using rubber foam tape which allowed one to adjust the diameter of the bundle. The bundle was lubricated to allow the corresponding ABS segment to be pulled over it. The rubber foam ensured that there was a very tight fit between the bundle and the walls of the ABS tube. This allowed the mass to be in contact with the walls of the cylinder and prevent movement of the weights and cables inside the cylinder. The sections were glued together using a 2.85 cm (1.125 in) long ABS sleeve machined to fit inside the ABS tubes with a wall thickness of 1.6 mm (0.0625 in), and a solution of Methyl Ethyl Ketone (MEK) and ABS shavings. This glue provided a strong watertight weld between the joints. After calibration of the cylinder, these joints were then sealed once again on the outside by coating the joints with the MEK/ABS solution. The photographs in Figure 3.10 illustrate the construction procedure.

The tension cells were screwed into the ends of the cylinder and were linked to the loadcell assembly by a U-joint which provided the pin boundary condition at each end of the cylinder as shown schematically in Figure 3.9. The instrumented ends of the cylinder were attached to rigid supports, one at the bottom of the pit and the other 1.07 m (3.5 ft) above the still water level (SWL). The two end supports consisted of two identical aluminum plates mounted on rigid frames. The plates had holes corresponding to the spacings and orientations of interest. Six orientations were chosen, 0° , 11.25° , 22.5° , 45° , 67.5° , and 90° . The 0° orientation (tandem) was in the North-South direction. Holes were drilled at $0.5D$ (1.588 cm, 0.625 in) intervals up to a spacing of $5D$ and then at larger intervals to a maximum of $20D$ (0.635 m, 25 inch). Each hole had an offset alignment hole for a dowel pin on the mating fitting to facilitate the alignment of the cylinder when moved. The bottom plate was mounted on a rigid frame 0.457 m (1.5 ft) high and placed at the center of the pit bottom, anchored in place by approximately 900 N (202 lb) of lead weight. The top plate was mounted on a rigid frame attached the instrumentation bridge. Figures 3.11 and 3.12

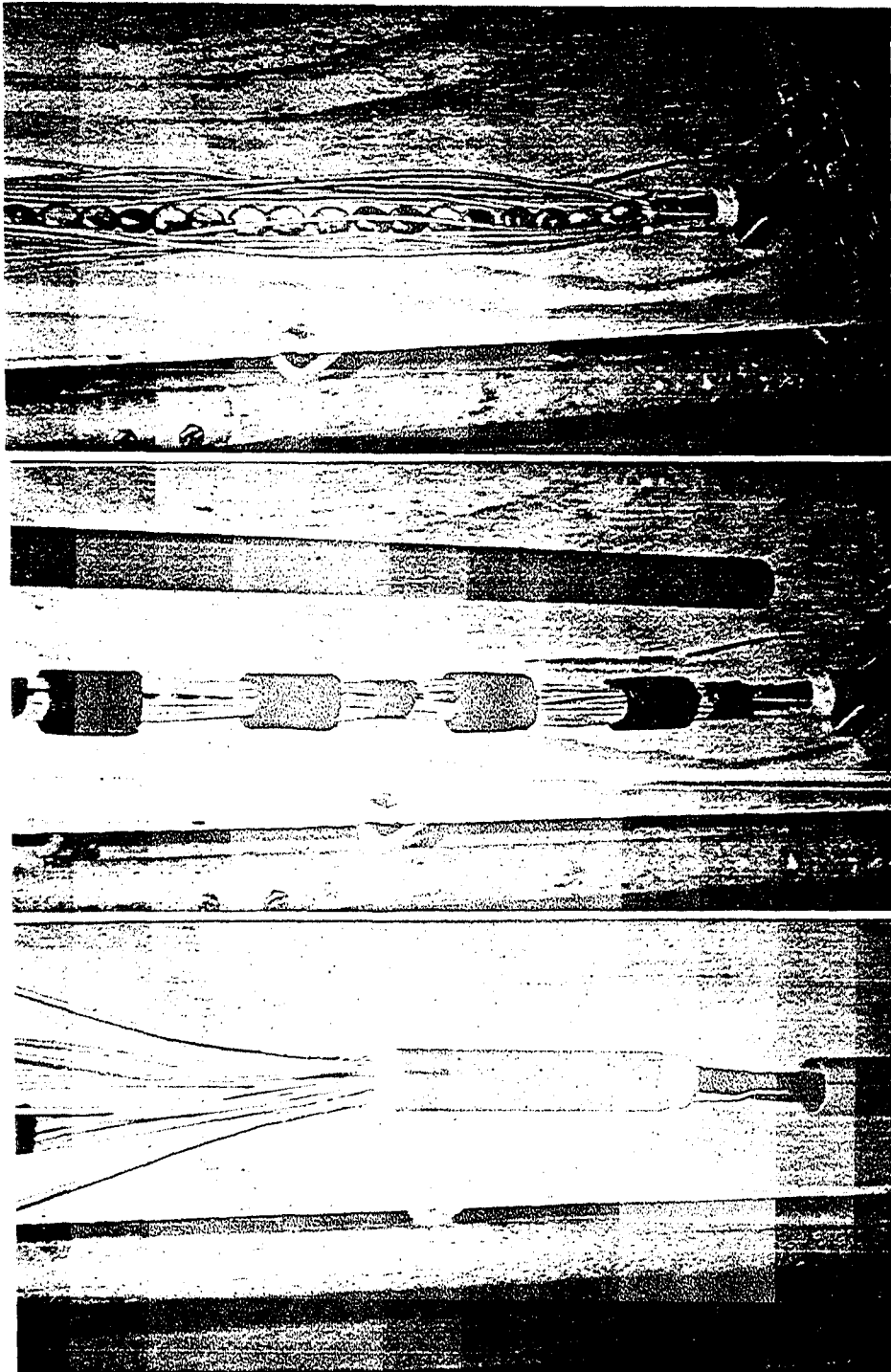


Figure 3.10: Assembly of the flexible cylinder models.

show the two fixtures.

A tensioning device was designed to fit at the top of each cylinder to allow pre-tensioning of the cylinder. The device consisted of a shaft attached to the top of the loadcell assembly, with a wire cable at the other end. The shaft was supported by a linear bearing which allowed up and down movement of the shaft but no rotation. At the bottom of the tensioner was a fixed split collar. The cylinder was pre-tensioned by placing the desired weights on the wire cable arrangement and clamping the split collar on the shaft. The tensioning device was designed so that its overall dimensions allowed the centers of the cylinders to come within $1.5D$. At the top of the tensioner was a threaded shaft and dowel pin to mate with the top support plate. The tensioning device can be seen in Figure 3.11.

Due to the length and flexibility of the cylinders, care had to be taken that the cylinders were not overstressed during installation. For installation the cylinders were attached to a rigid 20 m (65.6 ft) steel tower using cable ties. Using the overhead crane, lift bags and two divers, the tower was hoisted over the tank and then carefully lowered into the pit and uprighted. The cylinders were then cut away from the tower and attached to the supports and tensioned. Figure 3.13 illustrates the installation process. A working platform, supported by the overhead crane was placed around the cylinder installation to provide a platform to work from without loading the bridge which was very flexible and could cause the cylinder to be over tensioned. Access to and from the cylinder installation was made by boat once the cylinders were pre-tensioned.

3.8 Experimental Program Summary

The experimental program was conducted in three stages. The first concerned the creation and testing of drive signals for the wave maker to provide the desired wave conditions. The second phase focused on the single cylinder tests which were conducted for all tension and wave conditions to provide data for comparison with the paired cylinder tests. The final phase focused on the paired cylinder tests and took a majority of the testing effort. A total of 20 days were spent in actually conducting the tests.

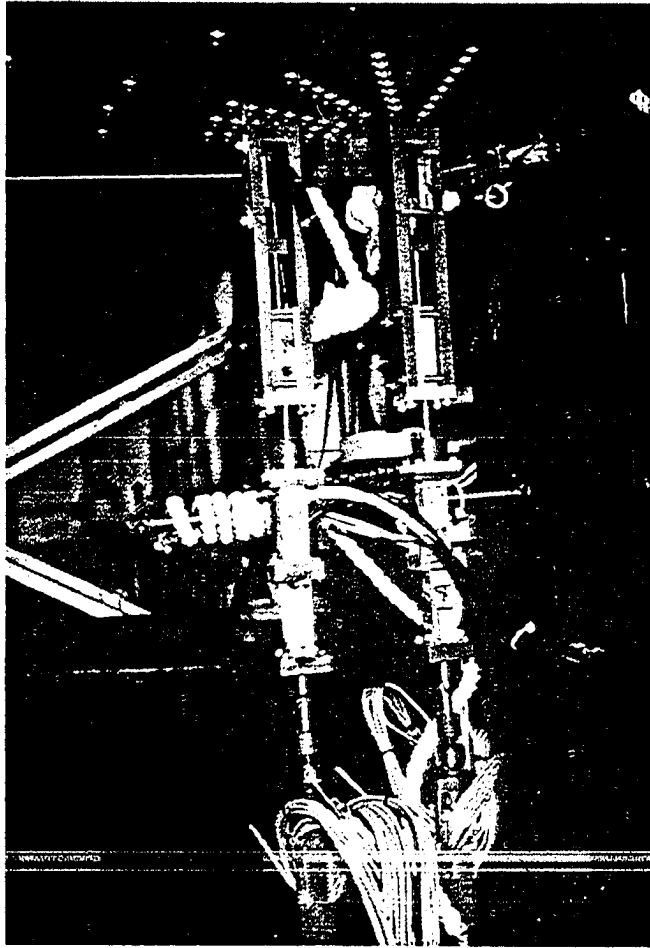


Figure 3.11: Attachment of cylinder model to top support plate.

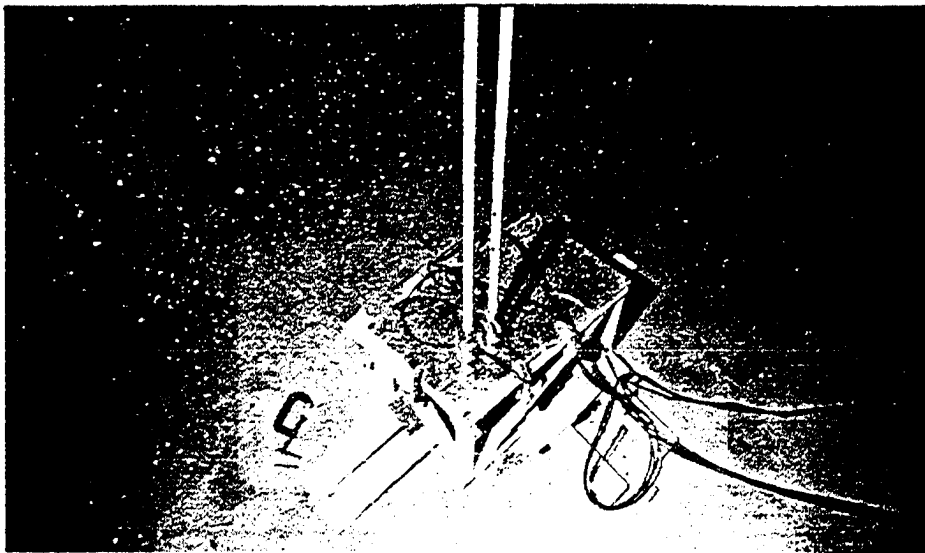


Figure 3.12: Attachment of cylinder model to bottom support plate.

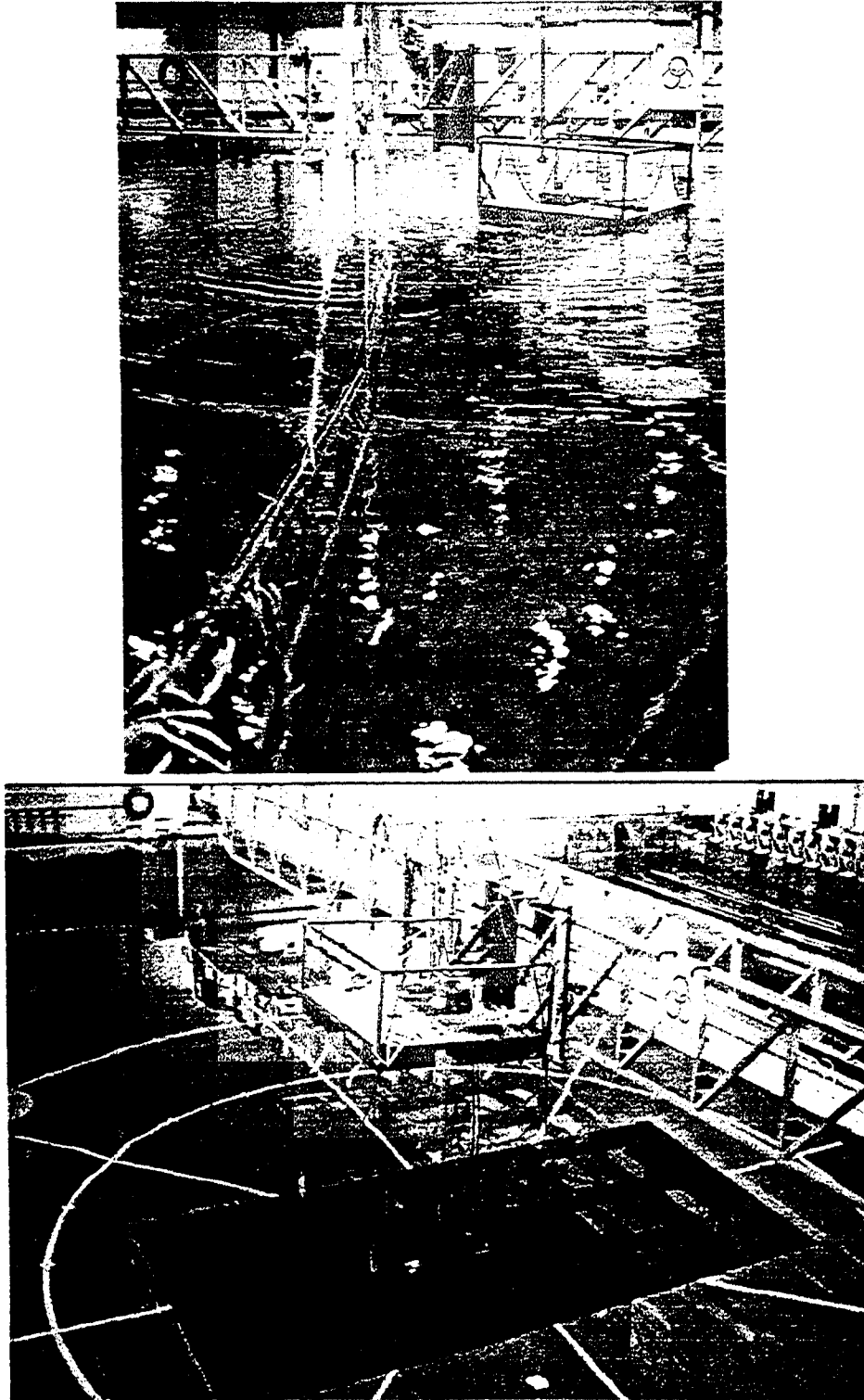


Figure 3.13: Installation of the flexible cylinder models.

3.8.1 Wave Conditions

There were three objectives in this phase of the experimental program: to obtain the desired wave conditions, to determine the reflection coefficients for the wave conditions desired, and to determine the maximum duration possible of continuous random wave generation.

The wave probes were arranged in an array of 5 probes for the reflection analysis, with the lead probe at the location of the lead cylinder (above the center of the pit). Reflection analysis was performed using the three-probe method (Mansard and Funk 1987), with software provided with GEDAP. The regular wave periods were set-up easily as the drive signals only required modification to the amplitude to achieve the target conditions within 1%. Reflection coefficients ranged from less than 5% for the 1.4 second wave to 20% for the 3.1 second wave.

Arriving at the target random wave spectrum proved to be more difficult as initially there were large discrepancies between the target and measured spectra, especially at the high frequency end. The increase in energy at the high frequency end caused crosstank waves in the wave basin, corrupting the wave field and increasing the settling time of the basin. This problem was solved by modifying the drive signals using the transfer function between the target and measured spectra. This yielded excellent results, with good agreement between the target and measured spectra and almost eliminating the crosstank waves, reducing the settling time by half.

The reflection coefficient for the random waves was around 5% for periods of 2.5 seconds and smaller and increased to approximately 10% for waves of longer periods. The reflection coefficients for the random wave simulations were lower due to the steepness of the waves which caused breaking in the wave basin and as the waves interacted with the absorber. The random wave tests also indicated that random wave simulations could be run for at least 409.6 seconds without any significant corruption of the wave field. For the target wave conditions this yielded about 200 waves per random wave test of duration 409.6 seconds.

3.8.2 Single Cylinder and Paired Cylinder Tests

As described earlier there were three types of wave conditions, regular wave tests, random wave tests for r.m.s. response estimates (200 waves) and random wave tests for extreme response and collision behavior ($\simeq 1000$ waves). One random wave simulation was required to provide data for r.m.s. estimates, while an additional five simulations

were required to provide approximately 1000 waves for the extreme response tests. Two specific pretensions were considered, T_1 where the pretension was equal to 222.4 N (50 lb) for tendon-like natural frequencies and T_2 where the pre-tension was 135.7 N (30.5 lb) for riser-like natural frequencies.

The first series of experiments was conducted with a single cylinder to provide data for comparison with the paired cylinder tests. The comparison provided information pertaining to the interaction between the cylinders as a function of cylinder proximity and the incident waves. The tests were conducted for two pretensions T_1 and T_2 , for all the wave conditions. Table 3.5 summarizes the tests performed with the single cylinder.

Table 3.5: Summary of the single cylinder tests.

Tension	Regular	Random rms (extreme)	Total
T_1	4	1 (5)	10
T_2	4	1 (5)	10

The second phase of the experiments was with the pair of cylinders. Here the focus was on the extreme response and collision behavior of the cylinders, and on the characterization of the forces and response as a function of orientation and spacing. Most tests were conducted with the cylinders pretensioned in the $[T_1, T_1]$ arrangement, but for certain locations the pretension arrangements were modified to study the influence of cylinder pretension difference on the response. Table 3.6 summarizes the paired cylinder tests.

3.8.3 Testing Procedure

The wave gages were calibrated daily at the start of the tests. After calibration, access to the cylinders was made by boat and the cylinders were pretensioned using the weight and pulley system described earlier. The cylinders were then struck with a blunt object and the free vibration measured using the data acquisition system. The natural frequencies of the cylinder were then compared to those desired as illustrated in Tables 3.6 and 3.7 to confirm that the pretension had been applied properly and that the cylinders had the desired dynamic characteristics. The next section discusses this in more detail.

Table 3.6: Summary of the paired cylinder tests.

Orientation	Spacing	Tension	Regular	Random r.m.s. (extreme)	Total
0°	2.5D	[T ₁ , T ₁]	4	1 (5)	10
0°	2.5D	[T ₁ , T ₂]	4	1 (5)	10
0°	2.5D	[T ₂ , T ₁]	4	1 (5)	10
0°	3.5D	[T ₁ , T ₁]	4	1	5
0°	3.5D	[T ₁ , T ₃]	4	1	5
0°	5D	[T ₁ , T ₁]	4	1 (5)	10
0°	5D	[T ₁ , T ₂]	4	1	5
0°	7.5D	[T ₁ , T ₁]	4	1	5
0°	10D	[T ₁ , T ₁]	4	1	5
0°	10D	[T ₂ , T ₂]	4	1	5
0°	15D	[T ₁ , T ₁]	4	1	5
0°	15D	[T ₂ , T ₂]	4	1	5
22.5°	2.5D	[T ₁ , T ₁]	4	1	5
22.5°	5D	[T ₁ , T ₂]	4	1	5
45°	2.5D	[T ₁ , T ₁]	4	1	5
45°	2.5D	[T ₁ , T ₂]	4	1 (5)	10
45°	5D	[T ₁ , T ₁]	4	1	5
67.5°	2.5D	[T ₁ , T ₁]	4	1	5
67.5°	5D	[T ₁ , T ₁]	4	1	5
90°	2.5D	[T ₁ , T ₁]	4	1 (5)	10
90°	2.5D	[T ₁ , T ₂]	4	1	5
90°	5D	[T ₁ , T ₁]	4	1	5

Offsets were taken before each test to zero all the channels. Regular wave tests were conducted at the rate of about 2 tests/hour while the random wave tests were conducted about 1 every 50 minutes. Each test was started only after the water level had settled to a maximum fluctuation of 5 mm over 25 seconds. The procedure files were run immediately after the data was acquired. They produced summary statistics for all channels and plotted spectra and time histories of specified channels. The curvature data was low-pass filtered at 5 Hz decimated to a rate of 10 Hz and copied to the VAX 9000 mainframe at the university. The curvature data were integrated to obtain the displacements at specified locations and then copied back to the VAX 3500. All data were backed up to tape in the form of VMS save sets. Appendix C contains tables showing all the pertinent data acquisition information, including the test log which was updated after each test and the name of the saveset in which it was archived.

3.9 Comparison of Predicted and Measured Natural Frequencies

To verify that the cylinders had the desired dynamic characteristics, the cylinder was periodically re-tensioned and free vibration tests were conducted to estimate the natural frequencies. The measured natural frequencies were compared to the desired natural frequencies from the finite element model and the procedure was repeated until the desired tolerance was met. This was very important as a change in tension (due to creep or slippage in the tensioner) could modify the natural frequencies of the cylinder. The pretension was monitored from the offset readings from the tension cell before the start of each test.

Figures 3.14 and 3.15 show the spectra of the free vibration response of the cylinders under the two pretension conditions, T_1 and T_2 . The natural frequencies are represented by the peaks in the spectra and are tabulated in Tables 3.6 and 3.7. From the figures it is seen that the natural frequencies are closely spaced at even intervals, especially for the lower modes. This represents dynamic behavior of a string where the modes are evenly spaced with an interval equal to the first natural frequency. It is also seen that after about the fifth mode the spacing increases with each mode. This is due to the increasing importance of the bending stiffness contribution to the dynamic behavior of the cylinder. The tables also contain predicted natural frequencies from finite element models of (1) the prototype tendon and riser detailed in Table 3.2, scaled down to model scale, and (2) the model cylinder in Table 3.3. The measured natural frequencies compare very well with the predictions for the

model cylinder while the comparison is good for the first four modes of the actual riser/tendon models and then overpredicts the natural frequencies with increasing errors. This is due to the bending stiffness of the model cylinder being an order of magnitude greater than that determined by the scaling laws.

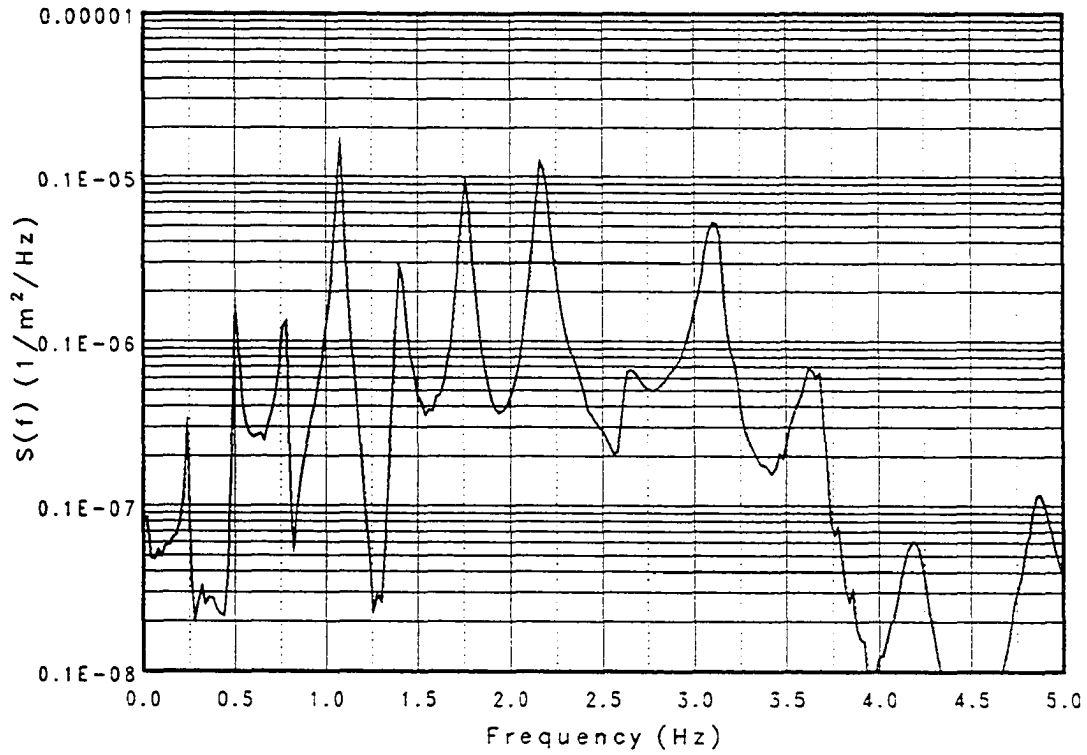


Figure 3.14: Measured free vibration spectrum for pretension T_1 .

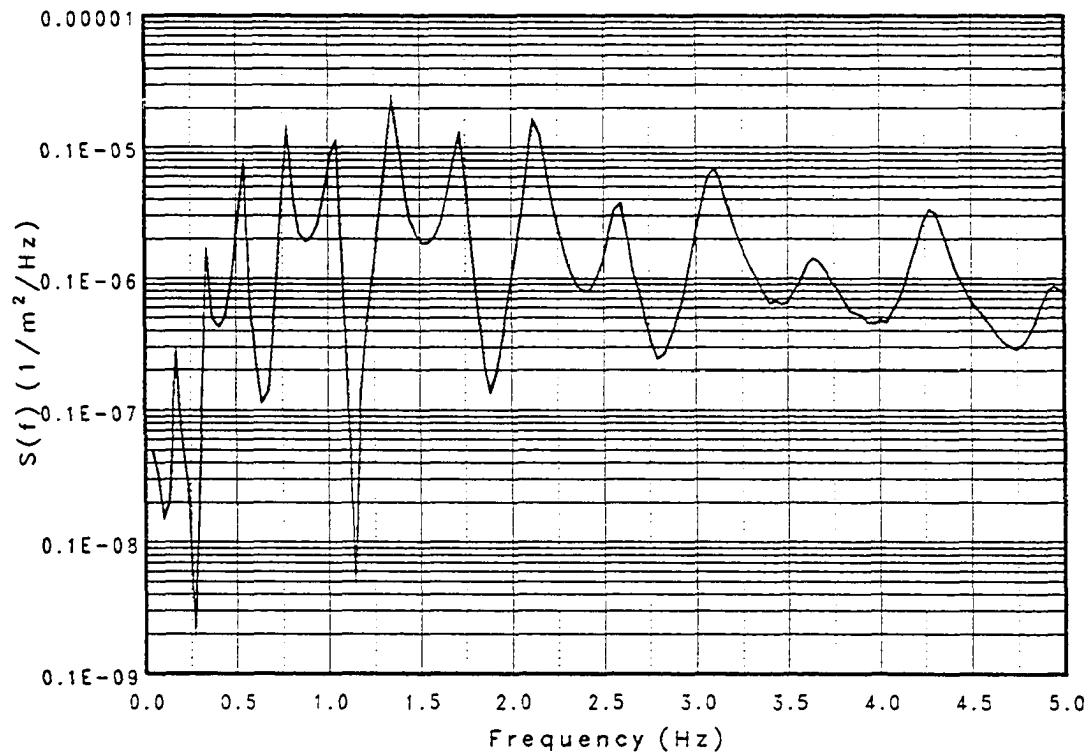


Figure 3.15: Measured free vibration spectrum for pretension T_2 .

Table 3.7: Measured, predicted and desired natural frequencies [T_1].

Mode #	Natural Frequencies (Hz)		
	Prototype (scaled)	FE (model)	Measured
1	0.24	0.24	0.24
2	0.49	0.49	0.52
3	0.73	0.76	0.77
4	0.98	1.05	1.08
5	1.23	1.36	1.41
6	1.49	1.71	1.76
7	1.75	2.09	2.20
8	2.01	2.52	2.64
9	2.28	2.98	3.12
10	2.55	3.49	3.63
11	2.84	4.04	4.20
12	3.12	4.63	4.85

Table 3.8: Measured, predicted and desired natural frequencies [T_2].

Mode #	Natural Frequencies (Hz)		
	Prototype (scaled)	FE (model)	Measured
1	0.17	0.16	0.16
2	0.33	0.34	0.35
3	0.50	0.54	0.53
4	0.67	0.77	0.78
5	0.84	1.03	1.04
6	1.01	1.34	1.37
7	1.18	1.68	1.70
8	1.36	2.08	2.15
9	1.53	2.51	2.61
10	1.71	3.00	3.12
11	1.88	3.54	3.68
12	2.06	4.12	4.29
12	2.24	4.75	4.85

4. CHARACTERIZATION OF CYLINDER RESPONSE IN WAVE FLOWS

The data obtained from the experimental program are analyzed with the objective of providing some insight into the complex wave-flexible cylinder interaction phenomenon. Where applicable, the experimental data are compared to results obtained from the finite element model described in Appendix A.

The section begins with a brief overview of the wave-structure interaction process and previous experimental investigations pertinent to this study. Sample data from a single cylinder test with random waves are presented and discussed to provide a description of the data from the various transducers and to point out some response features which are analyzed in more detail in later sections. The single cylinder data are analyzed in detail as a function of wave and structural parameters with reference to results from previous studies. The inline top reaction, curvature and displacement are also compared to predictions from the finite element model. The paired cylinder data are presented in the form of graphs characterizing the r.m.s. response of the cylinders as a function of orientation and spacing. A few cases are chosen to analyze the interaction phenomenon in more detail. Finally, the relative motion between the cylinders is analyzed to study the collision behavior of the cylinders and provide the background for the probabilistic analysis in Section 5.

4.1 Background

Experimental studies of fluid interaction with cylinders have been conducted with a variety of flow and cylinder conditions. The studies have been conducted using various materials, fluids and model scales. Most studies have focused on single, rigid cylinders subjected to steady flow, oscillating flow or surface waves while fewer have considered cylinder groups and flexible cylinders. The following paragraphs provide a brief overview of the wave-structure interaction phenomenon as pertains to this study. An extensive review of the existing literature is presented in Sarpkaya and Isaacson (1981) and Blevins (1990).

Fluid-induced forces on cylinders can act both inline and transverse to the direction of flow. For steady flow the inline force is primarily due to fluid drag, while for

oscillating flow or waves the inline force is considered to be the sum of an inertia force and a drag force as proposed by Morison et al. (1950). The inertia and drag forces are related to the fluid particle acceleration and velocity respectively. Transverse forces are caused by the flow separation or shedding of vortices from the cylinders. The vortex shedding process is very complex and is dependent on several fluid and structural parameters (Blevins 1990).

The inline wave force on a cylinder has been the subject of numerous studies over the last four decades. The main focus has been on the estimation of the drag and inertia coefficients to be used with the Morison's equation. These coefficients are sensitive to fluid and structural parameters which is reflected in the large scatter observed in the published data. Most of the studies have considered the wave force on a single rigid cylinder, although there have been some studies concerned with the cylinders' flexibility and group arrangement.

The transverse force on a cylinder due to wave loading has not received the extensive attention accorded to the inline force. However, there have been numerous studies on transverse forces due to steady flow (Blevins 1990). These studies have considered both rigid and flexible cylinders, both single and in groups. No satisfactory analytical or numerical method has been found that adequately describes this phenomenon, though there are some models, e.g., the wake oscillator model, that do represent some vortex shedding characteristics but require calibration with experimental results.

Most studies of the interaction of fluid with cylinders in close proximity have been conducted with steady flow (e.g., Zdravkovich, 1985 and King and Johns, 1976). Tests have been conducted with pairs and groups of rigid and flexible cylinders, in both air and water, and flow-induced forces and response characterized as a function of the cylinder orientation and spacing. For the tandem case (one behind the other), interference effects were observed up to a spacing greater than eight cylinder diameters. This occurs when the trailing cylinder is in the wake of the lead cylinder (up to 20°). For the side-by-side configuration (transverse to the flow direction), interference was limited to a spacing of two to three diameters. In general inline drag force was reduced by a maximum of 50% while the transverse force was found to increase up to 200%. The vortex shedding phenomenon was found to be a function of cylinder spacing, position and flexibility.

Studies of cylinder pairs or groups with oscillating flow and waves have been more limited in scope. Bushnell (1977) used rigid cylinders 7.62 cm in diameter and determined interference coefficients for a pair of cylinders and a 3×3 array. The spacing

was maintained at three diameters and the inline and transverse forces measured for several incidence angles and amplitude of flow oscillation. He observed that the inline drag force was reduced up to 50% while the maximum transverse force observed was three to four times that for a single cylinder. Interference effects were observed to increase with relative flow displacement. Sarpkaya and Cinar (1980) determined the inertia, drag and lift coefficients for a pair of rigid cylinders subjected to harmonic flow. The cylinder diameter ranged between 6.4 to 12.7 cm, the spacing was varied between 1.5 to 3.5 diameters, and the position of the two cylinders changed with respect to the flow direction. For the tandem and side by side position both drag and inertia coefficients were found to depend on the Keulegan-Carpenter number, cylinder spacing and amplitude of flow oscillation. The transverse force was observed to triple for some circumstances.

Chakrabarti (1979, 1980) determined the hydrodynamic coefficients for the inline wave force on an array of cylinders with diameters of 7.62 cm and lengths of 3.05 m, arranged in a row transverse to the wave direction (side-by-side). He observed that the largest scatter in coefficients was for small cylinder spacings. In general the inertia and drag coefficients increased as the cylinder spacing decreased. Verley and Every (1977) studied the response of flexible cylinders under regular wave loading. They considered a single, pair and a 4×3 array of flexible cylinders with diameters of 2.54 cm and lengths of 76 cm. Cylinders were placed in tandem and side by side at various spacings. Interference was observed to occur in the side by side position at spacing of two diameters or less. The transverse response was seen to increase by up to 170% while a slight reduction was observed in the inline response.

The above discussion shows that though flow-structure interaction has been studied extensively, very little attention has focused on cylinder flexibility and group arrangement subjected to regular and random waves. Most studies with waves and harmonic flow have focused on rigid cylinders with the objective of obtaining coefficients for use with the Morison's equation. Studies concerning cylinder flexibility and group effects have been conducted primarily with steady flow. The present study therefore contributes new information regarding the complex interaction phenomenon of regular and random waves with continuously flexible cylinders.

4.2 General Description of Data

Before undertaking a detailed analysis of the data obtained during this experimental program, it is appropriate to describe a data set which is representative of the majority of the data collected to point out the characteristics of each measurement and to provide an overall picture of the response behavior of the cylinder.

The data set chosen for this general description was Test # SRN1T1_001, random wave interaction with a single cylinder with pretension [T_1]. Figures 4.1—4.6 show time series and spectra of six channels of data obtained during this test, each one representative of a different measurement:

- incident wave elevation
- tension at the top of the cylinder
- inline (X) curvature at location -2.91 m
- transverse (Y) curvature at location -2.91 m
- inline (X) reaction at top pin connection
- transverse (Y) reaction at top pin connection

Figure 4.1 shows the time series and spectrum of a measured realization of the random sea used (JONSWAP: $H_s = 0.5$ m, $T_p = 2.94$ sec., $\gamma = 2.0$). The wave elevation during the tests was measured by a wave gage placed 1.5 m to the west of the cylinder. Superimposed on the figure is the target spectrum. The figure shows that the generated sea matched the target conditions very well. The waves were generated for a duration of 409.6 seconds and contained approximately 188 waves which were sufficient to provide accurate estimates of the significant wave height and of r.m.s. estimates of response. The wave elevation was the sole input measurement made; all other measurements were of the cylinder response.

Figure 4.2 illustrates the fluctuation in tension at the top of the cylinder in response to the random waves. The tension fluctuations are related to the inline and transverse displacement of the cylinder. The zero value on the graph corresponds to the pretension applied to the cylinder before the waves were generated (for this test, $T_1 = 224.6$ N). The spectrum and the time series indicate significant energy at frequencies lower than that of the incident wave energy. This is due to the viscous drift forces exerted by the waves, causing the cylinder's mean position to be displaced from the rest position. The tension fluctuations also occur at twice the frequency of cylinder displacement as each cycle of displacement leads to two cycles of tension

fluctuation. For this specific test the mean tension was 9.16 N ($\simeq 5\%$ of T_1) with a maximum value of 70.3 N ($\simeq 35\%$ of T_1). As discussed in earlier sections the tension in the cylinder is a very important parameter as it provides most of the “stiffness” to the structure. Therefore variation in tension is very important as it implies system characteristics that are time varying.

Figures 4.3 and 4.4 present inline and transverse curvature measurements 2.91 m below the still water level (SWL). The inline spectrum (Figure 4.3) shows that a majority of the response energy is at the incident wave frequencies; however, it is seen that there are smaller peaks at much higher frequencies. Figure 4.4 shows that the transverse response has the majority of its energy at these high frequencies with almost none at the wave frequencies. Comparing the frequencies at which these peaks occur to those in Table 3.7 it is seen that they are very close to the natural frequencies measured from the free vibration tests on the cylinder, corresponding to modes 3–8 of the cylinder. The transverse curvature has 804 zero crossings compared to 430 for the inline curvature. The curvature measurements are also sensitive to high frequency response due to the large curvatures (bending stresses) associated with response in high modes.

Figures 4.5 and 4.6 present the measured inline and transverse reactions respectively at the top U-joint. The reaction at either end of the cylinder is due to two components of force: (1) the force exerted on the cylinder by the wave kinematics, and (2) the inertial forces due to the mass and acceleration of the vibrating cylinder. The inline reaction has most of its energy at the incident wave energy with peaks of smaller magnitude at natural frequencies of the cylinder, similar to that observed for the inline curvature. The transverse reaction has all its energy at the natural frequencies of the cylinder, with modes in the range 1–2.5 Hz. with approximately the same energy, with relatively very little energy at the incident wave frequencies. It is also seen that the inline reaction has approximately 193 zero crossings compared to 674 for the transverse reaction. The Figures 4.3–4.6 of the inline response indicate that high frequency peaks are at the same frequencies as those of the transverse response. Interestingly the transverse response shows no significant energy at the wave frequency where the inline response has most of its energy. This phenomenon is analyzed in more detail later in this section.

Figures 4.7–4.8 show plots of the instantaneous curvature and displacement along the length of the cylinder for intervals of 0.2 seconds for both the inline and transverse axes respectively. The solid circles in the curvature sequence correspond to

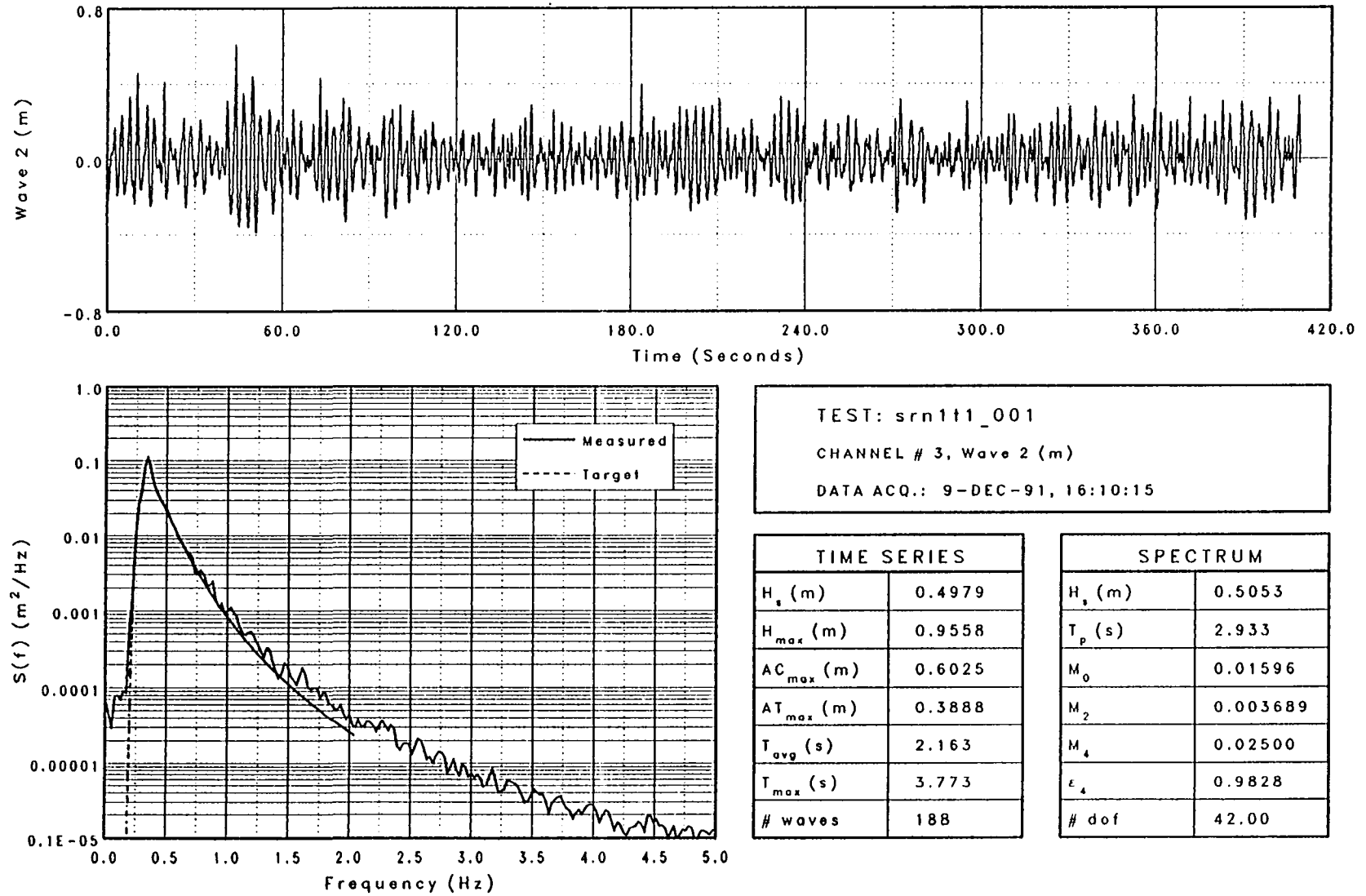


Figure 4.1: Sample data: random wave elevation.

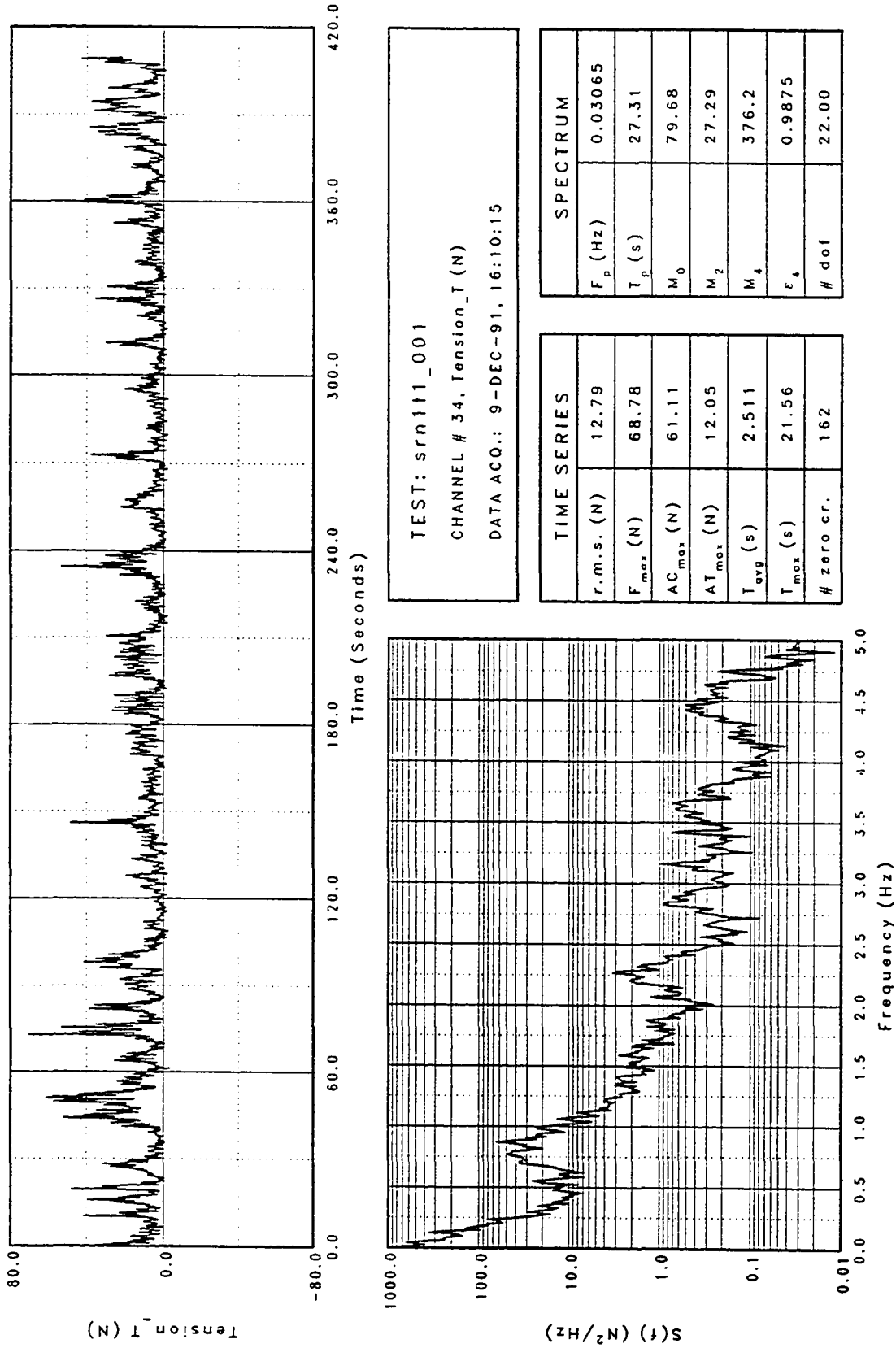


Figure 4.2: Sample data: top tension.

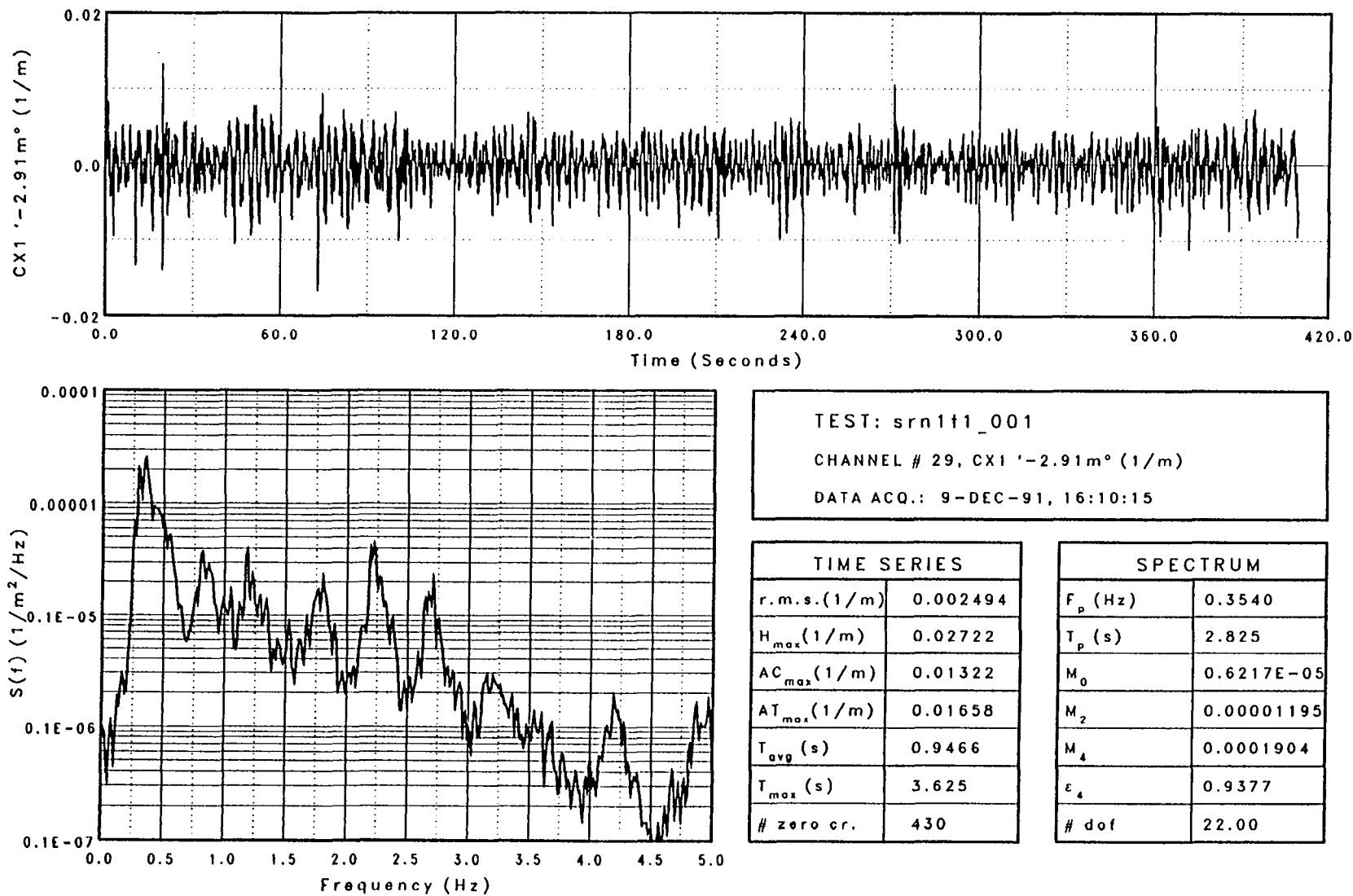


Figure 4.3: Sample data: inline curvature (-7.47 m).

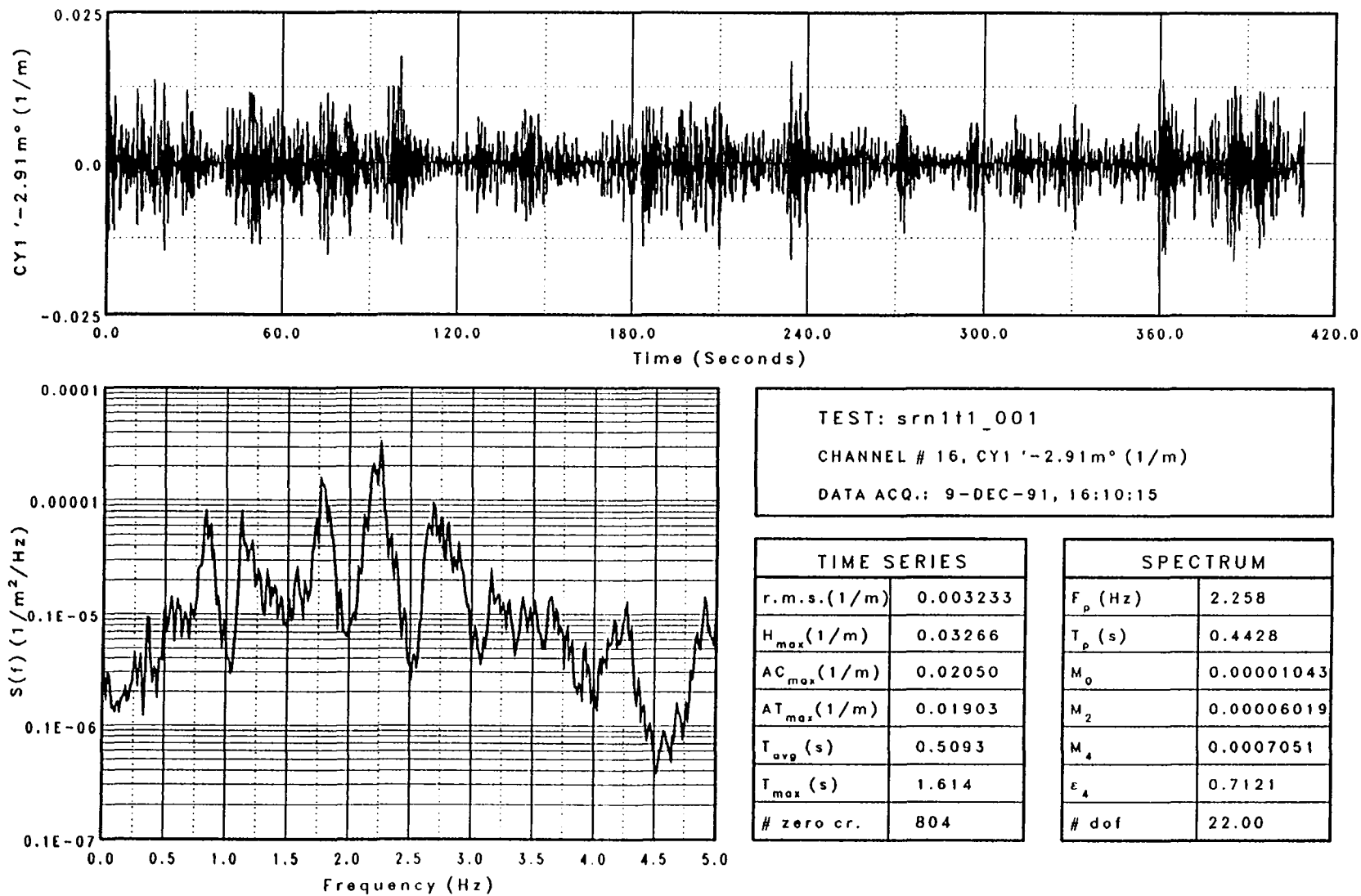
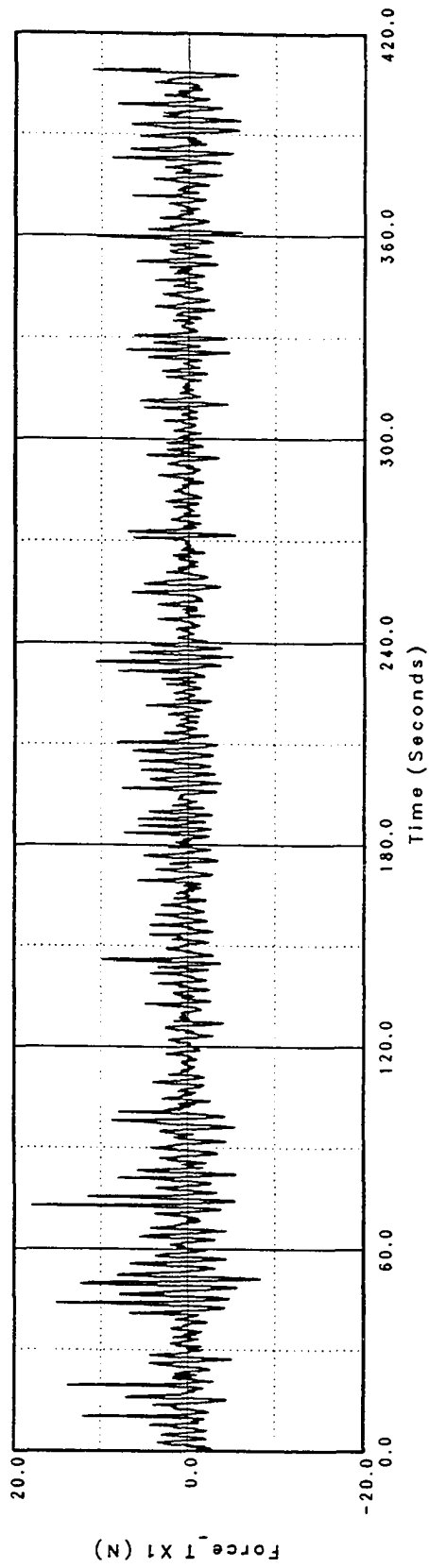


Figure 4.4: Sample data: transverse curvature (-7.47 m).



TEST: srn1t1_001
 CHANNEL # 35, Force_T X1 (N)
 DATA ACQ.: 9-DEC-91, 16:10:15

TIME SERIES		SPECTRUM	
r.m.s. (N)	2.432	F_p (Hz)	0.3294
F_{max} (N)	23.31	T_p (s)	2.825
AC_{max} (N)	17.64	M_0	5.745
AT_{max} (N)	8.653	M_2	1.756
T_{avg} (s)	2.092	M_4	26.19
T_{max} (s)	4.061	ϵ_4	0.9897
# zero cr.	193	# dof	22.00

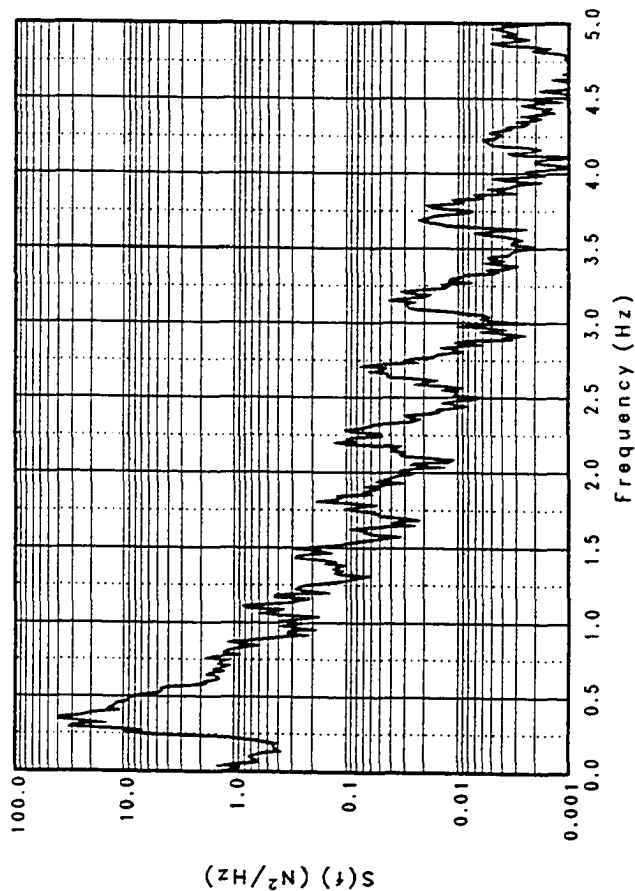


Figure 4.5: Sample data: inline top reaction.

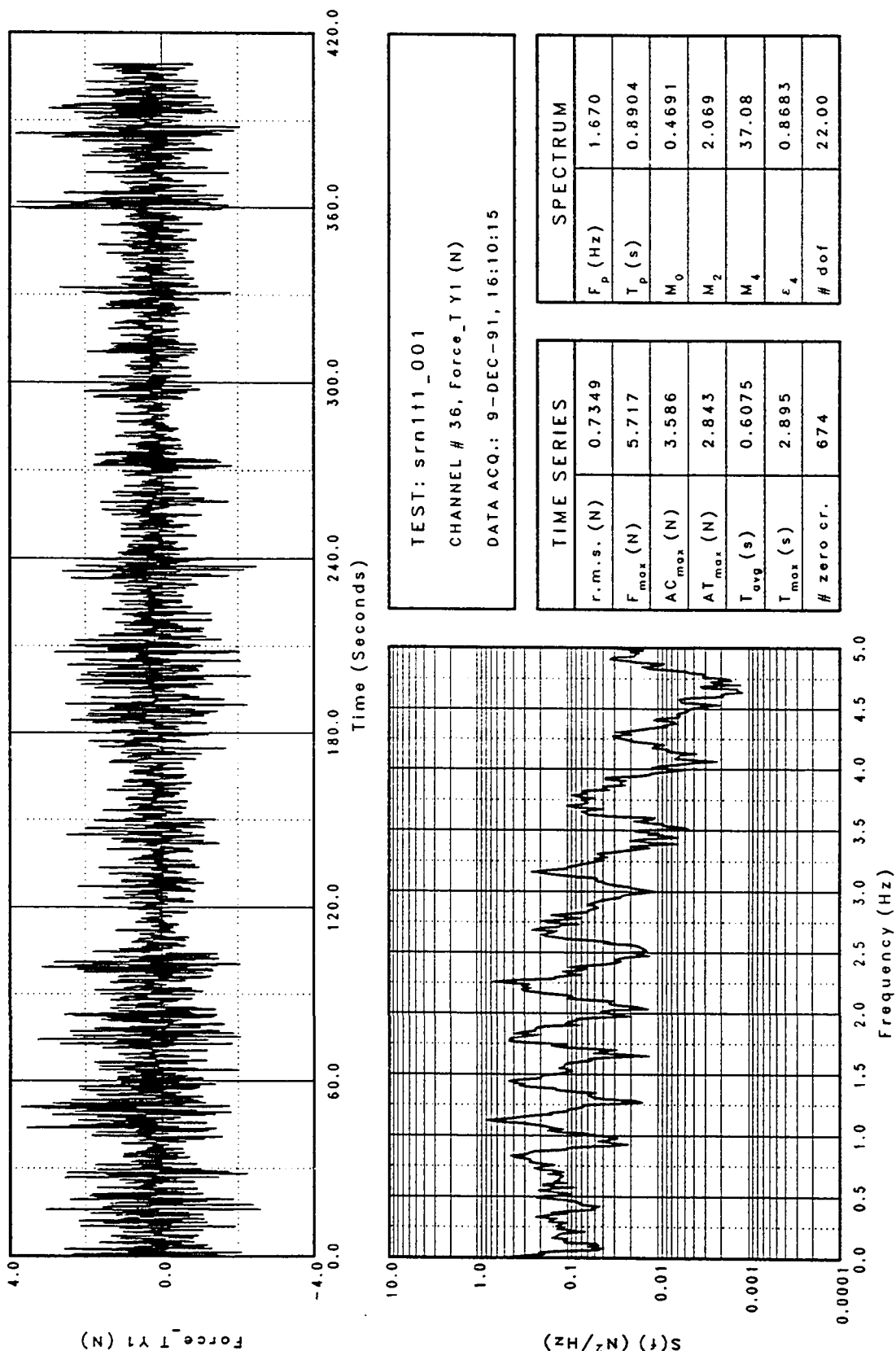


Figure 4.6: Sample data: transverse top reaction.

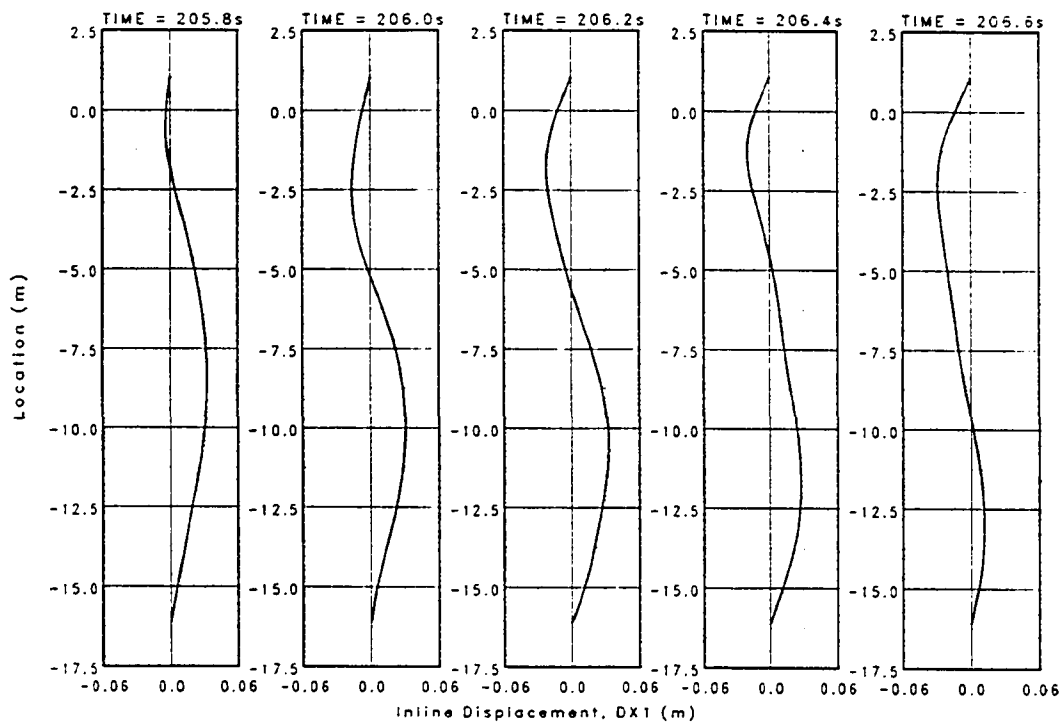
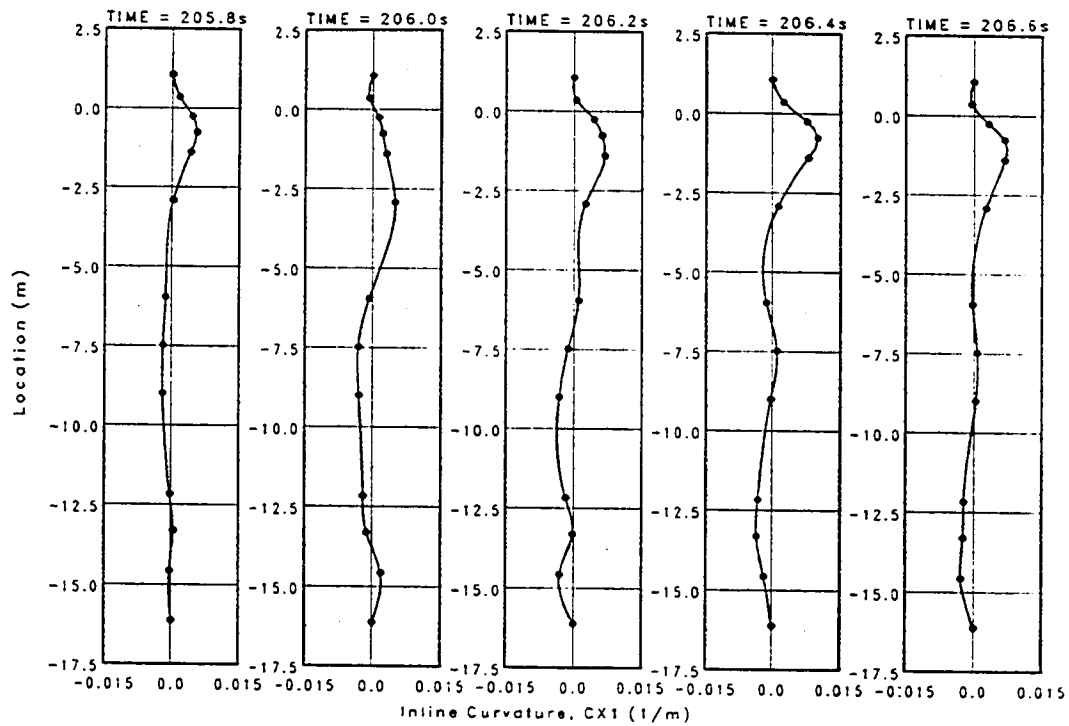


Figure 4.7: Time snapshots of inline curvature and the estimated displacement of the single cylinder.

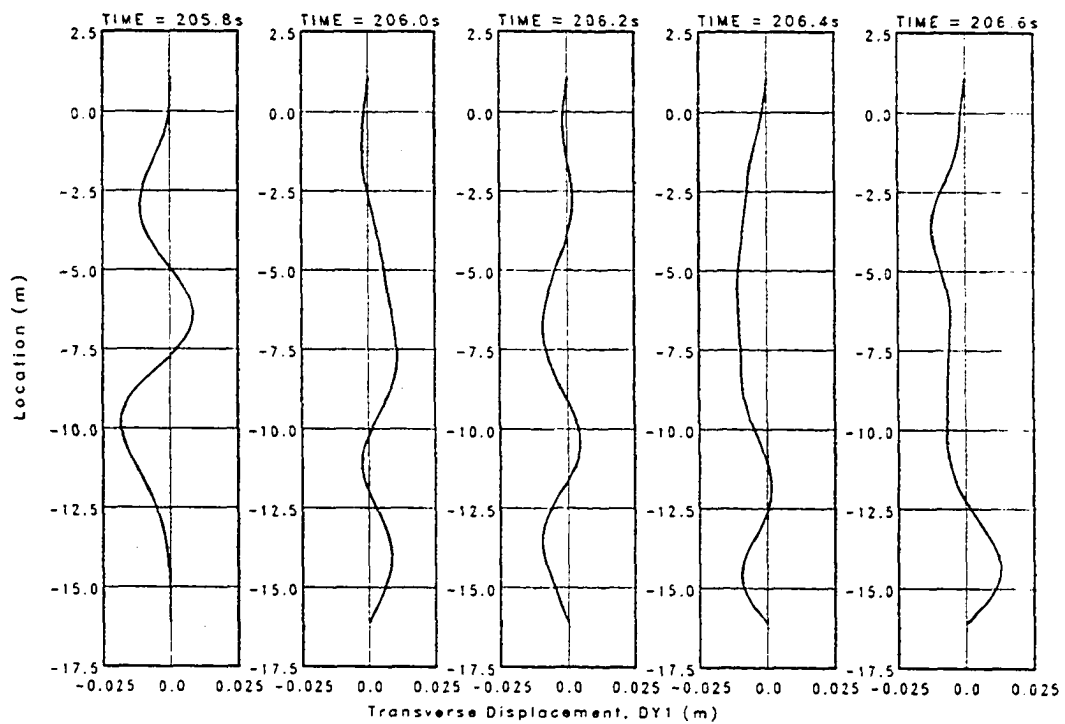
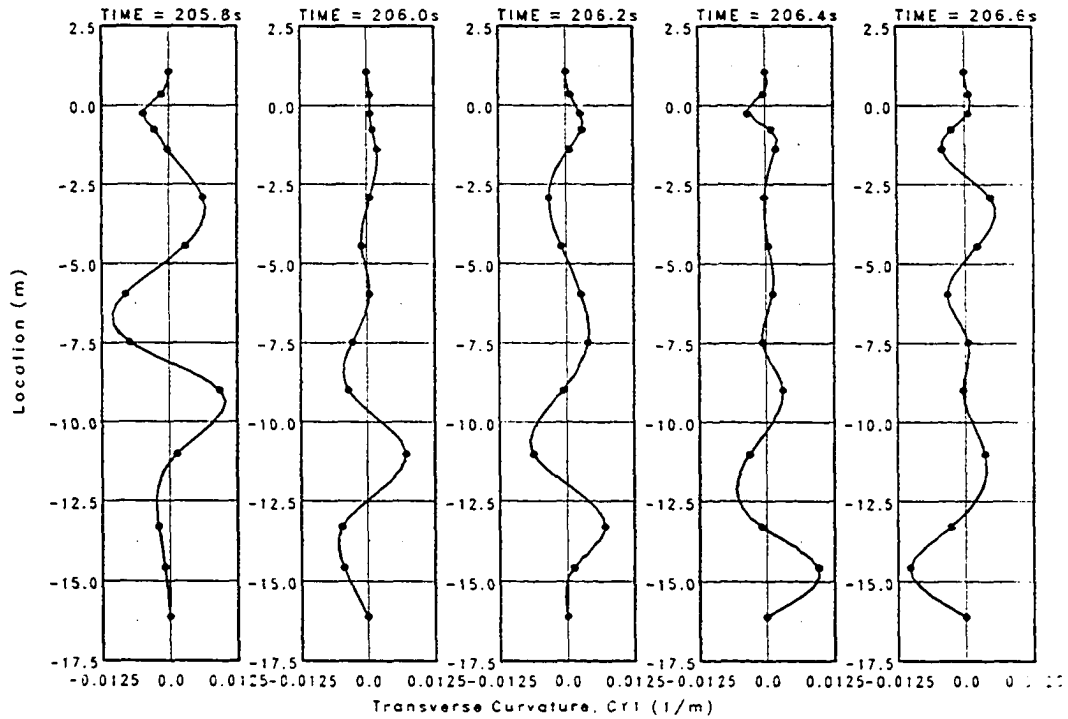


Figure 4.8: Time snapshots of transverse curvature and the estimated displacement of the single cylinder.

the discrete measurements of the curvature while the solid line is the cubic spline fit through the measurements. It is seen that the number and location of the transducers are sufficient to pick up the important modes of vibration of the cylinder. The displacement sequences are obtained by integrating the curvature distribution estimated by the cubic spline as described in Section 3. The displacement estimates are used extensively in studying the relative motion between the cylinders which is used to characterize the collision behavior of the cylinders in Section 5.

4.3 Analysis of the Single Cylinder Data

The single cylinder data serve two major purposes: (1) to provide some insight into the wave-flexible cylinder interaction and allow comparison of the results with those obtained by other investigators, and (2) to serve as a comparison to the paired cylinder data to determine interference effects between two cylinders in close proximity.

The single cylinder data were comprised of 20 tests where the cylinder response was measured when subjected to regular and random waves at two pretension conditions (T_1 and T_2). The single cylinder analysis first focuses on the regular wave data where results are presented to provide comparison with existing results for rigid and flexible cylinders in steady, oscillating and wave flows. The random wave data, some of it already presented in Figures 4.1—4.8, are then analyzed in more detail. Inline curvature, reaction and displacement results for both regular and random waves are compared to estimates from the finite element model and discussed.

4.3.1 Regular Waves

Four regular wave cases were considered with a wide range of Keulegan–Carpenter numbers (N_{KC}). Previous investigators have shown that the wave induced forces and response can be classified based on the N_{KC} , and other non-dimensional parameters like the reduced frequency (U_r) and the Strouhal number (S) which are primarily used for transverse forces and response in fluid flow. The reduced velocity and Strouhal numbers are defined as

$$U_r = \frac{UD}{f_v} \quad (4.1)$$

$$S = \frac{f_s D}{U} \quad (4.2)$$

where, U is the maximum wave horizontal particle velocity at the SWL, D the cylinder diameter, f_v the frequency of vibration of the cylinder, and f_s the frequency of vortex

shedding. The following paragraphs present the regular wave results as a function of Keulegan–Carpenter number and the reduced frequency and compare the present experimental findings with those obtained from previous investigations.

At this point it is important to point out some physical characteristics of the fluid-structure interaction problem being analyzed as compared to previous studies with steady, harmonic and wave flows. Due to the very large water depth (16.76 m at model scale), with the cylinders extending from the free surface to the bottom, only a portion of the cylinder is directly acted upon by the wave kinematics. The remainder of the cylinder is free to oscillate, subject to damping induced by the fluid and present in the structure. Due to the exponential decay of the wave kinematics with water depth, the fluid loading on the cylinder is not constant along its length at any given instant of time. This is in contrast to tests conducted in harmonic and steady flow where the flow kinematics are constant along the length of the cylinder at any given time. Another important consideration is that the cylinders are continuously flexible with structural behavior similar to that of a string. As there are many closely spaced natural frequencies in the range of wave excitation and its harmonics, one or more of the natural frequencies can be excited leading to a multi-modal structural response. This is in direct contrast to many previous studies involving cylinder flexibility where the cylinder was a flexibly mounted rigid cylinder with one or two clearly defined natural frequencies.

Figures 4.9—4.12 present time series and spectra of the inline and transverse top reaction, for the four different Keulegan–Carpenter number cases. The top reaction is chosen as it best represents the wave forces on the cylinder (the top reaction resists the majority of the wave forces) and serves as a comparison to previous studies. The time series data are presented for each N_{KC} for one cycle of the incident wave. The spectra are computed from a segment of the acquired data containing an average of 20 waves. Spectral peaks occurring at the wave frequency or its harmonics are indicated by the ratio of the peak frequency to the wave frequency. Peaks corresponding to response at natural frequencies are indicated with roman numerals indicating the mode excited. The following discussion on vortex shedding follows the classification outlined in Blevins (1990).

Period=1.4 sec, $N_{KC}=10.6$: This case falls in the $8 \leq N_{KC} \leq 15$ range and exhibits vortex shedding behavior similar to that observed in previous studies, where the predominant vortex shedding frequency, f_s , is at twice the incident wave frequency

and is very regular. The inline reaction is mainly at the wave frequency with traces of higher harmonics. The inline curvature shows larger amounts of energy at twice the wave frequency than the inline top reaction as the curvature measurement is more sensitive to high frequency vibration. It is interesting to note that for this case the incident wave frequency is close to the third natural frequency of the cylinder and the transverse response at twice the wave frequency is close to the fifth mode of the cylinder as illustrated later.

Period=2.0 sec, $N_{KC}=21.6$: This falls in the $15 \leq N_{KC} \leq 22$ range and the dominant frequency of transverse response and reaction is at 3 times the incident wave frequency. The inline response and reaction are at the wave frequency with some higher order contributions at integer multiples of the wave frequency. This is also consistent with the classification presented by Blevins (1990).

Period=2.6 sec, $N_{KC}=36.6$: This falls in the $N_{KC} \geq 30$ range where the flow is considered to be quasisteady and the large database of results from steady flow tests are considered applicable. Based on this classification previous studies (Blevins 1990) indicate that the dominant vortex shedding frequency can be computed based on a Strouhal number of 0.2 and reduced velocities in the range $5.5 \geq U_r \geq 8.5$. From the figures it is seen that the response is at a variety of frequencies corresponding to higher harmonics of the incident wave frequency and at several natural frequencies of the cylinder.

Period=3.1 sec, $N_{KC}=52.7$: This case is similar to the $N_{KC} = 36.6$ case where the cylinder response is at many frequencies with the peak frequency corresponding to the sixth mode of vibration of the cylinder, with significant energy at a number of frequencies.

Table 4.1 presents the peak vibration frequencies of the cylinder from the curvature transducers along its length and the corresponding reduced velocities for all the regular wave conditions. The peak frequencies are divided based on the “forced” and “free” regions of the cylinder; the “forced” region being that portion of the cylinder acted upon by the wave kinematics and the “free” region the remainder of the cylinder free to oscillate. Table 4.1 shows that assuming a Strouhal number of approximately 0.2 and reduced frequencies in the range $5.5 \leq U_r \leq 8.5$ as noted in Blevins (1990) does not always yield the peak frequency of the response, especially

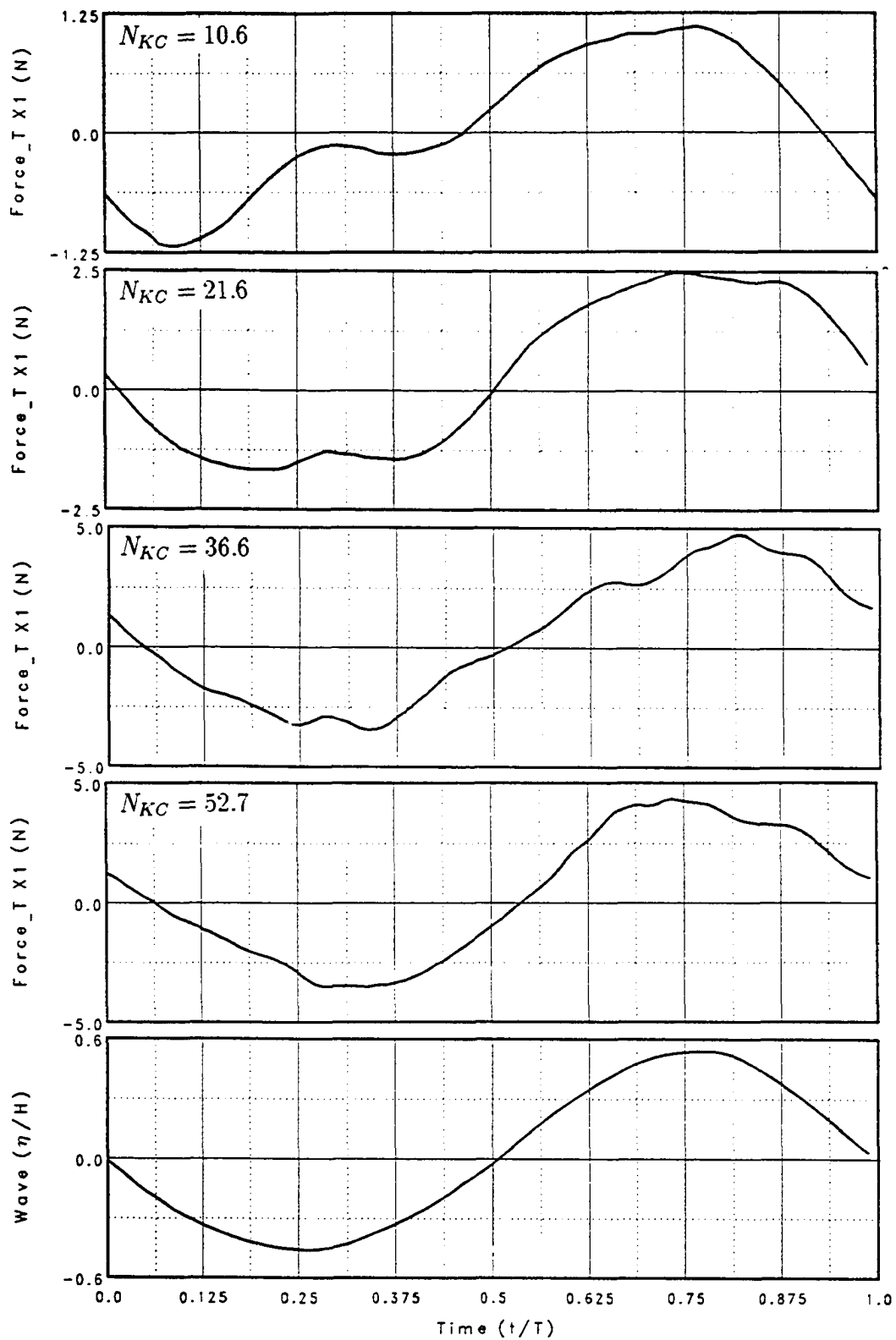


Figure 4.9: Inline top reaction for a single wave cycle as a function of N_{KC} .

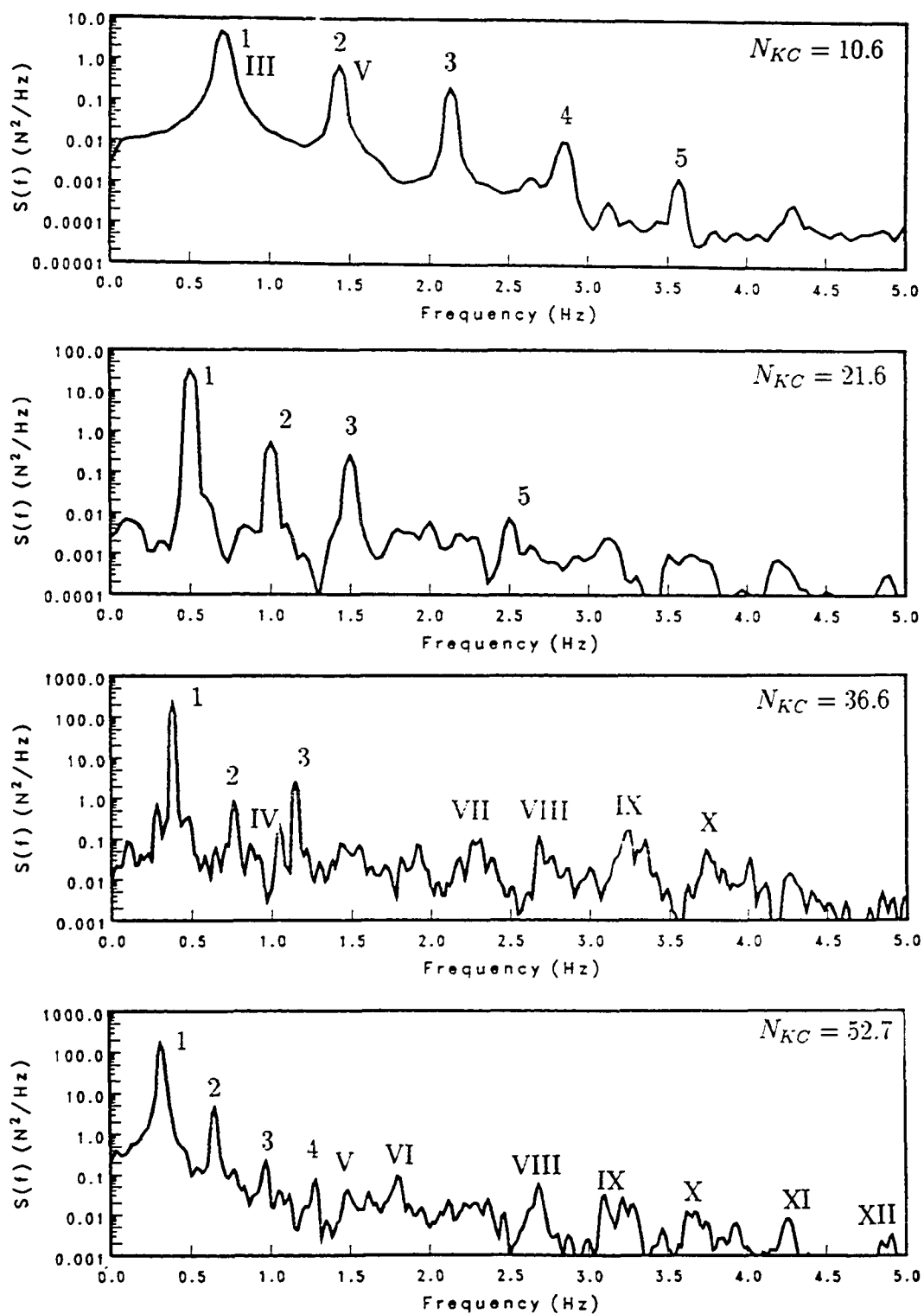


Figure 4.10: Spectra of inline top reaction as a function of N_{KC} .

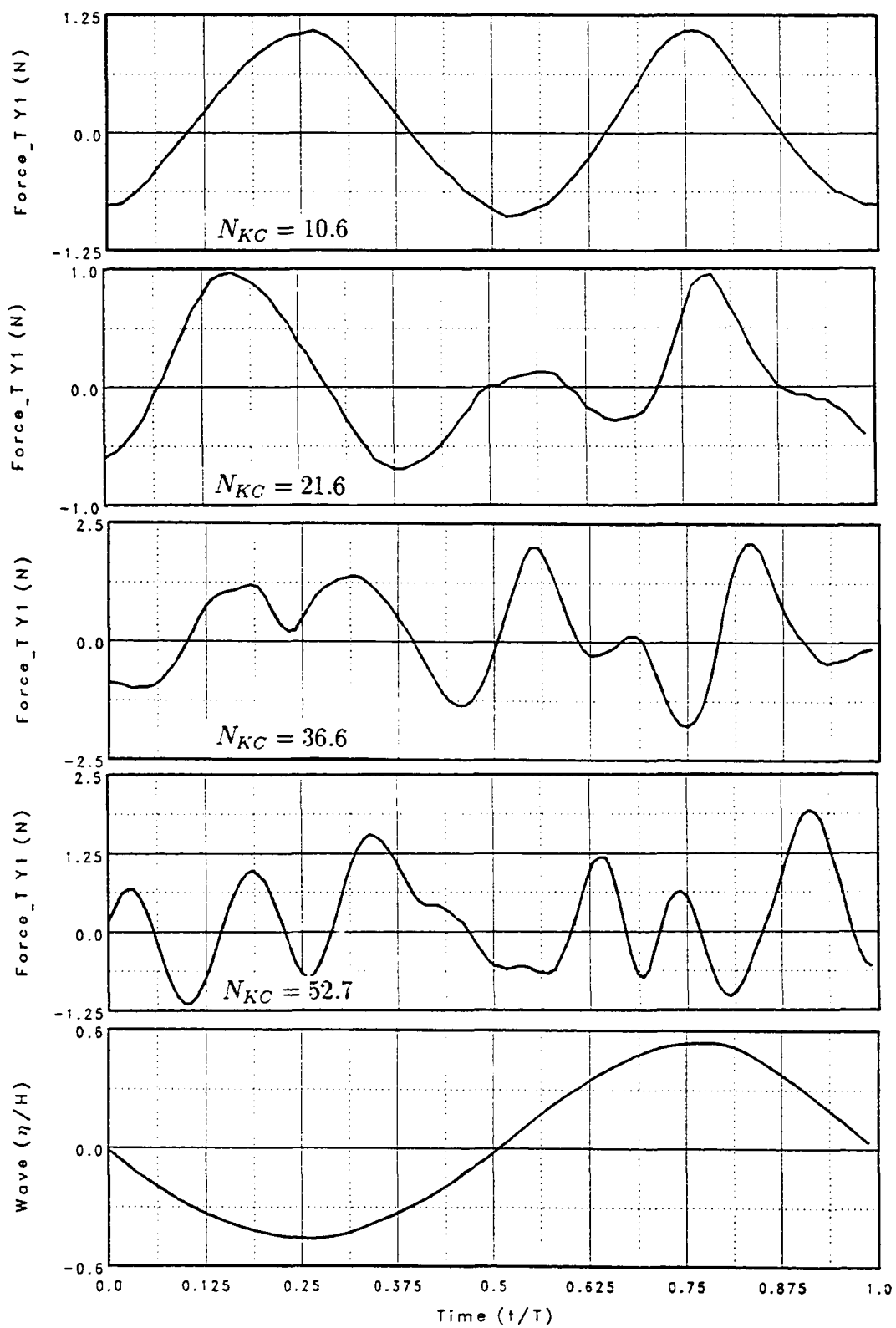


Figure 4.11: Transverse top reaction for a single wave cycle as a function of N_{KC} .

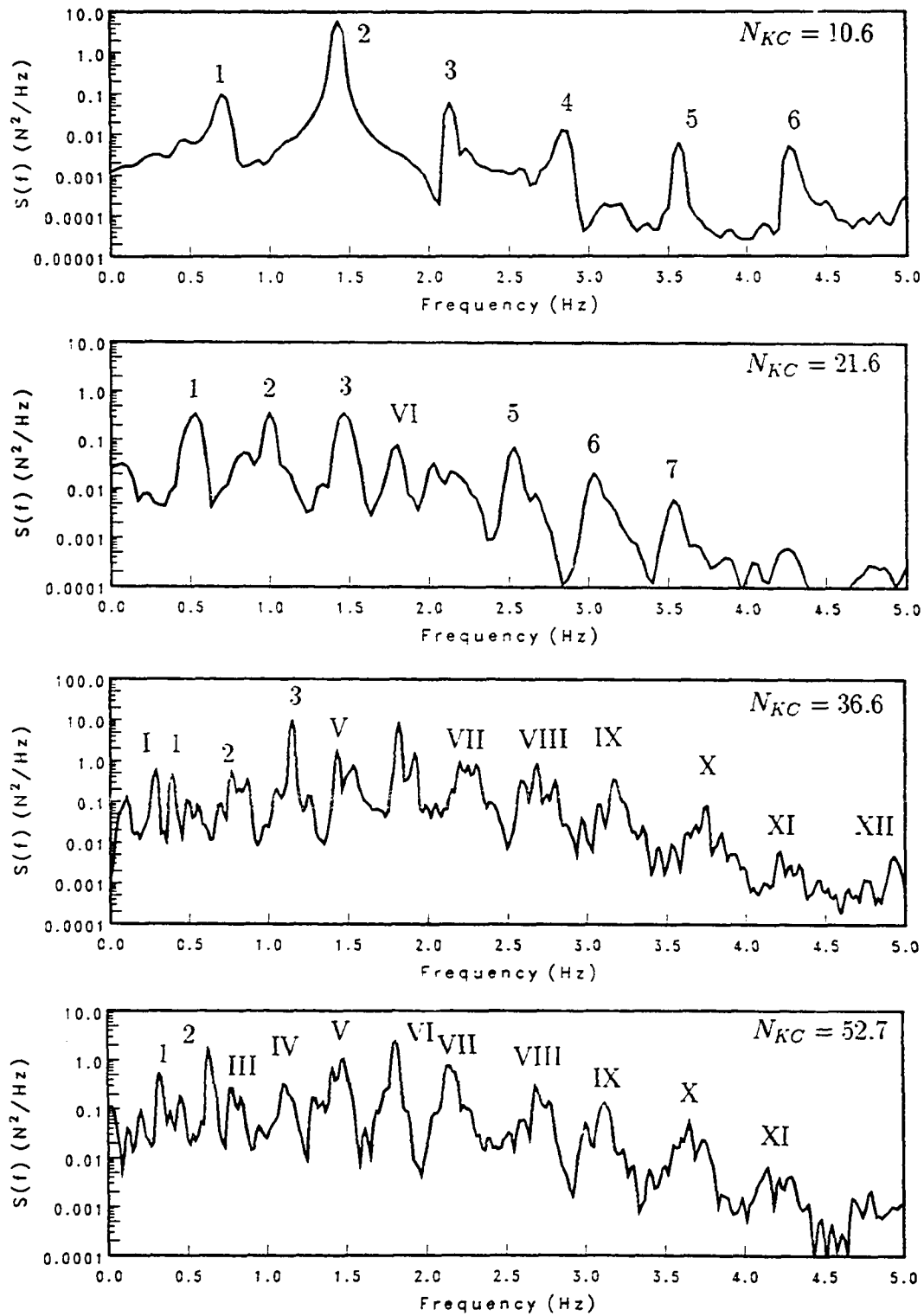


Figure 4.12: Spectra of transverse top reaction as a function of N_{KC} .

Table 4.1: Peak natural frequencies and corresponding reduced velocities for all single cylinder regular wave conditions.

Period (sec)	N_{KC}	Tension	Direction	Peak Vibration Frequencies (Hz)		Reduced Velocity, U_r	
				Forced	Free	Forced	Free
1.4	10.6	T_1	X	0.7, 2.13	0.7, 1.0, 1.43		
			Y	1.43	1.43	5.28	5.28
		T_2	X	0.7	0.7, 2.13, 2.83		
			Y	1.43	1.43	5.28	5.28
2.0	21.6	T_1	X	0.5	0.5, 1.5		
			Y	1.03, 1.43, 1.53, 2.53	1.00, 1.43, 1.53	10.5, 7.58, 7.08, 4.28	10.8, 7.58, 1.53
		T_2	X	0.5	0.5, 1.5		
			Y	1.00, 1.50	1.0, 1.53, 2.00	10.8, 7.08	10.8, 7.08, 5.4
2.6	36.6	T_1	X	0.38	0.38		
			Y	1.15, 1.82	1.15, 1.82	12.24, 7.75	12.24, 7.75
		T_2	X	0.38	0.38		
			Y	1.52, 1.93, 2.28	1.52, 1.93	9.28, 7.28, 6.16	9.28, 7.28
3.1	51.7	T_1	X	0.32	0.32		
			Y	1.80, 2.13	1.48, 1.8, 2.13	9.45, 7.97	11.46, 9.45, 7.97
		T_2	X	0.32	0.32		
			Y	0.65, 1.52, 2.73	0.65, 1.52, 1.83	26.16, 11.21, 6.22	26.16, 11.21, 9.27

for high Keulegan–Carpenter numbers.

Table 4.2 shows the influence of pretension on the r.m.s. response of the cylinder. The tension column lists the pretension, and the mean and the standard deviation of the tension fluctuation. The curvature data represent the largest r.m.s. curvature measured along the cylinder. The pretension influences the response of the cylinder with a decrease in pretension leading to an increase in the inline curvature and mean tension in the cylinder. The increase in mean tension is quite significant for the long wave periods where it is greater than 10% of the pretension and influences the natural frequencies of the cylinder. It is also seen that a decrease in pretension generally leads to a decrease in the top inline reaction. This could be due to a decrease in the drag force on the cylinder due to the larger cylinder velocities.

Table 4.2: Influence of pretension on r.m.s. cylinder response.

Period T (s)	Tension			Curvature		Top Reaction	
	T_0 (N)	μ (N)	σ (N)	X (1/m)	Y (1/m)	X (N)	Y (N)
1.4	222.4	3.730	2.431	0.003165	0.004323	0.7284	0.6733
1.4	135.7	4.840	3.001	0.004668	0.004097	0.4813	0.6699
2.0	222.4	6.246	3.626	0.004374	0.002035	1.518	0.3864
2.0	135.7	8.520	5.897	0.006968	0.002290	1.108	0.2683
2.6	222.4	17.55	6.760	0.008649	0.005581	2.796	1.112
2.6	135.7	26.91	11.15	0.01233	0.005961	2.859	1.023
3.1	222.4	14.95	3.000	0.007297	0.003983	2.694	0.7424
3.1	135.7	24.19	10.42	0.009792	0.004435	2.547	0.7641

To study the behavior in more detail, two cases representative of the observed wave-structure interaction are chosen corresponding to $N_{KC} = 10.6$ and 36.6. Comparisons are also made between the data and the finite element predictions for the inline curvature and top reaction. Figures 4.13 and 4.14 further illustrate the response of the cylinder when subjected to the 1.4 second wave ($N_{KC} = 10.6$). Figure 4.13 traces the loci of the inline and transverse top reaction and the curvature at location -7.47 m for five wave cycles. The figure shows the response is very regular and repeatable with two cycles of transverse vibration for each cycle of inline vibration.

Also note that the magnitude of curvature (bending stress) is approximately the same in both directions. The inline vibration at 0.71 Hz is very close to the third natural frequency of the cylinder (0.77 Hz) and the transverse response at 1.43 Hz is close to the fifth natural frequency (1.41 Hz). This is illustrated in Figure 4.14 which presents the inline and transverse displacement envelopes over the entire length of the cylinder which show almost pure modal response in the two modes. Another interesting result is that the motion at the bottom of the cylinder is equal to or greater than that near the top. One reason for this is that even though the cylinder is subject to hydrodynamic damping, the effective tension of the cylinder near the bottom is about half of that at the top, implying less stiffness at the bottom end of the cylinder. This is due to the effective weight of the cylinder which reduces the effective tension linearly with depth (see Equation 2.10).

Figure 4.15 compares the measured inline curvature (-7.47 m) and the top reaction with predictions from the finite element model. The inline force was computed using force coefficients from Sarpkaya and Isaacson (1981) for the Keulegan-Carpenter and Reynolds numbers of the case being considered (Table 3.4). For the 1.4 second wave $C_m = 1.1$ and $C_d = 2.0$. The comparisons are fair for both the top reaction and curvature estimates, especially if one excludes the high frequency oscillations (twice the wave frequency) present in the data but not predicted by the model.

Figure 4.16 presents the loci of the top reaction and curvature (-7.47 m) for the 2.6 second wave ($N_{KC}=36.6$). For this case the response is very complicated and irregular and is in direct contrast to the regular response for the 1.4 second wave. The inline response is seen to contain many high frequency oscillations, especially noticeable in the curvature measurements (see Figure 4.18). This high frequency content in the inline response is analyzed in Figure 4.17 by comparing the inline and transverse curvature. This is accomplished by separating the inline response into two components by low-pass and high-pass filtering the signal at 0.5 Hz. The first graph in Figure 4.17 compares the low-pass filtered curvature to the wave profile, showing the response at the wave frequency. The second graph compares the high-pass filtered curvature to the transverse curvature at the same location. The figure illustrates that the inline and transverse curvatures are correlated suggesting that the transverse oscillations of the cylinder feed into the inline oscillations. As the transverse curvature signal has almost no energy at the wave frequency the reverse is not true. This excludes the possibility of this being due to imperfect cylinder shape or crosstalk between the transducers. This result was observed for a variety of wave

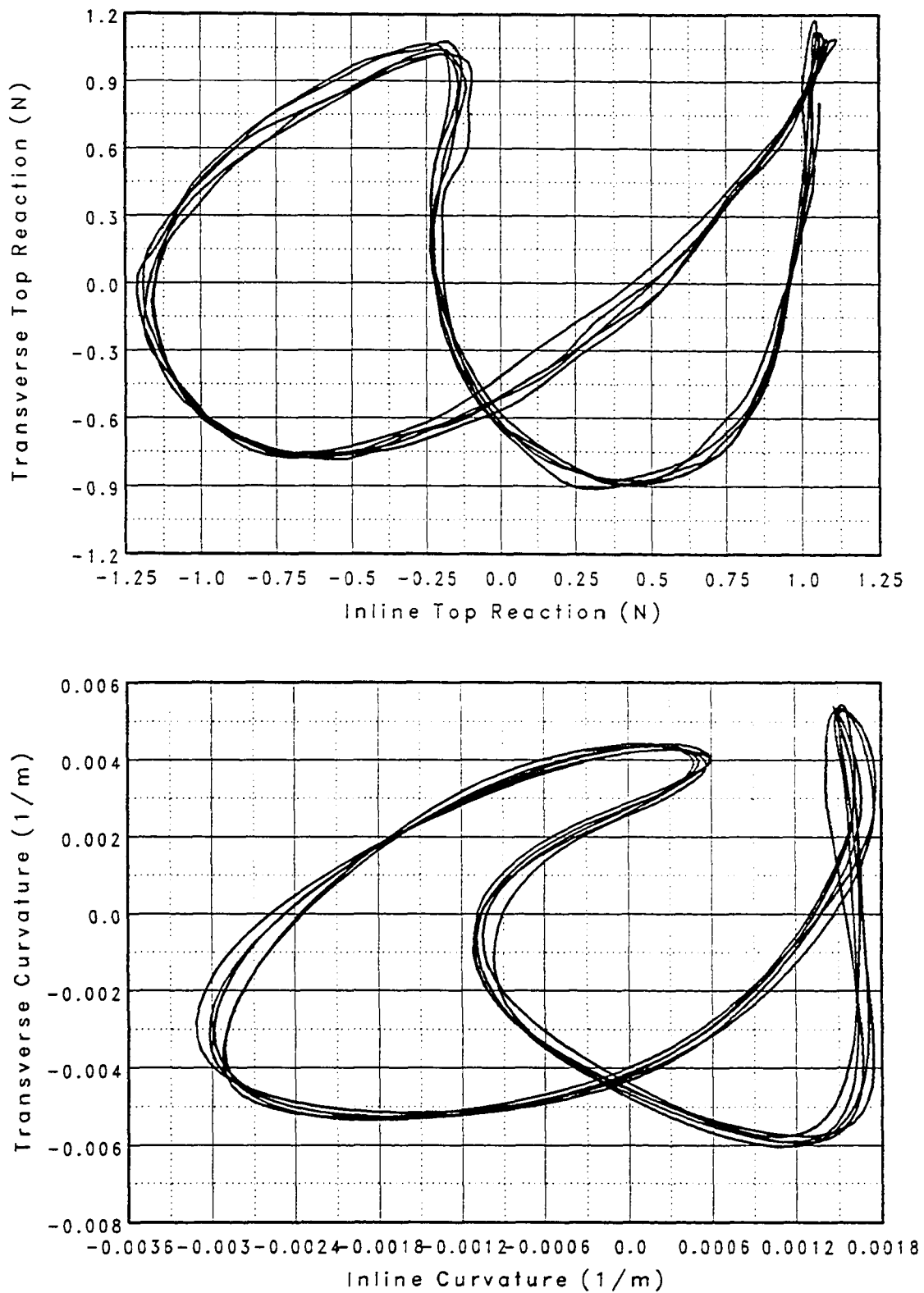


Figure 4.13: Top reaction and curvature (-7.47 m) patterns for 5 wave cycles, $T = 1.4$ seconds.

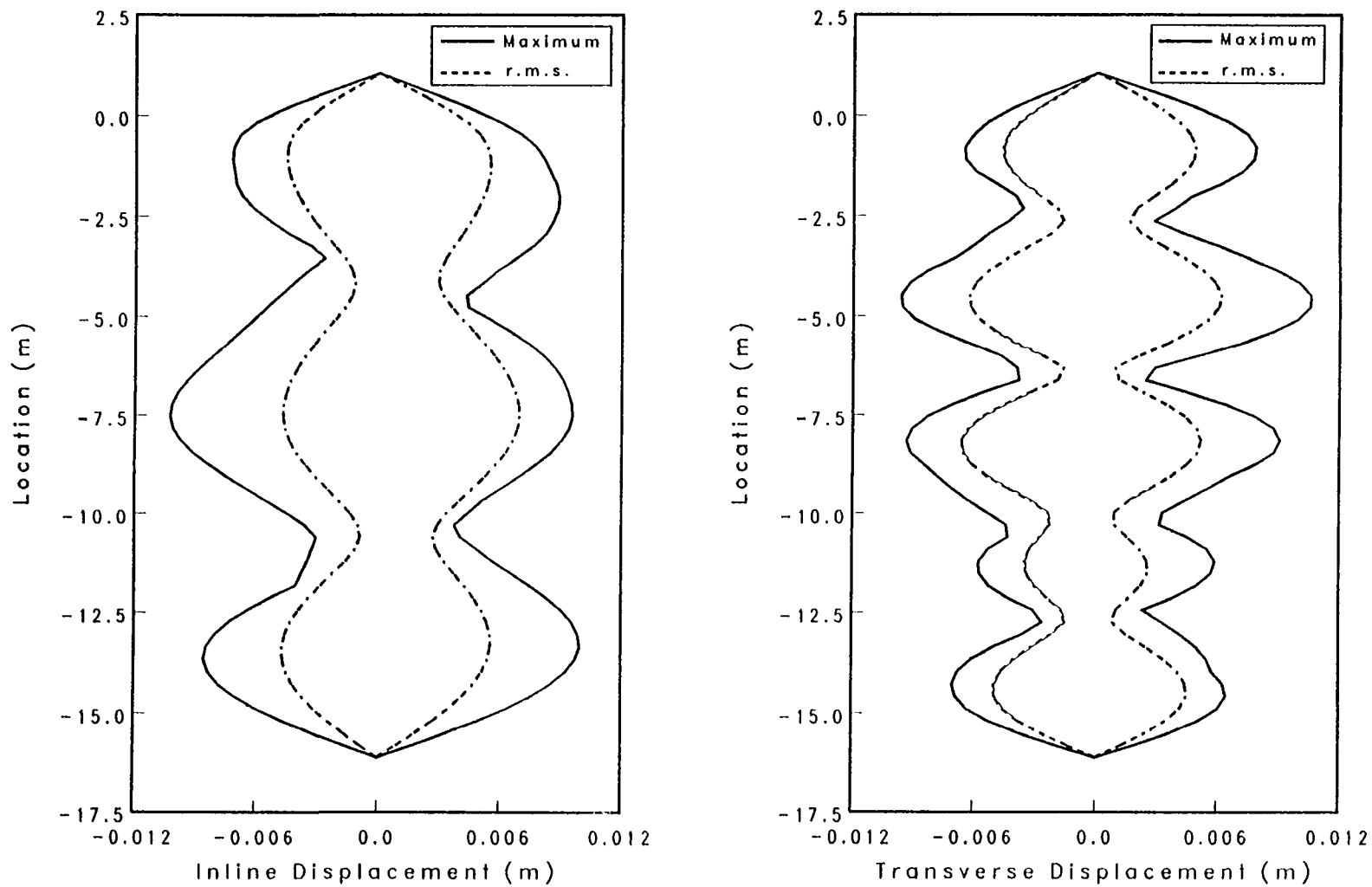


Figure 4.14: Inline and transverse displacement envelopes for a single cylinder with $T=1.4$ seconds, and pretension, T_1 .

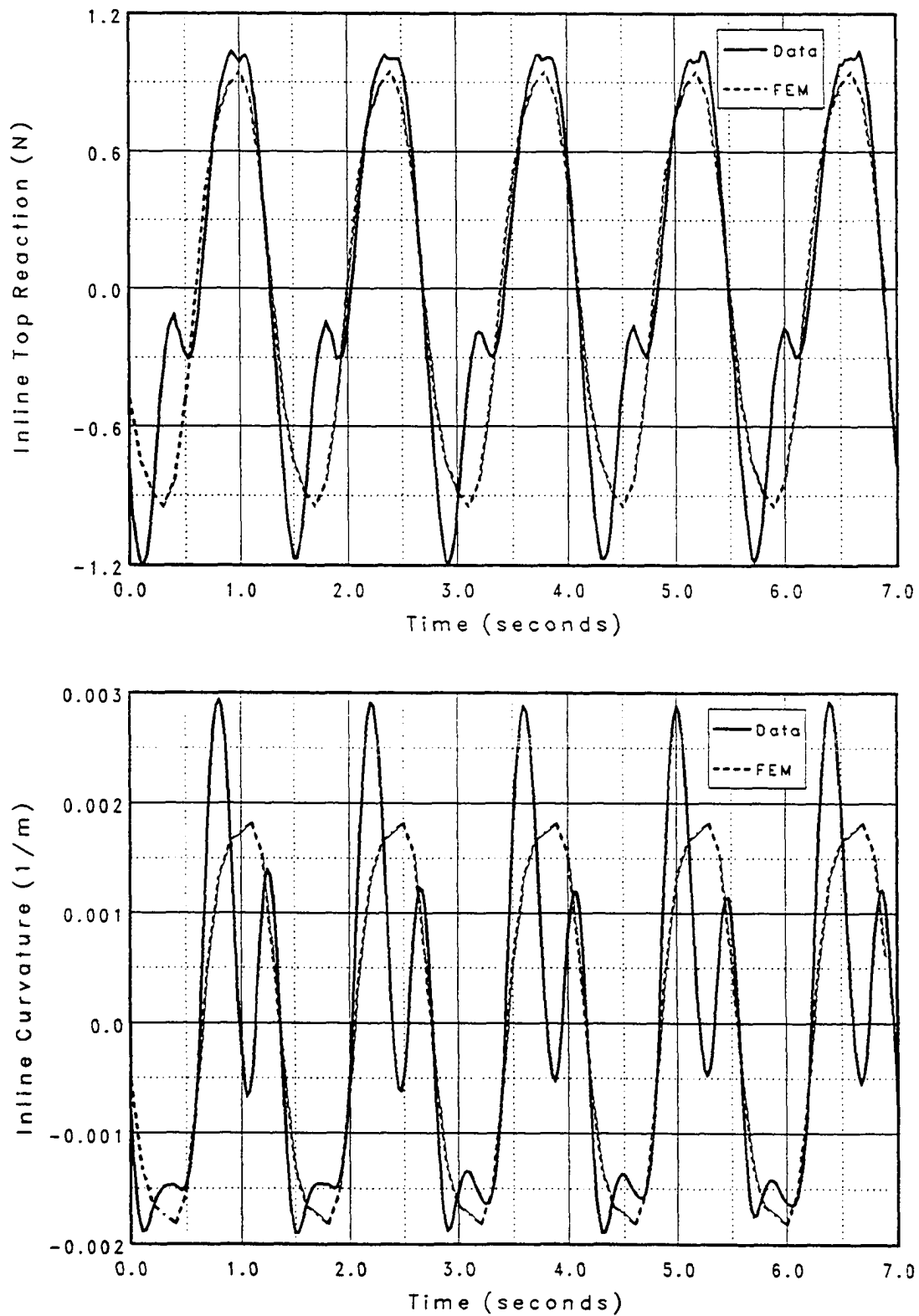


Figure 4.15: Comparison between FE predictions and measured data for inline top reaction and curvature (-7.47 m) with $T = 1.4$ seconds.

conditions both regular and random. This seems to imply that if these oscillations were due to vortex shedding, the shedding of vortices behind the cylinder exerts a force both inline and transverse to the wave motion (i.e., the resultant is at an angle behind the cylinder). This has also been observed in previous experiments with rigidly mounted cylinders (Borthwick and Herbert 1988).

Figure 4.18 compares the finite element predictions computed with $C_m = 1.7$ and $C_d = 1.4$ to the inline top reaction and curvature (-2.91m) for the 2.6 second period wave. Once again the comparison is fair with the finite element model describing the response at the wave frequency well but not able to describe the high frequency response. This is especially true with the curvature data which has considerable high frequency content as shown in Figure 4.17. Figure 4.19 compares the finite element prediction to the filtered curvature data. The top figure is low-pass filtered at 0.4 Hz, allowing response at the wave frequency only while the second is low-pass filtered at 0.8 Hz, allowing the second harmonic. It is seen that the finite element model is fair in describing the low frequency response.

4.3.2 Random Waves

The random wave tests were conducted using several realizations of duration 409.6 seconds each from the JONSWAP wave spectrum described earlier. The cylinder was pretensioned at two tensions T_1 and T_2 . Each realization contained about 180—200 waves, generally considered sufficient to provide estimates of the r.m.s. wave elevation and response at frequencies equal to or greater than the wave frequencies. For estimates of the extreme response analyzed in Section 5, all six realizations were used. A comparison of the r.m.s. response from each realization showed the overall difference was less than 2.5%, confirming that a realization of duration 409.6 seconds provided accurate r.m.s. response estimates.

A general description of the random wave data for pretension T_1 is provided in the beginning of this section. In this section the response spectra are analyzed using Autoregressive (AR) spectral estimates (Newton 1988) to allow easier comparison.*

*The AR spectral estimate is a parametric spectral estimate in contrast to that computed using a FFT which is non-parametric. The true spectral density of a process can be written as an infinite order autoregression is approximated by a p th order AR process. The optimal order is obtained using the CAT criterion. The AR spectral estimate has the ability to provide smooth spectral estimates maintaining the sharp peaks unlike a windowed non-parametric estimate where “smoothing” the estimate results in reducing the sharpness of the peaks.

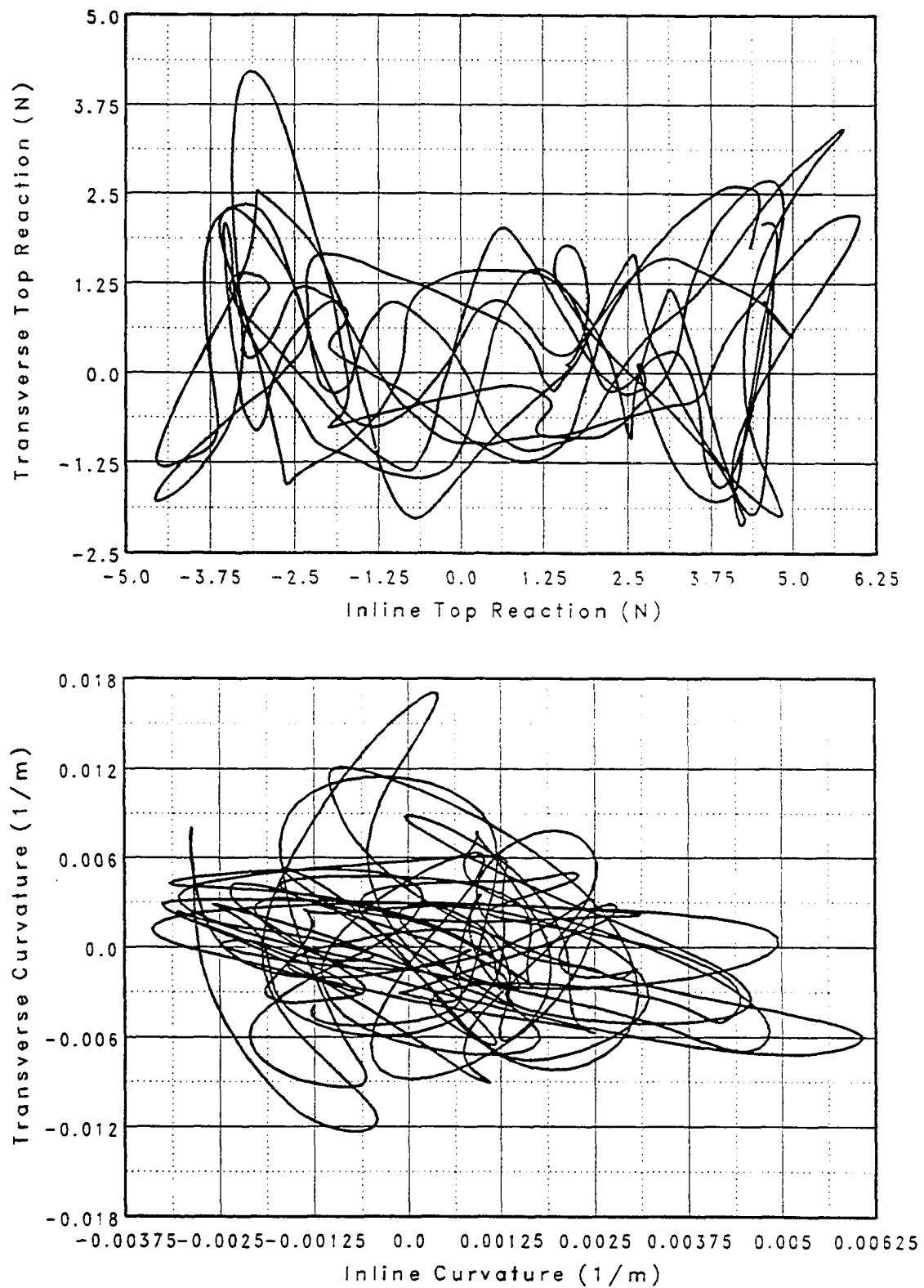


Figure 4.16: Top reaction and curvature (-7.47 m) patterns for 5 wave cycles, $T = 2.6$ seconds.

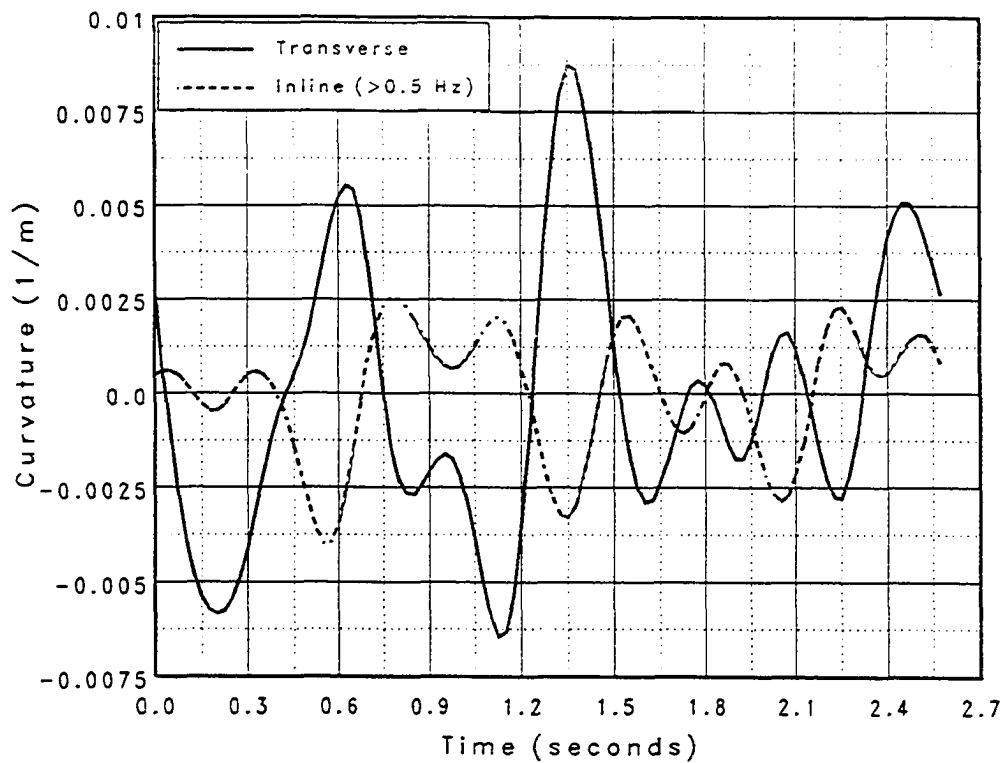
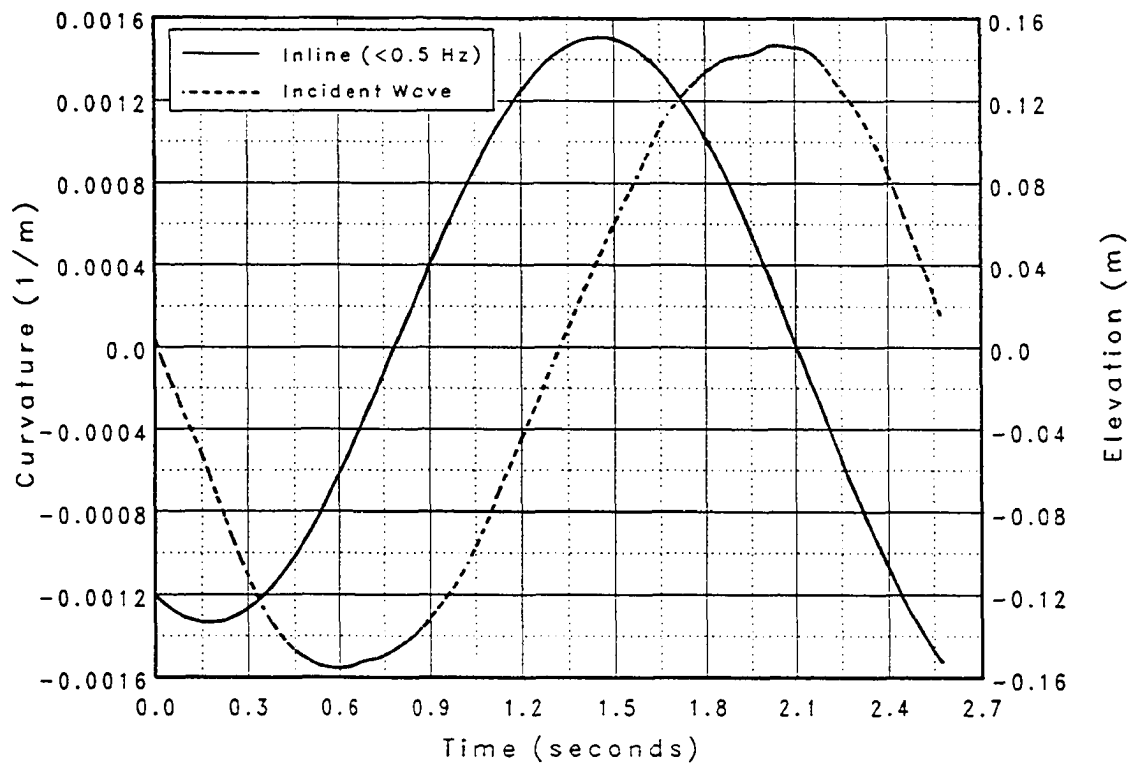


Figure 4.17: Comparison of filtered components of the inline curvature (-7.47 m) to (a) incident wave elevation and (b) transverse curvature.

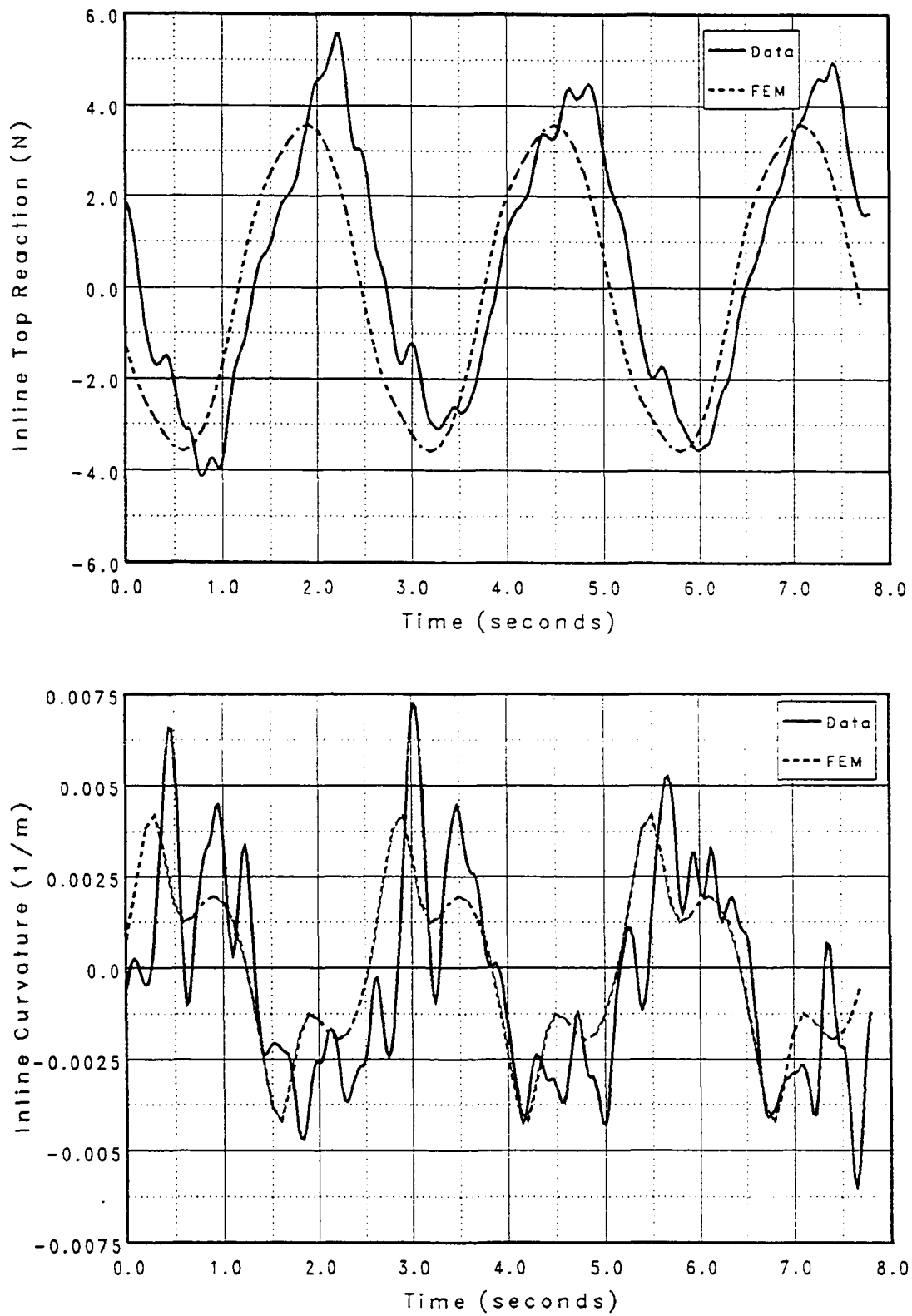


Figure 4.18: Comparison between FE predictions and measured data for inline top reaction and curvature (-2.91 m), $T = 2.6$ seconds.

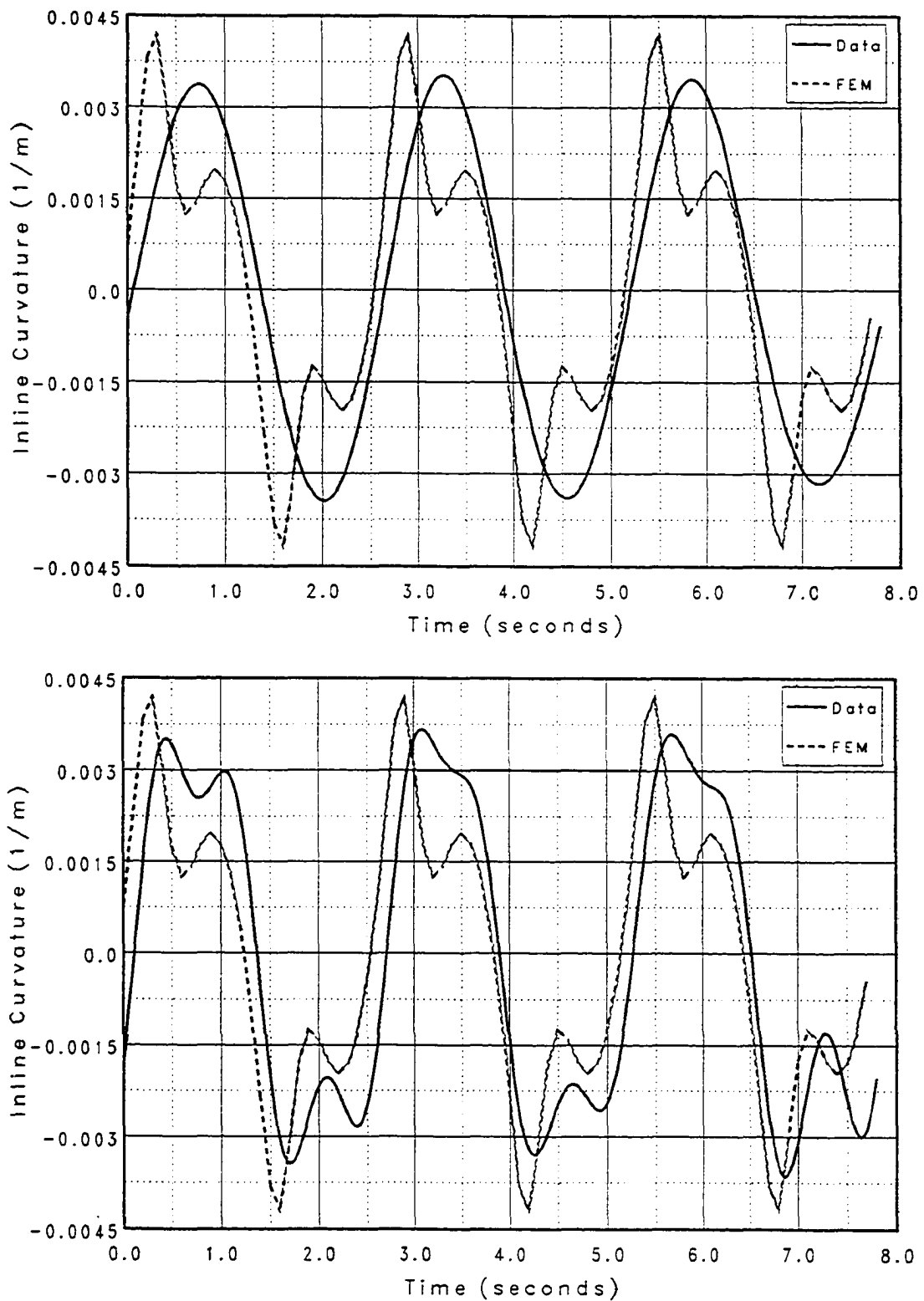


Figure 4.19: Comparison between low-pass filtered components of the inline curvature (-2.91 m) and FE predictions at (a) 0.4 Hz, and (b) 0.8 Hz.

Figures 4.20 and 4.21 compare the measured spectra for the inline and transverse top reactions and curvatures (-7.47m), respectively, for the two pretension conditions. The inline response is observed to be primarily at the wave frequencies with smaller peaks due to excitation of the natural frequencies of the cylinders. The two pretension conditions correspond to different natural frequencies which appears in the figures as shifts in the high frequency peaks to closely correspond to the natural frequencies tabulated in Tables 3.6 and 3.7. Figure 4.21 indicates an increase in r.m.s inline curvature with little change in the transverse curvature as the pretension decreases. As in the case of regular waves (Table 4.2), the decrease in pretension generally leads to an increase in displacement and mean tension and a small reduction in r.m.s. inline reaction.

Figure 4.22 compares the measured inline top reaction and curvature (-7.47m) spectra to those predicted by a 409.6 second simulation of the finite element model with $C_m = 1.7$ and $C_d = 1.35$ chosen from Sarpkaya and Isaacson (1981) based on the statistical Keulegan–Carpenter and Reynolds numbers and assumed independent of frequency. The random wave simulation had a high frequency cutoff of 1 Hz due to the problems of simulating wave kinematics at high frequencies. This is seen in the sharp drop off in the predicted spectra of the response at 1 Hz. Also notice that for both the reaction and curvature spectra there is a high deviation between the measured and predicted spectra in the range 0.5–1.0 Hz. The measured force spectrum shows the presence of the viscous drift forces due to the large difference between the measured and predicted spectra near the 0 Hz end. The difference in the curvature spectra is not that pronounced as curvature measurements are not very sensitive to drift. Figure 4.23 compares the estimated displacement spectrum at location -3.22 m , obtained by integration of the curvature data, to that predicted by the finite element model. It is seen that the displacement is fairly well predicted up to 1 Hz and then drops down rapidly. The viscous drift phenomenon is also indicated in the differences between the displacement spectra at the 0 Hz end of the spectra.

4.4 Analysis of the Paired Cylinder Data

An earlier section of this section provided an overview of some of the studies that have been conducted with a pair or groups of cylinders for a variety of flow and structural parameters. These studies showed that interference occurred when the cylinders were sufficiently close to one another, or when one cylinder was adjacent to or in the wake of the other cylinder. The first condition was termed proximity interference and was

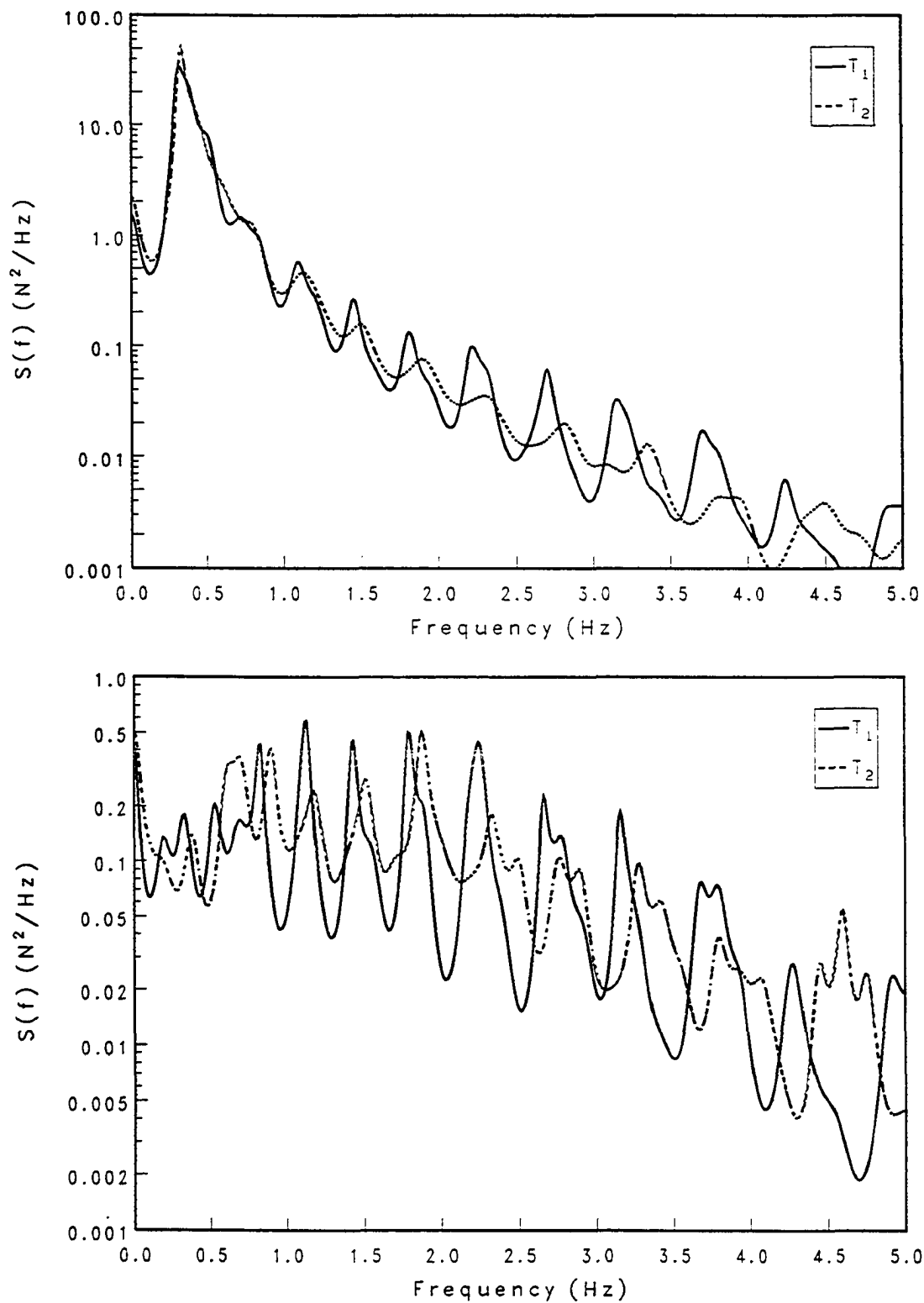


Figure 4.20: Comparison between inline and transverse top reaction spectra for the two pretension conditions, random wave case.

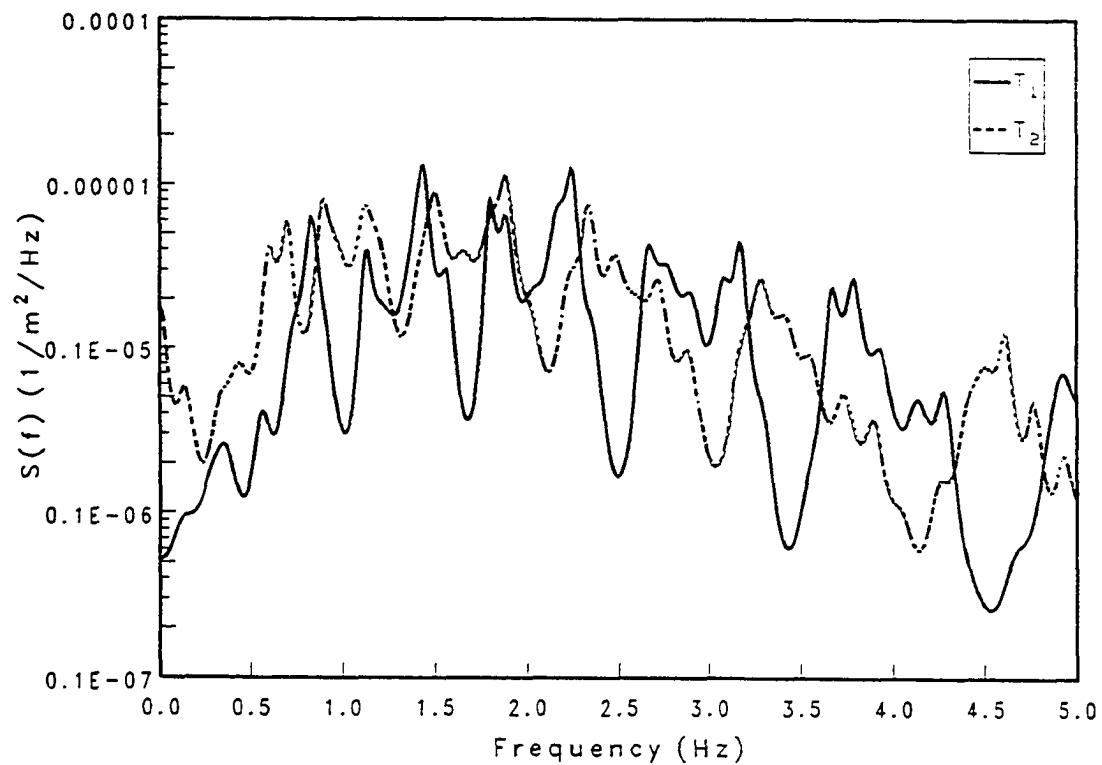
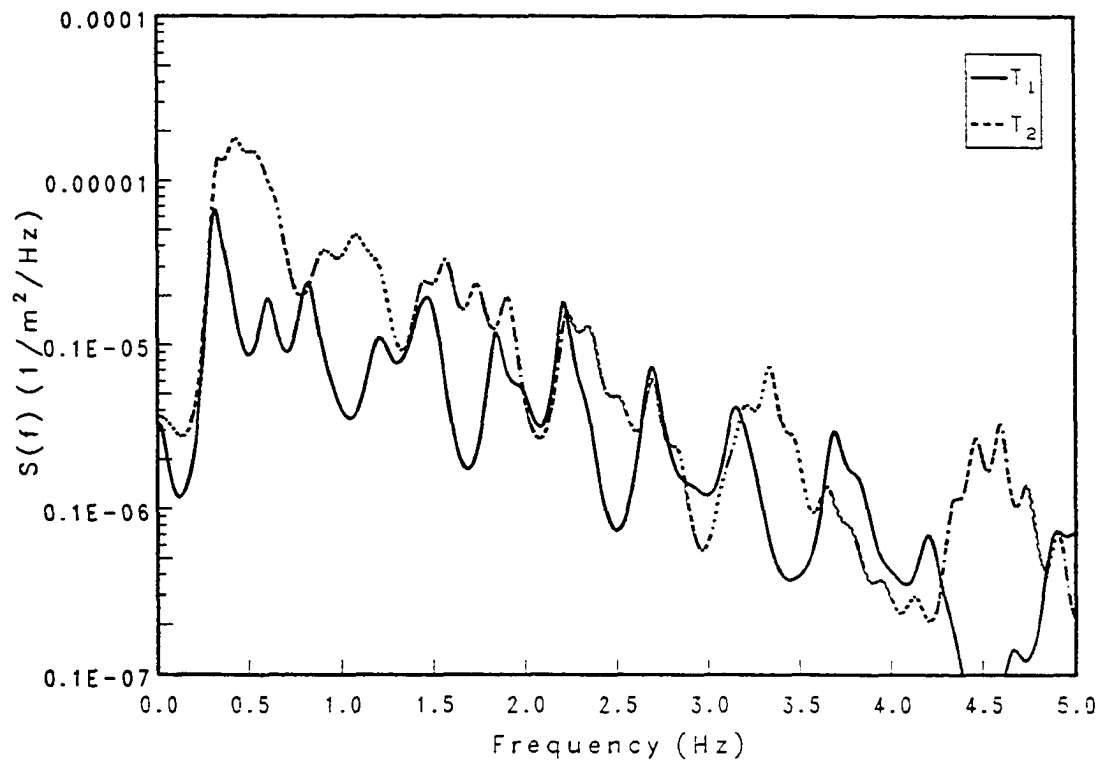


Figure 4.21: Comparison between inline and transverse curvature (-7.47 m) spectra for the two pretension conditions, random wave case.

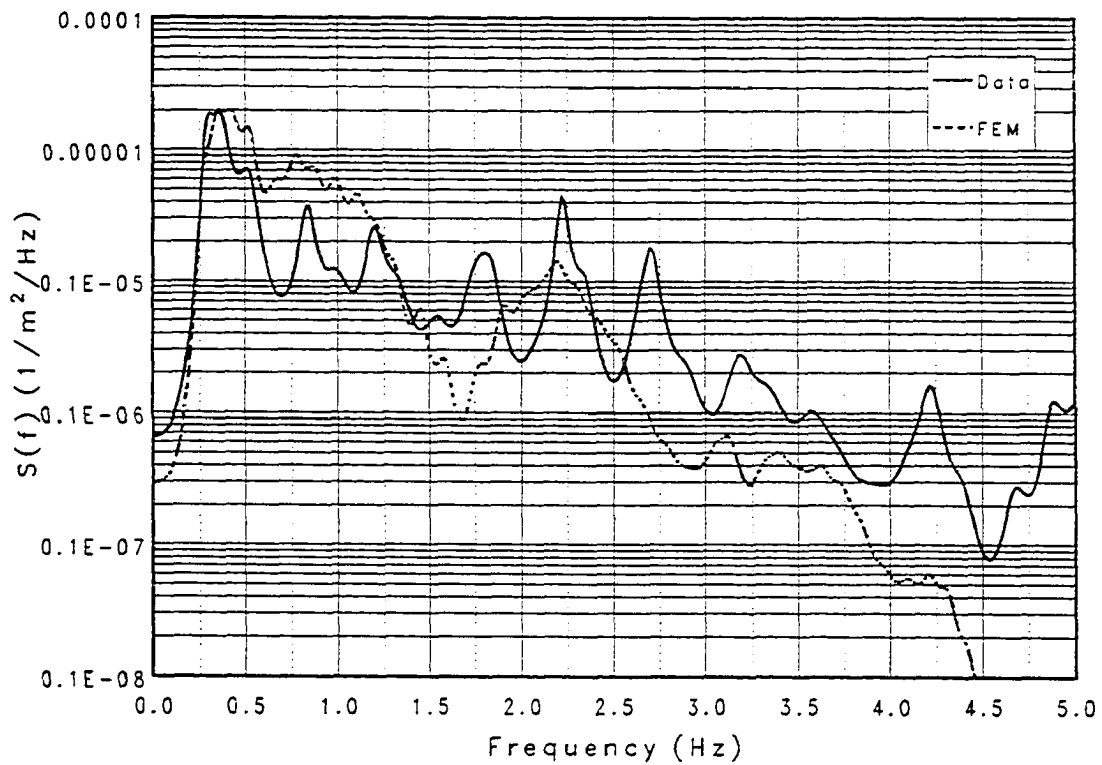
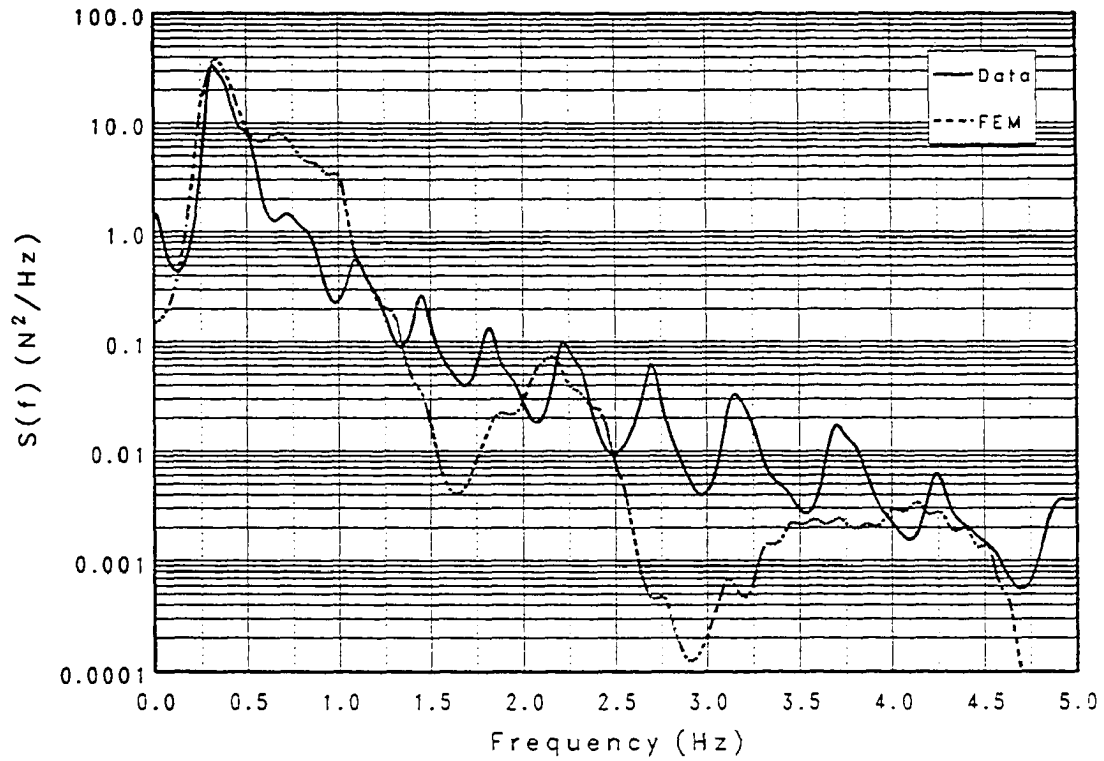


Figure 4.22: Comparison between spectra from FE model and the measured inline top reaction and inline curvature (-7.47 m).

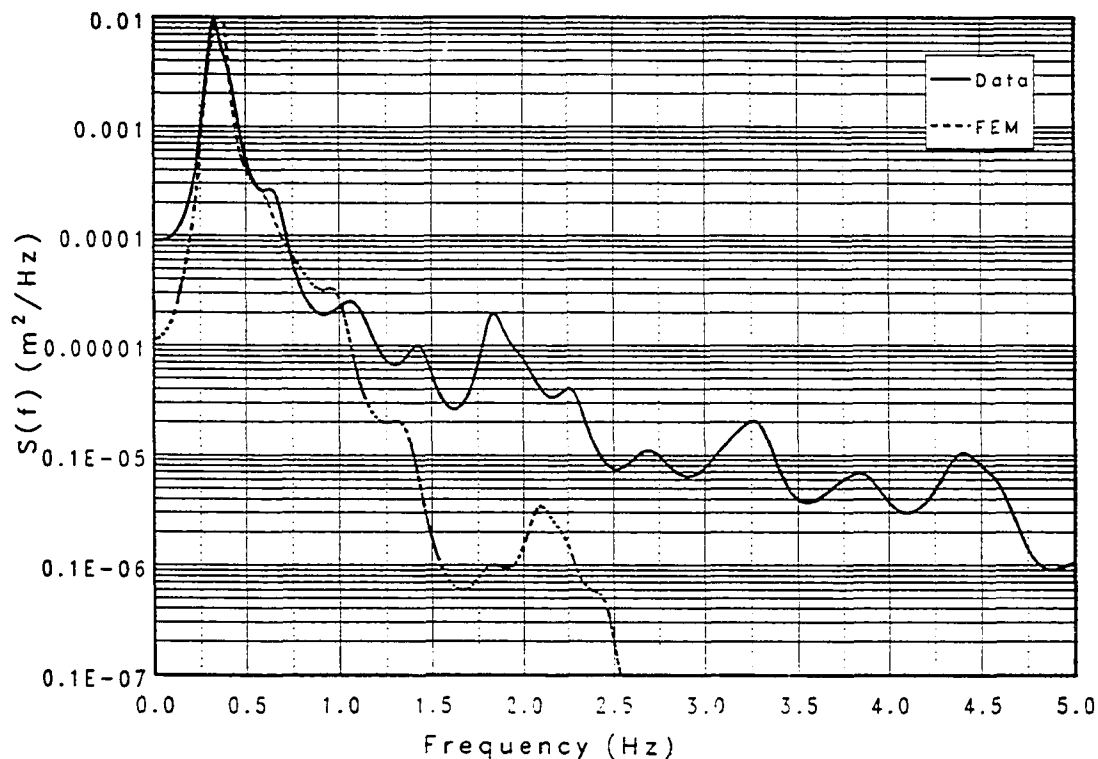


Figure 4.23: Comparison between displacement spectra from FE model and estimated from the curvature data.

generally restricted to a radius of 4 cylinder diameters. The second was termed wake interference and was restricted to about 20° on either side of the upstream cylinder. The wake region was shown to extend for a longer distance and was also restricted by the path length for harmonic and wave flows.

In this study the experiments focused on the tandem arrangement to study the relative motion/collision process of the cylinders and so a majority of the tests were conducted for this orientation. However, several tests were conducted at other orientations to provide a global picture of the interference and shielding between the cylinders. Details of the orientations, spacings and pretension conditions are provided in Table 3.6.

There were two main objectives in conducting the paired cylinder tests:

- to characterize the r.m.s. response of the cylinder as a function of orientation and spacing for the various wave and structural parameters, and
- to observe and record the relative motion between the cylinders to analyze the collision behavior of the cylinders.

4.4.1 Characterization of Paired Cylinder Response

This section provides a synopsis of the interference phenomenon studied during the paired cylinder tests. The interference is characterized by presenting r.m.s. estimates of the cylinder response in the form of ratios between the paired cylinder measurement and that of the corresponding single cylinder measurement. This information is useful in providing general estimates of changes in amplitudes of response as a function of orientation and spacing.

The data are presented in a series of three dimensional graphs where the X and Y axes represent the tandem (0°) and side-by-side (90°) orientations respectively. The axes are non-dimensionalized to represent the pitch-to-diameter ratio (P/D). The Z axis is a measure of the amplification of the paired cylinder response defined as the ratio of paired cylinder response to that of a single cylinder. The amplification is represented as a mesh surface obtained by interpolating between the data points marked by solid circles. Note that the X and Y axis are scaled differently; the X axis extends to 15 cylinder diameters while the Y axis to 5 diameters. The data sets chosen are for the $[T_1, T_1]$ condition so that the data represent the influence of cylinder orientation and spacing only for a pair of cylinders with identical system characteristics.

Figures 4.24—4.27 present the interference ratios for the random wave tests for the inline and transverse top reactions (FX and FY) and curvatures (CX and CY) at -2.91 m of Cylinders 1 and 2 respectively. Cylinder 1 is the cylinder at location $(0,0)$. In the figures FX , FY , CX , and CY correspond to the r.m.s. response for a single cylinder, while $FX1$ etc. corresponds to the r.m.s. response of Cylinder 1 and $FX2$ etc. to that of Cylinder 2. The arrow on the graphs indicate the direction of the incoming waves. From the figures one sees that the ratios for the inline response vary from approximately 0.7 to 1.2 with most of the interference at the $2.5D$ and $5D$ locations. This is consistent with the proximity interference region defined by Zdravkovich (1985) and other investigators. In general the transverse response decreases to ratios of approximately 0.7 to 0.9. These magnitudes of change in response are not very large compared to previous studies which were conducted with harmonic and steady flows. This is expected for wavy flows and harmonic flows because for every half cycle of the wave the flow reverses and the cylinder which was at the rear of the other is now at the front. This is also seen by comparing the inline reaction graphs in Figures 4.24 and 4.25 where the interference ratios are very similar. For the side by side location at $2.5D$ the response is seen to increase to a ratio of 1.2. Most

of the interference occurs in the $2.5D$ — $7.5D$ spacings for the tandem arrangement which is in the proximity-wake and wake interference regions.

Figures 4.28—4.31 present interference ratios of the r.m.s. inline and transverse top reactions for two regular wave cases in a similar fashion to that presented for the random waves. Figures 4.28 and 4.29 represent the 1.4 second period wave responses. For both cylinders, the inline and transverse response interference patterns are similar. As in the random wave case, the maximum inline response is at the $2.5D$ spacing for the 90° orientation for both cylinders. Again most of the interference is present at the $2.5D$ and $5.0D$ spacings and along the tandem orientation up to $7.5D$ — $10D$. The transverse response is reduced drastically up to ratios of 0.2 especially along the tandem orientation.

Figures 4.30 and 4.31 present the 2.6 second period wave data. Consistent with the other data the maximum inline response is along the 90° orientation at $2.5D$ and a minimum response in the $2.5D$ — $5D$ region behind Cylinder 1. Once again the transverse response is reduced, though not to the levels observed for the 1.4 second case. Comparing the 2.6 second period interference data to those for the random waves it is seen that they are very similar.

The above discussion characterizes the interaction between the waves and the pair of cylinders in terms of the r.m.s. response. However, this is not a complete description of the response between the cylinders as it does not indicate the other changes in response like the frequencies of vibration or differences in phase between the two cylinders. Figure 4.32 illustrates this by showing the top reaction patterns at three locations for the pair of cylinders with pretensions $[T_1, T_1]$ for the 1.4 second period wave. The top reaction pattern for a single isolated cylinder is shown in Figure 4.13. The patterns are for two locations in tandem ($2.5D$ and $10D$), and one oriented at 22.5° and at spacing $2.5D$. Interestingly the response patterns are very regular but show large variations in behavior as a function of location. These figures show that the modification in cylinder response is not restricted to a change in amplitude alone, but also to changes in frequency and the overall behavior, showing the complexity of the interference problem.

Figure 4.33 compares the displacement time series at a location 9.06 m below the still water level for Cylinders 1 and 2 arranged in tandem $2.5D$ apart with pretensions $[T_1, T_1]$, for the 2.6 second period wave. The time series show that the two displacements have basically the same magnitude and phase, but Cylinder 2 shows more high frequency content, probably due to flow separation and vortex shedding

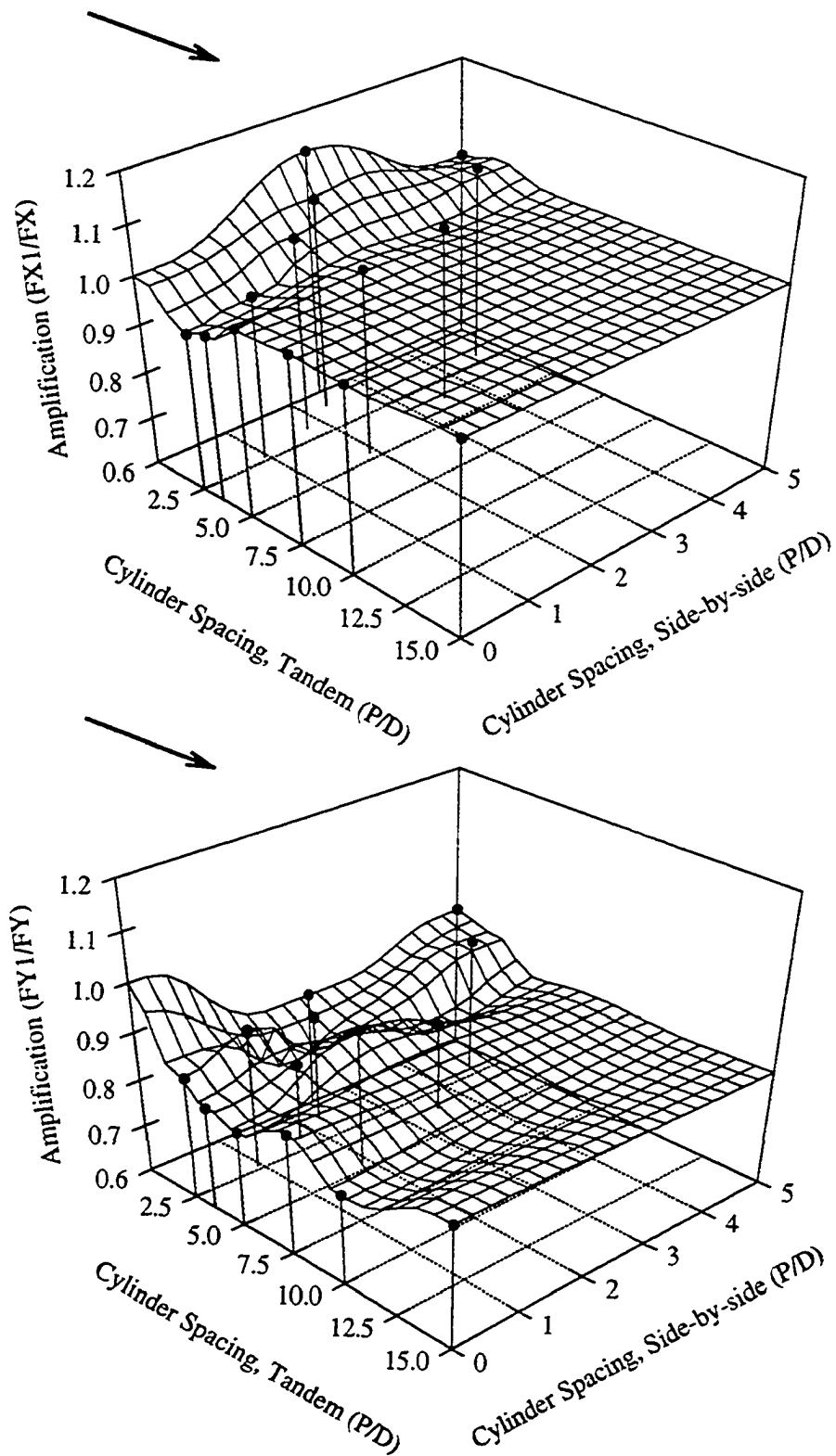


Figure 4.24: Interference ratios for the inline and transverse top reactions for Cylinder 1, random wave case.

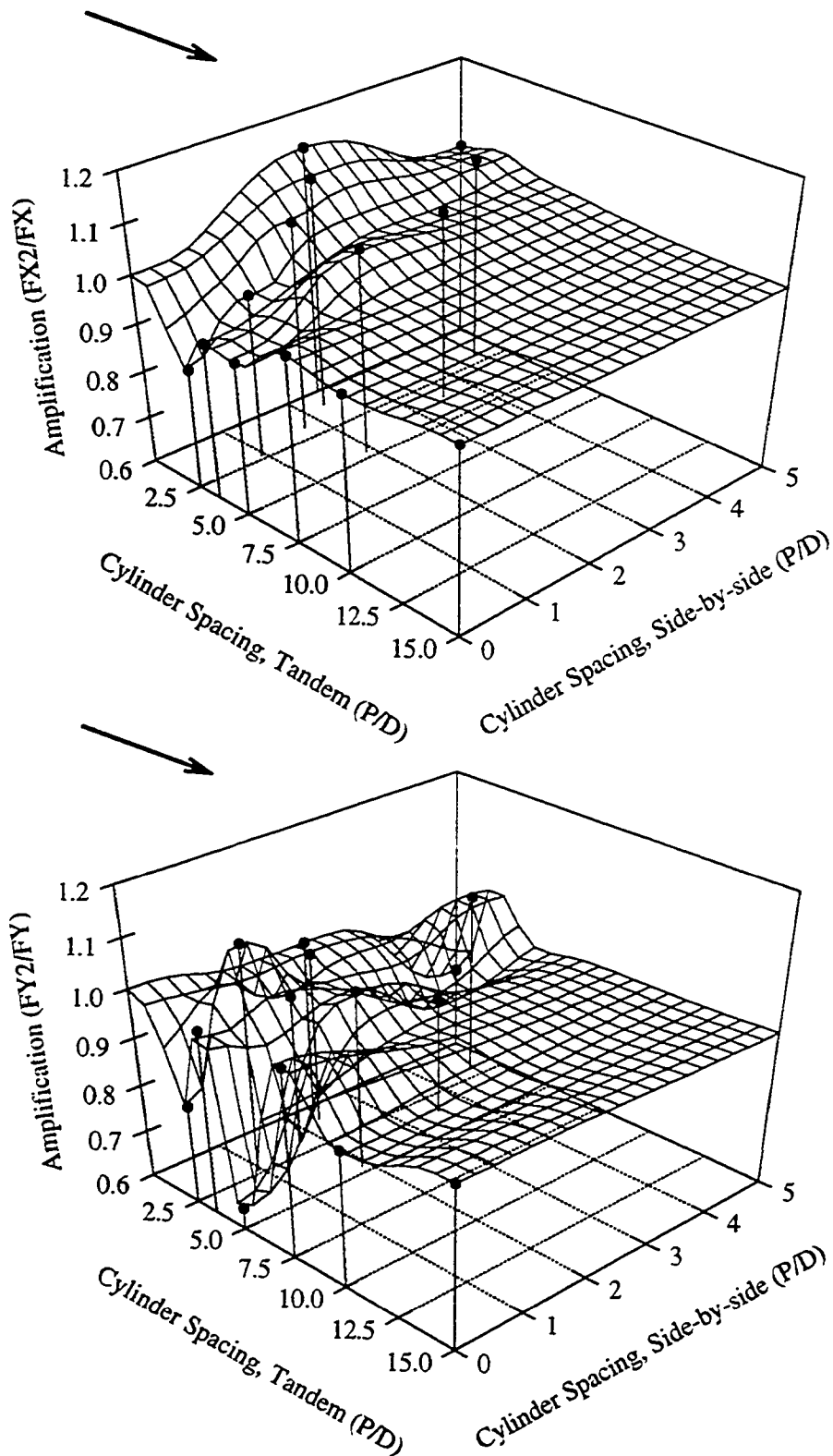


Figure 4.25: Interference ratios for the inline and transverse top reactions for Cylinder 2, random wave case.

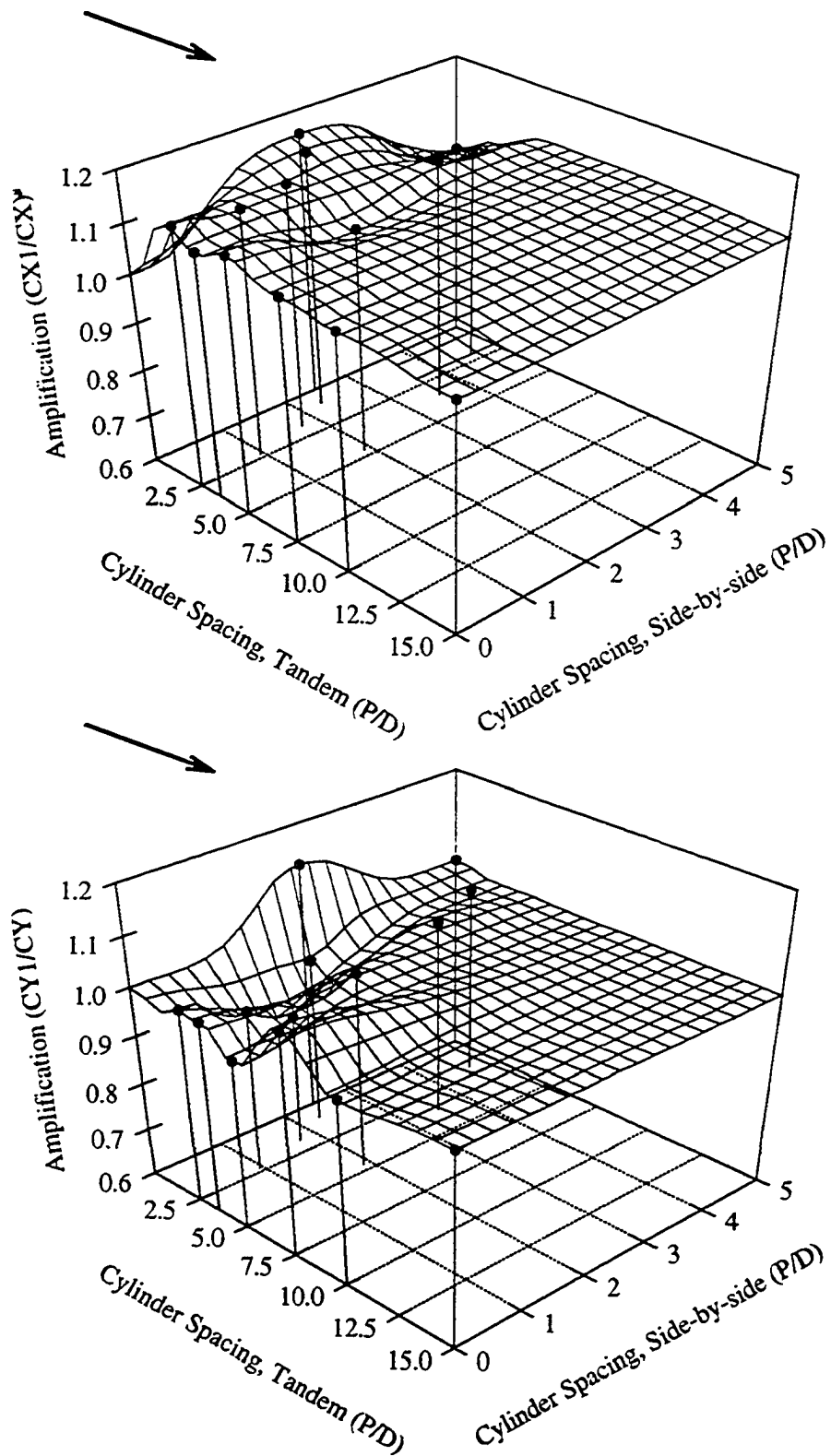


Figure 4.26: Interference ratios for the inline and transverse curvature (-7.47 m) for Cylinder 1, random wave case.

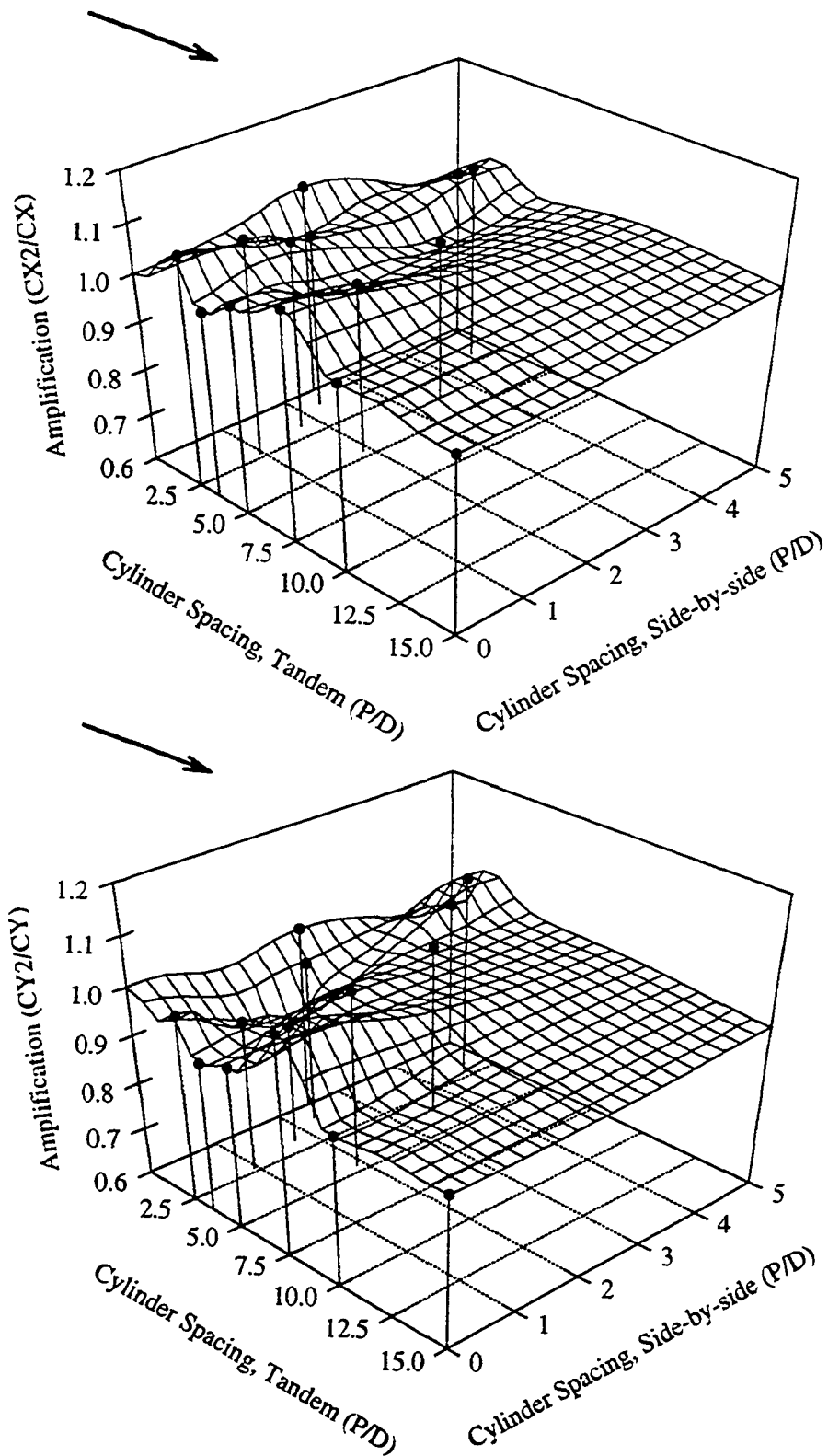


Figure 4.27: Interference ratios for the inline and transverse curvature (-7.47 m) for Cylinder 2, random wave case.

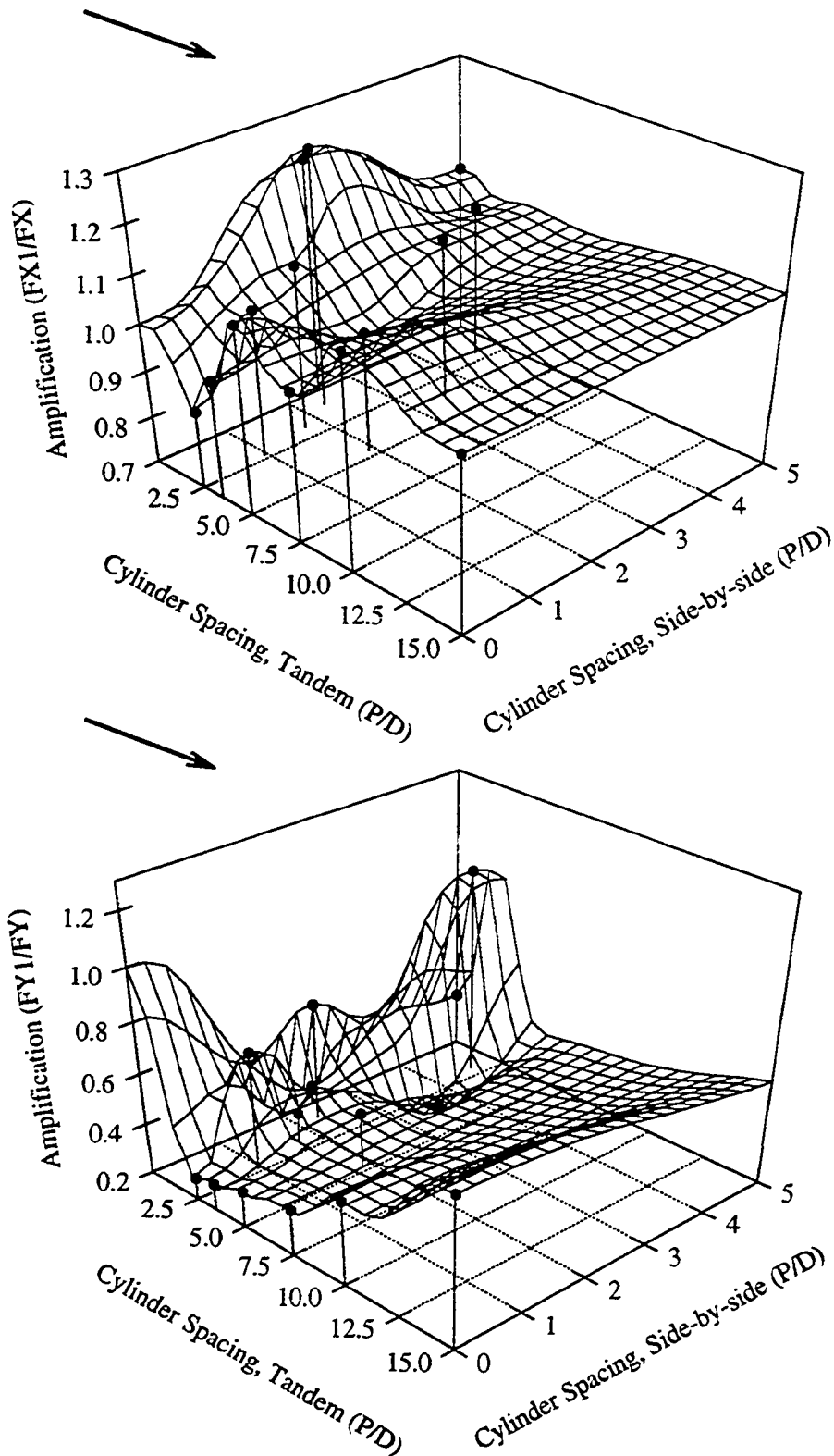


Figure 4.28: Interference ratios for the inline and transverse top reactions for Cylinder 1, $T = 1.4$ seconds.

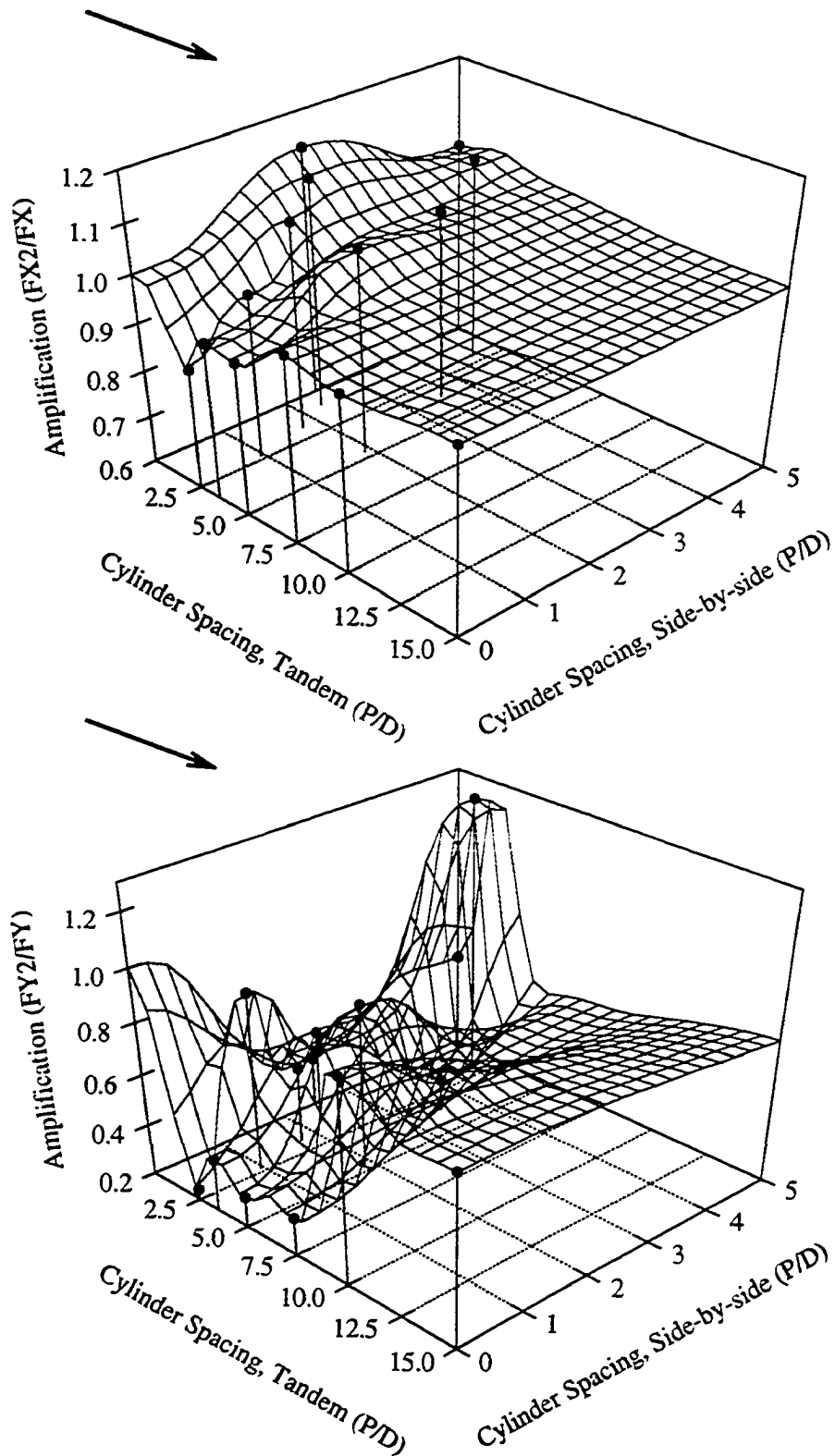


Figure 4.29: Interference ratios for the inline and transverse top reactions for Cylinder 2, $T = 1.4$ seconds.

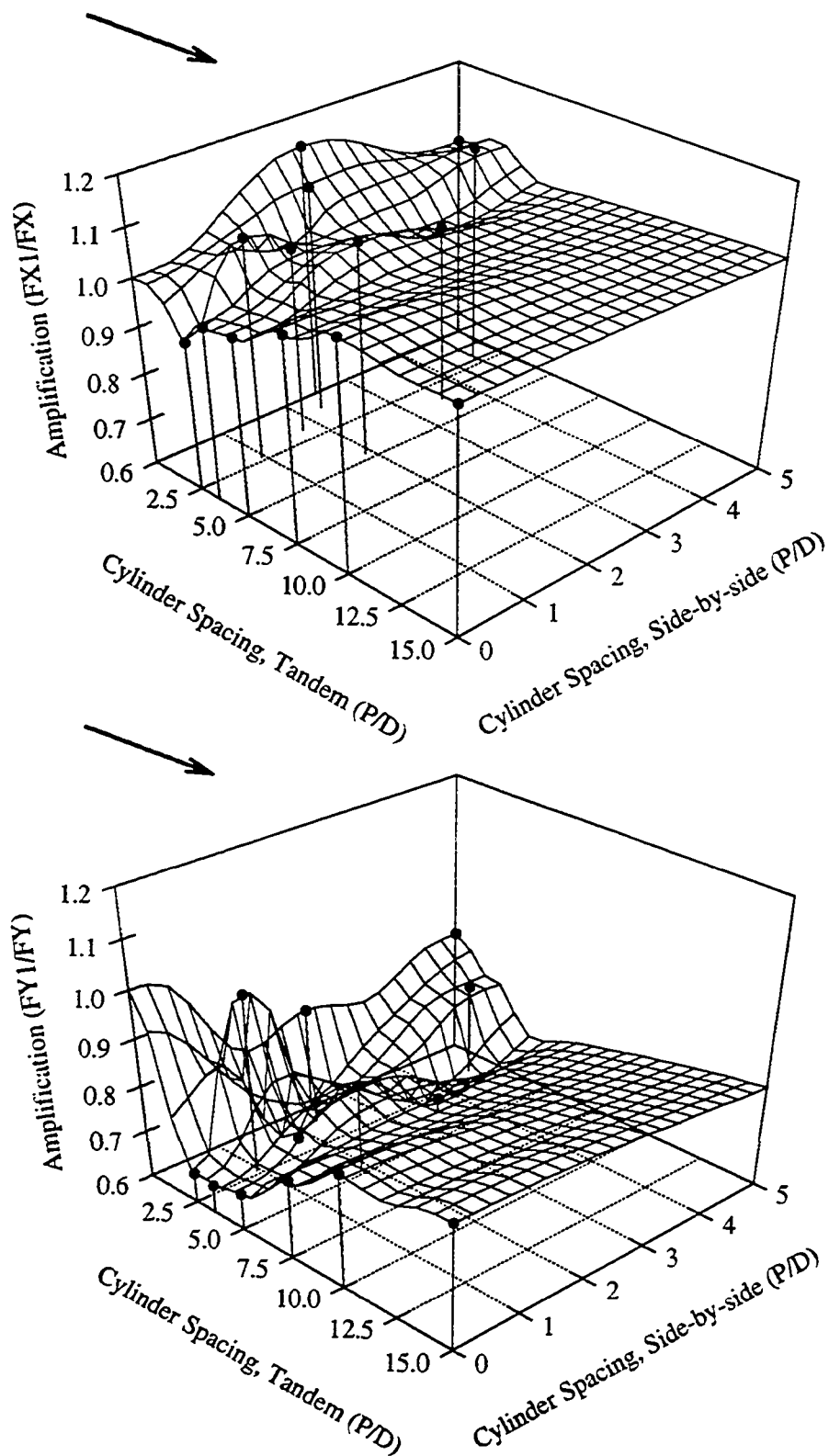


Figure 4.30: Interference ratios for the inline and transverse top reactions for Cylinder 1, $T = 2.6$ seconds.

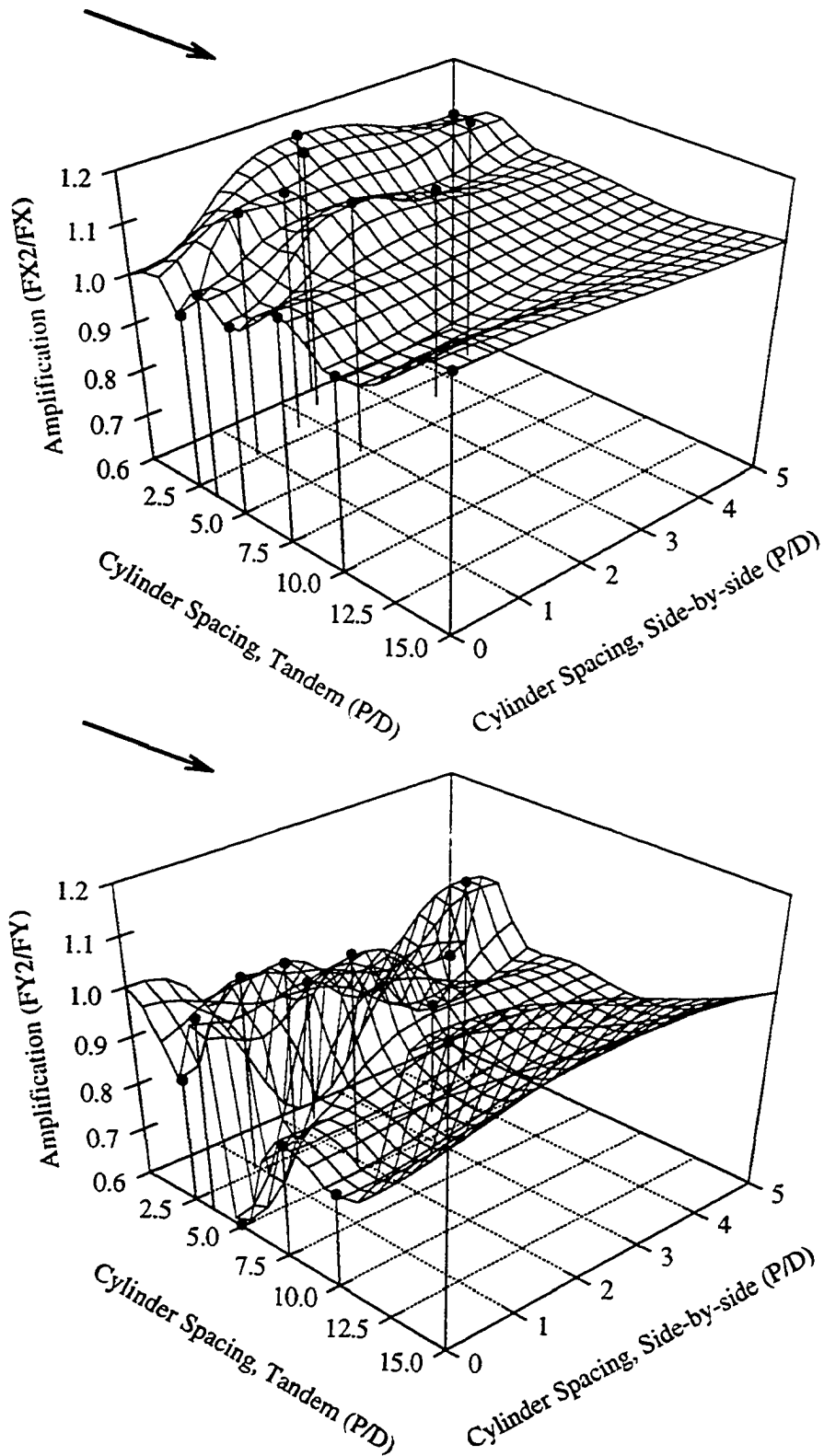


Figure 4.31: Interference ratios for the in-line and transverse top reactions for Cylinder 2, $T = 2.6$ seconds.

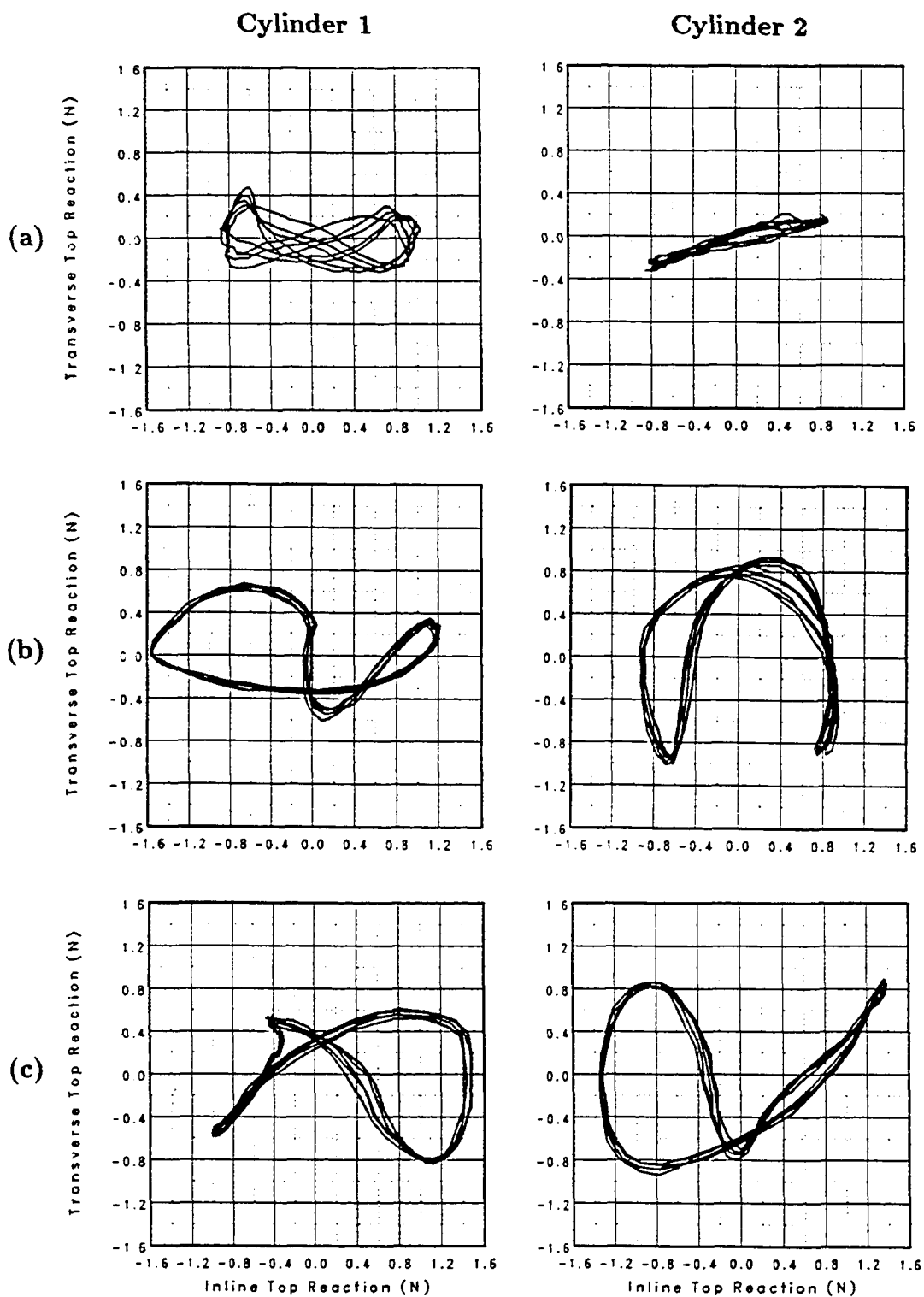


Figure 4.32: Top reaction patterns for Cylinders 1 and 2 for $T = 1.4$ seconds. (a) tandem (0°), $2.5D$, (b) tandem (0°), $10D$, and (c) 22.5° , $2.5D$.

from the upstream cylinder. This is also observed in Figure 4.34 which compares the displacement spectra for Cylinders 1 and 2 for the random wave excitation at the same location. The displacement spectrum for Cylinder 2 shows that the high frequency energy is an order of magnitude greater than that for Cylinder 1.

4.4.2 The Relative Motion/Collision Process

This section focuses on the relative motion between a pair of cylinders in close proximity, specifically in the tandem orientation. This leads directly to studying the collision behavior of the cylinders which is analyzed in a probabilistic framework in the next section. The relative motion is defined as the difference in displacement between Cylinders 1 and 2 at a specific location along the length of the cylinder. The relative motion is a function of the cylinder response characteristics, which in turn have been shown to be a function of the incident waves, cylinder pretension and spacing between the cylinders.

The relative motion process is obviously a function of the amplitude, frequency and phase between the displacements of the two cylinders. The previous sections have indicated changes in response amplitudes and frequency. Another important parameter influencing relative motion is the difference in phase between the displacements of the two cylinders. This can be brought about by the spacing between the two cylinders (change in wave or excitation phase) and the pretension difference between the two cylinders (change in structural response phase). A third contribution can also be due to changes in flow conditions (interference or hydrodynamic coupling) between the two cylinders leading to modifications of the wave loading in amplitude, frequency and phase.

Finite element simulations were conducted to study the effects of spacing and pretension difference on the relative motion of the cylinders for the random wave condition and compared to the experimental results. The finite element model accounts for the phase change due to spacing (waves/forcing) and that due to structural response (due to the pretension difference), but does not account for hydrodynamic interference or coupling between the two cylinders, i.e., no shielding or modification of the wave loads. The relative motion simulations were run for each cylinder separately using the linear wave dispersion relationship to account for changes in random wave kinematics from the location of Cylinder 1 to Cylinder 2. Figure 4.35 shows the influence of pretension difference between the two cylinders on the r.m.s. relative motion for a pitch-to-diameter ratio of $2.5D$. The relative motion is computed at a location

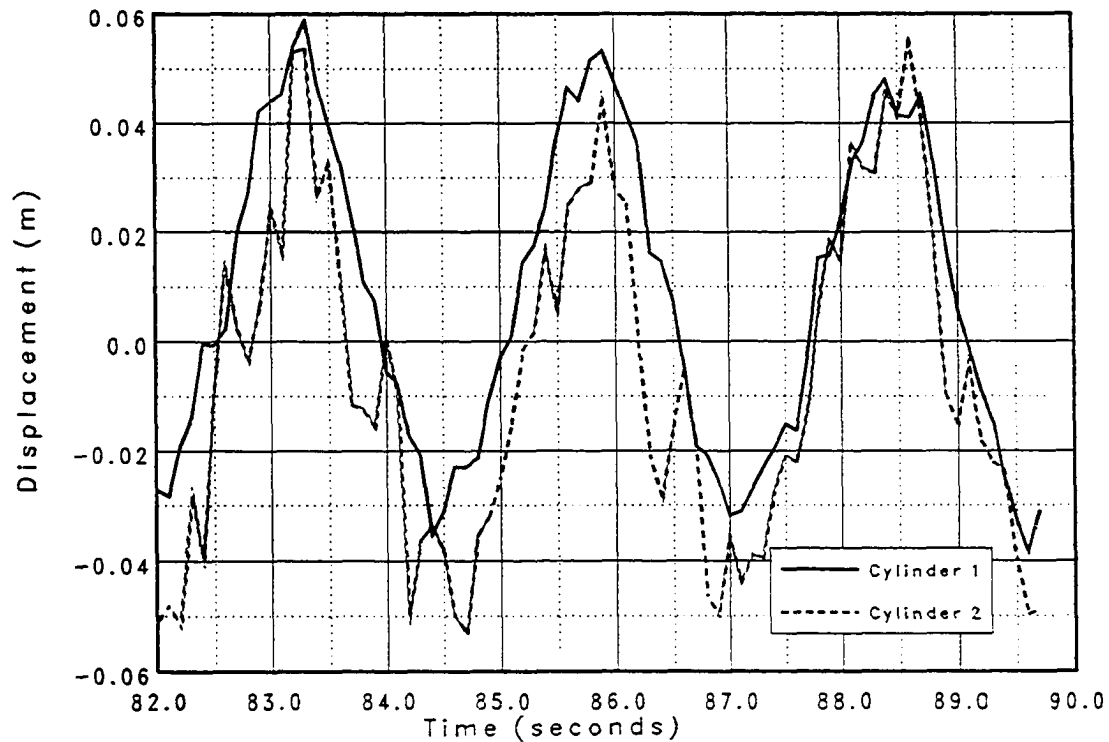


Figure 4.33: Displacement time series for $T = 2.6$ seconds at location -9.06 m for Cylinders 1 and 2 (tandem, $2.5D$).

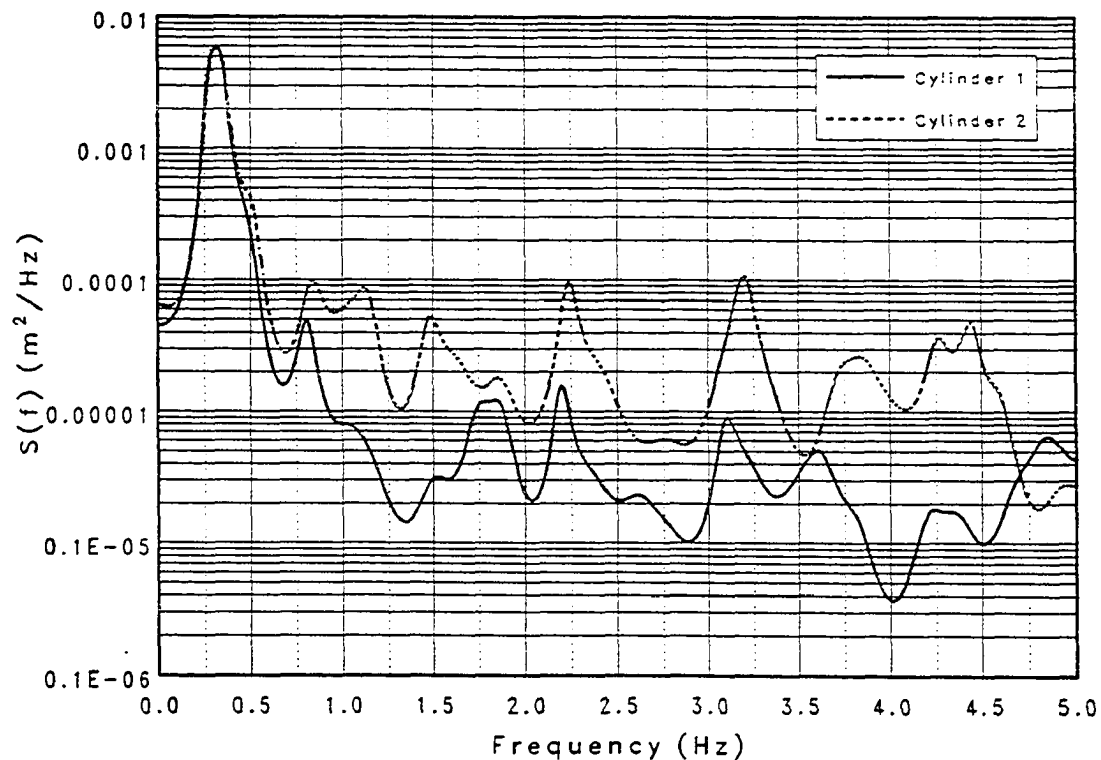


Figure 4.34: Displacement spectra for random wave excitation at location -9.06 m for Cylinders 1 and 2 (tandem, $2.5D$).

9.06 m beneath the still water level. The pretension difference is non-dimensionalized by the pretension of Cylinder 1, while the relative motion response is normalized by the cylinder spacing. Both the data and the finite element model show an increase in relative motion with an increase in the difference in pretension, though the relative motion measured experimentally is much larger than that predicted by the finite element model. From earlier simulations the r.m.s. displacement of a single cylinder was shown to be predicted fairly well by the finite element model (0.023 m compared to 0.025 m measured experimentally). The finite element model predicts almost no relative motion when the cylinder pretensions are the same, while the experimental data show significant relative displacement. In fact, for this pretension case $[T_1, T_1]$ the cylinders were actually observed to collide as presented in the next section.

Figure 4.36 presents data from the finite element simulation and from the experiments to show the influence of cylinder spacing on r.m.s. relative motion, also for a location 9.06 m beneath the still water level. Data are presented for the tandem orientation with both cylinders with pretension $[T_1, T_1]$. The relative motion r.m.s. displacement is non-dimensionalized by the cylinder spacing. The finite element simulations indicates that the r.m.s. relative displacement to spacing ratio does not vary as a function of cylinder spacing as seen from Figure 4.35. The experimental data show much larger relative motion as in Figure 4.36 and also large fluctuations with cylinder spacing in the proximity-wake regime (up to three times).

The data presented from the finite element simulations indicate that the change in phase of the wave elevation due to the spacing between the cylinders is not important due to the small ratio of cylinder spacing to wave length considered. However, changes in displacement phase due to differences in pretension are shown to increase with an increase in pretension difference both in the finite element simulations and in the experimental data. However, large differences between the experimental data and the finite element simulations indicate that there are other phenomenon that influence the cylinder response that are not accounted for in the finite element simulations. Even though the finite element model predicts the r.m.s. inline response fairly accurately, it fails to predict the relative motion between the two cylinders with any degree of accuracy. This indicates that there is a mechanism between the two cylinders that influences the relative motion that is not modeled by the finite element program. One obvious mechanism is the interference or hydrodynamic coupling between the two cylinders which was shown to be significant when the cylinders were in close proximity. The hydrodynamic coupling is influenced by the “shielding” be-

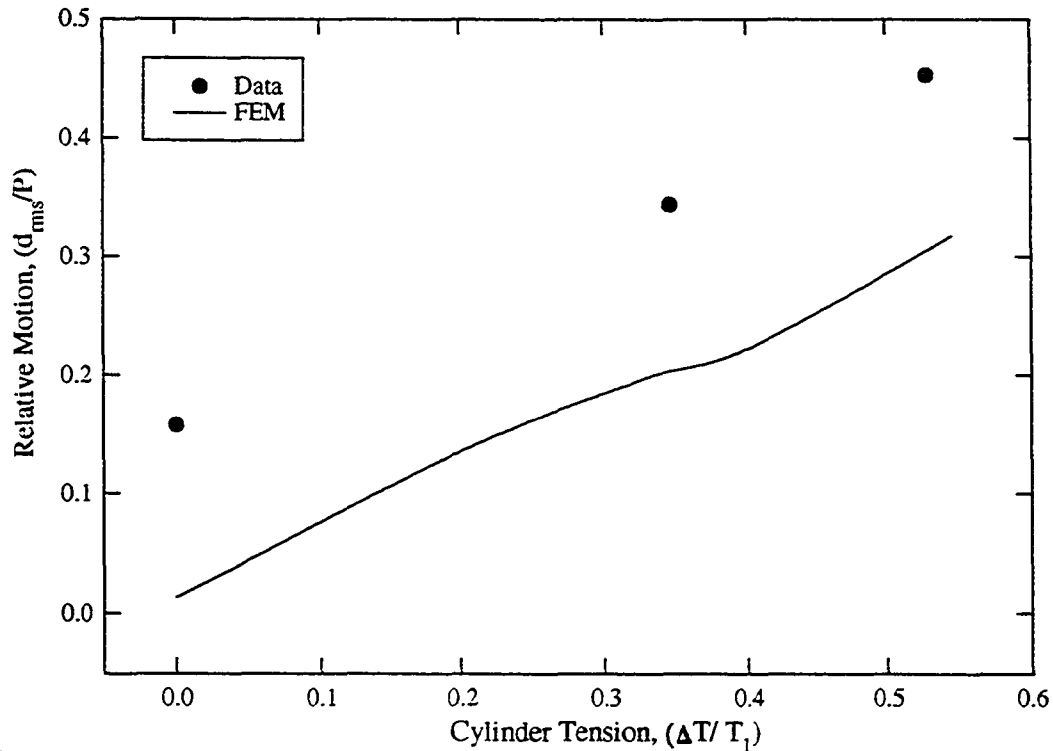


Figure 4.35: Relative motion as a function of tension difference between cylinders for random wave excitation (tandem, $2.5D$).

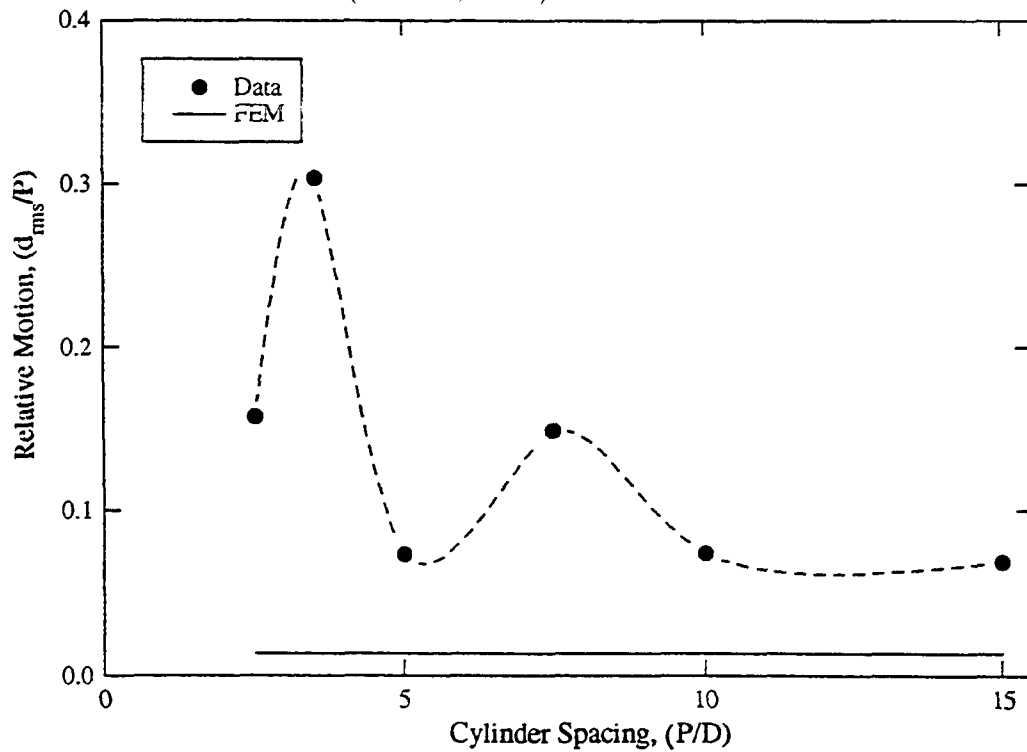


Figure 4.36: Relative motion as a function of cylinder spacing for random wave excitation with pretension $[T_1, T_1]$.

tween the cylinders and the flow separation around the cylinders causing vortices to be shed. This flow separation leads to confused wave kinematics in the proximity of the cylinders which influences the cylinder response. A better understanding of the hydrodynamic coupling thus requires a knowledge of the change in wave kinematics in the region of the two cylinders caused by the flow separation around them. At the present time no adequate analytical or numerical model is available to address the flow separation phenomenon for the flow conditions addressed in this study.

4.5 Summary of Data Analysis

This section analyzed the experimental data obtained from the experimental investigation studying the interaction of regular and random waves with a pair of flexible cylinders. The analysis focused on two sets of data: (1) the single cylinder tests and (2) the paired cylinder tests.

The single cylinder data analysis analyzed the wave-structure interaction problem as a function of non-dimensional parameters, like the Keulegan–Carpenter number and the reduced velocity, which have been used to classify the fluid-structure interaction phenomenon in previous experimental studies. The classification of transverse wave forces as outlined in Blevins (1990) appears to hold for the transverse response, especially for low N_{KC} , where the response is at fixed harmonics of the incident wave frequency. For the high N_{KC} and the random wave tests, peak response was observed at several harmonics of the wave frequency and at various natural frequencies of the cylinders. The reduced velocity computed at the frequency of peak response for the high N_{KC} numbers was much larger than the $5.5 \leq U_r \leq 8.5$ range suggested by Blevins (1990) and several other investigators. A comparison between the inline and transverse response for high N_{KC} cases showed that the high frequency content of the inline response was correlated to the transverse response, though no such correlation was observed between the transverse and inline response at the wave frequency. This indicated that the flow separation around the cylinder resulted in both transverse and inline response. Comparison of the measured inline response with finite element estimates, based on the relative motion form of the Morison equation with drag and inertia coefficients from Sarpkaya and Isaacson (1981), showed fair agreement, especially if one neglected the high frequency content related to the transverse response of the cylinder.

Interference coefficients relating the r.m.s. response of the pair of cylinders to that of a single cylinder are presented as a function of orientation and spacing. In

general paired cylinder inline response was seen to vary from 0.7 to 1.2 times that of a single cylinder, with most of the variance being in the proximity and proximity-wake regimes. Transverse response was generally reduced for all cases to 0.2 times that of a single cylinder. Other results show that the interference phenomenon also causes changes in the frequency and phase of the response. These results were unlike those observed for steady and harmonic flows where large reductions in the drag force and large increases in the transverse force were measured.

The section closed with an introduction to the relative motion between the cylinders, important in studying the collision behavior of the cylinders. Comparisons were made between the experimental results and the finite element predictions to study the relative motion process as a function of spacing and pretension difference between the cylinders, arranged in a tandem orientation. The results showed that the finite element simulations greatly under-predicted the relative motion between the cylinders, even though they compared fairly well with estimates for single cylinder r.m.s. response. This led to the conclusion that the hydrodynamic interference between the cylinders, not accounted for in the finite element simulations, greatly influenced the relative motion response. The relative motion/collision process is analyzed in more detail in the following section.

5. PROBABILISTIC ANALYSIS OF THE PAIRED CYLINDER COLLISION BEHAVIOR

The relative motion process, introduced in the previous section, is formulated to represent the collision process between a pair of cylinders in the tandem arrangement. Examples of the collision process are shown graphically to supplement the introduction provided in the previous section. The collision process is treated as a random process where a collision between the cylinders is equivalent to the random process crossing a barrier equal to the spacing between the cylinders. The problem is first formulated for a Gaussian process using the well established relationships first developed by Rice (1944, 1945). Due to the non-Gaussian nature of the response measured in the experimental program, the Hermitian transformation technique developed by Winterstein (1985, 1988) is used to obtain non-Gaussian statistics for the barrier-crossing problem. Comparisons are made between the Gaussian and non-Gaussian estimates of the extreme response and to non-parametric estimates obtained from the data. The appropriateness of the first-passage formulation for the collision behavior and importance of including the non-Gaussianity in evaluating these extreme response estimates is discussed.

5.1 Collision Process Formulation

Figure 5.1 illustrates the formulation of the problem for a pair of cylinders in tandem with spacing, r . The displacement of the cylinders in the X direction is denoted by $x_1(z, t)$ and $x_2(z, t)$ for Cylinders 1 and 2 respectively, with origins at the respective centerlines. The relative displacement, $R_{12}(z, t)$, is defined as

$$R_{12}(z, t) = x_1(z, t) - x_2(z, t) \quad (5.1)$$

A collision between the cylinders at an elevation z_c occurs when the relative displacement between the two cylinders at that location is greater than the spacing between the cylinders.

$$R_{12}(z_c, t) = x_1(z_c, t) - x_2(z_c, t) \geq r \quad (5.2)$$

In the previous section Figures 4.33—4.36 studied the relative displacement between two cylinders in the tandem arrangement and compared finite element predictions

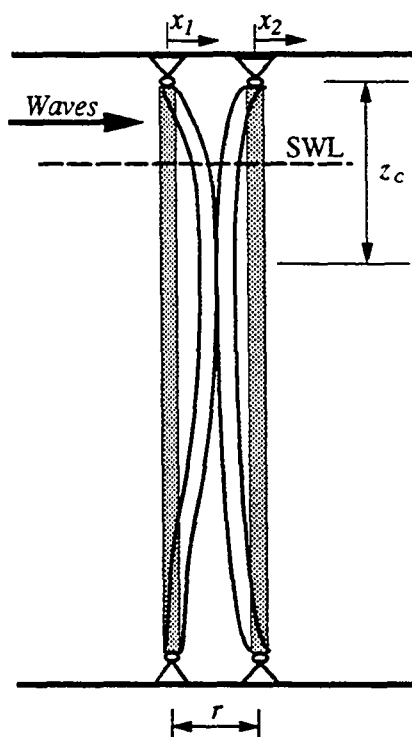


Figure 5.1: Definition sketch: relative displacement/cylinder collision process.

with experimental data. Based on the comparison it was concluded that the relative displacement between the two cylinders was a function of the pretension difference between the two cylinders (which affects the change in phase of the structural responses), the spacing (which affects the change in forcing phase) and the hydrodynamic coupling between the two cylinders which was not modeled in the finite element simulations. The finite element model predicted negligible relative displacement between the two cylinders when the pretensions were the same. In fact, as shown in Figure 5.2 collisions did occur when the two cylinders were under the same pretension.

Figure 5.2 presents the relative motion between a pair of cylinders in tandem with spacing $2.5D$ and pretension $[T_1, T_1]$ subjected to random wave excitation (Test # TRN5T1_25_001). Each frame of the figure represents a “snapshot” of the relative displacement of the cylinders at intervals of 0.1 seconds. It is seen that the cylinders have a tendency to move together except at $T = 388.9$ seconds when the response suddenly changes and the cylinders come very close together or “collide”. This test was videotaped from the East observation port in the wave basin as indicated in the test log (see Appendix C) and this collision recorded. The collision behavior indicated

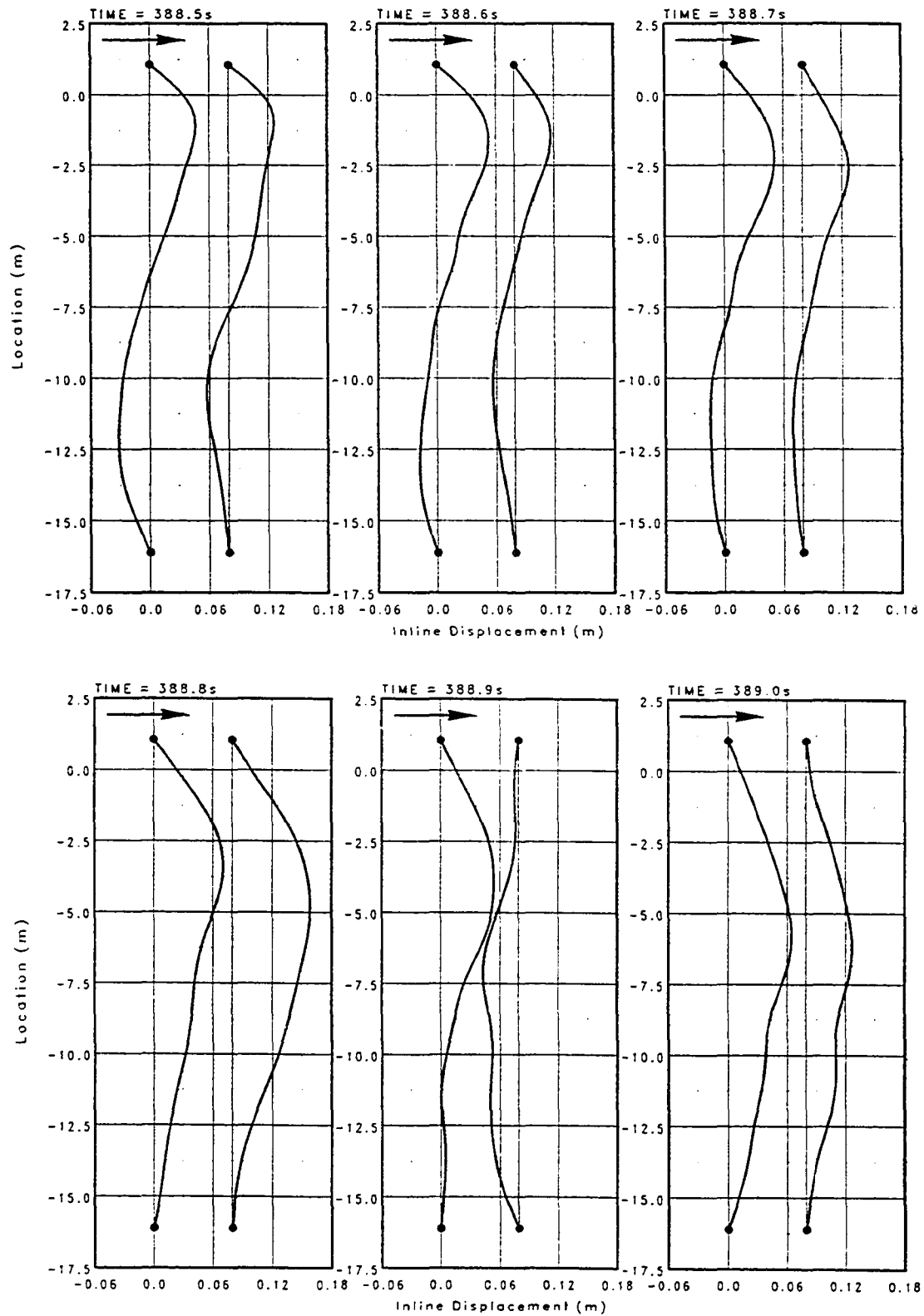


Figure 5.2: Time snapshots for a pair of cylinders (tandem, $2.5D$) with pretension $[T_1, T_1]$ for random waves.

in the figure is also a measure of the accuracy of the scheme of integrating discrete curvature measurements to estimate the displacement of the cylinders. Another collision was observed at a lower elevation during the same random wave simulation.

The figure shows that even when the cylinders have the same pretension and the spacing between the cylinders does not cause an appreciable change in forcing phase, the cylinders can still have erratic response and can collide. This illustrates the importance of the hydrodynamic interference between the cylinders which is the mechanism not accounted for in the finite element model. This hydrodynamic interference is hypothesized to be due to vortex shedding and flow separation around the cylinders, leading to a confused state of local fluid kinematics causing differences in displacement between the two cylinders. Figures 4.33 and 4.34 illustrated that the displacement of Cylinder 2 contained larger amounts of high frequency energy than that for Cylinder 1.

The effect of the difference in pretension is illustrated in the collision snapshots presented in Figure 5.3 and 5.4 for a pair of cylinders in tandem with spacing of $2.5D$ and for a regular wave of period 2.6 seconds. Figure 5.3 is for a pretension $[T_1, T_1]$ and Figure 5.4 for pretension $[T_1, T_2]$ with the wave excitation being identical for each case. Figure 5.3 shows the two cylinders moving together without much difference in phase and magnitude. Figure 5.4, which is at the same time during wave generation as Figure 5.3, shows the two cylinders exhibiting different displacement behavior, both in phase and magnitude and a collision occurring at $T = 101.5$ seconds.

The above figures also show that the collision process is a function of the pretension, spacing and the hydrodynamic interference between the two cylinders. The process is further complicated by the fact that collisions can occur over a fairly large portion of the cylinders. Figures 5.5 and 5.6 present the individual r.m.s. displacements of Cylinders 1 and 2 and the r.m.s. relative displacement between the two cylinders when subjected to random wave excitation, for pretensions $[T_1, T_1]$ and $[T_1, T_2]$ respectively. In both cases the individual r.m.s. displacements of the cylinders are similar, however the r.m.s. relative displacement for the pretension $[T_1, T_2]$ is much greater than for the $[T_1, T_1]$ case. This also indicates the influence of the pretension difference on the relative displacement process. Also, the location of maximum r.m.s. relative displacement changes. However, a fairly large portion of the cylinder, centered around the middle of the cylinder, is susceptible to collisions due to the relatively large relative displacement.

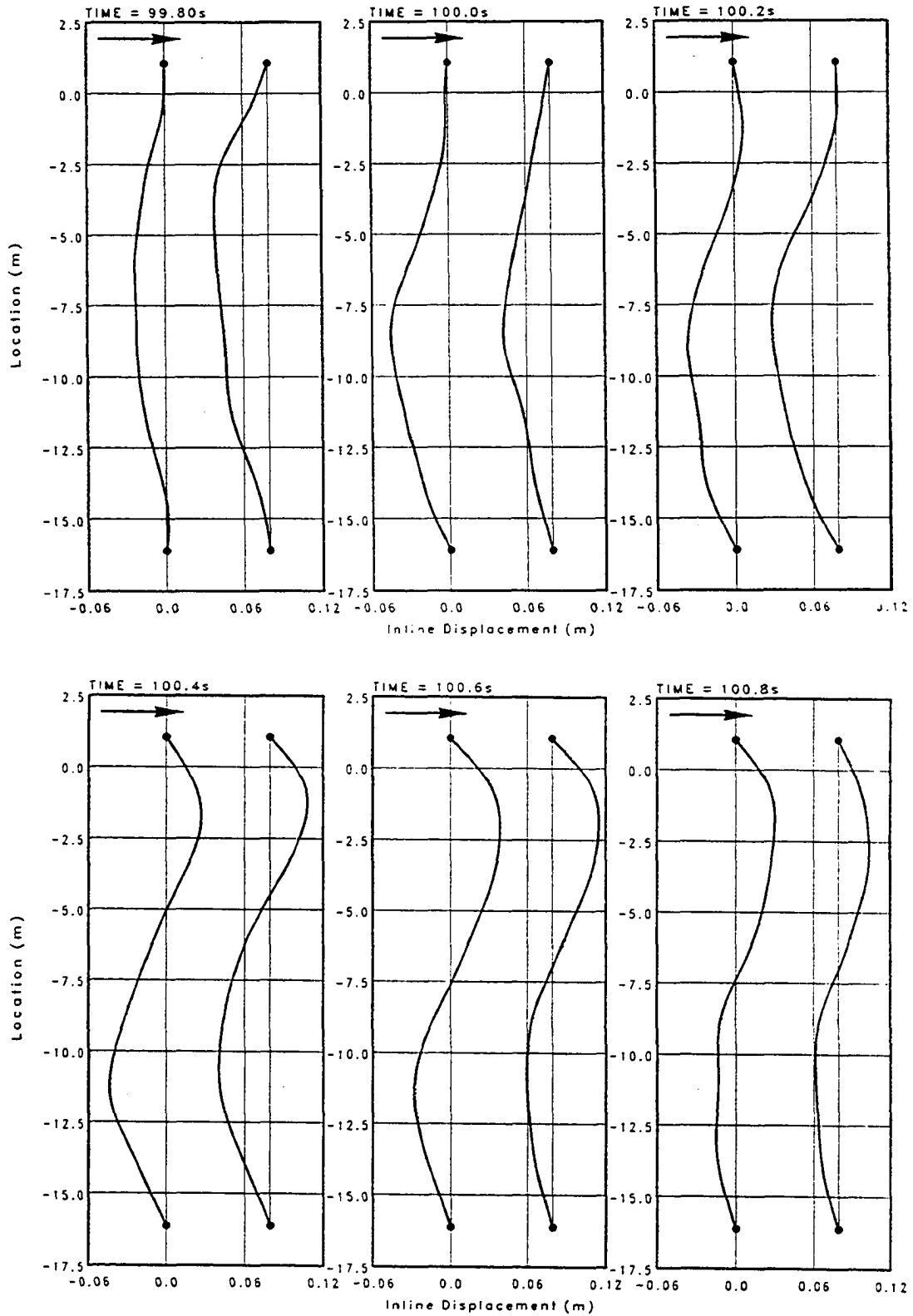


Figure 5.3: Time snapshots for a pair of cylinders (tandem, $2.5D$) with pretension $[T_1, T_1]$ for $T = 2.6$ seconds.

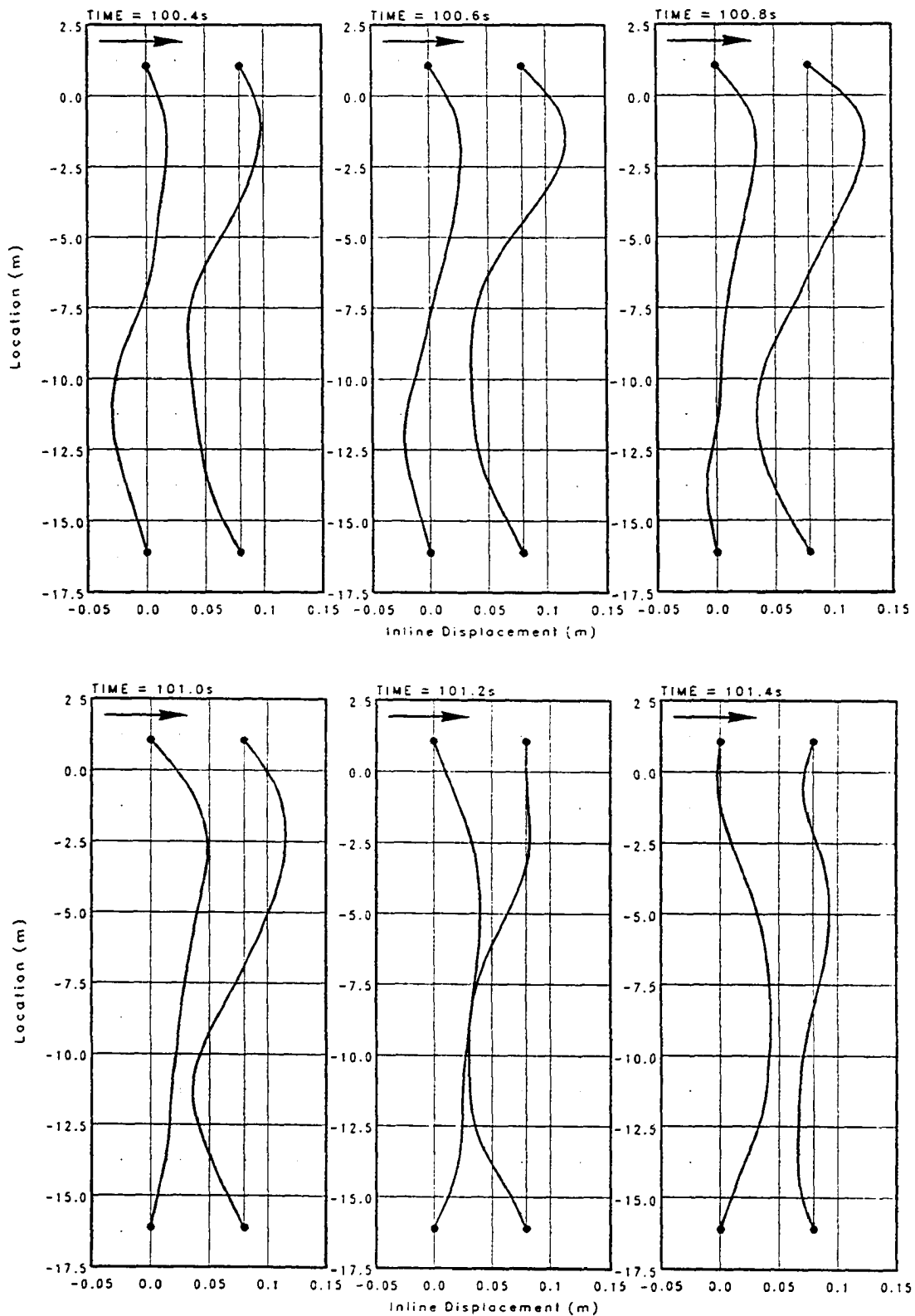


Figure 5.4: Time snapshots for a pair of cylinders (tandem, $2.5D$) with pretension $[T_1, T_2]$ for $T = 2.6$ seconds.

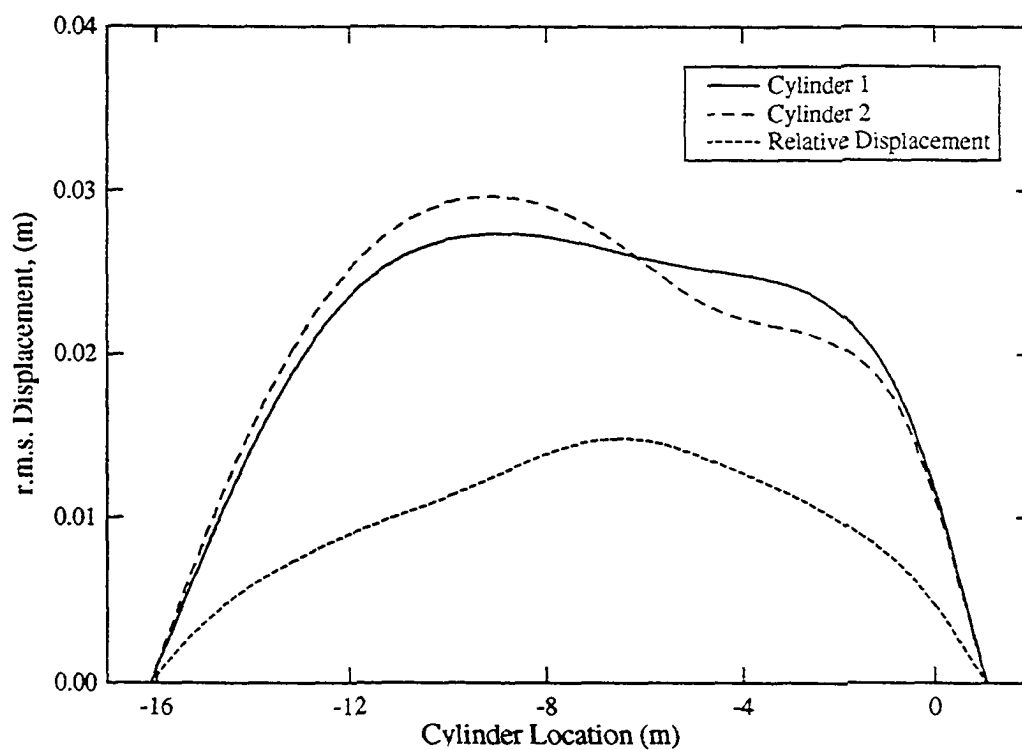


Figure 5.5: R.m.s. relative displacement as a function of cylinder length for the pair of cylinders (tandem, $2.5D$) with pretension $[T_1, T_1]$ for random waves.

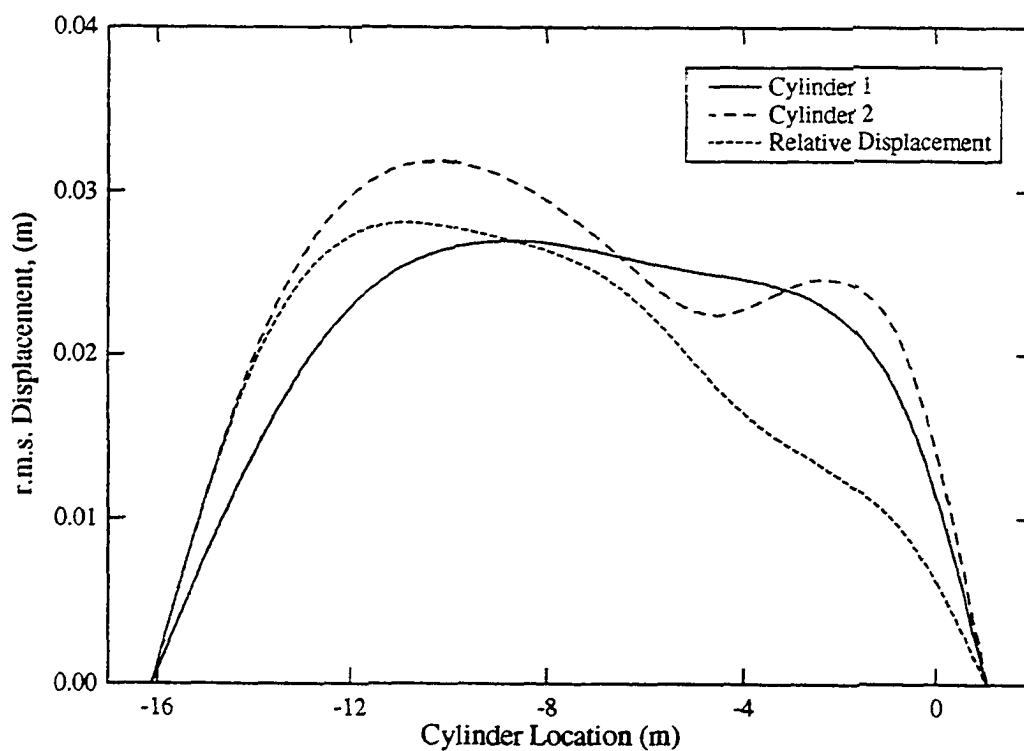


Figure 5.6: R.m.s. relative displacement as a function of cylinder length for the pair of cylinders (tandem, $2.5D$) with pretension $[T_1, T_2]$ for random waves.

5.2 Probabilistic Formulation of the Collision Process

The relative displacement process studied in this section considers the cylinders in a tandem arrangement, subjected to random waves. As part of the experimental program, a series of “extreme” tests were conducted at specific cylinder locations to arrive at the extreme response statistics. The extreme tests consisted of 6 random wave simulations (from the 100 year storm JONSWAP spectrum) of duration 409.6 seconds each for a total duration of 2457.6 seconds (204.8 minutes at prototype scale) for each set of constant cylinder parameters. This provided response estimates for a minimum of 1000 waves. For some locations the tests were repeated under different pretension conditions to study the influence of tension on the collision behavior. The waves generated had extreme waves with heights greater than 1 m (3.28 ft) in the wave basin corresponding to 25 m (82 ft) at prototype scale. Wave breaking was observed frequently during the tests.

Table 5.1: Computed moments of the incident waves and various response measurements.

Measurement	Mean μ	Std. Dev. σ	Skewness α_3	Kurtosis α_4
Wave Elevation (m)	0.002968	0.1248	0.20408	3.1464
Top Tension (N)	9.5529	9.3636	2.0438	9.6870
Curvature X , (1/m)	-0.00001398	0.002923	-0.090124	4.8774
Curvature Y , (1/m)	-0.0001126	0.003037	-0.21981	4.8629
Top Reaction X (N)	0.42025	2.4901	1.36	9.1150
Top Reaction Y (N)	0.24448	0.75487	0.42024	4.6935

Most probabilistic analysis of wave-structure interaction assumes the wave kinematics to be Gaussian (normal). Due to the nonlinear nature of wave loading (the drag term in the Morison’s equation), the wave loading is non-Gaussian leading to non-Gaussian response. Table 5.1 lists the first 4 moments of the various random processes measured for a series of extreme random wave tests on a single cylinder under pretension T_1 . This is for the same configuration which was used as an example of the data acquired in Section 4 (Figures 4.1—4.6). The wave elevation data is seen to be weakly non-Gaussian which is expected as the waves were very steep with

higher crests than troughs, and were observed to break. All the response measurements from the various transducers are seen to have a kurtosis greater than 3 which is characteristic of the drag loading on the structure (softening system). The tension and the top inline reaction are observed to have very large skewness and kurtosis; the other response estimates have fairly large kurtosis but show very little skewness. In a later section, the non-parametric estimates of the probability density functions (pdf) of these processes are compared to equivalent Gaussian pdfs, and non-Gaussian estimates based on the first 4 moments of the response.

If the collision process of the cylinder is considered to be a random process, then from Equation 5.2 a collision is equivalent to crossing a barrier greater than or equal to the spacing between the cylinders. This relates directly to the barrier-crossing behavior of the random process which forms the basis for the extreme value problem associated with random processes. In the subsections to follow, a brief overview of this classical problem is outlined as pertaining to the collision problem, pointing out the features and assumptions behind the formulations. The results are first presented for a Gaussian process, and then non-Gaussian formulations are presented by applying the Hermite transformation technique (Winterstein 1985, 1988).

5.2.1 The First-Passage Time

Consider a stationary random process, $X(t)$. As defined in Figure 5.7 the first-passage time of $X(t)$ is the time at which the process first crosses the barrier, r . This problem is referred to as the single barrier problem and will be the focus of the following formulation due to its application to the cylinder collision process. The first-passage time is a random variable related to the process $X(t)$. For such a problem the probability of surviving such a crossing in an interval $[0, t]$, $L_{T_f}(t)$, can be defined as (Nigam 1983)

$$\begin{aligned} L_{T_f}(t) &= P[X(0) < r, T_f > t] \\ &\simeq P[X(0) < r] \cdot P[T_f > t] \end{aligned} \quad (5.3)$$

$L_{T_f}(t)$ thus requires knowledge about the process at time $t = 0$ and the distribution of the first-passage time, T_f . For the remainder of this discussion the probability of survival at $t = 0$, $L_{T_f}(0)$, is assumed to be 1.0 and the focus will be on the distribution of T_f which is a classical problem in probabilistic mechanics that has defied exact solution except for very idealized and simplified systems.

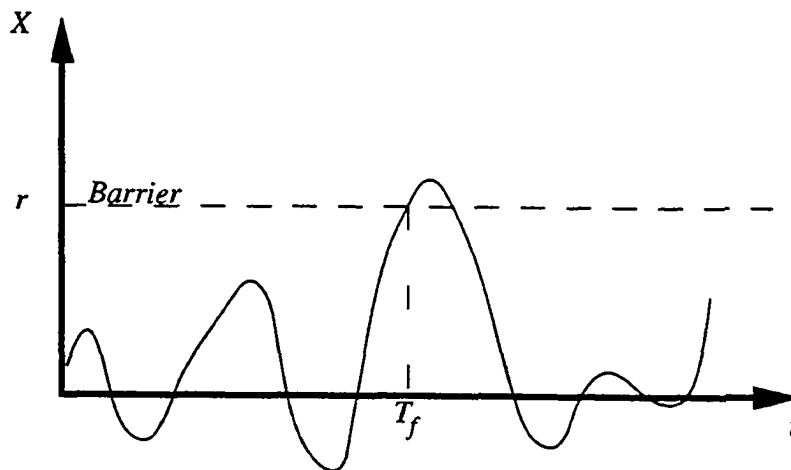


Figure 5.7: Definition sketch: first-passage time.

The extreme value X_m of a random process $X(t)$ in a given time interval $[0, t]$ is closely related to the first-passage time (Nigam 1983)

$$F_{X_m}(r) = P[X_m < r] = P[T_f > t] = L_{T_f}(t) \quad (5.4)$$

Therefore a knowledge of the distribution of the first-passage time is required to predict statistics related to the extremes of the process. The inclusion-exclusion series of Rice (1944, 1945) is an exact solution but is too cumbersome computationally to be solved accurately. Several approximations have been attempted to arrive at accurate solutions of this problem ranging from complicated analytical or numerical methods to empirical methods (Lutes, Chen and Tzuang 1980). Most of the approaches are for specific systems and cannot be applied directly to more general systems.

Intuitively the crossing of a very high barrier can be considered a rare event and the crossings to be independent. Under these conditions the barrier crossing can be considered a Poisson process with a rate of arrival ν_r , where the probability of k crossings in a time $[0, t]$ is given as (Nigam 1983)

$$P[N(t) = k] = \frac{(\nu_r t)^k e^{-\nu_r t}}{k!} \quad (5.5)$$

where, $N(t)$ is the counting process. Therefore the probability of no crossings in $[0, t]$,

$P[T_f > t]$, implies $k = 0$. Therefore

$$P[T_f > t] = P[N(t) = 0] = e^{-\nu_r t} \quad (5.6)$$

The probability of survival, $L_{T_f}(t)$, is

$$L_{T_f}(t) = F_{X(0) < r} e^{-\nu_r t} \quad (5.7)$$

The main problem is to determine the arrival rate, ν_r . From Rice (1944, 1945) the average upcrossing rate of a random process, $X(t)$, for a barrier, r , is given by

$$\nu_X(r) = \int_0^\infty v p_{X\dot{X}}(r, v) dv \quad (5.8)$$

where $p_{X\dot{X}}(u, v)$ is the joint probability density function for the process $X(t)$ and its derivative process $\dot{X}(t)$.

For a stationary normal random process the two processes $X(t)$ and $\dot{X}(t)$ are independent and $p_{X\dot{X}}(u, v)$ is given by the product of the two individual Gaussian probability density functions for $X(t)$ and $\dot{X}(t)$

$$\begin{aligned} p_{X\dot{X}}(u, v) &= p_X(u) \cdot p_{\dot{X}}(v) \\ &= \frac{\exp(-u^2/2\sigma_X - v^2/2\sigma_{\dot{X}})}{2\pi\sigma_X\sigma_{\dot{X}}} \end{aligned} \quad (5.9)$$

where, σ_X and $\sigma_{\dot{X}}$ are the standard deviations of $X(t)$ and $\dot{X}(t)$ respectively. Substituting Equation 5.9 into Equation 5.8, the average crossing rate of a Gaussian process for a barrier, r , is given by

$$\nu_X(r) = \nu_X(0)e^{-r^2/2\sigma_{\dot{X}}^2} \quad (5.10)$$

where, $\nu_X(0)$ is the zero crossing rate of the process $X(t)$ equal to $(1/2\pi)(\sigma_{\dot{X}}/\sigma_X)$.

The Poisson crossings assumption (PCA) assumes the average upcrossing rate $\nu_X(r)$ to be the arrival rate, ν_r , used in the first-passage time formulation. This also corresponds to the first term in Rice's inclusion-exclusion series. This assumption has been shown to converge asymptotically to the correct solution for very high barriers, but is very conservative for lower barriers. This is because for low barriers and for narrow-band processes, the barrier crossings occur in clusters or clumps, with a crossing of a barrier followed by others. These crossings cannot be considered independent events and violates the assumptions made earlier.

A number of formulations have been proposed to account for the tendency of the barrier crossings to occur in clumps (Nigam 1983). One approach is to consider the crossings of the barrier by the envelope process, $A(t)$, of $X(t)$ to be a Poisson process. In this case the model would be the same as the Poisson crossing model for independent $X(t)$ crossings except that the arrival rate ν_r would be given by $\nu_A(r)$, where $\nu_A(r)$ is the average upcrossing rate of the barrier by the envelope process. This model has been shown to be good for narrow-band processes at low threshold levels but is highly conservative for high barrier levels as an envelope crossing may occur without an $X(t)$ crossing. For broad-band processes the model may break down as the envelope process may not follow the peaks of $X(t)$ closely enough.

Several approximations have been made to account for the clump size of the crossings as a function of the process and the barrier level (Nigam 1983), the most widely used being that of Vanmarcke (1975) for a stationary random narrow-band process where the arrival rate, ν_r is given by

$$\nu_r = \nu_X(r) \frac{1 - \exp\left(-\frac{\nu_A(r)}{\nu_X(r)}\right)}{1 - \frac{\nu_X(r)}{\nu_X(0)}} \quad (5.11)$$

which for a stationary Gaussian narrow-band process reduces to

$$\nu_r = \nu_X(r) \frac{1 - e^{\sqrt{2\pi}q_e r / \sigma_X}}{1 - e^{-r^2 / 2\sigma_X^2}} \quad (5.12)$$

where q_e is a bandwidth parameter given by

$$q_e = \left\{ \left[1 - \frac{\lambda_1^2}{\lambda_0 \lambda_2} \right]^{\frac{1}{2}} \right\}^{1.2} \quad (5.13)$$

where λ_n is the n th spectral moment defined as

$$\lambda_n = \int_0^\infty \omega^n S(\omega) d\omega \quad (5.14)$$

Vanmarcke's formulation has compared reasonably well with simulation data for lightly damped, narrow-band processes. However, Toro and Cornell (1986) showed that Vanmarcke's formulation failed for broad-band, multi-peaked processes as the envelope did not follow the peaks of the $X(t)$ process closely. Using concepts introduced by Vanmarcke (1975) they formulated a model for a bimodal process with well separated narrow-banded peaks. However, they claim that extension of their model

to broad-band, multi-peaked processes would be very complicated and may not have the simple form discovered for the bimodal process.

Another approach has been formulated in terms of the energy fluctuation in the process (Winterstein and Cornell 1984, Winterstein 1988). Here the clustering is related to the energy fluctuation scale, θ_E . The bandwidth of the process associated with θ_E , $(1/\nu_0\theta_E)$, is less sensitive to the high frequency components than the traditional bandwidth estimates utilizing spectral moments. The energy fluctuation, θ_E is given by (Winterstein and Cornell 1984)

$$\theta_E \simeq 4\pi \int_{-\infty}^{+\infty} S_X^2(\omega) d\omega \quad (5.15)$$

For an arbitrary spectral estimate (say from experimental data), θ_E , can be related to the "equivalent" damping ratio, ζ (Winterstein 1988)

$$\theta_E \simeq \left(\frac{1}{2\pi\zeta\nu_0} \right) \quad (5.16)$$

where

$$\zeta = \left[\frac{8\nu_0\pi^2}{\sigma_X^4} \int_{-\infty}^{+\infty} S_X^2(\omega) d\omega \right]^{-1} \quad (5.17)$$

The above overview of the first-passage time formulation and the related distribution of extremes shows that the model formulations are dependent upon (1) the accurate estimation of the average upcrossing rate of the barrier, r , by the process $X(t)$ (first-order statistics); and (2) assessment of the response bandwidth and clustering effects of the upcrossings for the barrier desired (second-order statistics). In the sections to follow the importance of accurately estimating both effects will be discussed along with the importance of non-Gaussianity on the overall first-passage time and extreme value distribution.

5.2.2 Non-Gaussian Statistics by Hermitian Transformation of a Gaussian Process

As illustrated in Table 5.1, the cylinder response is strongly non-Gaussian even though the incident wave kinematics are very weakly non-Gaussian due to the nonlinearity of the wave loading. The large kurtosis ($\alpha_4 > 3$) observed, which is characteristic of drag loading, implies larger tails than an equivalent Gaussian process. As shown by many investigators (Winterstein 1985, 1988 and Wang and Lutes 1991) neglecting

this non-Gaussian nature of the response can lead to severe underestimation in the extreme statistics of the response and in the fatigue life of the structure.

In this section the Hermite transformation technique, which utilizes the ability to generate a non-Gaussian process by applying a nonlinear transformation on a Gaussian process, is presented (Winterstein 1985, 1988). This method allows one to estimate probability density functions and related processes like the upcrossing rates and extreme response distributions from estimates of a few moments of the parent process (usually the first four moments are sufficient).

The non-Gaussian process $X(t)$ can be generated from a Gaussian process $Z(t)$ by the application of a monotonic nonlinear transformation, $g[\cdot]$

$$X(t) = g[Z(t)] \quad (5.18)$$

For convenience, the two processes, $X(t)$ and $Z(t)$ will be replaced by their standardized form ($\mu = 0, \sigma = 1$), $X_0(t)$ and $U(t)$ respectively.

For a softening system, ($\alpha > 3$), the nonlinear transformation function, $g[\cdot]$ is approximated by a Hermite polynomial expansion of the form (Winterstein 1988)

$$X_0(t) = \kappa \left[U + \sum_{n=3}^N c_n H_{e_{n-1}}(U) \right] \quad (5.19)$$

where, κ is a scale factor to ensure that $X_0(t)$ has unit variance, and the coefficients c_n control the shape of the standard distribution. The Hermite polynomials are of the form (Winterstein 1985)

$$H_{e_n}(u) = (-1)^n \exp\left(\frac{u^2}{2}\right) \frac{d^n}{du^n} \left[\exp\left(-\frac{u^2}{2}\right) \right] \quad n = 1, 2, \dots \quad (5.20)$$

for example, $H_{e_0}(u) = 1$, $H_{e_1}(u) = u$, $H_{e_2}(u) = u^2 - 1$, $H_{e_3}(u) = u^3 - 3u$, etc.

The coefficients, c_n are related to the Hermite moments, h_n , given by (Winterstein 1988)

$$h_n = \frac{1}{n!} E[H_{e_n}(X_0)] = \frac{\alpha_n}{n!} - \frac{\alpha_{n-1}}{1! 2(n-2)!} \dots \quad (5.21)$$

where, $\alpha_n = E[X_0^n]$ are the n^{th} moments of the process, $X(t)$. For example, α_3 and α_4 are the skewness and kurtosis respectively.

As higher moments tend to have high sampling variability, the Hermite series is truncated at $N = 4$, (includes the skewness (α_3) and kurtosis (α_4)), the coefficients, c_n , can be computed by applying a Hermite polynomial to Equation 5.19 and taking expectations. The values of the coefficients are presented in Table 5.2, where the first order coefficients are valid for mild nonlinearities and the second order coefficients are correct to $O(c_m c_n)$ (Winterstein 1988).

Table 5.2: Value of c_n for a softening system ($\alpha_4 > 3$).

Coefficient	First Order	Second Order
κ	1	$(1 + 2c_3^2 + 6c_4^2)^{-1/2}$
c_3	$\alpha_3/6$	$\alpha_3/(4 + 2\sqrt{1 + 1.5(\alpha_4 - 3)})$
c_4	$(\alpha_4 - 3)/24$	$(\sqrt{1 + 1.5(\alpha_4 - 3)} - 1)/18$

Based on the above equations, for $\alpha_4 > 3$ the value x of the actual non-Gaussian variable/process is related to the level u of a standard Gaussian variable/process by

$$x(u) = \mu_x + \kappa\sigma_x \left[u + c_3(u^2 - 1) + c_4(u^3 - 3u) \right] \quad (5.22)$$

Application to Upcrossing Rates and Probability Density Functions

The non-Gaussian upcrossing rates and probability density functions transform directly from the Gaussian results (Winterstein 1988). The Hermite model for the average upcrossing rate, $\nu_X(x)$ is given by

$$\nu_X(x) = \nu_0 \exp\left(-\frac{u^2(x)}{2}\right) \quad (5.23)$$

and, the Hermite model for the cumulative density function, $F_X(x)$ is

$$F_X(x) = P[X(t) \leq x] = \Phi[u(x)] \quad (5.24)$$

For a four moment model, $u(x)$ is given by (Winterstein 1988)

$$u(x) = \left[\sqrt{\xi^2(x) + c + \xi(x)} \right]^{1/3} - \left[\sqrt{\xi^2(x) + c - \xi(x)} \right]^{1/3} - a \quad (5.25)$$

$$\xi(x) = 1.5b \left(a + \frac{x - \mu_x}{\kappa\sigma_X} \right) - a^3 \quad (5.26)$$

where $a = c_3/3c_4$, $b = 1/3c_4$, and $c = (b - 1 - a^2)^3$.

These four moment pdfs and upcrossing rates have been shown to be much more stable and able to handle a much larger degree of nonlinearity than the commonly used Gram–Charlier or Edgeworth series (Winterstein 1988). They maintain their unimodal form and do not exhibit negative probability densities which are a notorious feature of the Gram–Charlier and Edgeworth estimates.

Application to First-Passage Time and Extreme Value Problems

For a single barrier problem (e.g., the cylinder collision problem) the Poisson crossings model is given by Equation 5.6. For the extreme value problem the Hermite transformation model is of the form (Winterstein 1988)

$$P[E \leq x] = \exp \left\{ -\nu_0 T \exp \left[-\frac{u^2(x)}{2} \right] \right\} \quad (5.27)$$

This Hermite model uses the average upcrossing rate of the barrier as the arrival rate and thus provides a first-order Hermite estimate. Clustering and response bandwidth effects (second-order) can be accounted for using the energy fluctuation related model (Winterstein 1988)

$$P[E \leq x] = \exp \left(-\nu_0 T \exp \left[-\frac{u^2(x)}{2} \right] \left\{ 1 - 2\Phi \left[-\sqrt{\pi\zeta} u(x) \right] \right\} \right) \quad (5.28)$$

where, ζ is given by Equation 5.17. Related distributions like the distribution of maxima and minima can be obtained in a similar fashion. Equations 5.27 and 5.28 can be used to get reliability estimates ($P[E \leq x]$) as a function of time for a fixed barrier, and also as a function of barrier level for fixed intervals of time.

5.3 Analysis of the Collision Behavior

Figures 5.8–5.13 present the probability density functions for the measurements whose moments were presented in Table 5.1. Each figure contains three estimates of the normalized pdf; (1) the Hermite estimate using the four moments listed in Table 5.1, (2) an equivalent Gaussian pdf computed from the first two moments, and (3) a non-parametric estimate of the pdf obtained from the data using a kernel density

estimator (Newton 1988).^{*} The scatter in the tails of the kernel estimates indicate the density of data available. The pdf's are presented on a semi-log scale to accentuate the tail behavior, since this is important for extreme response prediction.

Figure 5.8 presents the pdf of the wave elevation, the sole input measurement made. The data is weakly non-Gaussian as indicated earlier, which was expected due to the very large waves generated with larger crests than troughs. The Hermite estimate compares very well with the kernel estimate.

Figure 5.9 illustrates the pdf for the top tension. The tension measurement is highly non-Gaussian as indicated in the figure and in Table 5.1, with a very large positive tail. However, the non-Gaussianity of the tension alone does not imply that the overall response of the system was non-Gaussian as the tension would be non-Gaussian even if the response were Gaussian. It is observed that the tail behavior is severely underestimated by the Gaussian pdf. The Hermite model fits the large positive tail well but does not do so well on the negative side. This seems to indicate that for this particular process, higher moments than the first four may be required to better estimate its behavior.

Figures 5.10 and 5.11 present the pdfs for the inline and transverse curvature at location -7.47 m. The two pdfs are very similar with large symmetric tails and very little skewness. The Hermite model shows excellent agreement with the kernel estimates for both cases. Figures 5.12 and 5.13 show the pdfs for the top inline and transverse reactions. The inline top reaction has a distribution similar to the tension, with a large positive tail which is estimated very well by the Hermite model. The Hermite model also fits the transverse top reaction very well which has a pdf very similar to that of the curvature.

The figures presented illustrate the non-Gaussian nature of the response of the cylinders. All the response estimates had a large kurtosis, implying larger tails than a Gaussian estimate, characteristic of drag loading (softening system). The hermite model was observed to show excellent agreement with the kernel estimates while the Gaussian estimates greatly underestimated the tail behavior. This is very critical in

^{*}The kernel probability density estimator is a non-parametric density estimator like a histogram, i.e. it does not assume a functional form. The density estimate is computed by dividing the data into intervals that are allowed to overlap. The aim is to estimate the density at the center of each interval. The data points in the interval are weighted using a function (kernel) as a weighting function, with a maximum value at the center. For this study the kernel is chosen with a Gaussian form with bandwidth computed as recommended in Newton (1988).

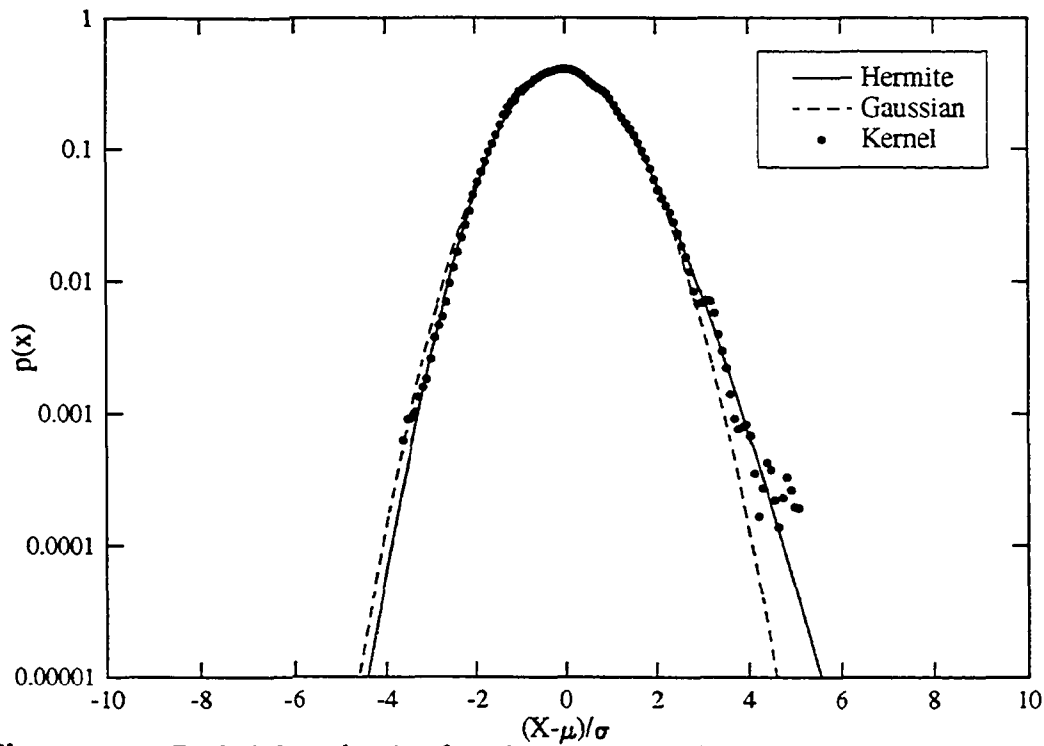


Figure 5.8: Probability density function estimates for the incident random wave elevation (single cylinder, pretension T_1).

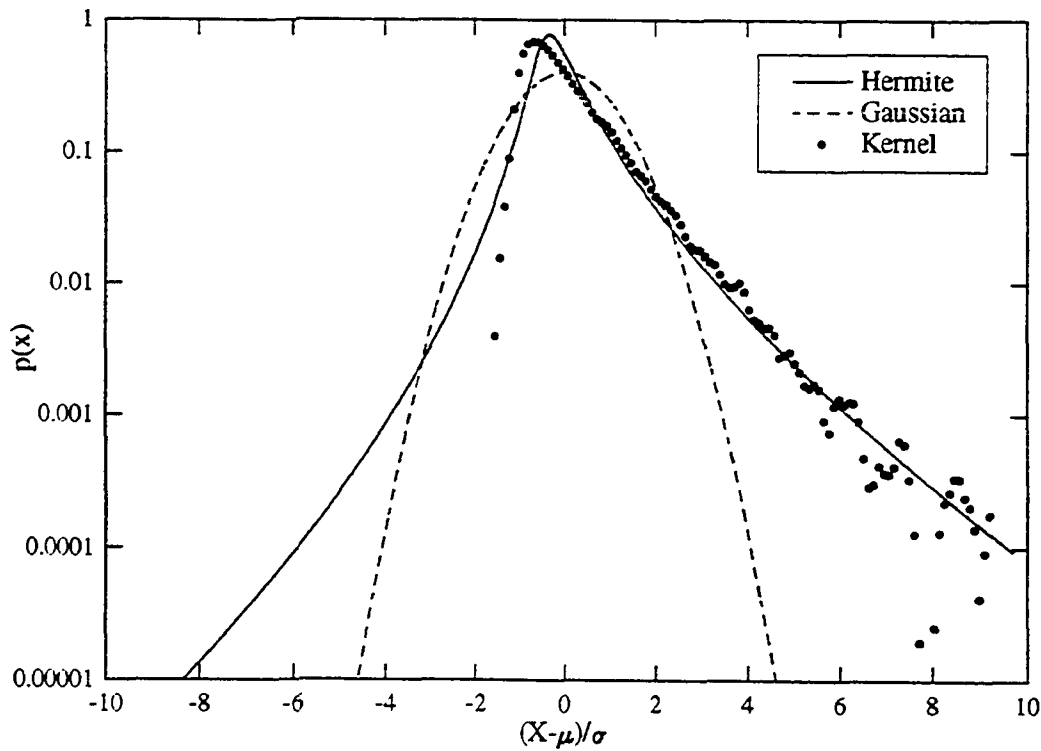


Figure 5.9: Probability density function estimates for the top tension (single cylinder, pretension T_1).

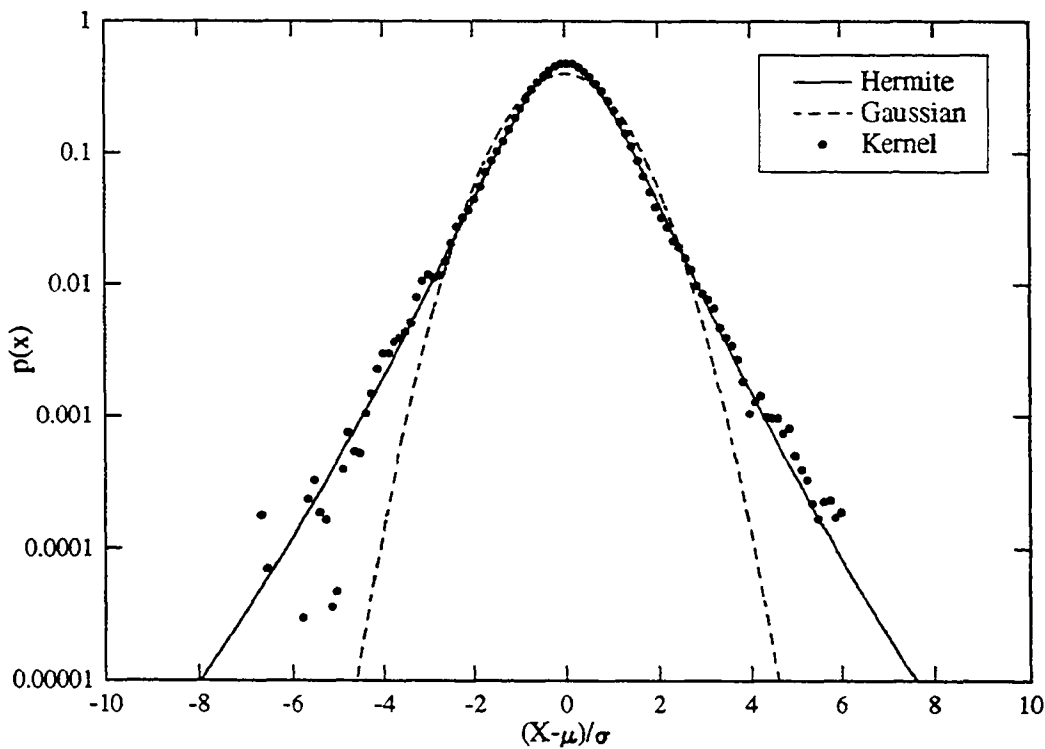


Figure 5.10: Probability density function estimates for the inline curvature at location -7.47 m (single cylinder, pretension T_1).

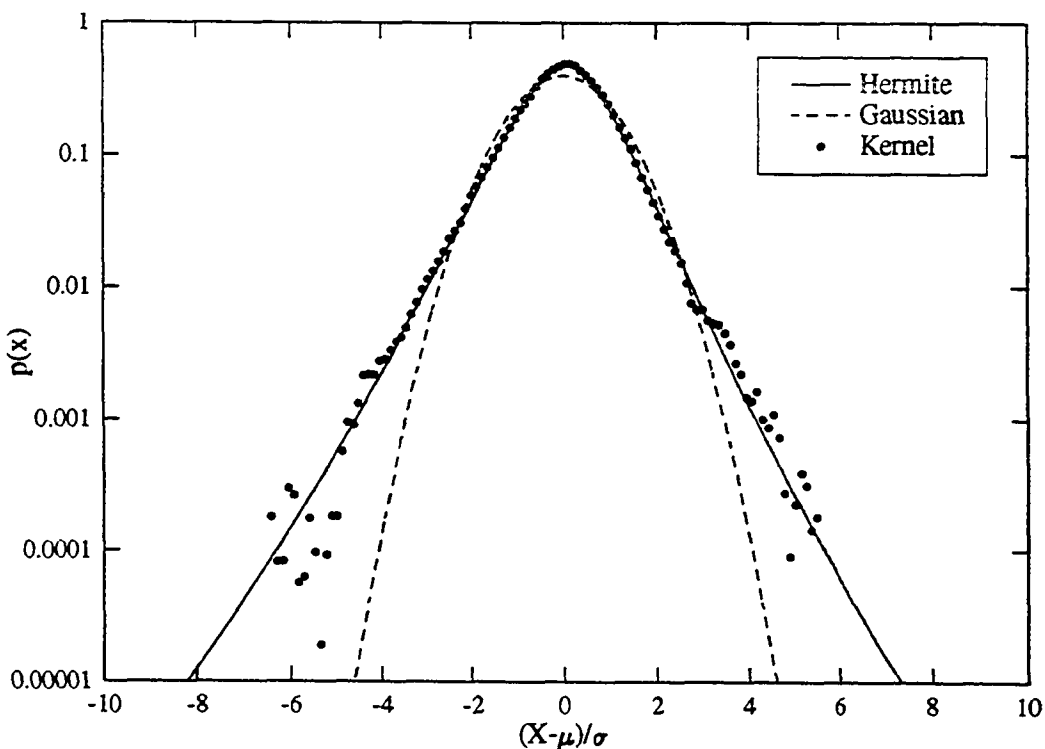


Figure 5.11: Probability density function estimates for the transverse curvature at location -7.47 m (single cylinder, pretension T_1).

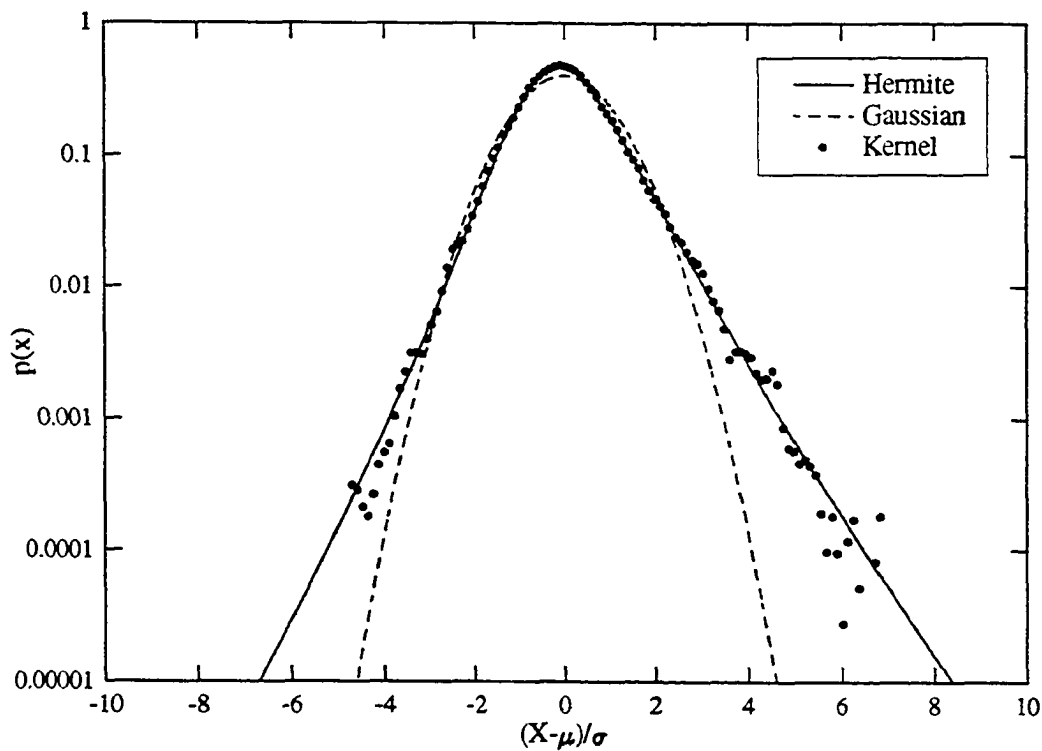


Figure 5.12: Probability density function estimates for the inline top reaction (single cylinder, pretension T_1).

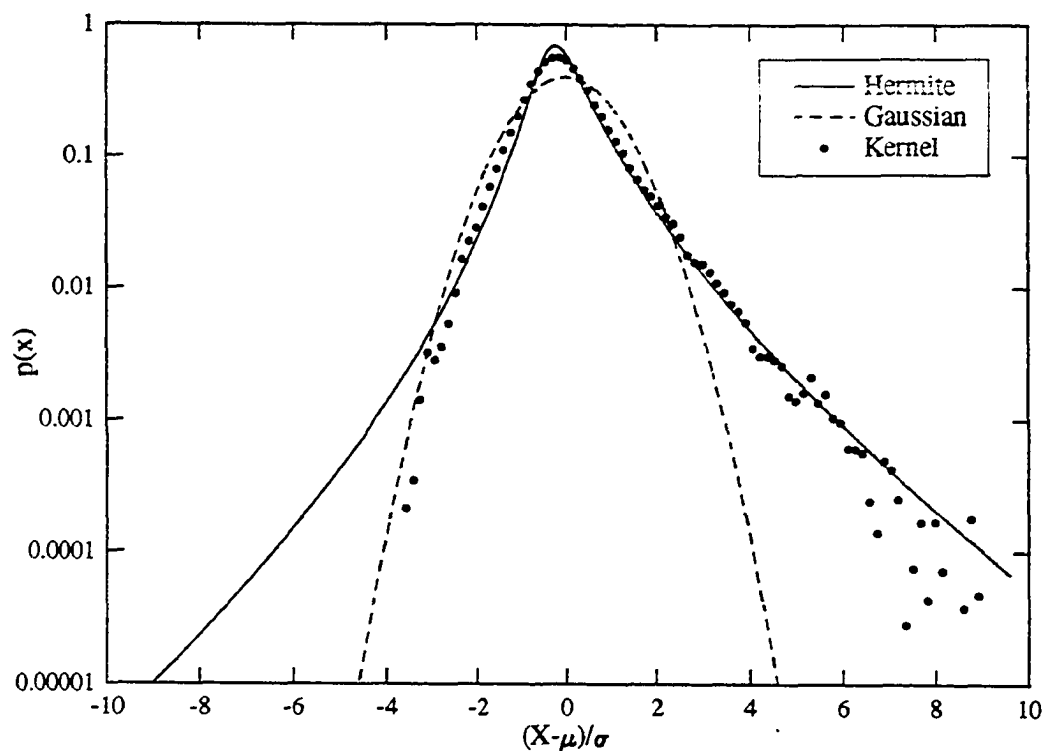


Figure 5.13: Probability density function estimates for the transverse top reaction (single cylinder, pretension T_1).

estimating the extreme response as is shown in the following discussion.

Long duration tests were conducted at 2 spacings in the tandem orientation ($2.5D$ and $5D$). The $2.5D$ spacing tests were conducted at 3 pretension arrangements ($[T_1, T_1]$, $[T_1, T_2]$, $[T_2, T_1]$), while the $5D$ tests were conducted at one pretension $[T_1, T_1]$. This section analyzes the collision behavior of the cylinders at these spacings and pretension conditions. Probability density functions, upcrossing rates, and first-passage behavior of the collision process are studied to determine (1) the relative importance of the first-order (average upcrossing rate) and second-order (clustering and response bandwidth) on the extreme value problem, (2) the importance of the non-Gaussianity of the process, and (3) the overall accuracy of the first-passage formulation. This is accomplished by analyzing the pdfs of the process, the upcrossing rates, and the reliability of the system (for cylinder collision). Estimates from the Hermite model, Gaussian formulations and non-parametric estimates from the data are presented for each case.

The collision process is analyzed for two pretension conditions, $[T_1, T_1]$ and $[T_1, T_2]$ respectively for spacing $2.5D$ at a location -8.13 m beneath the still water level. Figures 5.14 and 5.15 present the pdfs of the two relative displacement processes respectively. Both cases have the same shape, with high kurtosis and almost symmetric tails, very similar to the curvature pdfs seen earlier. The Hermite model predicts the pdf very well, while the Gaussian estimate is very unconservative in the tail region.

Figures 5.16 and 5.17 show the normalized upcrossing rates ($\nu(r)/\nu(0)$) for normalized barriers (r/σ_R) for the two pretension cases. The data represented by the solid circles were obtained by performing an upcrossing analysis of the data. For both cases the Hermite model predicts the behavior better than the Gaussian estimate, especially at high barrier levels, where it is under-predicted by the Gaussian estimate. In fact the Hermite estimate is slightly conservative, which is similar to that observed by Winterstein (1988) for simulations with $\alpha_4 > 3$. This indicates the accuracy of the Hermite model in determining the upcrossing rates. This verification is especially important since the model uses a transformation of an expression derived for normal processes under the assumption that the process and its derivative are independent which is not always true for a non-Gaussian process.

Figures 5.18 and 5.19 present the reliability of the system (cylinder collision), $P[R(t) < r]$ as a function of time for a barrier level equal to the spacing between the cylinders. The figures compare the Hermite estimates with the Poisson crossings assumption (Equation 5.27) and the influence of clumping and response bandwidth

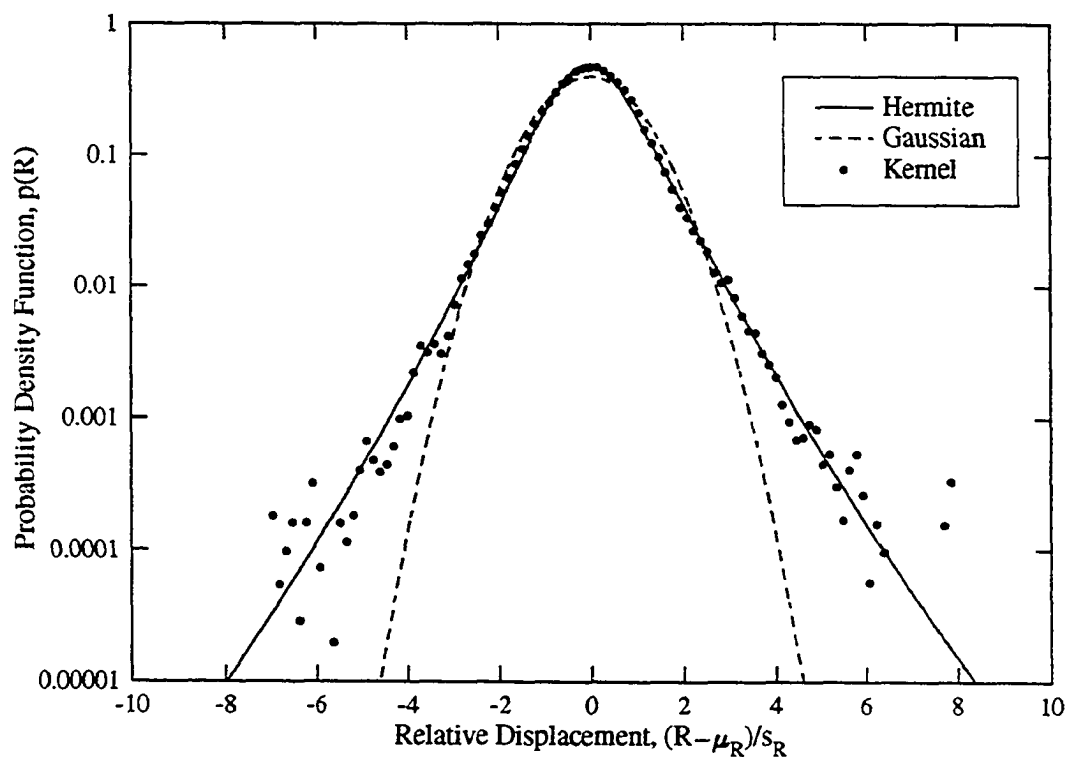


Figure 5.14: Probability density function estimates for the collision process at location -8.13 m (tandem, $2.5D$) with pretension $[T_1, T_1]$.

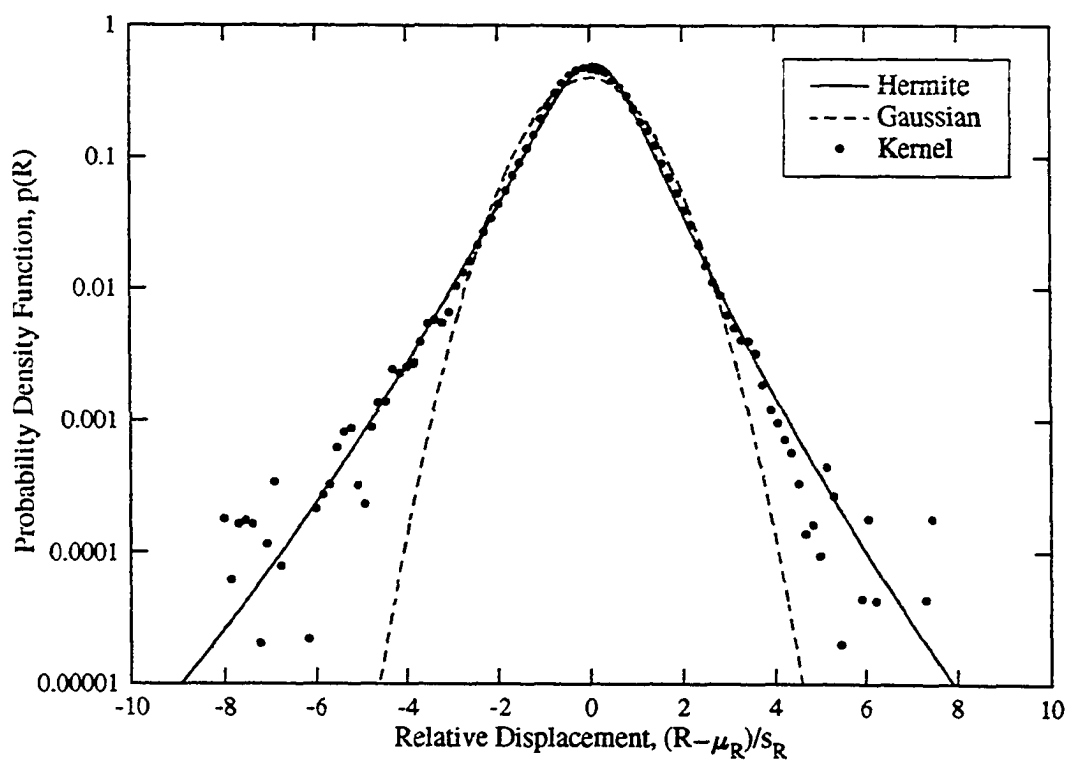


Figure 5.15: Probability density function estimates for the collision process at location -8.13 m (tandem, $2.5D$) with pretension $[T_1, T_2]$.

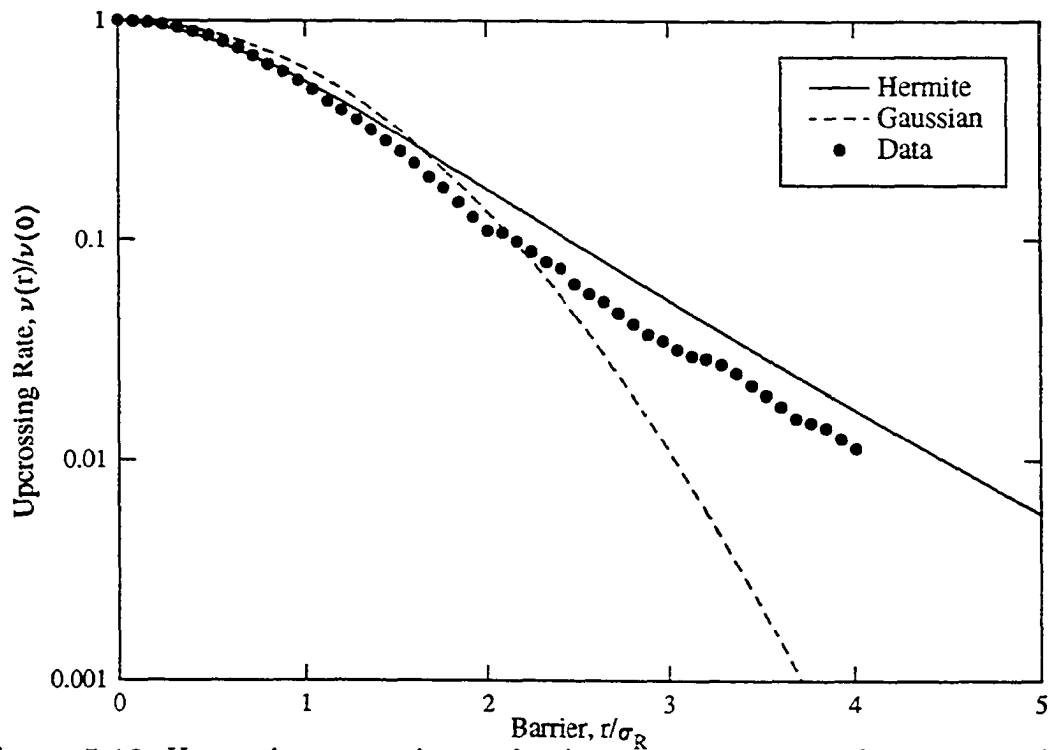


Figure 5.16: Upcrossing rate estimates for the collision process at location -8.13 m (tandem, $2.5D$) with pretension $[T_1, T_1]$.

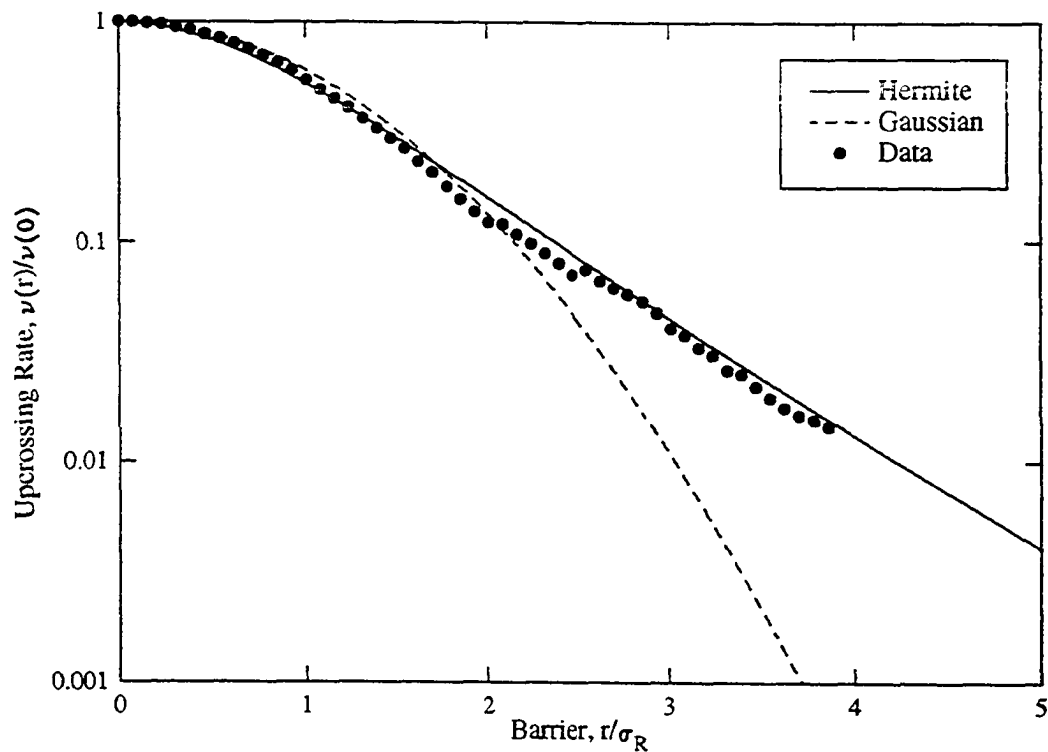


Figure 5.17: Upcrossing rate estimates for the collision process at location -8.13 m (tandem, $2.5D$) with pretension $[T_1, T_2]$.

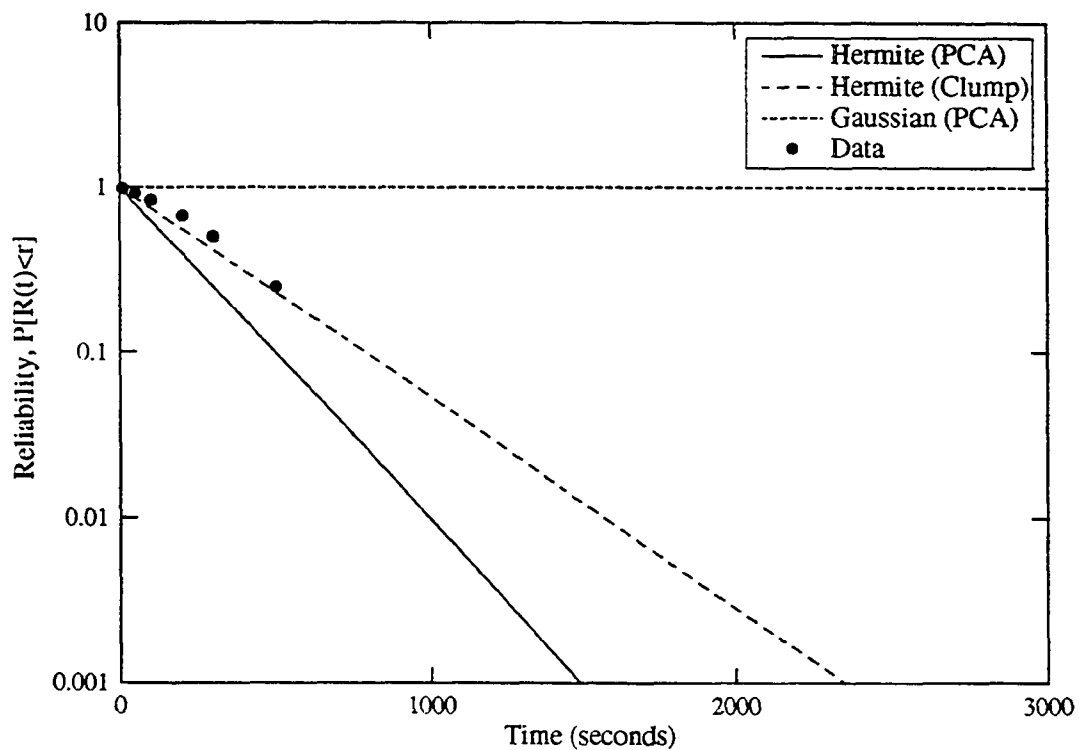


Figure 5.18: Reliability estimates for a barrier of $2.5D$ for the collision process at location -8.13 m (tandem, $2.5D$) with pretension $[T_1, T_1]$.

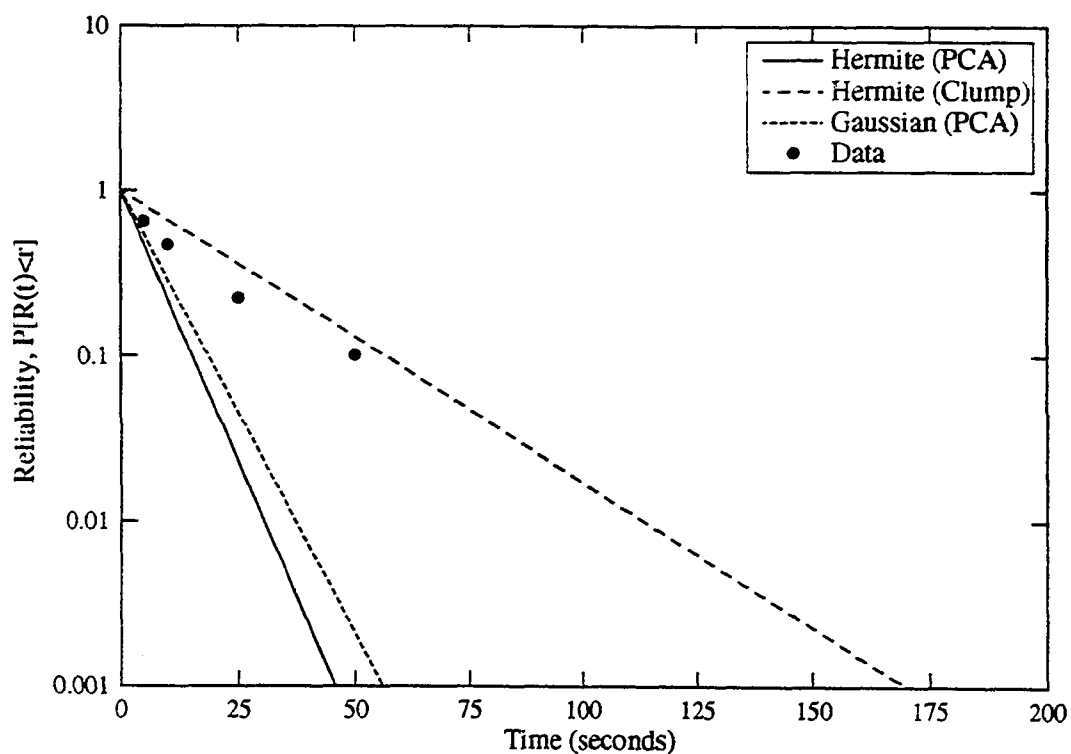


Figure 5.19: Reliability estimates for a barrier of $2.5D$ for the collision process at location -8.13 m (tandem, $2.5D$) with pretension $[T_1, T_2]$.

(Equation 5.28), with a Gaussian estimate based on PCA and limited reliability estimates obtained from the data. Figure 5.18 considers the pretension case $[T_1, T_1]$. The normalized barrier level is 6.1σ ($r = 0.079375$ m), a high barrier. The figure indicates that the Hermite (PCA) estimate of the reliability is conservative, while the Gaussian (PCA) is very unconservative, predicting almost 100% reliability over the entire duration. The Hermite estimate accounting for clumping (second-order) compares very well with the limited results obtained directly from the data.

Figure 5.19 is for the pretension case $[T_1, T_2]$ where the normalized barrier level is 2.6σ . This is a much lower barrier than the previous example. Once again the Hermite (PCA) estimate is conservative, while the Gaussian (PCA) estimate is also conservative due to the low barrier level. The Hermite (clump) compares well with the data, though a little unconservative for all durations, but this could also be due to the larger variability associated with those data points.

Figures 5.20 and 5.21 present the reliability, $P[R(T) < r]$ as a function of the normalized barrier level for the $[T_1, T_1]$ and $[T_1, T_2]$ pretension cases for a duration, $T = 100$ seconds at a spacing $2.5D$. This is the distribution of the extreme value (Equation 5.4). The Hermite model for this problem is given by Equations 5.27 and 5.28 as in the previous case. The Hermite and the Gaussian (PCA) estimates are compared to estimates computed from the data from 100 second segments. Figure 5.20 is for the $[T_1, T_1]$ case and has a computed zero crossing frequency, ν_0 of 1.8518 Hz. The data lie between the Gaussian (PCA) estimate and the Hermite (clump) estimate, with the Gaussian prediction being on the unconservative side. For high barrier levels the data fall very close to the Hermite estimates. The Hermite (PCA) prediction forms a very conservative upper bound. Figure 5.21 presents the same information for the $[T_1, T_2]$ case with a zero crossing frequency of 1.5361 Hz. For this example the data lie between the Gaussian (PCA) and the Hermite (PCA) curves. At low barrier levels, the Hermite estimates are conservative, while for high barriers, the Hermite (PCA) forms an upper bound and the Hermite (clump) is a bit on the unconservative side. Except for the very low barrier values, the Gaussian estimate is very unconservative.

Figures 5.22—5.24 show the same information discussed above for the $[T_1, T_1]$ case for finite element simulations conducted with the two cylinders $2.5D$ apart. The r.m.s. response value of the relative displacement is fairly high and is comparable with the measured response but as seen in Figure 5.22 the simulated relative displacement is almost Gaussian. As seen in Figure 5.24 the reliability predicted from

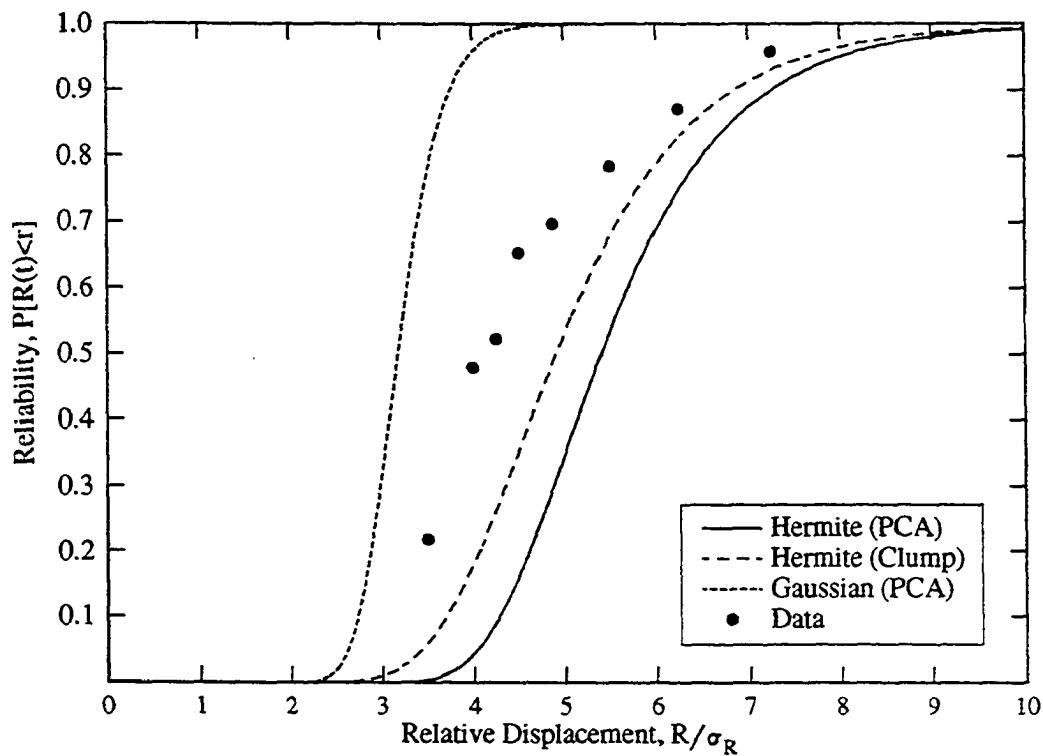


Figure 5.20: Reliability estimates for a duration $T = 100$ seconds for the collision process at location -8.13 m (tandem, $2.5D$) with pretension $[T_1, T_1]$.

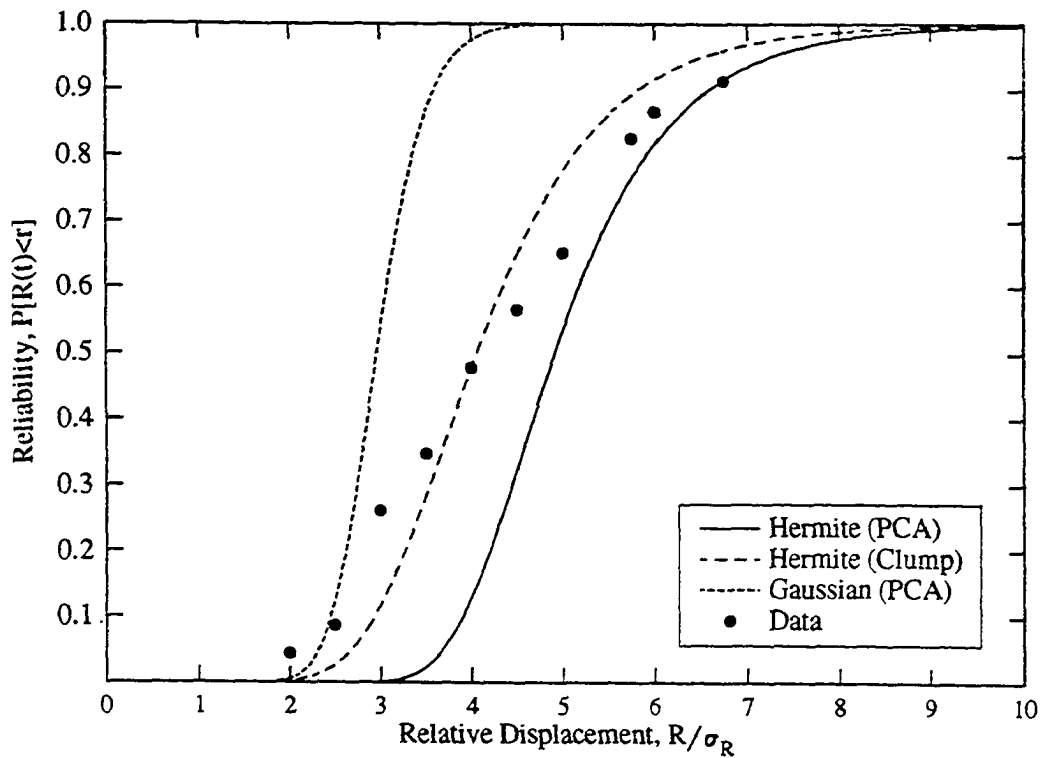


Figure 5.21: Reliability estimates for a duration $T = 100$ seconds for the collision process at location -8.13 m (tandem, $2.5D$) with pretension $[T_1, T_2]$.

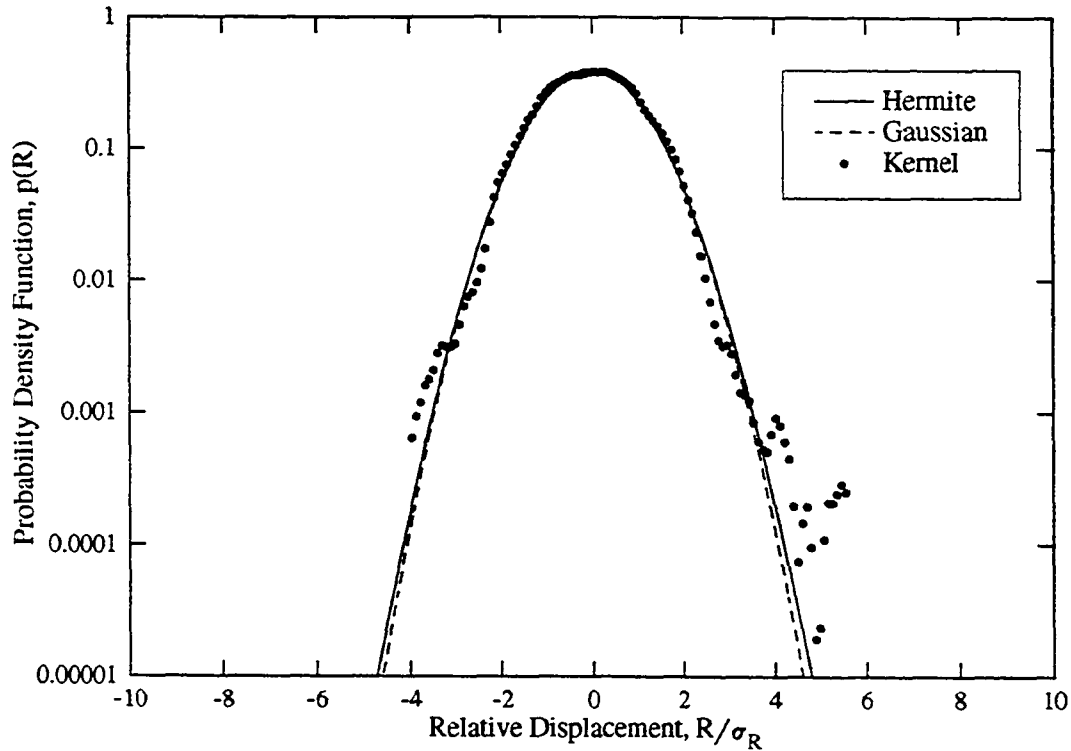


Figure 5.22: Probability density function of the simulated (FEM) collision process at -9.06 m (tandem, $2.5D$) with pretension $[T_1, T_2]$.

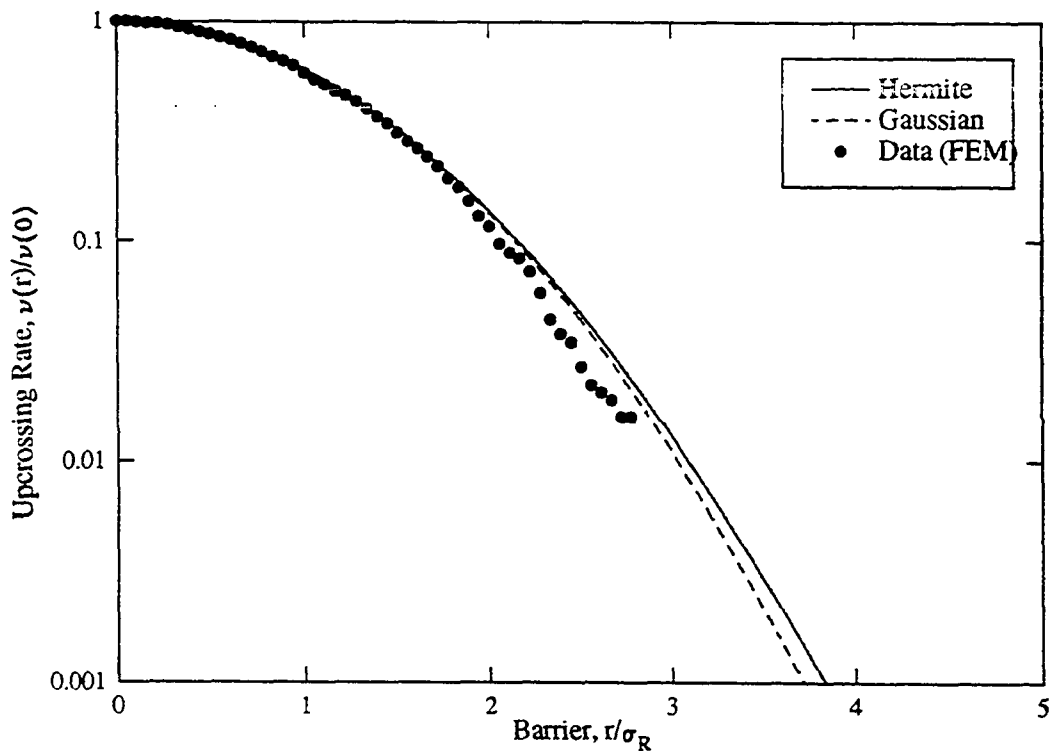


Figure 5.23: Upcrossing rates for the simulated (FEM) collision process at location -9.06 m (tandem, $2.5D$) with pretension $[T_1, T_2]$.

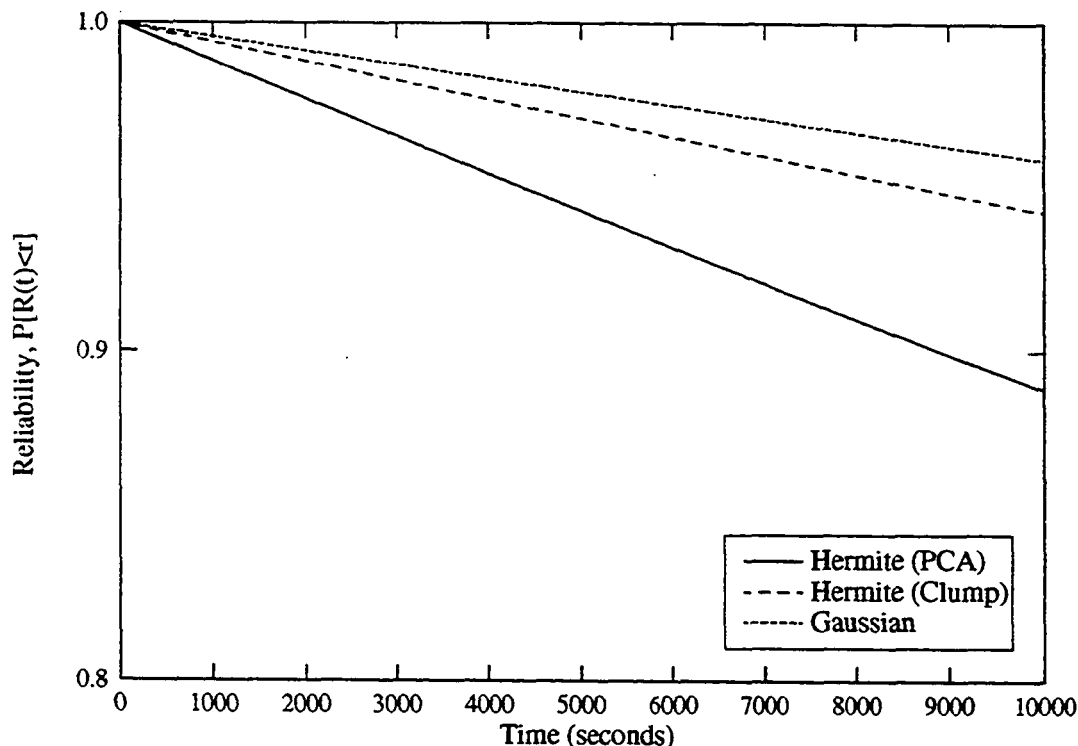


Figure 5.24: Reliability estimates for the simulated (FEM) collision process at location -9.06 m (tandem, $2.5D$) with pretension $[T_1, T_2]$.

these simulations is very high when compared to that from the experiments. This again shows the importance of the interaction phenomena between the cylinders not accounted for in the finite element formulation.

5.4 Summary

The collision behavior between the pair of cylinders arranged in tandem was first presented in the form of graphs obtained from the data. Cylinders were observed to collide under conditions when the pretension conditions for both cylinders were the same $[T_1, T_1]$, and when they were different $[T_1, T_2]$. The r.m.s. relative displacement was seen to be fairly large over the middle to bottom portion of the cylinders, i.e., in the region where the cylinders were free to oscillate and where the effective tension (stiffness) was less than in the forced region of the cylinder.

The objective behind the analysis of the collision behavior in this study was to provide some insight into the collision process between the two cylinders. The data obtained from the experimental program were limited to a few specific cases in the tandem orientation. The collision behavior was formulated as a random process with a collision being equivalent to a barrier crossing. This allowed the use of the first-

passage time and barrier crossing formulations from probabilistic mechanics which have been the topic of active research for many decades. The Poisson crossings assumption (PCA) was introduced and discussed in terms of the average upcrossing rate (first-order estimate) and models accounting for the tendency of crossings to occur in clumps (second-order estimate). The measured response of the cylinders was observed to be non-Gaussian due to the nonlinear wave loading on the slender structures. Non-Gaussian estimates of the extreme value problem were obtained using the Hermite transformation model.

Comparison of the Hermite and Gaussian estimates of the pdfs, upcrossing rates and the reliability distributions, with non-parametric estimates from the data show the importance of accounting for the non-Gaussianity of the response in estimating extreme statistics or the reliability of the system. For very high barriers, which is generally the area of interest, the Gaussian (PCA) approach was very unconservative, even though for Gaussian processes the Gaussian PCA formulation is conservative for low barriers and asymptotically correct for high barriers. The non-Gaussian Hermite estimates were seen to predict the extreme response very well, with the first-order Hermite (PCA) providing a conservative upper bound and the second-order Hermite estimate accounting for the clumping providing a fairly accurate estimate of the reliability for all cases considered. This also indicated the appropriateness of accounting for the crossing of barriers in clumps and the response bandwidth in terms of the energy fluctuation parameter formulated by (Winterstein and Cornell 1985). The comparisons also indicated the appropriateness of the non-Gaussian formulation of the first-passage problem to describe the collision behavior of the cylinder.

6. SUMMARY AND CONCLUSIONS

This research study focused on the interaction of regular and random surface waves with a pair of flexible cylinders, representative of TLP tendons or risers in 1006 m of water. The main emphasis was on studying the mean square and extreme response of the cylinders as a function of wave and structural parameters. Due to the complexity and uncertainty of the wave-flexible structure interaction and the probabilistic nature of the incident wave kinematics, the phenomenon was studied by making an extensive experimental investigation and analyzing the extreme response in a probabilistic framework. A major emphasis of the experimental program was on the accurate scaling of the fluid and structural properties important in modeling the dynamic response of the cylinders. The data obtained were also used in conjunction with probabilistic models to study the extreme response and the collision behavior of the cylinders.

The main findings and conclusions of this study addressed the categories:

- distorted scale modeling methodology and application;
- fundamental fluid-structure interaction phenomenon; and
- probabilistic modeling and model verification based on large scale test data.

This study provided further development of the ideas on multiple scale model tests and provided a real application. The experimental program which was successfully completed, yielded a wealth of new information on the behavior of long, slender flexible cylinders in waves. Conventional finite element models were employed first as a design tool to optimize the number and locations of curvature sensors and later as a means of comparing predictions with the measured data. Both the strengths and weaknesses of the finite element model were identified and new insight gained regarding further development of numerical models. Due to the random nature of the phenomenon a probabilistic approach to analyzing the collision behavior was utilized with special consideration of non-Gaussian processes. The first-passage formulation of the collision behavior was found to be very appropriate and the importance of considering the non-Gaussian nature of the response was repeatedly demonstrated for various extreme response estimates.

6.1 Distorted Scale Modeling Methodology and Application

Distorted scale modeling was shown to be required to model deepwater structures at reasonably large scales, even in deep wave basin facilities like the wave basin at the OTRC. The methodology was outlined by the consideration of three examples of increasing difficulty. The inspectional analysis approach (Le Méhauté 1965) was used to derive consistent distorted scale relationships from the equations of motion. The approach was first applied to a uniform beam under constant tension and the distorted scale relationships were shown to be consistent, scaling the natural frequencies and lateral displacement with the horizontal scale as required. Distorted scale laws were then derived for a TLP tendon or riser, allowing for a uniformly varying tension. Due to the physics of the problem involved, the mass and weight did not scale consistently. Guidelines were presented to arrive at consistent models by maintaining the mass ratio from the prototype and adjusting the pretension to provide the desired natural frequencies. The final example illustrated the usefulness of the distorted scale modeling technique by applying it to model a TLP in 2000 m of water. The hull was scaled using the horizontal scale only, equivalent to the scale used for the waves, while the vertical scale of the tendons and risers were distorted by the ratio of tank depth to prototype depth. This allowed the determination of model scale based on the optimal operating conditions of the wave basin rather than the available depth. This is especially important in the conceptual testing of deepwater structures where tests are conducted to study the overall behavior all the components of the structure.

The flexible cylinder models used in the experimental investigation were designed using the distorted scale relationships derived. A horizontal scale of 1:25 and a vertical scale of 1:60 were chosen based on the performance characteristics of the wave basin and the prototype structure considered. Free vibration tests of the models showed the success achieved in modeling the dynamic characteristics. Due to the requirement of knowing the displacement field over the entire length of the cylinder direct displacement measurements could not be made. Unique instrumentation and techniques were developed to accurately estimate the displacement from discrete measurements of curvature along the length of the cylinder. The curvature data were then integrated to obtain the displacement. Extensive finite element simulations were performed to optimize the number and location of the transducers. Other measurements included the inline and transverse top and bottom reactions and variation of cylinder tension. A total of 60 channels of data were acquired for the paired cylinder tests. Tests were conducted with 4 regular wave conditions and several random wave

simulations from a 100 year JONSWAP random wave spectrum. A total of 160 regular and random wave tests were conducted for both the single and paired cylinder configurations.

6.2 Fluid-Structure Interaction Phenomena

The single cylinder data were first analyzed as a function of non-dimensional parameters like the Keulegan–Carpenter number and the reduced velocity to provide comparison with previous experimental results in steady and harmonic flow. The comparisons showed agreement with the classification of the vortex shedding process as a function of the Keulegan–Carpenter number but did not agree entirely on the classification of the frequency of maximum response as a function of reduced velocity, especially for high Keulegan–Carpenter numbers. At high Keulegan–Carpenter numbers the cylinder response was very complicated and irregular, with peaks at several wave harmonics of the incident wave frequency and at several natural frequencies of the cylinder. Maximum response occurred at reduced velocities out of the range suggested by Blevins (1990). Comparison of the single cylinder inline response results with the finite element model predictions showed the ability of the finite element model to provide reasonable agreement with the cylinder response at the wave frequency but failed to predict the high frequency response. The high frequency content of the inline response measurements was shown to be correlated to the transverse response indicating that flow separation, not modeled by the finite element program, induced both transverse and inline response at frequencies higher than the incident wave frequencies. The high frequency oscillations, though causing small displacements, had high values of curvature (bending stress) and for many cases the r.m.s. transverse curvature was equal to or greater than the inline curvature. This was also true for the random wave simulations.

The fluctuation of cylinder tension, though not the focus of this study, was a very important system characteristic. For the long regular waves a large mean tension was observed, consistent with a constant drift force acting on the cylinder. This constant tension was observed to change the natural frequencies of the cylinder. For random waves, the mean was observed to be slowly varying, once again consistent with the viscous drift force. Maximum tension fluctuations were observed to be greater than 50% of the applied pretension. This tension behavior could have a major influence on the fatigue life of the tendons and further study is warranted.

The paired cylinder tests were analyzed to provide some insight into the wave

interaction with the pair of flexible cylinders as a function of orientation and spacing with respect to the incident waves. Interaction ratios, comparing the paired cylinder r.m.s. response to that of a single cylinder, showed that the paired cylinder response varied between 0.8 to 1.2 times that of a single cylinder. Most of the variation in response occurred in the proximity and wake-proximity regions between $2.5D$ and $5D$. The paired cylinder interference ratios were based on r.m.s. estimates and thus cannot be considered as a global shielding or interference coefficient for structural design of such systems as they do not account for changes in frequency and phase of the response. This was illustrated by analysis that showed that even though the r.m.s. response estimates showed very little variation, the response behavior in frequency and phase was also influenced by the presence of another cylinder. For the cylinders in tandem, the displacement spectrum of the rear cylinder showed a lot more high frequency content than that of the cylinder in front, indicating possible influence from flow separation from the cylinder in front.

6.3 Probabilistic Modeling of the Collision Behavior

The relative displacement process measured between the two cylinders in tandem was compared to similar processes obtained from finite element simulations. Based on the comparisons it was seen that the change in phase due to cylinder spacing (forcing phase) was not as important as the difference in cylinder pretensions, which caused a structural response difference in amplitude, frequency and phase. For cylinders with equal pretensions the r.m.s. relative displacement measured was much greater than that predicted by the finite element program. This was hypothesized to be due to the hydrodynamic interference between the two cylinders caused by flow separation and vortex shedding about the cylinder modifying the wave kinematics to affect the response of the cylinders. This was also evident for the case with different pretensions where the experimentally measured response was much greater than the finite element predicted response. The hydrodynamic coupling was identified as an important mechanism that influences the relative motion; however it was noted that presently no adequate analytical or numerical solution exists to address the change in wave kinematics due to flow separation around cylinders for the flow conditions considered.

The relative displacement/collision process was seen to be a function of three main mechanisms : (1) change in structural response amplitude, frequency and phase due to differences in cylinder pretension, (2) change in phase due to spacing between the

cylinders, and (3) the hydrodynamic interference between the cylinders caused by flow separation and vortex shedding from the cylinders. Some examples of collisions observed during the experimental program were presented, indicating the various mechanisms described. Collisions were observed at a spacing of $2.5D$ for all three pretension conditions tested. At spacings greater than $5D$, the spacing was large enough to prevent collisions for the cylinder and wave parameters considered in this study.

The collision behavior was formulated as a random process with a collision being equivalent to the process crossing a barrier equal to the spacing between the cylinders. This allowed the application of the classic first-passage and barrier crossing formulations from probabilistic mechanics. The formulation of the first-passage time and related extreme value problem was introduced and the Poisson crossings assumption (PCA) approach described. As the response measurements were observed to be non-Gaussian in nature with large kurtosis, the results were extended to account for non-Gaussian behavior using the Hermite transformation approach of Winterstein (1988). The problem associated with barrier crossings occurring in clumps, especially for low barriers and narrow-band processes, was described and approaches to account for this behavior addressed.

Comparisons were made between the non-Gaussian (Hermite), Gaussian and non-parametric estimates for the probability density function (pdf), upcrossing rates and the first-passage time. The pdfs showed large tails associated with the high kurtosis, characteristic of drag-loaded structures. The Hermite model agreed very well with the non-parametric estimate, while the Gaussian estimate severely underestimated the tails. The upcrossing rate predicted by the Hermite model also fit the data obtained from an upcrossing analysis well, and once again was underestimated by the Gaussian estimate. For the reliability estimates, the Hermite (PCA) model (first-order) was observed to be a conservative lower bound for all response levels. The Gaussian estimate (PCA) was found to be very unconservative for high barriers and conservative for very low barriers. The Hermite model accounting for the clumping and response bandwidth (second-order) using the energy fluctuation model was observed to be particularly effective in predicting the reliability of the system fairly accurately. These comparisons showed the appropriateness of the first-passage formulation for collision behavior and the importance of accounting for the non-Gaussian nature of the response in determining the extreme statistics.

6.4 A Perspective on Future Research

This study represents an extensive experimental investigation of the wave interaction with a pair of long, flexible cylinders. The test program was designed to provide a reasonable amount of data to meet the various objectives of the study. However, due to the complexity of the wave-structure interaction phenomenon being considered and the large number of wave and structural parameters influencing the phenomenon, there are several areas in which future research, both experimental and analytical, can provide a better understanding of the phenomenon.

A total of 160 tests were conducted with regular (96) and random (64) waves for both the single (20) and paired cylinder (140) configurations. The paired cylinder tests were conducted at various orientations and spacings with an emphasis on the tandem (0°) orientation. The influence of pretension difference was studied for a few specific cases.

The data analysis to understand the phenomenon focused on regular wave tests to identify the fluid-structure interaction process and random wave seastates to provide more realistic estimates of the overall response. The regular wave analysis showed markedly different response behavior as a function of Keulegan-Carpenter number but could not be classified as done in previous experimental studies for more idealized systems. To classify the response a more detailed test program with regular waves is required where the influence of wave parameters like period and height, and the structural parameters like the cylinder diameter and dynamic characteristics are explored to aid in response behavior estimation and classification.

The characterization of the paired cylinder tests as a function of orientation and spacing was successful in illustrating the interaction phenomenon for the ranges considered. However, the focus was on the tandem orientation, and for the other orientations only two spacings each were considered. The analysis also indicated the changes in frequency and phase of the response, not characterized by the r.m.s. estimates. A better understanding of this interaction could be developed by defining a finer test grid and extending the range of the test region. Other parameters like cylinder pretension difference also need to be considered.

The collision behavior study focused on the tandem arrangement of the cylinders for a limited number of spacings and pretension conditions. The study has indicated the importance of the pretension difference on the relative displacement process which requires further study using experimental data and numerical simulations. The extreme random wave tests provided data for comparison with extreme value prediction

models but the verification of these models would be enhanced by larger data sets.

Comparisons between the experimental results and the finite element model based on the Morison's equation, indicated the high frequency response observed in the experimental data is an important feature not modeled by the Morison's equation. The development of a model accounting for the transverse loading due to waves, and its coupling with the inline loading, would greatly enhance numerical estimates of the cylinder response. This would involve obtaining a better understanding of flow separation around cylinders for the wave conditions considered and its influence on the wave kinematics in the proximity of the cylinder. This could then be extended to studying the hydrodynamic coupling between the two cylinders, shown to be an important mechanism in determining the relative motion between a pair of cylinders. This obviously ties in with the research effort described concerning classification of cylinder behavior to provide the basis of development and verification of such a model.

Finally, the above discussion of future research apply to direct extensions of the research conducted in this study. There are several broader avenues in which this research can be expanded. Some examples concern the influence of wave directionality, currents, the combination of waves and currents, the difference in cylinder physical properties, groups of cylinders, changes in the top boundary condition to represent vessel motion, etc. This research study provides a strong foundation for future research efforts in these areas.

REFERENCES

- [1] American Petroleum Institute (1987). *Recommended practice for planning, designing and constructing fixed offshore platforms*. API Recommended Practice 2A (RP 2A), 17th edition, Washington, DC.
- [2] Blevins, R. D. (1990). *Flow-induced vibration*. Van Nostrand Reinhold, New York, NY.
- [3] Borthwick A. G. L., and Herbert, D. M. (1988). "Loading and response of a small diameter flexibly mounted cylinder in waves," *J. of Fluids and Structures*, Vol. 2, 479—501.
- [4] Britton, P. (1992). "Offshore oil: how far can they go," *Popular Science*, January, 80—88, 96—97.
- [5] Bushnell, M. J. (1977). "Forces on cylinder arrays in oscillating flow," *9th. Offshore Tech. Conf.*, OTC 2903, 193—198.
- [6] Carneiro, F. L. L. B. (1981). "Some aspects of the dimensional analysis applied to the theory and the experimentation of offshore platforms," *Offshore Engg. Proc.*, 3rd. Int. Symp. COPPE, Brazil, 542—557.
- [7] Chakrabarti, S. K. (1979). "Wave forces on a vertical array of tubes," *Proc. Civil Engg. in the Oceans*, San Francisco, CA, 241—259.
- [8] Chakrabarti, S. K. (1980). "Hydrodynamic coefficients for a vertical tube in an array," *App. Ocean Res.*, 70—80.
- [9] Chakrabarti, S. K. (1990). *Nonlinear methods in offshore engineering*. Elsevier Press, Amsterdam, New York, NY.
- [10] Chen, S. S. (1986). "A review of flow-induced vibration of two circular cylinders in crossflow," *J. Pressure Vessel Tech.*, Vol. 198, 383—393.
- [11] Craig, R. R. (1981). *Structural dynamics: an introduction to computer methods*. John Wiley and Sons, New York, NY.

- [12] Dawson, T. H. (1976). "Scaling of fixed offshore structures," *Ocean Engg.*, Vol. 3, 421—427.
- [13] Demirbilek, Z. (1989). *Tension leg platform: a state of the art review*. ASCE, New York, NY.
- [14] Dillingham, J. T. (1984). "Recent experience in model-scale simulation of tension leg platforms," *Marine Tech.*, Vol. 21, No. 2, 186—200.
- [15] Hunter A. F., Zimmer, R. A., Wang, W-J., Bozeman, J. D., Adams, C. J., Rager, B. L. (1990). "Designing the TLWP," *22nd Offshore Tech. Conf.*, OTC 6360, 147—158.
- [16] King, R., and Johns, D. J. (1976). "Wake interaction with two flexible cylinders in flowing water," *J. of Sound and Vibration*, Vol. 45, No. 2, 259—283.
- [17] Lappegaard, O. T. and Solheim, B. J. (1991). "Snorre project strategies and status," *23rd Offshore Tech. Conf.*, OTC 6626, 617—624.
- [18] Le Méhauté, B. (1962). "Theory, experiments, a philosophy of hydraulics," *J. Hydraulics Div.*, Proc. ASCE, Vol. 88, No. HY 1, 45—66.
- [19] Le Méhauté, B. (1965). "On Froude-Cauchy similitude," *Proc. ASCE Conf. on Coastal Engg.*, Santa Barbara, CA, 327—346.
- [20] Lutes, L. D., Chen, Y-T. T, and Tzuang, S-H. (1980). "First-passage approximations for simple oscillators," *J. of Engg. Mech.*, Vol. 106, No. EM6, 1111—1124.
- [21] Mansard, E. P. D., and Funke, E. R. (1987). *On the reflection analysis of irregular waves*, Div. of Mech. Engg. Tech. Report TR-HY-017, National Research Council, Canada.
- [22] Measurements Group, Inc. (1988). *Strain gage based transducers: their design and construction*. Measurements Group, Inc., Raleigh, NC.
- [23] Mercier, R. S. (1991). Personal communication, Shell Development Company, Houston, TX.
- [24] Miles, M. D. (1990). *The GEDAP data analysis software package*, Div. of Mech. Engg. Tech. Report TR-HY-030, National Research Council, Canada.

- [25] Morison, J. R., O'Brien, M. P., Johnson, J. W., and Schaaf, S. A. (1950). "The forces exerted by surface waves on piles," *Petroleum Trans.*, AIME, Vol. 189, 149—157.
- [26] Munson, B. R., Young, D. F., and Okiishi, T. H. (1990). *Fundamentals of fluid mechanics*. John Wiley and Sons, Inc., New York, NY.
- [27] Newton, H. J. (1988). *Timeslab: a time series analysis laboratory*. Wadsworth and Brooks/Cole Publishing Company, Pacific Grove, CA.
- [28] Nigam, N. C. (1983). *Introduction to random vibrations*. The MIT Press, Cambridge, MA.
- [29] Palazzolo, A. B. (1988). *Theory of finite elements*. MEMA 647 Class Notes, Texas A&M University, College Station, TX.
- [30] Pranesh, M. R., and Mani, J. S. (1988). "Similitude engineering—ocean structure interaction," *Ocean Engg.*, Vol. 15, No. 2, 189—200.
- [31] Press W. H., Flannery, B. P., Teukolsky, S. A., and Vetterling, W. T. (1988). *Numerical recipes: the art of scientific computing*. Cambridge University Press, New York, NY.
- [32] Rice, S. O. (1944, 1945). "Mathematical analysis of random noise," *Bell System Technical Journal*, Vols. 23 and 24. (Reprinted in *Selected Papers on Noise and Stochastic Processes*, N. Wax ed., Dover Publications, Inc., New York, N.Y., 1954, 133—294.)
- [33] Sarpkaya, T., and Cinar, M. (1980). "Hydrodynamic interference of two cylinders in harmonic flow," *12th Offshore Tech. Conf.*, OTC 3775, 333—340.
- [34] Sarpkaya, T., and Isaacson, M. (1981). *Mechanics of wave forces on offshore structures*. Van Nostrand Reinhold Company, New York, NY.
- [35] Toro, G. R., and Cornell, C. A. (1986). "Extremes of Gaussian processes with bimodal spectra," *J. of Engg. Mech.*, Vol. 112, No. 5, 465—484.
- [36] Vandiver, J. K. and Chung, T. Y. (1988). "Predicted and measured response of flexible cylinders in shear flow." *Int. Sym. on Flow-Induced Vibration and Noise*, ASME, Vol.1, 1—23.

- [37] Vanmarcke, E. H. (1975). "On the distribution of the first-passage time for normal stationary random processes," *J. of App. Mech.*, Vol. 42, 215—220.
- [38] Verley, R. L. P., and Every, M. J. (1977). "Wave induced vibrations of flexible cylinders," *9th Offshore Tech. Conf.*, OTC 2899, 167—174.
- [39] Wang, J. and Lutes, L. D. (1991). "Nonlinear and non-Gaussian aspects of Morison equation induced fatigue damage," *23rd Offshore Tech. Conf.*, OTC 6608, 451—460.
- [40] Winterstein, S. R. (1985). "Non-normal responses and fatigue damage," *J. of Engg. Mech.*, Vol. 111, No. 10, 1291—1295.
- [41] Winterstein, S. R. (1988). "Nonlinear vibration models for extremes and fatigue," *J. of Engg. Mech.*, Vol. 114, No. 10, 1772—1790.
- [42] Winterstein, S. R., and Cornell, C. A. (1985). "Energy fluctuation scale and diffusion models," *J. of Engg. Mech.*, Vol. 111, No.2, 125—142.
- [43] Zdravkovich, M. M. (1985). "Flow induced oscillations of two interfering circular cylinders," *J. of Sound and Vibration*, Vol. 101, 511—521.

APPENDIX A

FINITE ELEMENT MODEL

A two-dimensional finite element model was developed to study the wave-structure interaction phenomenon. It was used extensively in the design of the physical model, to estimate the wave-induced forces and response, and in the development and optimization of the technique developed to estimate the displacement of the cylinders. The finite element model also provided a comparison with the experimental results.

The two-dimensional finite element model used linear beam elements to model the structure, and the relative motion form of the Morison equation and linear wave theory to model the inline wave force. The cylinders were assumed to be vertical and have pin-pin boundary conditions. The material properties were assumed to be constant over the entire length of the cylinders. The tension was assumed to vary linearly along the length of each element, and was related to the constant tension applied at the top and the effective weight of the cylinder along its length.

A.1 Finite Element Formulation

From Section 2, the equation of motion of a long vertical cylinder, subjected to a top tension, T_o , and a linearly varying tension along its length is

$$EI \frac{\partial^4 x}{\partial z^4} - [T_o - T'z] \frac{\partial^2 x}{\partial z^2} + T' \frac{\partial x}{\partial z} + \rho A \frac{\partial^2 x}{\partial t^2} = f(z, t) \quad (\text{A.1})$$

The discrete finite element representation of Equation A.1 is obtained using Lagrange equations equating the work done by the non-conservative forces on system to the sum of the total kinetic and potential energy of the system (Craig 1981, Palazzolo 1988). The global matrix form of the finite element equations are

$$M\ddot{\mathbf{x}} + C\dot{\mathbf{x}} + K\mathbf{x} = \mathbf{F} \quad (\text{A.2})$$

where, M , C and K are the global mass, structural damping, and stiffness matrices

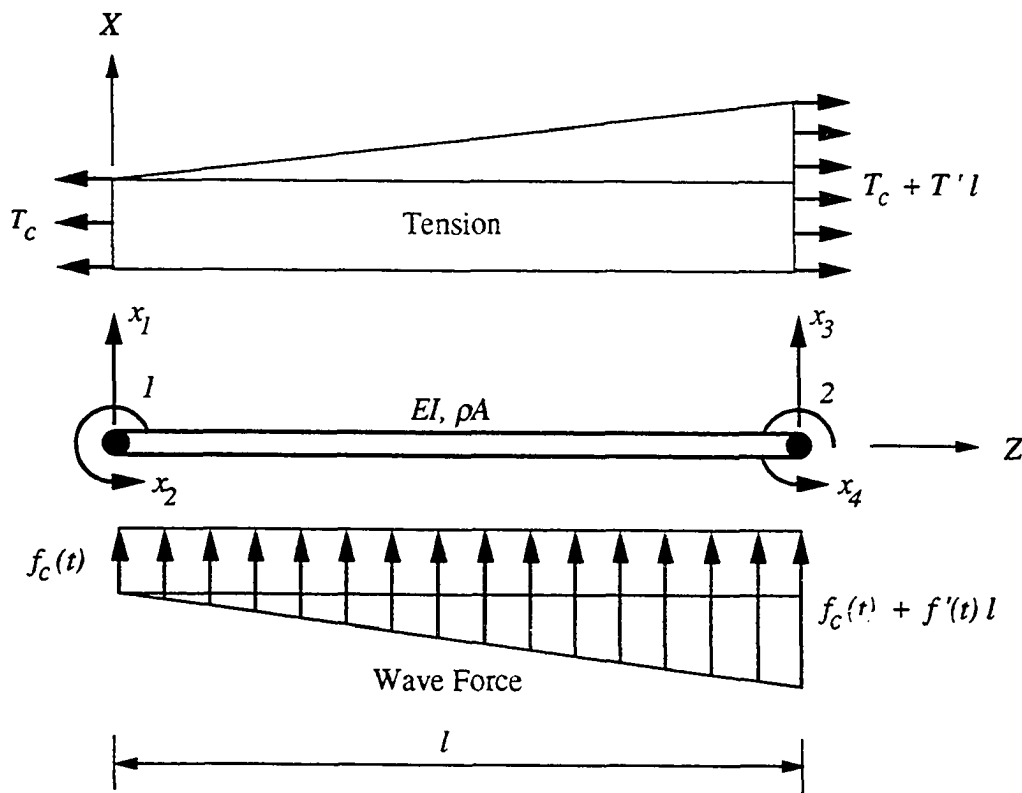


Figure A.1: Linear beam element used in finite element model of flexible cylinder.

respectively, \mathbf{F} is the global external force vector, and \mathbf{x} is the global displacement vector. Each global matrix and the global force vector is assembled from the element matrices and vectors defined in the next section.

A.1.1 Element Matrices

Figure A.1 illustrates the element used for the finite element model. A two-dimensional, 2 node linear beam element was used, with 2 degrees of freedom (translation and rotation) at each node. The assumed tension and wave force distribution on the element are also indicated.

Element mass matrix

The consistent element mass matrix, $[m]$, used for the beam element is

$$[m] = \frac{\bar{m}l}{420} \begin{bmatrix} 156 & 22l & 54 & -13l \\ & 4l^2 & 13l & -3l^2 \\ & & 156 & -22l \\ Sym. & & & 4l^2 \end{bmatrix} \quad (A.3)$$

where \bar{m} is the total mass per unit length of the element and includes the added mass if the element is submerged.

Element stiffness matrix

The element stiffness matrix, $[k]$, is comprised of components from the bending stiffness, EI , and axial tension present in the element. As we have a linearly varying tension along each element, the tension contribution is the sum of a constant tension, T_c , equal to the value at local node 1, and that of a linearly varying tension, T' which has a value of 0 at local node 1 and a value of $T'l$ at local node 2, where l is the length of the element as shown in Figure A.1. Therefore the element stiffness matrix can be assembled as

$$[k] = [k]_{EI} + [k]_{T_c} + [k]_{T'} \quad (A.4)$$

where,

$$[k]_{EI} = \frac{2EI}{l^3} \begin{bmatrix} 6 & 3l & -6 & 3l \\ & 2l^2 & -3l & l^2 \\ & & 6 & -3l \\ Sym. & & & 2l^2 \end{bmatrix} \quad (A.5)$$

$$[k]_{T_c} = \frac{T_c}{30l} \begin{bmatrix} 36 & 3l & -36 & 3l \\ & 4l^2 & -3l & -l^2 \\ & & 36 & -3l \\ Sym. & & & 4l^2 \end{bmatrix} \quad (A.6)$$

$$[k]_{T'} = \frac{T'}{60} \begin{bmatrix} 36 & 6l & -36 & 0 \\ & 2l^2 & -6l & -l^2 \\ & & 36 & 0 \\ Sym. & & & 6l^2 \end{bmatrix} \quad (A.7)$$

Element force vector

Assuming the force to vary linearly over the length of the element, the element external force vector, $\{f(t)\}$, is defined as

$$\{f(t)\} = \frac{f_c(t)}{12} \begin{Bmatrix} 6l \\ l^2 \\ 6l \\ -6l^2 \end{Bmatrix} + \frac{f'(t)}{60} \begin{Bmatrix} 9l^2 \\ 2l^3 \\ 14l^2 \\ -3l^3 \end{Bmatrix} \quad (\text{A.8})$$

where $f_c(t)$ is the constant force over the element and $f'(t)$ is the linear variation over the element, as shown in Figure A.1.

The external forcing due to waves is modeled using the relative motion form of the Morison's equation. The relative motion between the waves and the structure introduces the hydrodynamic damping into the system. The force/unit length, $f(t)$, is expressed as the sum of inertial and drag components

$$f(t) = C_m \rho_w \frac{\pi D^2}{4} a(t) + C_d \frac{1}{2} \rho_w D [u(t) - \dot{x}(t)] | [u(t) - \dot{x}(t)] | \quad (\text{A.9})$$

where, $x(t)$ is the structural displacement, $u(t)$ and $a(t)$ are the wave horizontal particle velocity and acceleration respectively. C_m and C_d are the empirical inertia and drag coefficients respectively. Linear wave theory is used to estimate the wave velocity and acceleration. Random wave forces are computed by simulating a time series from a target spectrum using the random phase method (Chakrabarti 1991). Though wave kinematics generally decay exponentially with depth, the element lengths were chosen small enough to allow an accurate element-wise linear approximation.

A.2 Finite Element Program

The finite element program was written in FORTRAN based on the structure outlined in Palazzolo (1988). IMSL routines were used for the eigen analysis, basic matrix algebra, and random number generation. Output from the program included the structural kinematics, total wave force, and stress and curvature estimates at the specified nodes.

The global matrices were assembled using the element matrices described above and by applying the pin boundary condition at each end. Structural damping was introduced by implementing Rayleigh proportional damping (Craig 1981). The global structural damping matrix was computed from the global mass and stiffness matrices

$$\mathbf{C} = a_0 \mathbf{M} + a_1 \mathbf{K} \quad (\text{A.10})$$

where a_0 and a_1 were obtained by choosing the damping values for any two modes and solving

$$\zeta_r = \frac{1}{2} \left(\frac{a_0}{\omega_r} + a_1 \omega_r \right) \quad (\text{A.11})$$

where ζ_r and ω_r are the damping coefficient and eigenvalue for the mode r . The $a_0 \mathbf{M}$ contribution to ζ_r is inversely proportional to ω_r , while the $a_1 \mathbf{K}$ provides a contribution that increases linearly with ω_r . In this program the damping factors for the first two modes were assumed to obtain the global structural damping matrix.

The system of equations (Equation A.2) was solved in its unmodified non-linear form using the Newmark-Beta scheme (Craig 1981). As structural kinematic terms were included in the external forcing vector, the solution was obtained by iteration. The curvature (stress) estimates were obtained from the displacement solution as described in Palazzolo (1988).

For displacement estimates alone, a 26 element model was found to be sufficient. However, for stress and curvature estimates a 104 element model was needed for accurate results. This was determined by studying the convergence of the finite element results for the desired estimates.

APPENDIX B

INSTRUMENT CALIBRATION AND DATA ACQUISITION

This appendix provides additional details about the instrument calibration and data acquisition. Instrument calibration range, excitation voltage, and channel gains are tabulated in Table B.1. Sample calibration curves are presented to illustrate the loading increments used and the accuracy of the instruments used. Channel lists for the various cylinder configurations providing channel descriptions and comments about specific transducers are also presented.

Table B.1 lists the instrument type and range over which the calibration is performed. All channels were provided with a 2-pole Bessel with a cut-off frequency of 10 Hz, to ensure no aliasing of the data which was sampled at 40 Hz. Figures B.1—B.4 provide sample calibration curves for each transducer to indicate the loading increments and the accuracy of each transducer. Figure B.1 is for a shear web force transducer used to measure the reactions at both ends of the cylinder. The loadcell was loaded over the range indicated in the figure and then rotated 180° and loaded once again to provide a calibration over the complete loading cycle, computed by taking the average of the two calibrations for the two orientations of the loadcell.

Table B.1: Instrument calibration details.

Instrument	Units	Excitation Voltage	Gain	Calibration Range
Top Force	N	7.0 V	10,000	-44.45 to 44.45
Bottom Force	N	7.0 V	40,000	-18.7 to 18.7
Curvature (ABS)	1/m	2.5 V	2,000	-0.033 to 0.033
Tension	N	7.0	4,000	-51.16 to 117.9
Wave Gage	m	n/a	4	-0.48 to 0.56

Figure B.2 presents a calibration curve for a submersible tension cell, where the calibration was performed about a representative mean pretension. The magnitude of the mean tension did not have a significant influence on the calibration factor. Figure B.3 is a calibration curve for one of the curvature transducers. The curvature transducers were calibrated after the entire cylinder was assembled. The cylinder was stretched on the floor under a representative mean pretension and placed over precisely machined curves (tolerance of 0.0254 mm) with the desired curvature. Two such surfaces were used, and by rotating the cylinder through 180° and repeating the procedure, 4 calibration points were obtained. This calibration procedure was found to be very repeatable.

Figure B.4 presents a calibration curve for a wave gage. The wave gages were calibrated daily by placing the wave gages on a calibrator and moving them through the distances indicated in the figure. After calibration the wave gages were placed in their respective positions.

Tables B.2 and B.3 contain the channel lists for the two cylinder orientations used for the single cylinder tests. In the channel descriptions, the subscripts 'B' and 'T' for the force and tension transducers refer to the bottom [-16.1116 m (-52.86 ft)] and the top [1.0668 m (3.5 ft)] of the cylinder respectively. '1' and '2' refer to Cylinder 1 and 2 respectively, while 'X' and 'Y' refer to the inline and transverse response. The two channel lists were necessary as during the experiments some inline curvature transducers failed and the cylinder was rotated through 90° so that sufficient curvature transducers were available to obtain accurate inline displacements. The comments column in the tables indicate the transducers which failed during the testing. Table B.2 is for the configuration when both inline and transverse transducers were functioning and provided estimates of inline and transverse displacement. For the tests conducted with the channel list in Table B.3, accurate estimates of the transverse displacement field could not be obtained. Also note that due to an orientation error, all curvature data for the single cylinder tests should be multiplied by -1 to ensure that positive inline displacement is towards the South of the wave basin and positive transverse displacement is towards the East as per the coordinate system used. This is not necessary for the paired cylinder tests.

Tables B.4 and B.5 present the channel lists for the two configurations used during the paired cylinder tests. This was made necessary due to the failure of transverse curvature transducers in Cylinder 1 (Table B.4). For the tests conducted for the side-by-side (90°) orientation only, Cylinder 1 was rotated through 90° (Table B.5)

so that sufficient curvature transducers were available to provide accurate transverse displacement estimates. However, inline displacements could not be estimated for Cylinder 1 for that orientation. When the cylinders were in the configuration indicated in Table B.4, transverse displacement estimates for Cylinder 1 could not be made accurately. This was the channel list used for all other tests excluding the side-by-side orientation. The comments column also indicates changes in the calibration factors for some loadcells. Note that the primary data file (.pdf) and the port file (.pf) for each test (Appendix C) contains all the calibration and data acquisition information at the time of the test.

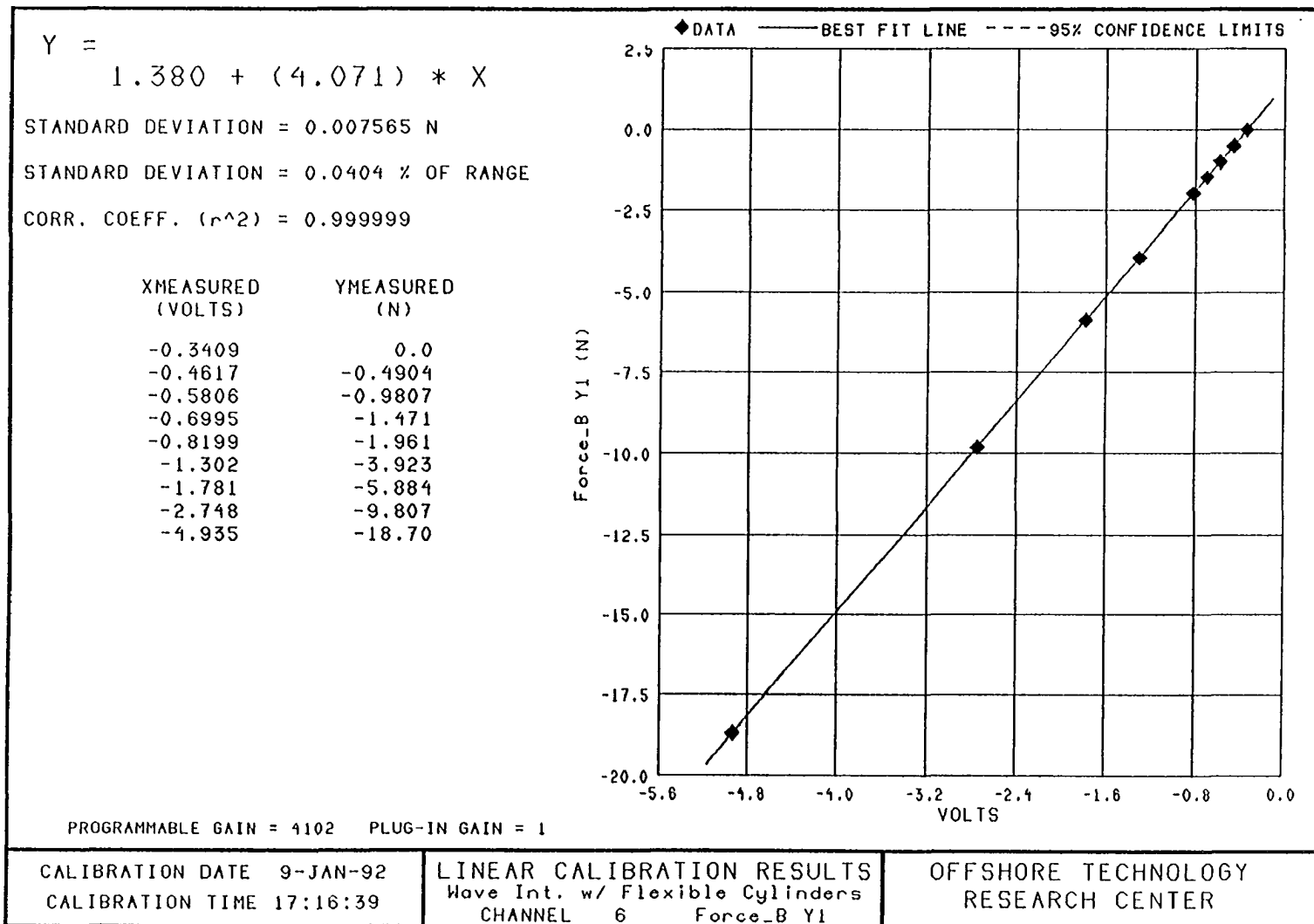


Figure B.1: Sample calibration curve: shear web force transducer.

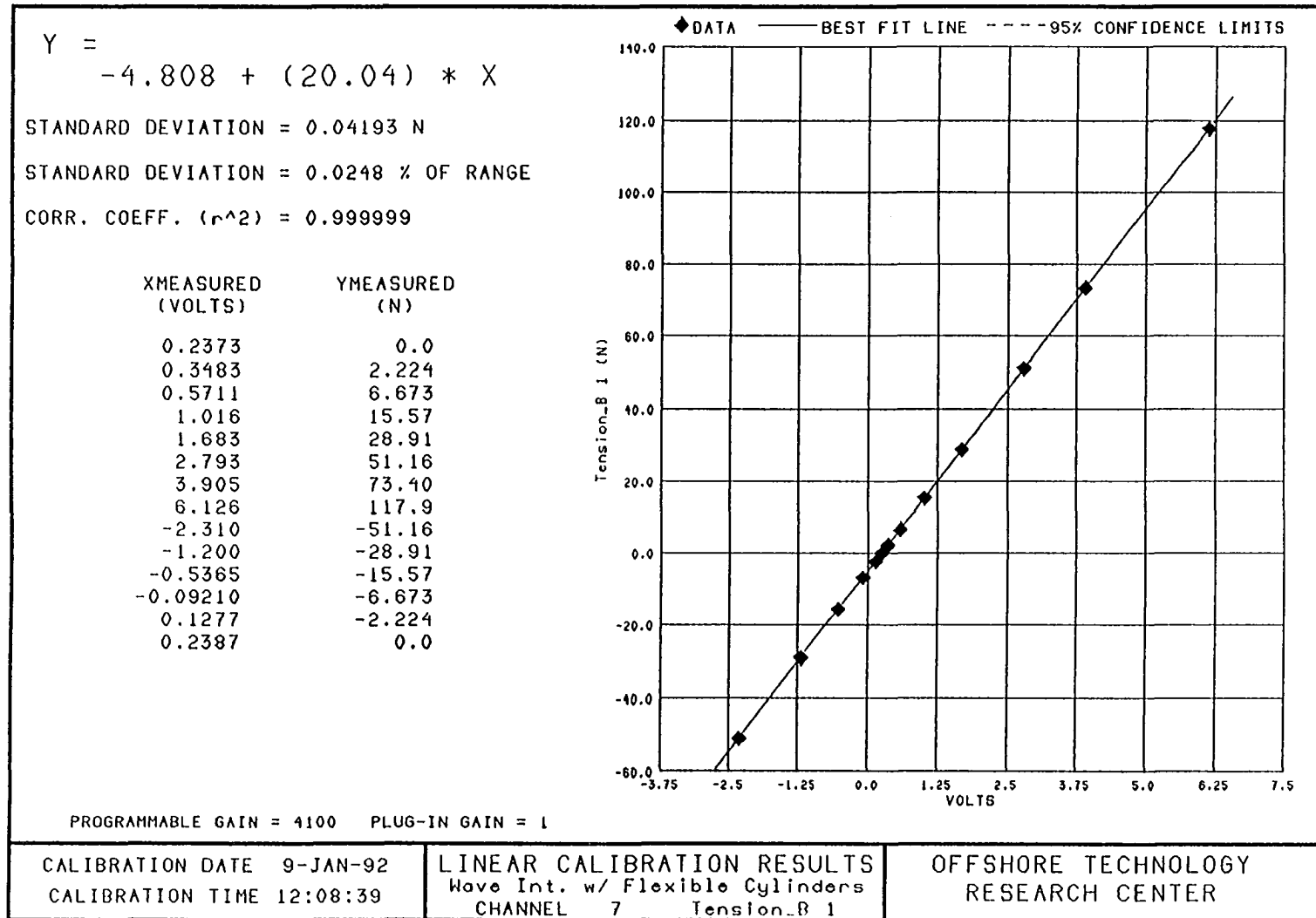


Figure B.2: Sample calibration curve: tension cell.

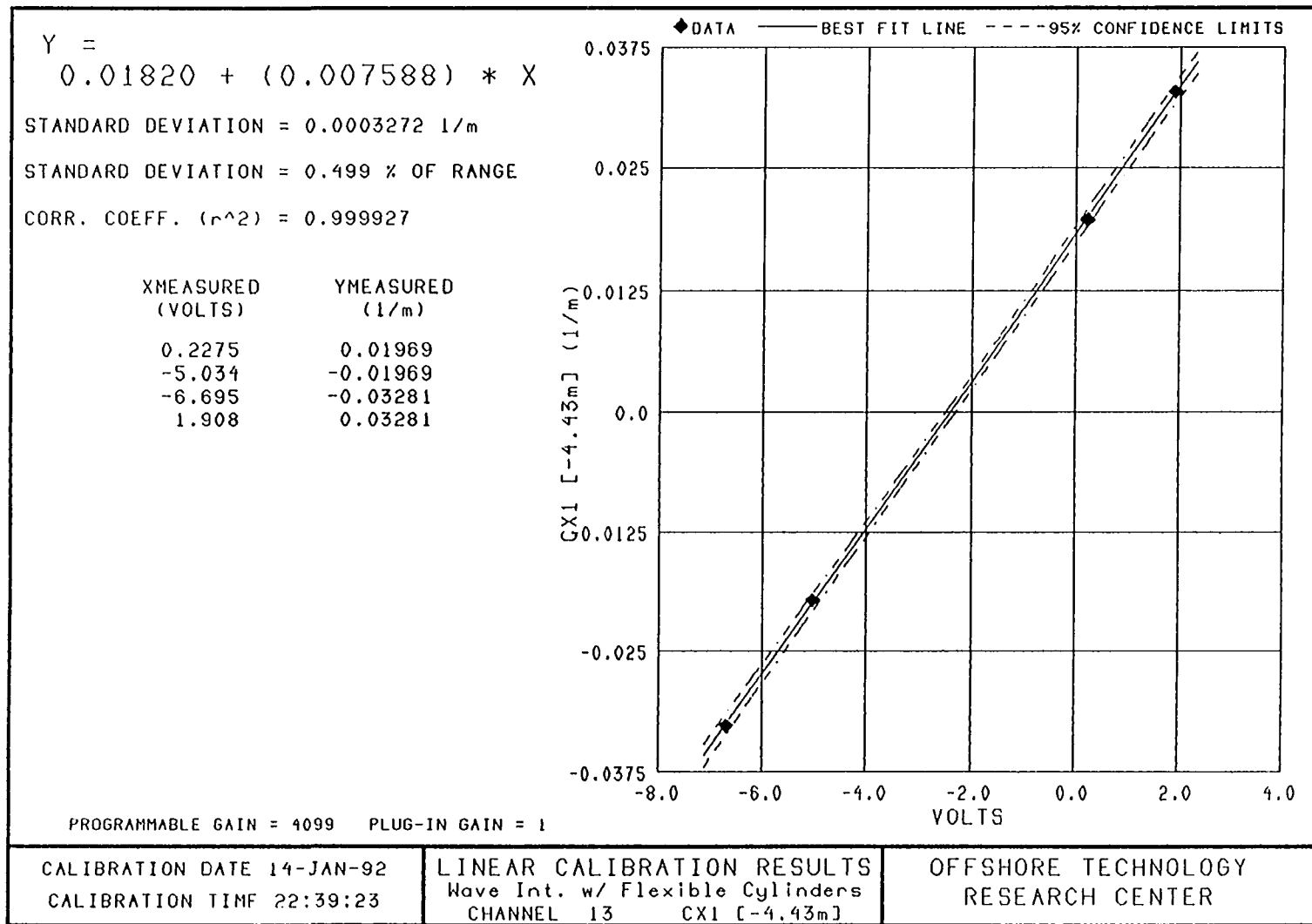


Figure B.3: Sample calibration curve: curvature transducer (ABS).

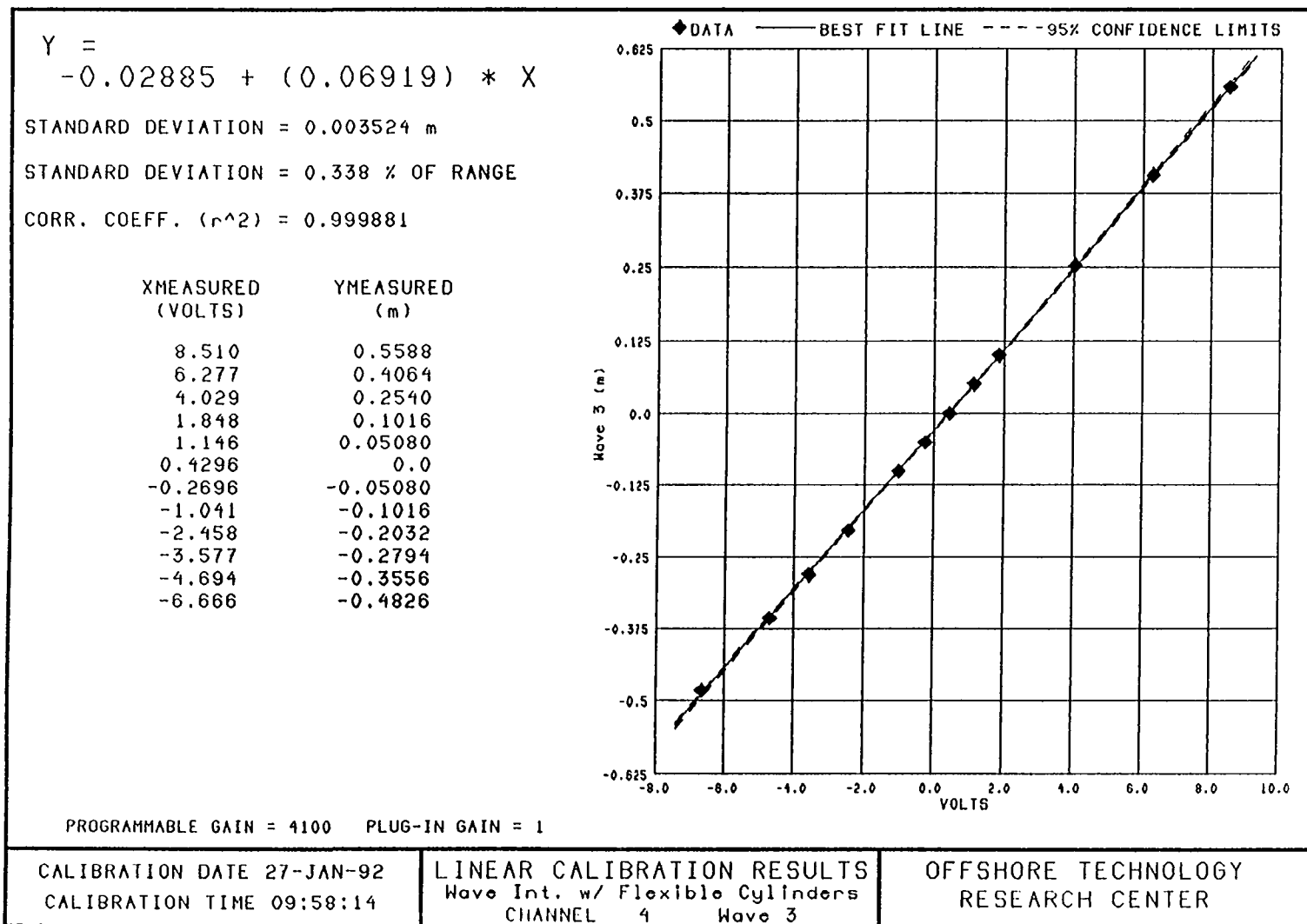


Figure B.4: Sample calibration curve: wave gage.

Table B.2: Single cylinder tests: channel list 1.

Channel #	Channel Description	Instrument Type	Location	Comments
1	Stroke 24	MLDT	Paddle 24	Gain set too high, overanged.
2	Wave 1	Wave Gage	West 5ft	
3	Wave 2	Wave Gage	East 5ft	
4	Wave 3	Wave Gage	Spare	
5	Force_B X1	Force X	Bottom	
6	Force_B Y1	Force Y	Bottom	
7	Tension_B 1	Tension	Bottom	
8	CY1 [-14.57m]	ABS X (Blue 1)	z=-14.5700m	
9	CY1 [-13.30m]	ABS X (Blue 2)	z=-13.3024m	
10	CY1 [-12.16m]	ABS X (Blue 3)	z=-12.1620m	Dead 12/9/91.
11	CY1 [-11.02m]	ABS X (Blue 4)	z=-11.0156m	
12	CY1 [-8.99m]	ABS X (Blue 5)	z=-8.9940m	
13	CY1 [-7.47m]	ABS X (Blue 6)	z=-7.4748m	
14	CY1 [-5.95m]	ABS X (Blue 7)	z=-5.9547m	
15	CY1 [-4.43m]	ABS X (Blue 8)	z=-4.4322m	
16	CY1 [-2.91m]	ABS X (Blue 9)	z=-2.9131m	
17	CY1 [-1.39m]	ABS X (Blue 10)	z=-1.3922m	
18	CY1 [-0.76m]	ABS X (Blue 11)	z=-0.7573m	
19	CY1 [-0.25m]	ABS X (Blue 12)	z=-0.2516m	
20	CY1 [+0.36m]	ABS X (Blue 13)	z=+0.3563m	
21	CX1[-14.57m]	ABS Y (Yellow 1)	z=-14.5700m	
22	CX1[-13.30m]	ABS Y (Yellow 2)	z=-13.3024m	
23	CX1[-12.16m]	ABS Y (Yellow 3)	z=-12.1620m	
24	CX1[-11.02m]	ABS Y (Yellow 4)	z=-11.0156m	Dead 12/9/91.
25	CX1 [-8.99m]	ABS Y (Yellow 5)	z=-8.9940m	
26	CX1 [-7.47m]	ABS Y (Yellow 6)	z=-7.4748m	
27	CX1 [-5.95m]	ABS Y (Yellow 7)	z=-5.9547m	
28	CX1 [-4.43m]	ABS Y (Yellow 8)	z=-4.4322m	Dead 12/9/91.
29	CX1 [-2.91m]	ABS Y (Yellow 9)	z=-2.9131m	
30	CX1 [-1.39m]	ABS Y (Yellow 10)	z=-1.3922m	
31	CX1 [-0.76m]	ABS Y (Yellow 11)	z=-0.7573m	
32	CX1 [-0.25m]	ABS Y (Yellow 12)	z=-0.2516m	
33	CX1 [+0.36m]	ABS Y (Yellow 13)	z=+0.3563m	
34	Tension_T 1	Tension	Top	
35	Force_T X1	Force X	Top	
36	Force_T Y1	Force Y	Top	

Table B.3: Single cylinder tests: channel list 2.

Channel #	Channel Description	Instrument Type	Location	Comments
1	Stroke 24	MLDT	Paddle 24	Gain set too high, overanged.
2	Wave 1	Wave Gage	West 5ft	
3	Wave 2	Wave Gage	East 5ft	
4	Wave 3	Wave Gage	Spare	Not functioning all the time.
5	Force_B X1	Force X	Bottom	
6	Force_B Y1	Force Y	Bottom	
7	Tension_B 1	Tension	Bottom	
8	CX1[-14.57m]	ABS X (Blue 1)	z=-14.5700m	Dead 12/16/92.
9	CX1[-13.30m]	ABS X (Blue 2)	z=-13.3024m	
10	CX1[-12.16m]	ABS X (Blue 3)	z=-12.1620m	Dead 12/9/92.
11	CX1[-11.02m]	ABS X (Blue 4)	z=-11.0156m	
12	CX1 [-8.99m]	ABS X (Blue 5)	z=-8.9940m	
13	CX1 [-7.47m]	ABS X (Blue 6)	z=-7.4748m	
14	CX1 [-5.95m]	ABS X (Blue 7)	z=-5.9547m	
15	CX1 [-4.43m]	ABS X (Blue 8)	z=-4.4322m	
16	CX1 [-2.91m]	ABS X (Blue 9)	z=-2.9131m	
17	CX1 [-1.39m]	ABS X (Blue 10)	z=-1.3922m	
18	CX1 [-0.76m]	ABS X (Blue 11)	z=-0.7573m	
19	CX1 [-0.25m]	ABS X (Blue 12)	z=-0.2516m	
20	CX1 [+0.36m]	ABS X (Blue 13)	z=+0.3563m	
21	CY1 [-14.57m]	ABS Y (Yellow 1)	z=-14.5700m	Dead 12/13/92.
22	CY1 [-13.30m]	ABS Y (Yellow 2)	z=-13.3024m	Dead 12/13/92.
23	CY1 [-12.16m]	ABS Y (Yellow 3)	z=-12.1620m	Dead 12/16/92.
24	CY1 [-11.02m]	ABS Y (Yellow 4)	z=-11.0156m	Dead 12/9/92.
25	CY1 [-8.99m]	ABS Y (Yellow 5)	z=-8.9940m	
26	CY1 [-7.47m]	ABS Y (Yellow 6)	z=-7.4748m	
27	CY1 [-5.95m]	ABS Y (Yellow 7)	z=-5.9547m	
28	CY1 [-4.43m]	ABS Y (Yellow 8)	z=-4.4322m	Dead 12/9/92.
29	CY1 [-2.91m]	ABS Y (Yellow 9)	z=-2.9131m	
30	CY1 [-1.39m]	ABS Y (Yellow 10)	z=-1.3922m	
31	CY1 [-0.76m]	ABS Y (Yellow 11)	z=-0.7573m	
32	CY1 [-0.25m]	ABS Y (Yellow 12)	z=-0.2516m	
33	CY1 [+0.36m]	ABS Y (Yellow 13)	z=+0.3563m	
34	Tension_T 1	Tension	Top	
35	Force_T X1	Force X	Top	
36	Force_T Y1	Force Y	Top	

Table B.4: Paired cylinder tests: channel list 1

Channel #	Channel Description	Instrument	Location	Comments
1	Stroke 24	MLDT	Paddle 24	
2	Wave 1	Wave Gage	West 5ft	Not functioning all the time.
3	Wave 2	Wave Gage	East 5ft	
4	Wave 3	Wave Gage	Spare	Not functioning all the time.
5	Force_T X2	Force X	Top	
6	Force_T Y2	Force Y	Top	Reacalibrated. Multiply by 1.0087
7	Tension_B 2	Tension	Bottom	Gain not set right 1/21/92
8	CX2[-14.57m]	ABS X (Blue 1)	z=-14.5700m	Noisy/dead 1/28/92.
9	CX2[-13.30m]	ABS X (Blue 2)	z=-13.3024m	
10	CX2[-11.02m]	ABS X (Blue 4)	z=-11.0156m	Drifting 1/28/92; dead 1/29/92.
11	CX2 [-8.99m]	ABS X (Blue 5)	z=-8.9940m	
12	CX2 [-7.47m]	ABS X (Blue 6)	z=-7.4748m	
13	CX2 [-4.43m]	ABS X (Blue 8)	z=-4.4322m	
14	CX2 [-2.91m]	ABS X (Blue 9)	z=-2.9131m	
15	CX2 [-1.39m]	ABS X (Blue 10)	z=-1.3922m	
16	CY2 [-0.76m]	ABS Y (Yellow 11)	z=-0.7573m	
17	CX2 [-0.25m]	ABS X (Blue 12)	z=-0.2516m	
18	CX2 [+0.36m]	ABS X (Blue 13)	z=+0.3563m	
19	CY2 [-14.57m]	ABS Y (Yellow 1)	z=-14.5700m	
20	CY2 [-13.30m]	ABS Y (Yellow 2)	z=-13.3024m	
21	CY2 [-11.02m]	ABS Y (Yellow 4)	z=-11.0156m	Drift/overrange 1/28/92.
22	CY2 [-8.99m]	ABS Y (Yellow 5)	z=-8.9940m	
23	CY2 [-7.47m]	ABS Y (Yellow 6)	z=-7.4748m	
24	CY2 [-5.93m]	ABS Y (Yellow 7)	z=-5.9293m	
25	CY2 [-4.43m]	ABS Y (Yellow 8)	z=-4.4322m	Drift/dead 1/21/92.
26	CY2 [-2.91m]	ABS Y (Yellow 9)	z=-2.9131m	
27	CY2 [-1.39m]	ABS Y (Yellow 10)	z=-1.3922m	
28	CY2 [-0.25m]	ABS Y (Yellow 12)	z=-0.2516m	
29	CY2 [+0.36m]	ABS Y (Yellow 13)	z=+0.3563m	
30	Tension_T 2	Tension	Top	
31	Force_B Y2	Force Y	Bottom	
32	Force_B X2	Force X	Bottom	Recalibrated. Multiply by 1.01198
33	Force_B X1	Force X	Bottom	
34	Force_B Y1	Force Y	Bottom	Failed 1/27/92; OK 1/28/92.
35	Force_T Y1	Force Y	Top	After 1/27/92, multiply Chan# 34
36	Force_T X1	Force X	Top	by 1.993003 (NGAIN changed).
37	CY1[-14.57m]	ABS X (Blue 1)	z=-14.5700m	Multiply Chan# 36 by -0.966571

Channel #	Channel Description	Instrument	Location	Comments
38	CY1[-13.30m]	ABS X (Blue 2)	z=-13.3024m	(calibrated after tests).
39	CY1[-12.16m]	ABS X (Blue 3)	z=-12.1620m	
40	CY1[-11.02m]	ABS X (Blue 4)	z=-11.0156m	
41	CY1 [-7.47m]	ABS X (Blue 6)	z=-7.4748m	Dead 1/27/92.
42	CY1 [-5.95m]	ABS X (Blue 7)	z=-5.9547m	
43	CY1 [-4.43m]	ABS X (Blue 8)	z=-4.4322m	
44	CY1 [-2.91m]	ABS X (Blue 9)	z=-2.9131m	
45	CY2[-12.16m]	ABS Y (Yellow 3)	z=-12.1620m	
46	Tension_B 1	Tension	Bottom	Dead 1/21/92.
47	CX1[-12.16m]	ABS Y (Yellow 3)	z=-12.1620m	
48	CY1 [+0.36m]	ABS X (Blue 13)	z=+0.3563m	Dead 1/21/92.
49	CX1[-14.57m]	ABS Y (Yellow 1)	z=-14.5700m	
50	CX1[-13.30m]	ABS Y (Yellow 2)	z=-13.3024m	
51	Tension_T 1	Tension	Top	
52	CX1[-11.02m]	ABS Y (Yellow 4)	z=-11.0156m	
53	CX1 [-8.99m]	ABS Y (Yellow 5)	z=-8.9940m	Dead 1/24/92.
54	CX1 [-7.47m]	ABS Y (Yellow 6)	z=-7.4748m	
55	CX1 [-5.95m]	ABS Y (Yellow 7)	z=-5.9547m	
56	CX1 [-4.43m]	ABS Y (Yellow 8)	z=-4.4322m	
57	CX1 [-2.91m]	ABS Y (Yellow 9)	z=-2.9131m	
58	CX1 [-1.39m]	ABS Y (Yellow 10)	z=-1.3922m	
59	CX1 [-0.25m]	ABS Y (Yellow 12)	z=-0.2516m	
60	CX1 [+0.36m]	ABS Y (Yellow 13)	z=+0.3563m	

Table B.5: Paired cylinder tests: channel list 2.

Channel #	Channel Description	Instrument	Location	Comments
1	Stroke 24	MLDT	Paddle 24	
2	Wave 1	Wave Gage	West 5ft	Not functioning all the time.
3	Wave 2	Wave Gage	East 5ft	
4	Wave 3	Wave Gage	Spare	Not functioning all the time.
5	Force_T X2	Force X	Top	
6	Force_T Y2	Force Y	Top	Reacalibrated. Multiply by 1.0087
7	Tension_B 2	Tension	Bottom	
8	CX2[-14.57m]	ABS X (Blue 1)	z=-14.5700m	
9	CX2[-13.30m]	ABS X (Blue 2)	z=-13.3024m	
10	CX2[-11.02m]	ABS X (Blue 4)	z=-11.0156m	
11	CX2 [-8.99m]	ABS X (Blue 5)	z=-8.9940m	
12	CX2 [-7.47m]	ABS X (Blue 6)	z=-7.4748m	
13	CX2 [-4.43m]	ABS X (Blue 8)	z=-4.4322m	
14	CX2 [-2.91m]	ABS X (Blue 9)	z=-2.9131m	
15	CX2 [-1.39m]	ABS X (Blue 10)	z=-1.3922m	
16	CY2 [-0.76m]	ABS Y (Yellow 11)	z=-0.7573m	
17	CX2 [-0.25m]	ABS X (Blue 12)	z=-0.2516m	
18	CX2 [+0.36m]	ABS X (Blue 13)	z=+0.3563m	
19	CY2 [-14.57m]	ABS Y (Yellow 1)	z=-14.5700m	
20	CY2 [-13.30m]	ABS Y (Yellow 2)	z=-13.3024m	
21	CY2 [-11.02m]	ABS Y (Yellow 4)	z=-11.0156m	
22	CY2 [-8.99m]	ABS Y (Yellow 5)	z=-8.9940m	
23	CY2 [-7.47m]	ABS Y (Yellow 6)	z=-7.4748m	
24	CY2 [-5.93m]	ABS Y (Yellow 7)	z=-5.9293m	
25	CY2 [-4.43m]	ABS Y (Yellow 8)	z=-4.4322m	Drift/dead 1/21/92.
26	CY2 [-2.91m]	ABS Y (Yellow 9)	z=-2.9131m	
27	CY2 [-1.39m]	ABS Y (Yellow 10)	z=-1.3922m	
28	CY2 [-0.25m]	ABS Y (Yellow 12)	z=-0.2516m	
29	CY2 [+0.36m]	ABS Y (Yellow 13)	z=+0.3563m	
30	Tension_T 2	Tension	Top	
31	Force_B Y2	Force Y	Bottom	
32	Force_B X2	Force X	Bottom	Recalibrated. Multiply by 1.01198
33	Force_B X1	Force X	Bottom	
34	Force_B Y1	Force Y	Bottom	
35	Force_T Y1	Force Y	Top	
36	Force_T X1	Force X	Top	Multiply Chan# 36 by -0.966571
37	CX1[-14.57m]	ABS X (Blue 1)	z=-14.5700m	(calibrated after tests).

Channel #	Channel Description	Instrument	Location	Comments
38	CX1[-13.30m]	ABS X (Blue 2)	z=-13.3024m	
39	CX1[-12.16m]	ABS X (Blue 3)	z=-12.1620m	
40	CX1[-11.02m]	ABS X (Blue 4)	z=-11.0156m	
41	CX1 [-7.47m]	ABS X (Blue 6)	z=-7.4748m	
42	CX1 [-5.95m]	ABS X (Blue 7)	z=-5.9547m	
43	CX1 [-0.76m]	ABS X (Blue 11)	z=-0.7573m	
44	CX1 [-2.91m]	ABS X (Blue 9)	z=-2.9131m	
45	CY2[-12.16m]	ABS Y (Yellow 3)	z=-12.1620m	
46	Tension_B 1	Tension	Bottom	Dead 1/21/92.
47	CY1[-12.16m]	ABS Y (Yellow 3)	z=-12.1620m	
48	CX1 [+0.36m]	ABS X (Blue 13)	z=+0.3563m	Dead 1/21/92.
49	CY1[-14.57m]	ABS Y (Yellow 1)	z=-14.5700m	
50	CY1[-13.30m]	ABS Y (Yellow 2)	z=-13.3024m	
51	Tension_T 1	Tension	Top	
52	CY1[-11.02m]	ABS Y (Yellow 4)	z=-11.0156m	
53	CY1 [-8.99m]	ABS Y (Yellow 5)	z=-8.9940m	
54	CY1 [-7.47m]	ABS Y (Yellow 6)	z=-7.4748m	
55	CY1 [-5.95m]	ABS Y (Yellow 7)	z=-5.9547m	
56	CY1 [-4.43m]	ABS Y (Yellow 8)	z=-4.4322m	
57	CY1 [-2.91m]	ABS Y (Yellow 9)	z=-2.9131m	
58	CY1 [-1.39m]	ABS Y (Yellow 10)	z=-1.3922m	
59	CY1 [-0.25m]	ABS Y (Yellow 12)	z=-0.2516m	
60	CY1 [+0.36m]	ABS Y (Yellow 13)	z=+0.3563m	

APPENDIX C

EXPERIMENTAL PROGRAM LOG

This appendix summarizes the test log maintained during the experimental program. The test log appears in chronological order, listing the test name and the name of VAX/VMS saveset under which the data set is archived using the VAX/VMS BACKUP command. Comments made during the experimental program, based on visual observation of the experiments, or concerning experimental conditions and changes in configuration are listed in the comments column.

The experimental log consists of two parts: Table C.1 covers the single cylinder experiments from December 9 through December 16, 1991, and Table C.2 covers the paired cylinder tests conducted from January 21 through February 3, 1992. The data from each test is stored in two binary files. The first file with the extension *.pdf* is called the primary data file and contains the multiplexed raw data from the test. The second file with the extension *.pfi* is called the port file and contains all the calibration and offset information, channel descriptions and units, etc. The test names were constructed based on the cylinder orientation and spacing, and the incident wave conditions.

All single cylinder tests begin with an 'S', all tandem (0°) tests begin with a 'T', and all staggered tests begin with a 'D' followed by a two digit number to indicate the orientation except for the 45° orientation where the 'D' alone is used, e.g., 'D22' implies staggered at 22.5° . The side-by-side orientation (90°) begins with 'SS'. The filenames also contain information of the pretension configuration, cylinder spacing, and the incident wave conditions. For example test SRN1T1.001 is for a single cylinder (S), subjected to random wave simulation 1 (RN1), with pretension, T_1 (T1). The number '001' at the end of the test name signifies that it is the first test run with that configuration. Another example: test TRG14T2.25.002 is the second test run for a pair of cylinders in tandem (T), subjected to regular a wave with a 1.4 second period (RG14), with pretension $[T_1, T_2]$ (T2), and with spacing $2.5D$. The savesets were usually created daily with the VAX/VMS BACKUP command with filenames based on the date the data was acquired.

Table C.1: Single cylinder test log.

Test #	Test Name	Comments
12/9/91		Start of Single Cylinder test program. Channel list in Table B.2. Data archived in saveset 11DEC1991.BAK. Computed displacements archived in D6JAN1992.BAK.
1	FV3T52	Free vibration test, T=52 lb. Natural frequencies OK
2	SRG14LT1	Duration=120 sec. Steady-state response begins after 60+ sec.
3	SRG14HT1	Data Acquired: 180 sec, for a longer steady-state response time history. Cross tank waves set up after 120 sec.
4	SRG20LT1	Data Acquired: 180 sec
5	SRG20HT1	Data Acquired: 180 sec
6	SRG26LT1	Data Acquired: 180 sec
7	SRG26HT1	Data Acquired: 180 sec
8	SRG31LT1	Data Acquired: 409.6 sec, wave maker stopped around 180 sec
9	SRG31HT1	Data Acquired: 180 sec
10	FV4T52	Free vibration test. Tension cells indicated a loss of 0.5N of tension over duration of tests. Natural frequencies OK.
11	FV5T52	Cylinder re-tensioned with 52 lb. Natural frequencies OK.
12	SRN1T1	First random wave test. Duration=409.6 s. DAS_START_DELAY=45 s.
13	SRN2T1	
14	SRN3T1	
15	SRN4T1	
16	SRN5T1	Tension loss=0.6N. Cylinder tension relieved to 26 lb.
12/13/91		Break in test program as repairs were made to the wave absorber. Some Curvature transducers lost over break: Chan # 21, 22. Cylinder rotated through 90 degrees with Channels 8-20 as Curvature X and Channels 21-33 as Curvature Y so that accurate estimates of the inline displacements can be made. Channel list in Table B.3. Stopped making all RG__H waves (large wave heights) as they did not have a good profile due to their size and were also damaging the wave absorber. Data archived in saveset 13DEC1991.BAK. Computed displacements archived in saveset 6JAN1992.BAK.
1	FV6T52	Free vibration test with Tension = 52 lb. Natural frequencies OK
2	SRN6T1	Channel 23 showing some drift.
3	SRN7T1	Channel 23 OK, Channel 8 drifting.
4	SRN8T1	Channel 8 dead.
5	SRN9T1	
6	SRN10T1	
7	SRN11T1	

Test #	Test Name	Comments
8	FVIT31	Free vibration test to determine tension to give riser-like natural frequencies, T2. Tension=31.5 lb, too low.
9	FVIT35	Free vibration test with tension=35.5 lb. Natural frequencies OK.
10	SRG14LT2	Channel 2 (Wave 1) dead. Offsets not taken (test repeated 12/16)
11	SRG20LT2	Duration=120 sec. Stopped 180 sec duration tests as cross tank waves were set up and settling time was increased.
12	SRG26LT2	
13	SRG31LT2	
14	SRN1T2	
12/16/91		MLDT not calibrated properly for previous tests as gain was set too high. Tests were repeated to check repeatability of wave conditions and response. Also provides a comparison between response/displacement estimates from the two orientations of the cylinder (Table B.2 and Table B.3). Data archived in saveset 16DEC1991.BAK. Displacements in D6JAN1992.BAK.
1	FV8T52	Natural frequencies OK.
2	SRG14LT1_002	Channel 23 not working.
3	SRG31LT1_002	
4	SRN1T1_002	
5	FV2T35	Free vibration test to get riser-like frequencies, frequencies too high. After a series of tests determined that 35.5 lb. was too high a tension to produce the desired behavior and reduced tension to get the desired frequencies.
6	FVIT30	Free vibration test, Tension=30.5 lb.
7	SRG14LT2_002	Repeat test as offsets were not taken for the first test.
8	SRN1T2_002	Test repeated to check repeatability.
		End of Single Cylinder Tests.

Table C.2: Paired cylinder test log.

Test #	Test Name	Comments
1/21/91		Start of Paired Cylinder test program. Cylinder 1 was rebuilt to restore the curvature transducers lost during the single cylinder tests. Channel list in Table B.4. Transducers not functioning at start of test: Channel #'s 25, 46, 48. Note: for test #'s 1-10, gain for Tension_B 2 (Channel # 7) was set to 1000 instead of 4000. Multiply data by 4 to get the right values. Gain corrected after Test # 10. Tandem orientation (0 degrees), cylinder spacing 5D, pretension [T1, T1]. Data archived in saveset 21JAN1992.BAK, displacements in D21JAN1992.BAK.
1	FV1T52	Free vibration test with 52 lb. on each cylinder. Natural freq. too high.
2	FV1T50	Free vibration test with 50.5 lb. Test not done well. Repeated.
3	FV2T50	Natural frequencies: Cylinder 1 OK, Cylinder 2 is a little high.
4	FV3T50	Cylinder 2 re-tensioned. OK.
5	TRG14T1_5	Channel 25 not functioning.
6	TRG20T1_5	
7	TRG26T1_5	Observed cylinder motion from East pit. Cylinders seem to move in phase, with Cylinder 2 having more high frequency oscillations than Cylinder 1
8	TRG31T1_5	Same behavior as noted above.
9	TRN1T1_5	No major "collision-type" motions observed.
10	TRN2T1_5	Similar behavior as above.
11	TRN5T1_5	NGAIN set to 4 for Channel 7. Previous tests Channel 7=Channel 7*4
12	TRN6T1_5	
13	TRN7T1_5	Cross tank waves set up with about 3 minutes to go.
14	TRN11T1_5	Channel 2 dead (Wave 1)
1/22/92		Channel 2 (Wave 1) not working and replaced by Wave 3. Placed 5 ft West of lead Cylinder (0, 0). Tandem orientation, spacing 5D, pretension [T1, T2], and spacing 2.5D with pretensions [T1, T2] and [T1, T1]. Data archived in saveset 22JAN1992.BAK and displacements in DPARTIAL_22JAN1992. Remainder in DP2_22JAN1992.BAK.
1	FV1T50_30	Cylinder 1 tension=50.5 lb. OK. Cylinder 2 tension = 30.5 lb. OK.
2	TRG14T2_5	Spacing 5D
3	TRG20T2_5	
4	TRG26T2_5	
5	TRG31T2_5	
6	TRN1T2_5	
7	FV2T50_30	Free vibration test. Cylinder 1 OK, Cylinder 2 too high.
8	FV3T50_30	Free vibration test. Cylinder 2 too high.

Test #	Test Name	Comments
9	FV4T50_30	Free vibration test. Cylinder 2 OK.
10	TRG14T2_25	
11	TRG20T2_25	
12	TRG26T2_25	
13	TRG31T2_25	
14	TRN1T2_25	
15	FV1T50	Free vibration test. Pretension [T1, T1]. Natural Frequencies OK.
16	TRG14T1_25	
17	TRG20T1_25	
18	TRG26T1_25	Observed from pit, cylinders come very close to one another.
19	TRG31T1_25	
20	TRN1T1_25	
21	TRN2T1_25	
22	TRN5T1_25	Videotaped from pit. Observed collision between cylinders.
23	TRN6T1_25	Videotaped.
24	TRN7T1_25	Videotaped, at one instance cylinders seemed to "stick" to one another and move together for a couple of seconds.
25	TRN11T1_25	Last test of day. Cylinder tension relieved.
1/23/92	Side-by-side (SS) tests (90 degrees). As Cylinder 1 did not have sufficient curvature transducers to estimate transverse displacements, Cylinder 1 was rotated through 90 degrees. Port file was updated, (Channel list in Table B.5) CX1 from Table B.4 is now CY1 and all calibration factors for CX1 were multiplied by -1 to account for the orientation change. Spacing 2.5D with pretensions [T1, T1] and [T1, T2] and spacing 5D with pretension [T1, T1]. Data archived in 23JAN1992.BAK, displacements archived in DPAR23JAN1992.BAK, with remainder in DP2_23JAN1992.BAK (Tape 2).	
1	FV23T50	Free vibration test. Tension=50.5 lb. Natural frequencies OK.
2	SSRN1T1_25	Observed cylinders from pit beneath wavemaker (North). Cylinders move in and out towards each other (East-West), especially at the top.
3	SSRN2T1_25	Videotaped. Cylinders were close to colliding.
4	SSRN5T1_25	
5	SSRN6T1_25	Videotaped from over the wavemaker.
6	SSRN7T1_25	Observed cross tank waves
7	SSRN11T1_25	
8	SSRG14T1_25	Videotaped.
9	SSRG20T1_25	Videotaped.
10	SSRG26T1_25	Videotaped.
11	SSRG31T1_25	Videotaped.

Test #	Test Name	Comments
12	FV23T50_30	Free vibration test [T1, T2]. Cylinder 1 OK, Cylinder 2 too high.
13	FV23T50_30_2	Free vibration test. Cylinder 2 too high. (FV23T50_30_002).
14	FV23AT50_30_2	Free vibration test. Cylinder 2 OK. (FV23AT50_30_002).
15	SSRG14T2_25	
16	SSRG20T2_25	Videotaped. No noticeable change from pretension [T1, T1] case.
17	SSRG26T2_25	
18	SSRG31T2_25	
19	SSRNIT2_25	DAS_START_DELAY set at 5.0 sec., data taken 40 sec. earlier.
20	FV23AT50	Free vibration test [T1, T1]. Cylinder 1 too low, Cylinder 2 OK.
21	FV23BT50	Cylinder 1 OK.
22	SSRNIT1_5	Videotaped (4 min). No large excursions.
23	SSRG14T1_5	
24	SSRG20T1_5	Videotaped.
25	SSRG26T1_5	
26	SSRG31T1_5	Last test of day. Cylinder tension relieved.
1/24/92	Cylinder 1 re-oriented 90 degrees to position of 1/21/92, Channel list in Table B.4. Old port file used (PORT1_T.PF with correct calibration factors. Channel 53 (CX1[-8.99m]) dead. Diagonal orientation (45 degrees) with spacing 5D and [T1, T1], and spacing 2.5D with pretensions [T1, T1] and [T1, T2]. Data archived in saveset 25JAN1992.BAK (typo - 24), and computed displacements in D24JAN1992.BAK.	
1	FV24AT50	Free vibration test. Both cylinders OK.
2	DRG14T1_5	Cylinders at spacing 5D.
3	DRG20T1_5	
4	DRG26T1_5	
5	DRG31T1_5	
6	DRNIT1_5	
7	FV24AT50_30	Free vibration test [T1, T2]. Cylinder 1 OK, Cylinder 2 too high.
8	FV24BT50_30	Free vibration test, Cylinder 2 too high.
9	FV24CT50_30	Free vibration test, Cylinder 2 OK.
10	DRG14T2_25	Cylinders at spacing 2.5 D
11	DRG20T2_25	
12	DRG26T2_25	
13	DRG31T2_25	
14	DRNIT2_25	
15	FV24AT50	Free vibration test [T1, T1]. Cylinders 1 and 2 OK.
16	DRG14T1_25	

Test #	Test Name	Comments
17	DRG20T1_25	
18	DRG26T1_25	
19	DRG31T1_25	Test name entered in BUF_CMD as DRG31T_5_001, test renamed to to right name but the old name may still be present in the B header.
20	DRN1T1_25	
21	DRN2T1_25	
22	DRN5T1_25	
23	DRN6T1_25	Channel 21 overanged during test. Reset after test and is OK..
24	DRN7T1_25	
25	DRN11T1_25	Last test of day. Cylinder tension relieved.
1/27/92	Tandem tests focusing on the collision behavior of the cylinders. Channel 34 (Force_B Y2) not functioning and tests run w/o it. Bad channels are 25, 34, 41, 48, 53. Tandem orientation with spacing 2.5D and pretension [T1, T2] and T3 [T2, T1]. Data archived in saveset 27JAN1992.BAK, displacements in DP27JAN1992.BAK (Tape 2).	
1	FV27AT50_30	Free vibration test. Cylinder 1 OK, Cylinder 2 too high.
2	FV27BT50_30	Free vibration test. Cylinder 2 too high.
3	FV27DT50_30	Free vibration test. Cylinder 2 OK.
4	TRN2T2_25	Completing random wave simulations for collision/extreme response TRN1T2_25 run (1/22/92). Cylinders observed from East pit and looked like they were close to colliding.
5	TRN5T2_25	
6	TRN6T2_25	Channel 8 (CX2[-14.5m]) looks noisy.
7	TRN7T2_25	Cross tank waves set up as usual.
8	TRN11T2_25	Videotaped. Observed "collisions".
9	FV27AT30_50	Free vibration test. Cylinder 1 tension=30.5 lb, Cylinder 2 50.5 lb. Cylinder 1 too high, Cylinder 1 OK.
10	FV27BT30_50	Free vibration test. Cylinder 1 too low.
12	FV27CT30_50	Free vibration test. Cylinder 1 too low.
13	FV27DT30_50	Free vibration test. Cylinder 1 OK.
14	TRN1T3_25	Videotaped.
15	TRN2T3_25	Videotaped.
16	TRN5T3_25	Videotaped. Observed "collisions".
17	TRN6T3_25	Videotaped. Probe Wave 3 (Channel # 4) got wet and is not working. Channel # 8 is still noisy.
18	TRN7T3_25	Cross tank waves as usual for this random wave simulation.
19	TRN11T3_25	Videotaped. Last segment on video tape 1.

Test #	Test Name	Comments
20	TRG14T3_25	Channel # 8 dead. Observed from East pit. Cylinder 1 moves more than Cylinder 2.
21	TRG20T3_25	Videotaped. First segment on Tape 2. Cylinders seem to move together and then apart like the side-by-side [SS] tests.
1/28/92		Continuing the tandem tests from 1/27/92. Channel 8 is dead, Channel 34 is working and seems OK. Data archived in saveset 28JAN1992.BAK. (Tape 2).
1	FV28AT30_50	Free vibration tests, Cylinder 2 OK, Cylinder 1 too high.
2	FV28BT30_50	Free vibration tests. Cylinder 1 OK.
3	TRG26T3_25	Videotaped. Channel # 34 cal. factor was too high (-1680 instead of -4.1445). Needs to be accounted for in data analysis.
4	TRG31T3_25	Videotaped.
5	TRN1T3_25_002	Repeated TRN1T3_25_001 to get bottom force measurement (Chan 34)
6	FV28AT50	Free vibration test. Channels 21 and 34 were unplugged and then re-plugged into the NEFF. Drift seems to settle. This was set up as a new procedure for drifting channels (repeated before every test). Cylinder 1 OK, Cylinder 2 too high.
7	FV28BT50	Free vibration test. Cylinder 2 OK.
8	TRG14T1_10	Tandem, spacing 10D
9	TRG20T1_10	
10	TRG26T1_10	Videotaped. (approximately 1:25 pm).
11	TRG31T1_10	
12	TRN1T1_10	Videotaped.
13	FV28AT30	Free vibration test [T2, T2]. Both Cylinders too high.
14	FV28BT30	Free vibration test. Cylinder 1 OK, Cylinder 2 too high.
15	FV28CT30	Free vibration test. Cylinder 2 OK.
16	TRG14T4_10	T4=[T2, T2]
17	TRG20T4_10	
18	TRG26T4_10	
19	TRG31T4_10	
20	TRN1T4_10	
21	FV28CT50	Free vibration test. Cylinder 1 OK, Cylinder 2 too high.
22	FV28DT50	Free vibration test. Cylinder 2 OK.
23	D22RG14T1_25	Staggered arrangement (22.5 degrees), spacing 2.5D. Channel 10 is drifting and overanges.
24	D22RG20T1_25	
25	D22RG26T1_25	Channel # 10 OK.

Test #	Test Name	Comments
26	D22RG31T1_25	
27	D22RN1T1_25	Channel # 10 overaged again.
1/29/92	Continuing Staggered (22.5) tests from 1/28/92. Data archived in 29JAN1992.BAK, displacements in DP29JAN1992.BAK. (Tape 2).	
1	FV29AT50	Free vibration tests. Cylinders 1 and 2 OK.
2	D22RG14T1_5	Channel # 10, 21, 25 overaged. Repeated
3	D22RG14T1_5_2	Channels reset and brought back to range.(D22RG14T1_5_002)
4	D22RG20T1_5	Channel # 10 dead (drifts all over).
5	D22RG26T1_5	Reset time on VAX 3500 to synchronize data acquisition time with video camera clock. The VAX was approximately 10 minutes behind.
6	D22RG31T1_5	
7	D22RN1T1_5	
8	FV29BT50	Free vibration test. Cylinders 1 and 2 OK.
9	D67RG14T1_25	Staggered (67.5 degrees), spacing=2.5D.
10	D67RG20T1_25	
11	D67RG26T1_25	
12	D67RG31T1_25	
13	D67RN1T1_25	
14	FV29CT50	Free vibration test. Cylinder 1 OK, Cylinder 2 too high.
14	FV29DT50	Free vibration test. Cylinder 2 OK.
15	D67RG14T1_5	Spacing = 5D
16	D67RG20T1_5	
17	D67RG26T1_5	
18	D67RG31T1_5	
19	D67RN1T1_5	
1/30/92	Continuing the tandem tests. Spacing= 7.5D, 15D. Data archived in 30JAN1992.BAK, displacements archived in DP30JAN1992.BAK. (Tape 2).	
1	FV30AT50	Free vibration tests. Cylinders 1 and 2 OK.
2	TRG14T1_75	
3	TRG20T1_75	
4	TRG26T1_75	
5	TRG31T1_75	Videotaped.
6	TRN1T1_75	Videotaped.
7	FV30BT50	Free vibration test. Cylinder 1 OK, Cylinder 2 too high.

Test #	Test Name	Comments
8	FV30CT50	Free vibration test. Cylinder 2 OK.
9	TRG14T1_15	
10	TRG20T1_15	
11	TRG26T1_15	
12	TRG31T1_15	File originally named TRG31T1_75_001.PDF;2. Renamed to right name after test. May remain in B header.
13	TRN1T1_15	Probe Wave 3 (Channel #4) got wet.
14	FVT4_001	Free vibration test [T2, T2]. Cylinders 1 and 2 too high.
15	FV30T30	Free vibration test. Cylinders 1 and 2 OK.
16	TRG14T4_15	
17	TRG20T4_15	
18	TRG26T4_15	
19	TRG31T4_15	
20	TRN1T4_15	Last test of day. Cylinder tensions relieved.
1/31/92	Tandem tests at spacing 3.5D. Data archived in saveset 31JAN1992.BAK, (Tape 2). Displacements in saveset D31JAN1992.BAK (Tape 2).	
1	FV31BT50	Free vibration test. Cylinder 2 too high.
2	FV31CT50	Free vibration test. Cylinder 2 OK.
3	TRG14T1_35	Spacing 3.5D
4	TRG20T1_35	
5	TRG26T1_35	
6	TRG31T1_35	
7	TRN1T1_35	
8	TRN5T1_35	Repeated another random wave simulation.
9	FVT5A	Free vibration test T5=[45lb, 50.5lb]. Both cylinders OK.
10	TR14T5_35	Spacing 3.5D. Wave maker hydraulics leaking. Stopped for repairs.
2/3/92	Continuing tests from 1/31/92. Spacing 3.5D, pretension T5. Data archived in saveset 3FEB1992.BAK (Tape 2), displacements in D3FEB1992.BAK (Tape 2).	
1	FV3T45_50	Free vibration test. Cylinder 1 too high.
2	FV3BT45_50	Free vibration test. Cylinder 1 still too high.
3	FV3CT45_50	Free vibration tests. Cylinder 1 too high..
4	FV3DT45_50	Free vibration tests. Both cylinders OK.
5	TRG20T5_35	
6	TRG26T5_35	

Test #	Test Name	Comments
7	TRG3IT5_35	
8	TRNIT5_35	
9	TRN5T5_35	Last test of day.
		End of Paired Cylinder Tests

VITA

Arun Sanjay Duggal was born in London, Great Britain on June 22, 1962. He graduated from St. Joseph's Boys' High School, Bangalore, India in December 1977 and completed his pre-university schooling at Bishop Cotton Boys' School, Bangalore, India in March 1980. He was admitted to the Indian Institute of Technology, Madras, India in July 1980 and graduated with a Bachelor of Technology (B. Tech.) degree in Civil Engineering in May 1985. Arun then entered the Applied Marine Physics Division at the Rosenstiel School of Marine and Atmospheric Science, University of Miami and graduated with a Master of Science (M. S.) degree in Ocean Engineering in December 1987. He then enrolled in the doctoral program in Ocean Engineering at Texas A&M University in January 1988. Arun also worked as a teaching assistant in the Department of Civil Engineering through May 1989, and then as a research assistant for the Offshore Technology Research Center at Texas A&M University until the completion of his Doctor of Philosophy (Ph.D.) degree.

His permanent address is:

143 Golf Links, New Delhi 110003, India.